Simplified Procedures for Estimating Earthquake-Induced Displacements

By

Jorge Luis Macedo Escudero

A dissertation submitted in partial satisfaction of the
requirements for the degree of
Doctor in Philosophy

In

Engineering – Civil and Environmental Engineering

in the

Graduate Division

of the

University of California, Berkeley

Committee in charge:
Professor Jonathan D. Bray, Chair
Professor Raymond B. Seed
Professor Douglas S. Dreger

Fall 2017

Abstract

Simplified Procedures for Estimating Earthquake-Induced Displacements

By

Jorge Luis Macedo Escudero

Doctor of Philosophy in Engineering – Civil and Environmental Engineering

University of California, Berkeley

Professor Jonathan D. Bray, Chair

Engineers find value in using simplified procedures to estimate seismically induced permanent displacements in their preliminary assessments of the seismic performance of earth structures and buildings. This research develops new, robust simplified procedures to estimate shear-induced displacements of earth and waste structures and natural slopes and to estimate shear-induced settlement of structures founded atop liquefiable soils.

Most simplified procedures for estimating seismic slope displacements are based on variations of the Newmark (1965) sliding block analyses. These procedures were developed largely using earthquake ground motions from shallow crustal earthquakes along active plate margins (e.g., California earthquakes). These semi-empirical procedures should not be applied directly to other seismo-tectonic settings, such as subduction earthquake zones, without evaluating their applicability for tectonic settings for which they were not originally developed. In this study, a simplified procedure for estimating seismic shear-induced permanent displacements in slopes located in subduction earthquake zones is developed. The primary source of uncertainty in assessing the likely performance of an earth slope or system during an earthquake is the input ground motion. Hence, a comprehensive database containing 810 recorded ground motions from subduction zone interface earthquakes was developed and used to compute seismic slope displacements. The proposed seismic slope displacement model captures the primary influence of the system's yield coefficient k_y, its initial fundamental period T_s, and the ground motion's spectral acceleration at a degraded period of the slope taken as 1.5 T_s. The new procedure uses the framework of the widely used Bray and Travasarou (2007) method developed for shallow crustal settings. The model separates the probability of "zero" displacement (i.e., < 0.5 cm) from the distribution of "nonzero" displacement, so that low values of calculated seismic displacement do not bias the results. The new seismic displacement model better captures the unique seismic setting of subduction zone earthquakes. It has been validated using observations of 12 case histories of seismic slope performance during recent earthquakes, including the 2011 Moquegua, 2007 Pisco, 2010 Maule, 2011 Tohoku, and 2016 Muisne earthquakes.

Current state of practice procedures typically separate the estimation of the ground motion intensity measure (*IM*) from the estimate of seismic displacement (*D*), given the selected IM hazard level. Thus, *D* is estimated based on a single *IM* value. A straightforward performance-

based seismic slope assessment procedure is proposed which considers the full range of potential *IM* values to estimate seismic slope displacements directly related to a hazard level. Seismic performance is assessed through either a Newmark-type seismic displacement estimate or a calibrated seismic coefficient that can be used in pseudostatic slope stability analyses. The procedures were developed for a wide range of earth systems for shallow crustal earthquakes and subduction zone earthquakes. Currently employed simplified slope displacement procedures do not provide consistent assessments of the actual seismic slope displacement hazard. The proposed procedures can be readily used in practice to perform rigorous performance-based seismic slope displacement hazard assessments.

Liquefaction-induced settlement of shallow-founded buildings continues to produce significant damage during earthquakes. The primary mechanisms of liquefaction-induced building settlement are shear-induced, volumetric-induced, and ejecta-induced ground deformation. The state-of-the practice still largely involves estimating building settlement using empirical procedures developed to calculate post-liquefaction, one-dimensional, reconsolidation settlement in the free-field away from buildings. These free-field analyses cannot possibly capture shear-induced deformations in the soil beneath shallow foundations. Performance-based design requires an improved assessment of liquefaction-induced building settlement. Nonlinear dynamic soil-structure-interaction (SSI) effective stress analyses have shown to be able to capture shear-induced liquefaction building settlement mechanisms.

Dynamic SSI effective stress analyses are performed to identify key trends in the settlement of buildings with shallow foundations affected by soil liquefaction. Over 1,300 dynamic SSI effective stress analyses are performed by systematically varying subsurface conditions and building properties while applying 36 earthquake motions. Shear-induced soil deformation mechanisms govern during strong shaking; whereas volumetric-induced deformation mechanisms contribute more significantly after shaking. The analytical results provide salient insights regarding the key parameters controlling liquefaction-induced building settlement. The relative density of the liquefiable layer is the key soil property, and its thickness is an important soil profile characteristic. Building contact pressure is the most important building parameter, and building width is also important. The ground motion intensity parameters that correlate best with building settlement are standardized cumulative absolute velocity, Arias intensity, and spectral acceleration at 1 s. The post-liquefaction bearing capacity factor of safety indicates when large building settlements are possible.

Volumetric-induced free-field ground deformation may be estimated with available empirical procedures. Although challenging to estimate, ground failure indices and experience can be used to estimate roughly ejecta-induced building settlement. Nonlinear dynamic SSI effective stress analyses are required to estimate shear-induced ground deformation. Results from these analyses identified earthquake, site, and building characteristics that largely control liquefaction-induced building settlement during strong shaking. A simplified procedure is developed based on the results of these analyses to estimate the shear-induced component of liquefaction building settlement. The standardized cumulative absolute velocity and 5%-damped spectral acceleration at 1 s period capture the ground shaking. A new parameter called the liquefaction building settlement index, which is based on the shear strain potential of the site, captures in situ ground conditions. Building contact pressure and width capture the building characteristics. Field case histories and centrifuge test results validate the proposed simplified procedure. Recommendations and an example for evaluating building performance at liquefiable sites are shared.

TABLE OF CONTENTS

ACKNOWLEDGEMENTS

Chapters 1, 2 and 3 of this thesis have been partially funded by the "Programa Nacional de Innovación para la Competitividad y Productividad (INNÓVATE-PERÚ)" under grant 092-14 and were also supported by funding from the Faculty Chair in Earthquake Engineering Excellence, University of California, Berkeley. Financial support for the research presented on Chapters 4, 5 and 6 was provided by the U.S. National Science Foundation (NSF) through grants CMMI-1332501 and CMMI-1561932, INNÓVATE-PERÚ through grant 092-14, and the Faculty Chair in Earthquake Engineering Excellence. The financial support from, the NSF and INNÓVATE-PERÚ, is greatly appreciated. Any opinions, finding and conclusions or recommendations expressed in this thesis do not necessarily reflect the views of either the NSF or INNÓVATE-PERÚ.

I take this opportunity to express my deepest gratitude to my research advisor Prof. Jonathan Bray for his mentorship and continuous support through this research. Prof. Bray is a great mentor and great engineer, but perhaps even more important, he is a great person. I will always see him as a professional and person model to follow, and I feel blessed to have been one of his students. Through this PhD journey, he has helped me to be a better engineer, better researcher and inspired me to be a better person. Prof. Bray's insights, guidance and engineering knowledge were essential in the completion of this research.

I would like to thank Professor Norman Abrahamson, his dedication to teaching is inspiring. Even with his many responsibilities and busy schedule he has always made time to share his knowledge, he was essential on the completion of Chapter 3 of this thesis. I will be always grateful to Professor Armen Der Kiureghian for teaching me the importance of risk and reliability in engineering and for always be responsive to my inquiries. Dr. Thaleia Travasarou was essential in the completion of the research presented in Chapters 2 and 3, she kindly shared technical resources and her vast knowledge in geotechnical earthquake engineering. I express also my gratitude to the dissertation committee formed by Professor Ray Seed and Professor Douglas Dreger for reviewing this PhD thesis and providing insightful comments.

Likewise, I would like to thank the Ph.D. students at Davis Hall for their friendship and for being an integral part of my Berkeley experience. Many thanks to Estefan Garcia, Robert Lanzafame, Heyder Carlosama, Roberto Luque, Christie Hale, Christopher Markham, Zee Beyzaei, Nathaliel Wagner, Michael Gardener, Maggie Parks, Mike George, and Chukwuebuka Nweke. My sincere thanks to the GeoSystems Engineering faculty at UC Berkeley: Professors Raymond Seed, Michael Riemer, Juan Pestana, and Nicholas Sitar. Furthermore, thanks to all the engineers that influenced on my view of engineering and soil mechanics in my early career as Mr. Mike Jefferies and Dr. Ken Been, among many others.

I owe a great debt of gratitude to my family, my parents Jorge Macedo and Aida Escudero, my brother Roger and my 3 nephews, for their endless love and encouragement, for always having confidence in me and supporting me in my endeavors.

Most of all, I would like to dedicate this work to my beautiful wife Jazmin, I am profoundly thankful for your sacrifices, your strength, and for always keeping me motivated during these years. This work could not have begun without your help and commitment.

LIST OF FIGURES

LIST OF TABLES

CHAPTER 1: INTRODUCTION

1.1 OVERVIEW

Evaluation of the seismic stability of slopes is of paramount importance in geotechnical earthquake engineering, because of the threat to human life, severe environmental impact, and financial losses inflicted by earthquake-induced slope displacements. Similarly, understanding the effects of soil liquefaction on the performance of shallow-founded buildings has been a challenging topic of primary importance in geotechnical engineering over the past few decades.

The estimation of seismically induced displacements of earth slopes in geotechnical systems (earth/waste systems and natural slopes) has benefited from the recent developments in modelling the dynamic response of geotechnical structures, the abundance of ground motion recordings, and the developments in performance-based engineering and probabilistic approaches. Semi-empirical models have been formulated based on properties of the slope system, such as the yield coefficient (k_y) and the initial slope fundamental period (T_s), as well as intensity measure (*IM*) parameters that represent the ground motion. Most of the available procedures for estimating seismically-induced displacements have been developed for shallow crustal active settings (e.g. California) and should not be extrapolated to other tectonic active settings such as subduction zones. However, there is a lack of robust simplified procedures to estimate seismically-induced displacements for systems located in subduction earthquake zones. Thus, engineers often resort to using procedures formulated for shallow crustal settings in subduction zones without a due consideration if the procedures are applicable or not.

A robust procedure should consider a large number of ground motions and be applicable to different types of slopes (i.e., slopes of different dynamic resistances and dynamic response characteristics). It should also be validated using observations from well documented field case histories. Earthquakes in subduction active zones (e.g., South America and Japan) have caused significant slope displacements and considerable damage in slopes of geotechnical systems. Some examples are the damage caused by the 15 August 2007 M_w 8.0 Pisco, Peru earthquake, the 27 February 2010 M_w 8.8 Maule, Chile, the 11 March 2011 M_w 9.0 Tohoku, Japan earthquake, and the 8 April 2014 M_w 8.2 Iquique, Chile earthquake. Thus, the development of a robust procedure to estimate seismic-induced slope displacements in subduction earthquake zones is warranted. The procedure should be validated using field case histories, and the potential conservatism or unconservatism of using current procedures developed for shallow crustal settings in subduction earthquakes zones should be investigated.

Pseudostatic slope stability procedures, wherein a horizontal seismic coefficient is applied to a potential sliding mass in a conventional slope limit equilibrium analysis, are also employed commonly in the seismic design of slopes. However, their use is also suspect unless the parameters utilized in the analysis reflect the potential seismic demand in the governing tectonic setting (i.e., shallow crustal active or subduction earthquake zones). The seismic coefficient that is employed in a pseudostatic slope stability analysis should be selected in a rational manner if this procedure is to form a sound basis for a seismic slope stability assessment.

Another important issue is that in current practice, the estimation of seismic displacements is based on procedures that do not incorporate the uncertainty in the properties of the slope system (i.e., k_y and T_s) and they rely on a single value of *IM*. However, uncertainty is present in every step of the evaluation, starting with the inherent variability in the properties of the slope system to the variability of the *IMs*. Easily implemented performance-based seismic slope procedures that

consider the uncertainty in the slope's properties and earthquake ground shaking are required. The outcome of the performance-based approach is a seismic displacement hazard curve that addresses directly the seismic hazard of slope displacement. An important aspect is that seismic displacement hazard curves allow relate directly the design hazard level with the expected seismic slope displacements (i.e., the engineering demand parameter for the slope). This is important because engineers often use the hazard associated to the *IM*, with the implicit assumption that the hazard level associated to the seismic slope displacement is the same. This assumption is examined in this study. As the state of practice evolves towards accounting for all key sources of uncertainty, it is expected that performance-based methods will replace *IM* hazard curves with seismic slope displacement hazard curves.

The loss of bearing capacity due to soil liquefaction experienced by residential buildings in the 1964 Niigata, Japan earthquake is still one of the most mentioned examples of the damaging effects of soil liquefaction. The devastation witnessed during the Niigata and Great Alaskan earthquakes of 1964 on buildings was pivotal in bringing soil liquefaction to the attention of engineers and researchers. More recent earthquakes, such as the 17 August 1999 M_w 7.4, Kocaeli earthquake, the 27 February 2010 M_w 8.8 Maule, Chile earthquake, the 2010-2011 Canterbury, New Zealand earthquake sequence, and the 11 March 2011 M_w 9.0 Tohoku, Japan earthquake, have caused widespread damage to buildings with shallow foundations due to soil liquefaction. Several research groups performing post-earthquake reconnaissance of these events has made available well documented field case histories that enable engineers to understand better the complexities of soil liquefaction effects on buildings. Through shaking table and centrifuge tests researchers have also investigated the seismic performance of rigid, shallow model foundations situated atop uniform deposits of saturated, loose-to-medium dense, clean sand (e.g., Yoshimi and Tokimatsu 1977, Dashti et al. 2010a,b). Using observations of field case histories and measurements during the physical tests, researchers have categorized liquefaction-induced ground movements as ejecta-induced, shear-induced, or volumetric-induced deformations (Bray and Dashti, 2014). When a significant amount occurs, the removal of materials beneath a structure due to the formation of sediment ejecta is often the dominant factor. In many other cases, building settlement is controlled primarily by shear-induced ground deformations as a result of soil-structure-interaction (SSI)-induced ratcheting and bearing capacity-type movements. Volumetric-induced ground deformations resulting from localized partial drainage, sedimentation, and post-liquefaction reconsolidation can also produce significant building settlement.

Numerical analyses have been also used by researchers to replicate the measured responses of the ground or structures during physical experiments (i.e., commonly centrifuge tests). For example, Adrianopoulos et al. (2010), Dashti and Bray (2013), and Karimi and Dashti (2016a,b) performed nonlinear dynamic SSI effective stress analyses to capture the response of model buildings on top of a soil deposits that commonly include a liquefiable soil layer. A few numerical studies have back-analyzed field case histories. Travasarou et al. (2006) and Luque and Bray (2015, 2017) performed numerical back-analyses of buildings that suffered liquefaction-induced damage in the 1999 Kocaeli and 2011 Christchurch earthquakes with success. Their analyses capture many of the key aspects of the soil and building responses well. Thus, carefully performed nonlinear dynamic SSI effective stress analyses with adequate soil constitutive models can be used with confidence to investigate the important liquefaction building settlement mechanisms, except ejecta which cannot be addressed with a continuum approach.

The observations after case histories, during physical tests as well as the results from numerical studies have highlighted the importance of shear-induced mechanisms in liquefaction-induced

settlements. However, the state-of-the practice for estimating liquefaction-induced building settlement still largely involves using empirical procedures developed to calculate post-liquefaction, one-dimensional, reconsolidation settlement in the free-field away from buildings. These free-field analyses cannot possibly capture shear-induced deformations in the soil beneath shallow foundations.

In this thesis, nonlinear effective stress fully coupled soil-structure interaction dynamic analyses are performed to identify the key parameters controlling liquefaction-induced settlement for buildings with shallow foundations. A simplified procedure is developed to estimate liquefaction-induced building settlement based on the analytical results. The simplified method is applied to several field case histories, centrifuge tests and shown to provide estimates of settlement consistent with those observed.

1.2 ORGANIZATION

This thesis is organized in the following chapters:

- Chapter 2 describes the formulation of a simplified procedure for estimating seismic slope displacements in subduction earthquake zones. The input ground motion is the primary source of uncertainty in assessing the seismic performance of a slope. Thus, a comprehensive database containing 810 two-component ground motion recordings from subduction zone interface earthquakes is developed and used to compute seismic slope displacements. This chapter, also describes the validation of the proposed procedure for 12 field case histories. It presents a comparison between the new formulated model for subduction zones and the Bray and Travasarou (2007) model formulated for shallow crustal active zones. Finally, the chapter presents a rational procedure to estimate a pseudostatic coefficient to be used in slope stability analysis of slopes located in subduction zones.
- Chapter 3 describes the formulation of performance-based procedures to estimate a seismic displacement hazard curve. The procedures use standard information that is currently used by engineers in practice, and they are based on the convolution of spectral acceleration hazard curves with seismic displacement models. The Bray and Travasarou (2007) model is used for shallow crustal active settings, and the model developed in this thesis, which is presented in Chapter 2, is used for subduction earthquake zones. The use of a seismic displacement hazard curve is appealing because it relates directly the design hazard level and the pertinent engineering demand parameter (i.e., seismic slope displacement). In this chapter, issues related with the aleatory and epistemic characterization of the variability in the properties of a slope system are presented. The influence of the epistemic uncertainty in the ground motion is also discussed. Additionally, comparisons between the performance-based procedures and procedures that largely form the state of practice are presented for three sites in the United States to gain insights. Finally, the proposed performance-based procedures are recast to formulate a rigorous probabilistic procedure to estimate a pseudostatic coefficient to be used in slope stability analyses.
- Chapter 4 describes the nonlinear dynamic SSI effective stress analyses performed to identify key trends in the settlement of buildings with shallow foundations affected by soil liquefaction. Over 1,300 dynamic SSI effective stress analyses are performed by systematically varying subsurface conditions and building properties while applying 36 earthquake motions. Key findings in terms of different mechanism contributing to liquefaction-induced settlements are discussed. The analytical results are used to gain insights regarding the key parameters

controlling liquefaction-induced building settlement, including soil foundation parameters, building parameters, and ground motion parameters.

- Chapter 5 describes the formulation of a simplified procedure to estimate liquefaction-induced building settlements. The procedure is formulated using the results from the nonlinear dynamic SSI effective stress analyses presented in Chapter 4. A new index, referred as liquefaction building settlement index (LBS), is proposed. LBS captures the influence of earthquake-induced shear strains within liquefiable layers and hence shear-induced liquefaction building settlement. The proposed procedure is validated against results from centrifuge tests and field case histories. Finally, recommendations are provided for the application of the proposed procedure in practice.
- Chapter 6 provides a summary of the research, presents its key findings, and provides recommendations for future research.

CHAPTER 2: SIMPLIFIED PROCEDURE FOR ESTIMATING SEISMIC SLOPE DISPLACEMENTS FOR SUBDUCTION ZONE EARTHQUAKES

The contents of this chapter are primarily from a journal article submitted to the Journal of Geotechnical and Geoenvironmental Engineering from the American Society of Civil Engineers (ASCE) by Bray, J.D., Macedo, J., and Travasarou, T. entitled: "Simplified procedure for estimating seismic slope displacements for subduction zone earthquakes", which has been accepted.

2.1 INTRODUCTION

Engineers often use simplified seismic slope displacement procedures that utilize a Newmark type sliding block model to evaluate the seismic performance of earth structures and natural slopes (e.g., Makdisi and Seed 1978, Bray and Travasarou 2007, and Rathje and Antonakos 2011). Dynamic nonlinear effective stress analyses using finite element or finite difference methods with robust soil constitutive models may be employed for critical earth systems or when liquefaction may occur. Even in cases when these analytical procedures are employed, Newmark sliding block analyses form the basis for a preliminary estimate of the expected seismic displacement of the earth system. Pseudostatic slope stability procedures, wherein a horizontal seismic coefficient is applied to a potential sliding mass in a conventional slope limit equilibrium analysis, are also often used in preliminary design.

This chapter describes a simplified semi-empirical procedure that can be used to estimate the seismic displacement of earth systems that undergo shear deformation during a subduction zone interface earthquake. The procedure is developed to work within a fully probabilistic seismic hazard assessment, but it can be used also as a straightforward predictive relationship. Pertinent previous studies are summarized, the subduction zone earthquake ground motion database is presented, and the seismic slope displacement model is described. The proposed seismic slope displacement model for subduction zone earthquakes is presented, and following validation through examination of several case histories of earth dam performance, recommendations are made for use of the procedure.

2.2 PREVIOUS STUDIES

Several seismic sliding block displacement procedures are available in the literature. Several of these procedures are formulated only for the case of rigid sliding blocks wherein the dynamic response of the potential sliding mass is neglected (e.g., Newmark 1965, Lin and Whitman 1986, Jibson 2007, and Rathje and Saygili 2008). The rigid sliding block model should not be used except if the potential sliding mass is shallow and stiff so that its fundamental period is nearly zero, or as a screening tool in regional assessments when there is insufficient information to characterize the earth slope. In all other cases, the dynamic response of a "non-rigid" sliding mass should be considered, because the dynamic response of the sliding mass has been shown to be an important factor (e.g., Makdisi and Seed 1978, Rathje and Bray 1999, 2000).

Many of the seismic slope displacement methods that capture the flexibility of the sliding mass during earthquake shaking employ the decoupled approximation (e.g., Makdisi and Seed 1978, Lin and Whitman 1983, Bray and Rathje 1998, and Rathje and Antonakos 2011). The seismic site response of the system is first calculated assuming no sliding occurs, and then its results are used

to calculate the amount of sliding displacement that occurs. Due to the inherent limitations of the decoupled approximation, fully coupled stick-slip sliding block analyses are preferred (Rathje and Bray 1999, 2000). The Bray and Travasarou (2007) model captures the simultaneous occurrence of the nonlinear dynamic response of the potential sliding mass and the effects of periodic sliding episodes.

Few simplified seismic slope displacement procedures are based on the results of two-dimensional (2D) or three-dimensional (3D) dynamic analyses. The largest source of uncertainty is due typically to the input earthquake ground motion. Hence, a simpler one-dimensional (1D) model is commonly used with many earthquake ground motions to calculate results that enable development of a simplified seismic slope stability procedure. This assumption is reasonably conservative for most cases; the exception is for shallow sliding adversely affected by topographic amplification (Rathje and Bray 2001).

Most seismic slope displacement procedures have been formulated only for shallow crustal earthquakes along active plate margins. These semi-empirical procedures should not be used in a different seismotectonic setting (e.g., subduction zone earthquakes) without evaluating their applicability to a setting for which they were not developed originally. There are few procedures developed explicitly for subduction zone earthquakes. Urzua and Christian (2013) proposed a relation to estimate seismic displacements, but this method is only applicable for rigid slopes and based on ground motion recordings from only three Chilean earthquakes. There is a lack of robust simplified seismic slope displacement procedures that can be used to evaluate earth systems and slopes in subduction earthquake zones. A comprehensive earthquake database of subduction interface earthquakes is first required. The records in this new database are used to formulate a model that captures seismic slope displacements of earth systems undergoing subduction zone interface earthquakes.

2.3 DATABASE FOR SUBDUCTION ZONE INTERFACE EARTHQUAKES

The uncertainty in the ground motion characterization is the dominant source of uncertainty in calculating seismic slope displacements (Bray and Travasarou 2007). Therefore, procedures based on a large number of actual earthquake ground motion recordings are superior to procedures based on artificial simulated ground motions or those based on a modest number of recorded earthquake ground motions.

A comprehensive database containing 1122 ground motion records (with each record having 2 horizontal components) from subduction zone inter-plate earthquakes was developed. Approximately 235 processed records were obtained from R. Darragh and PEER (personal communication), and the Central American database was obtained from J. Bommer. The remaining records were obtained from seismic agencies websites and processed in a uniform manner following the recommendations of Ancheta et al. (2013). The ground motion records from the developed database conform to the following criteria: a) $5.8 \leq$ moment magnitude (M) ≤ 9.0, b) epicentral distance (R) ≤ 450 km, c) IBC (2012) site class A, B, C or D (the site class was assigned based on local soil conditions or geological maps as shear wave velocity measurements were not often available), and d) frequencies in the range of 0.20 – 10 Hz have not been filtered out. Figure 2.1 shows the distribution of magnitudes and distances of the subduction zone interface earthquake ground motion database. Distance is not used to formulate the predictive equations, so epicentral distance is provided as a qualitative indicator of source-to-site distance, which was not always available. Table 2.1 lists the earthquakes in the database by region. Much of the data is from Japan; however, there is negligible bias in the model residuals of only the non-Japanese data.

Only the ground motion records from earthquakes with moment magnitude of at least 7.0 are used to generate the seismic displacements data, because large magnitude interface earthquakes typically govern the seismic hazard and to avoid bias from the underrepresented number of lower magnitude earthquakes in the database. Removal of low magnitude earthquakes resulted in 810 two-component ground motion recordings. Each horizontal component of a recording was applied to the base of the sliding block model described subsequently to calculate a seismic displacement. The seismic displacement values calculated from the two horizontal components were averaged. The opposite polarity of the components were then applied to compute an average seismic displacement for the other side of the recording. The maximum of the average seismic displacement values for each polarity was assigned to that recording.

2.4 EVALUATION OF SEISMIC DISPLACEMENTS

2.4.1 Nonlinear, coupled sliding block model

The nonlinear, coupled deformable stick-slip sliding model proposed by Rathje and Bray (1999) is used. In this study, however, the equation of motion is solved by a step-by-step analytical solution of the governing equations as recommended by Chopra and Zhang (1991), because it is numerically more stable than the Newmark integration method used by Rathje and Bray (1999). The seismic response of the sliding mass is captured by an equivalent-linear viscoelastic modal analysis that uses strain-dependent material properties to approximate the nonlinear response of the earth materials. Comparisons of this model with a rigid block stick-slip model, an uncoupled deformable model, a fully nonlinear deformable stick-slip model, and a deformable stick-slip model with more than one mode shape model are described in Rathje and Bray (1999, 2000). The model is validated using shaking table experiments by Wartman et al. (2003). The 1D nonlinear, coupled deformable stick-slip model represents a relatively wide vertical column of soil to allow for the use of a large number ground motions with a wide range of properties of the potential sliding mass. The 1D analysis can underestimate the seismic demand for shallow sliding at the top of 2D systems where topographic amplification is significant. For this case, the input PGA can be amplified by 1.3 for moderately steep slopes (Rathje and Bray 2001) and by 1.5 for steep (>60^o) slopes (Ashford and Sitar 2002).

The nonlinear, coupled deformable stick-slip sliding block model captures that part of the seismically induced permanent displacement attributed to shear deformation (i.e., either rigid body slippage along a distinct failure surface or distributed shearing within the deformable sliding mass). Ground movement due to volumetric compression is not captured explicitly by the Newmark-type sliding block model. Accordingly, shear and volumetric compression effects are evaluated separately. The results of the sliding block model analyses estimate shear-induced displacements. Another method that captures the seismic compression of soils should be used to estimate volumetric-induced displacements (e.g., Tokimatsu and Seed 1987). The estimated shear-induced ground displacement and volumetric-induced ground displacement are summed to estimate the total seismically induced ground displacement.

The sliding mass is assigned a constant unit weight of 19 kN/m^3. The strain-dependent shear modulus reduction and material damping ratio curves proposed by Darendeli (2001) for 1 atm. and PI = 15 are used. Sensitivity analyses indicate that reasonable adjustments of these parameters do not affect significantly the computed displacement. The nonlinear, coupled deformable stick-slip sliding model is characterized by its yield coefficient (k_y) and its initial fundamental period (T_s). These parameters are varied over reasonable ranges (i.e., k_y = 0.01, 0.02, 0.035, 0.05, 0.075, 0.1,

0.15, 0.2, 0.25, 0.3, 0.4, 0.5, and 0.8; and T_s = 0.0, 0.05, 0.1, 0.2, 0.3, 0.5, 0.7, 1.0, 1.4, and 2.0 s). For the baseline case, the overburden-stress corrected shear wave velocity (V_{s1}) is set to 270 m/s, and the shear wave velocity profile of the sliding block is developed using the relationship that shear wave velocity (V_s) is proportional to the fourth-root of the vertical effective stress. The sliding block height (H) is increased until the specified value of T_s is obtained. Other reasonable combinations of H and average V_{s1} for the same T_s value were used to confirm that the results were not sensitive to these parameters individually. For nonzero T_s values, H is varied between 3 m and 100 m, and V_{s1} is varied between 200 m/s and 450 m/s.

The model sliding blocks are classified as IBC Sites C or D. Thus, realistic values of the initial fundamental period and yield coefficient for a wide range of earth/rockfill dam, natural slope, heap leach pads, and solid-waste landfill are used. Over 490,000 sliding block analyses were performed in this study.

2.4.2 Distribution of seismic displacement

The calculated seismic displacement values are the "simulated data" used to develop the regression equations for estimating shear-induced seismic slope displacement (D). The seismic displacements calculated for cases wherein D exceeds 0.5 cm are shown in Figure 2.2. The variation of the calculated seismic displacements is plotted against the slope yield coefficient (k_y), the ground motion's spectral acceleration at 1.5 times the slope's initial fundamental period ($S_a(1.5T_s)$), the slope's initial fundamental period (T_s), and earthquake moment magnitude (M). The scatter in these graphs is significant. However, there are trends in the data. Seismic displacement generally decreases with increasing yield coefficient. Seismic displacement generally increases with increasing seismic demand as defined by the input ground motion's $S_a(1.5T_s)$ value and with increasing earthquake magnitude. There is a modest sensitivity of seismic displacement to the slope's fundamental period.

2.5 MODEL FOR ESTIMATING SEISMIC SHEAR-INDUCED SLOPE DISPLACEMENTS

2.5.1 Functional form

Seismic slope displacement is modeled as a mixed random variable, which has a certain probability mass at zero displacement and a probability density for finite displacement values (Bray and Travasarou 2007). The probability density function of seismic displacements is:

$$f_D(d) = \bar{P}\delta(d - d_0) + (1 - \bar{P})\bar{f}_D(d) \quad (2.1)$$

where $f_D(d)$ is the displacement probability density function; $\bar{P}$ is the probability mass at $D = d_0$; $\delta(d - d_0)$ is the Dirac delta function, and $\bar{f}_D(d)$ is the displacement probability density function for $D > d_0$. A mixed probability distribution has a finite probability at $D = d_0$ and a continuous probability density for $D > d_0$.

Small displacement values are not of engineering significance and can for all practical purposes be considered as negligible or "zero." Moreover, the regression of seismic displacement as a function of the model parameters should not be dictated by data at negligible levels of seismic displacement, which are not of practical significance. Although calculated values of seismic displacement of 0.01 cm and 0.1 cm differ by an order of magnitude they are both negligible in

practical terms. A similar approach was employed by Song and Rodriguez-Marek (2014) in developing a seismic slope displacement model for near-fault ground motions. The negligible seismic displacement data are still considered in the mixed random variable approach; they are not discarded. Instead, they are lumped together, and the meaningful values of seismic displacement govern the regression.

The selection of the "zero" displacement threshold (d_0) depends on the problem being investigated. Bray and Travasarou (2007) and Song and Rodriguez-Marek (2014) used d_0 = 1.0 cm, which is appropriate for evaluating seismic slope displacements in most cases (e.g., earth dams and solid-waste landfills), where displacements less than 10 cm are generally acceptable, which is an order of magnitude greater than d_0. Recently, the Bray and Travasarou (2007) procedure has been used to evaluate the seismic performance of earth retention systems where the threshold of tolerable displacements may be as low as 5 cm or even 2.5 cm. Accordingly, the "zero" displacement threshold was reset to be 0.50 cm in the proposed model. Values of seismic displacements that are smaller than 0.50 cm are lumped together at d_0 = 0.50 cm.

The probability of "zero" displacement depends primarily on the three independent variables: k_y, $S_a(1.5T_s)$, and T_s, which represent the slope's strength, shaking intensity, and stiffness. As shown by the data subset in Figure 2.3a, the probability of "zero" displacement increases significantly as the yield coefficient increases and decreases significantly as the ground motion's spectral acceleration at the degraded period increases (Figure 2.3b). The probability of "zero" displacement decreases initially as the fundamental period increases from zero, because the sliding mass is approaching a resonance condition, and it increases as sliding mass moves away from the resonance condition (Figure 2.3c). Similar trends in the calculated seismic displacement data were obtained by Bray and Travasarou (2007) for shallow crustal earthquakes along active plate margins. The data trends displayed in Figure 2.3 guided the selection of the functional form for the predictive equation for the probability of "zero" displacement. As opposed to the one-equation model used by Bray and Travasarou (2007), two equations were used with the first equation capturing better the trends of the data for most practical cases with T_s <= 0.7 s and the second equation fitting the data for cases with T_s > 0.7s. A probit regression analysis (Greene 2003) was employed to calculate the coefficients of the predictive equation for the probability of "zero" displacement.

In this mixed random variable formulation, the amount of "nonzero" displacement also needs to be estimated. Analysis of the data indicated that the parameters employed by Bray and Travasarou (2007) of k_y, $S_a(1.5T_s)$, T_s, and M (to represent duration) also capture the major trends in the predictive equation of the "nonzero" displacement. A truncated regression (Greene 2003) along with the principle of maximum likelihood was employed to calculate the coefficients of the predictive equation for "nonzero" displacement.

2.5.2 Simplified procedure for estimating seismic slope displacements

The shear-induced seismic slope displacement (D) is estimated in two steps: (1) the probability of "zero" displacements (i.e., $D \leq 0.50$ cm) and (2) the likely amount of "nonzero" displacement are calculated and combined through the mixed random variable formulation. The model for computing the probability of "zero" seismic slope displacement is:

$$P(D=0) = 1 - \Phi\left(-2.64 - 3.20Ln(k_y) - 0.17\left(Ln(k_y)\right)^2 - 0.49TsLn(k_y) + 2.09T_s + 2.91Ln\left(Sa(1.5T_s)\right)\right) \quad \text{for cases where } T_s \leq 0.7 \text{ s} \tag{2.2}$$

$$P(D=0) = 1 - \Phi\left(-3.53 - 4.78Ln(k_y) - 0.34\left(Ln(k_y)\right)^2 - 0.30TsLn(k_y) - 0.67T_s + 2.66Ln(Sa(1.5T_s))\right) \quad \text{for cases where } T_s \leq 0.7 \text{ s} \tag{2.3}$$

where $P(D = 0)$ is the probability of occurrence of "zero" seismic slope displacement (as a decimal number); D is the seismic slope displacement; Φ is the standard normal cumulative distribution function; k_y is the yield coefficient; T_s is the fundamental period of the sliding mass in seconds; and $S_a(1.5T_s)$ the spectral acceleration at a period of $1.5T_s$ in the units of g of design outcropping ground motion for the site conditions below the potential sliding mass (i.e., the ground motion intensity at the site if the potential sliding mass was removed). Some comparisons of the model estimates versus the simulated data and the Bray and Travasarou (2007) model are shown in Figure 2.3. As noted previously, the model separates the calculation of probability of "zero" displacements for typical systems with $T_s \leq 0.7$ s from those with high periods (i.e., $T_s > 0.7$ s) to track better the variation of the probability of "zero" displacement with the fundamental period of the sliding mass.

The amount of the "nonzero" seismic slope displacement (D) in centimeters is estimated as:

$$Ln(D) = a1 - 3.353Ln(k_y) - 0.390\left(Ln(k_y)\right)^2 + 0.538Ln(k_y)Ln\left(Sa(1.5T_s)\right) + 3.060Ln\left(Sa(1.5T_s)\right) - 0.225\left(Ln\left(Sa(1.5T_s)\right)\right)^2 + a2T_s + a3(T_s)^2 + 0.550M \pm \varepsilon \tag{2.4}$$

where k_y, T_s, and $S_a(1.5T_s)$ are as defined previously, M is moment magnitude, and is a normally distributed random variable with zero mean and standard deviation $\sigma = 0.73$. In Equation 2.4, for systems with $T_s \geq 0.10$ s, a1= -6.896, a2= 3.081, and a3= -0.803, and for $T_s < 0.10$ s, a1= -5.864, a2= -9.421, and a3= 0.0. There is only a slight change in the calculated seismic displacement across the value of $T_s = 0.10$ s. For the special case of the Newmark rigid-sliding block where $T_s = 0.0$ s, the amount of "nonzero" seismic slope displacement (D in cm) is estimated as:

$$Ln(D) = -5.864 - 3.353Ln(k_y) - 0.390\left(Ln(k_y)\right)^2 + 0.538Ln(k_y)Ln(PGA) + 3.060Ln(PGA) - 0.225\left(Ln(PGA)\right)^2 + 0.550M \pm \varepsilon \tag{2.5}$$

where PGA is the peak ground acceleration in the units of g of the input base ground motion. If there are important topographic effects to capture for localized shallow sliding, the input PGA value should be adjusted as discussed previously (i.e., 1.3 PGA_{1D} for moderately steep slopes, or 1.5 PGA_{1D} for steep slopes). For long, shallow potential sliding masses, lateral incoherence of

ground shaking would reduce the input PGA value employed in the analysis (e.g., 0.65 PGA_{1D} for moderately steep slopes, Rathje and Bray 2001).

The residuals (i.e., $Ln(D_{data}) - Ln(D_{Predicted})$) of Equation 2.4 and 2.5 are plotted in Figure 2.4 in terms of the yield coefficient, spectral acceleration at $1.5T_s$, earthquake magnitude, fundamental period, peak ground velocity (PGV), and significant duration ($D_{5\text{-}95}$). The residuals shown in Figure 2.4 are significant, but this is due to the inherent variability of estimating seismic slope displacement. The residuals versus the key parameters of k_y, $S_a(1.5T_s)$, M, T_s, PGV, and $D_{5\text{-}95}$ show negligible bias. The residuals versus other parameters (e.g., V_{s30}) also show negligible bias.

The proposed predictive equations can also be used to calculate the probability of the seismic displacement exceeding a selected threshold of displacement (d) for a specified earthquake scenario (i.e., $S_a(1.5T_s)$ and M) and earth slope properties (i.e., k_y, T_s). The probability of the seismic slope displacement (D) exceeding a specified displacement threshold (d) is calculated as:

$$P(D > d) = [1 - P(D = 0)]P(D > d/D > 0) \tag{2.6}$$

where $P(D = 0)$ is computed using Equation 2.2 or Equation 2.3. The term $(D > d|D > 0)$ is computed assuming that the estimated displacements are lognormally distributed as:

$$P(D > d/D > 0) = 1 - P(D \leq d/D > 0) = 1 - \Phi\left(\frac{Ln(d) - Ln(\tilde{d})}{\sigma}\right) \tag{2.7}$$

where $Ln(\tilde{d})$ is calculated using Equation 2.4 or 2.5, σ is the standard deviation of the random error equal to 0.73.

The trends for the proposed model are shown in Figure 2.5. The upper three plots (Figure 2.5a-c) show trends for a M = 9.0 subduction zone interface earthquake at a source-to-site distance of 35 km (this distance is representative for some sites along the South American coast and in New Zealand). The probability of negligible seismic displacements and the estimation of the seismic displacement depend significantly on yield coefficient. For this earthquake scenario, the influence of the initial fundamental period is more significant for systems with high yield coefficients. Figure 2.5d-e are for a M = 9.0 interface earthquake at several distances from the site so that the ground motion intensity parameters PGA and $S_a(1.5T_s)$ vary significantly for the case of a rigid sliding block or a deformable sliding block with an initial fundamental period of 0.3 s. The effect of earthquake magnitude at a specified ground motion intensity (i.e., $S_a(0.45s)$ = 0.8 g) is shown Figure 2.5f. The comparison of the calculated seismic slope displacement as a function of yield coefficient is only capturing part of the important effects of earthquake magnitude, because the ground motion intensity level was kept constant. The estimated value of spectral acceleration typically increases with increasing earthquake magnitude, which would increase further the seismic displacement.

2.5.3 Model Validation

The proposed model's estimates of seismic displacement are compared with observed displacements measured at nine earth dams (one dam underwent three events) and a coastline slope beneath a pipeline that were shaken by subduction zone interface earthquakes. The observations from these 12 case histories were used to validate the model and were not included in the dataset for the development of the predictive equations. The case histories used in the model validation are described in Table 2.2. In all cases, the maximum observed displacement (D_{max}) is that portion of the permanent displacement attributed to shear-induced seismic slope displacement (i.e., stick-

slip type movement and distributed shear within the deformable mass), and crest movement due to volumetric compression was subtracted from the total observed permanent displacement when appropriate to be consistent with the mechanism implied by the Newmark method. The observed seismic performance and best estimates of yield coefficient and initial fundamental period are based on the information provided in the references listed in the footnote of Table 2.2. Additional information on these case histories may be found in Appendix A.

The comparison of the proposed model estimates of seismic displacement (columns 8-9) with the maximum observed seismic permanent displacement (column 3) is shown in Table 2.2. For this comparison, only mean or median values of the slope's yield coefficient, initial fundamental period, and the spectral acceleration at 1.5 times the initial fundamental period are considered. The computed seismic displacement range shown in column 9 is for values that the probability of exceeding is 84% and 16%, which is computed using Equation 2.6 by solving d for P(D>d) = 0.84 and 0.16, respectively. The displacement range is due to the variability in the seismic displacement given the values of the slope properties and the seismic load (i.e., $\sigma = 0.73$ from Equation 2.4). Overall, the proposed model provides reasonable estimates of the observed seismic performances of the 12 earth system case histories examined in this study.

There are five case histories in which the observed seismic slope displacement was noted as being "None." The proposed method estimates high probabilities of "zero" displacement (i.e., 100% that $D \leq 0.5$ cm) for the dam in the Andes, Shitoki dam, and Surikamigawa dam. There is a 50% probability of "zero" displacement and a seismic displacement range of 0–2 cm for Esperanza dam, which is consistent with the negligible displacement observed at this earth dam after the 2016 Muisne, Ecuador earthquake. Lastly, there is a 65% probability of "zero" displacement and a seismic displacement range of 0–2 cm for Tutuven dam, which is also consistent with the negligible displacement observed at this dam after the 2010 Maule, Chile earthquake. Thus, the proposed method's assessment of seismic performance is consistent with the good seismic performance observed of these earth structures.

There are two case histories with observed seismic displacements of a few centimeters (i.e., 5 cm for Torata dam and 6 cm for the coastline slope in Peru). The proposed model is able to capture the observed seismic displacements for these cases. The estimated seismic displacement range is 1 to 7 cm for the Torata dam and 3 to 12 cm for the coastline slope. Good seismic performance was also observed for the La Villita Dam in Mexico (Elgamal et al. 1990). Its performance during three earthquake events is well-documented with increasing levels of the observed seismic displacements from Events S3, S4, and S5. The proposed model develops estimates of seismic displacement with the same trends. There is a high probability of "zero" displacements (80%) for Event S3 where the maximum observed displacement was 1 cm, which is considered a negligible level of displacement for an earth dam. There is a relatively low probability of "zero" displacement (10%) with a range of estimated seismic displacement from 1 to 7 cm, which encompasses the observed value of 4 cm for Event S5. The proposed model's estimates are intermediate for Event S4, which is consistent with the observed seismic performance of the dam for this event. Thus, the proposed method provides seismic displacement estimates that are consistent with the trends of the observed seismic performance of La Villita Dam for these earthquake events.

There is one case of moderate seismic displacement, which corresponds to the Nishigo dam shaken by the 2011 Tohoku Earthquake. Nishigo dam underwent approximately 40 cm of seismic displacement due to shear-induced deformation in this event. The proposed method estimates essentially no chance of "zero" displacement occurring for this case and a range of expected

seismic slope displacement (i.e., 14-58 cm) that includes the observed shear-induced seismic slope displacement of 40 cm.

A section of the upstream shell of Coihueco dam displaced a large amount (i.e., $D_{max} \approx 350$ cm) during the 2010 Maule, Chile earthquake (Verdugo et al. 2012). The proposed method estimates that there is a negligible chance of "zero" displacement occurring. The calculated shear-induced seismic slope displacement range is from 60 cm to 260 cm, which is indicative of large displacements likely occurring. The observed seismic slope displacement value is above the 84% seismic displacement estimate, but it is within 1.5 standard deviations of the median estimate of seismic slope displacement. Importantly, the proposed method is capable of predicting the unsatisfactory seismic performance of an earth dam, as it is unlikely that an engineer would accept the design of a dam that could undergo over 3 m of total seismic displacement (with up to 2.6 m of shear-induced displacement) for a reasonable earthquake scenario in this area of Chile.

2.6 COMPARISON OF THE SUBDUCTION ZONE EARTHQUAKE MODEL WITH THE SHALLOW CRUSTAL EARTHQUAKE MODEL

One of the motivations of this study was the recognition that engineers were using the Bray and Travasarou (2007) model (herein referred to as BT07) for subduction zone earthquakes, because robust statistical models based on subduction zone earthquake ground motion data were not available. The proposed model, which has been developed for subduction zone interface earthquakes, is compared to the seismic slope displacement estimates from the BT07 procedure, which was developed using only shallow crustal earthquake records, to discern potential differences and to investigate if they can be explained by differences in the seismotectonic settings.

Figure 2.6 shows the residuals obtained by applying the BT07 model, which is based on shallow crustal earthquake records, to the seismic slope displacement data calculated using subduction zone interface earthquake motions as input. The BT07 residuals of the subduction zone earthquake-induced displacement data when plotted against yield coefficient are more negative compared to the residuals using the equations derived in this study for subduction zone earthquakes (i.e., BMT17: Equation 2.4 and Equation 2.5 of this study). This observation implies that the BT07 procedure overestimates seismic slope displacements when used for subduction zone earthquakes (i.e., negative residual indicates that the median predicted seismic displacement is greater than the median of the seismic displacement data). However, the residuals do not show significant bias for lower (more common) values of k_y. There is significant bias only for higher values of yield coefficient. This is likely due in part to the wider range of k_y values employed in the present study (i.e., values up to 0.8) relative to the range used in the BT07 study (i.e., k_y values up to only 0.4). A conservative extrapolation of the BT07 predictive equations to higher k_y values is likely the primary cause of the bias and not a seismological difference between subduction zone and shallow crustal earthquakes.

The residuals of the BT07 model versus the simulated subduction zone earthquake seismic displacement data are slightly more negative compared with the residuals of the BMT17 model derived in this study for periods less than 0.5 s. For higher periods, the residuals of the BT07 predictive equations do not differ significantly from those of the proposed BMT17 predictive equations. Thus, there is no significant effect of the slope fundamental period due to the different ground motion databases.

The BT07 predictive equations are biased in terms the residuals of seismic slope displacement as a function of earthquake magnitude. The residuals using the BT07 equations are more negative than the residuals derived in this study at intermediate and lower magnitudes. The BT07 residuals

become less negative as magnitude increases and tend to zero for M = 9 earthquakes. The magnitude scaling term for the BT07 and BMT17 methods are 0.278 and 0.550, respectively. The higher magnitude scaling coefficient in the BMT17 relationship for subduction earthquakes is consistent with what has been observed for ground motion prediction equations (GMPE) for spectral acceleration for subduction earthquakes (e.g., Abrahamson et al. 2016) compared with shallow crustal earthquakes (e.g., Abrahamson et al. 2013). The higher magnitude scaling coefficient in the BMT17 relations may also be due to the longer duration of subduction earthquake records relative to records from shallow crustal earthquakes of similar magnitude. The extrapolation of the BT07 model, which was based on shallow crustal earthquakes with $M \leq 7.6$, to the higher magnitudes possible with large subduction zone interface earthquakes was conservative. It is fortuitous, that the BT07 model provides reasonable seismic slope displacement estimates for large magnitude subduction zone interface earthquakes. It provides poorer, although conservative, estimates of seismic displacement for lower magnitude subduction zone events.

This study (BMT17) considered 810 two-component ground motion recordings from subduction zone interface earthquakes whereas the BT07 model was developed using 688 two-component ground motion recordings from shallow crustal earthquakes along active plate margins. The new BMT17 model is based on a broader range of distances and magnitudes. As expected, there are differences attributed to the unique characteristics of ground motions from shallow crustal and subduction zone settings. For example, it has been observed empirically for a given earthquake magnitude, source-to-site distance, and site condition, that the ground motion records from shallow crustal settings tend to have a stronger long period content energy compared with ground motion records from subduction interface settings (i.e., in terms of spectral shape, spectral accelerations reduce at a slower rate over the long period range of the spectrum). This effect is captured by GMPEs proposed for these seismic settings (e.g., Abrahamson et al. 2013, and Abrahamson et al. 2016), as illustrated in Figure 2.7, which shows a comparison of the shape of 5% damped acceleration response spectra for shallow crustal and subduction zone earthquakes for a fixed magnitude, distance, and site condition. In Figure 2.7, the $S_a(1.5T_s)$ was anchored for a representative fundamental period of T_s = 0.3 s to observe differences in spectral shape. The acceleration response spectrum for a shallow crustal earthquake has a stronger long period energy content relative to its short period energy compared to the shape of the response spectrum for a subduction interface earthquake. Because the amount of seismic slope displacements is governed more by long period energy, the negative (conservative) residuals of the BT07 method (when used in subduction settings) is consistent with the described empirical observations and GMPEs.

2.7 PSEUDOSTATIC SEISMIC COEFFICIENT

Pseudostatic slope stability procedures are often used in engineering practice to evaluate preliminarily the likely seismic performance of earth/waste structures and natural slopes. Although these procedures have the advantage of being straightforward and relatively easy to use, they cannot offer a reliable assessment of the likely seismic performance of the system unless the parameters utilized in the analysis accurately reflect the potential seismic demand. Hence, the selection of the seismic coefficient used in a pseudostatic slope stability analysis is critically important. The seismic coefficient used in a pseudostatic slope stability analysis is typically taken to be some fraction of the maximum seismic coefficient, because slightly exceeding the maximum seismic resistance for a few instances will only lead to minor accumulated seismic displacement. Thus, even when using a pseudostatic approach, the performance goal is in terms of the expected range of seismic displacement (Bray and Travasarou 2009).

Bray and Travasarou (2009) proposed a rational basis for selecting a seismic coefficient (*k*) for use in a pseudostatic slope stability analysis by requiring it to provide a seismic assessment that is consistent with the results of the Bray and Travasarou (2007) seismic slope displacement analysis. Similarly, the results of the proposed seismic displacement procedure for subduction zone earthquakes can be used to develop a model that calculates a seismic coefficient that provides a consistent seismic assessment with the seismic slope displacement analysis. The predictive model for estimating seismic displacement (*D*) consists of two equations that calculate the probability of "zero" displacement, and the likely amount of "nonzero" displacement. The first equation can be neglected in this application, because it does not have a noticeable effect on k_y for a median seismic displacement value larger than 5 cm. For smaller displacements, neglecting the first equation yields conservative results (i.e., the true displacement will be less than or equal to the target displacement).

Equation 2.4 can be reworked to solve for k_y as a function of D and best-estimate values of the other parameters. If this value of k_y is used in a pseudostatic slope stability analysis as the seismic coefficient *(k*) and the calculated factor of safety (*FS*) ≥ 1, then the selected percentile estimate of the seismic displacement will be less than or equal to the allowable seismic displacement (D_a).

The calibrated allowable displacement-dependent value of the seismic coefficient (*k*) is:

$$k = exp(\frac{-a+\sqrt{b}}{0.780}) \tag{2.8a}$$

Where:

$$a = 3.353 - 0.538Ln(Sa(1.5T_S)) \tag{2.8b}$$

$$b = a^2 - 1.560(Ln(D_a) - a1 - 3.060Ln\big(Sa(1.5T_S)\big) + 0.225Ln\big(Sa(1.5T_S)\big)^2 - a2T_S - a3(T_s)^2 - 0.550M - \varepsilon) \tag{2.8c}$$

In Equation 2.8c, a1= -6.896, a2= 3.081, and a3= -0.803 for $T_s \geq 0.10$ s, and a1= -5.864, a2= -9.421, and a3= 0.0 for $T_s < 0.10$ s. The engineer should first establish the allowable seismic displacement (D_a in cm) and the percent exceedance of this displacement threshold (e.g., median displacement estimate for ε = 0 or 16% exceedance displacement estimate for ε = σ = 0.73) considering the consequences of unsatisfactory performance at displacement levels greater than this threshold in consultation with the owner. The 16% displacement level is about a half of the median displacement level, and if selected, it would lead to a higher seismic coefficient. The initial period of the potential sliding mass (T_s) is estimated, and seismic demand is defined in terms of the design spectral acceleration for the site conditions below the sliding mass (which may include topographic amplification) at the degraded period of the sliding mass (i.e., $S_a(1.5T_s)$) and the design moment magnitude (*M*) of the controlling earthquake event.

The design spectral acceleration will vary for each project and depend on important seismic factors such as source-to-site distance, earthquake magnitude, site conditions, topographic effects, slip-rate, etc. The ground motion hazard level (e.g., whether a 50% or 84% value is used in a deterministic assessment or whether the 475-year or 2475-year return period value is used from a probabilistic assessment) should be established based on the uncertainty in the seismic hazard characterization, the criticality of the project, and the consequences of poor performance.

Generally, median or best-estimate values of other design parameters, such as the dynamic shear strength of soil, its shear wave velocity, and the representative height of the potential sliding plane, should be used.

Seismic slope stability is evaluated through application of the seismic coefficient calculated with Equation 2.8 in a pseudostatic slope stability analysis that satisfies all three conditions of equilibrium. If the resulting FS is greater or equal to one, the system is judged to perform satisfactorily, because the selected percentile estimate of the calculated seismically induced permanent displacement will be less than D_a. Generally, the median displacement level should be used, but for critical projects, a lower percentile displacement level could be used (i.e., $\varepsilon > 0$). However, it is difficult to track the overall performance level of the system when for example, a 84% spectral acceleration value is used in combination with the 16% displacement level, so it is preferred to use median estimates throughout the calculation or use a value other than the median for only the most uncertain parameter. Moreover, the minimum value of the acceptable *FS* should not be set to be greater than 1.0, because *FS* varies nonlinearly as a function of the reliability of the system so the effects of achieving a *FS* greater than one cannot be assessed reliably.

Figure 2.8 presents the relationship between the seismic coefficient corresponding to a specified allowable displacement level and key seismic slope stability parameters. Allowable displacement values of 15 cm, 30 cm, and 50 cm were used to illustrate the dependence of the seismic coefficient on the selected level of allowable displacement for a magnitude 9 event. Results are also provided for the 30 cm displacement level for two magnitude scenarios representing a moderate event (M = 7) and a major event (M = 9). As shown in Figure 2.8a, the seismic coefficient increases systematically as the selected allowable displacement value decreases and the 5% damped elastic spectral acceleration of the ground motion increases. It also increases as the magnitude (i.e., duration) of the earthquake event increases. Thus, the seismic coefficient varies systematically in a reasonable manner as the allowable displacement threshold and design ground shaking level vary.

The seismic coefficient also depends on the potential sliding mass's fundamental period (Figure 2.8b). Relatively stiff slopes that have short fundamental periods (i.e., 0.1 s < T_s < 0.3 s) tend to displace more because of resonance with the ground shaking. More flexible slopes (i.e., T_s > 0.5 s) have relatively less potential for seismic displacement. For representative $S_a(1.5T_s)$ which for illustrative purposes has been selected to correspond to an M 9.0 earthquake scenario at a distance of 35 km, the seismic coefficient initially increases as the slope's period increases from zero (i.e., the rigid sliding mass case) until a peak value is reached and then it decreases progressively as the slope's period moves away from resonance. Hence, the seismic coefficient required to limit a specified allowable seismic displacement threshold is larger for shallow stiff sliding masses than for deep flexible sliding masses.

2.8 ILLUSTRATIVE EXAMPLE

The anticipated seismic performance of a representative earth dam is evaluated in terms of seismically-induced permanent slope displacement. A deterministic analysis is performed to evaluate a deep slide through the dam using the proposed simplified seismic slope displacement model. The geometry and properties of the dam are identical to the example used by Bray and Travasarou (2007). The maximum cross-section of the 57 m-high rolled earth-fill dam, which is founded on fractured rock, is shown in Figure 2.9. For the case of base sliding at the maximum height of this triangular-shaped potential sliding mass, the best estimate of its initial fundamental period is:

$$T_s = \frac{2.6\,H}{V_s} = \frac{2.6(57m)}{450m/s} \approx 0.33\text{s} \quad (2.9)$$

The yield coefficient for a deep failure surface was estimated to be 0.14 from a pseudostatic slope stability analyses performed with the total stress strength properties of c=14 kPa and Φ =21° based on undrained triaxial compression tests.

The deterministic design earthquake scenario is represented by a mean maximum magnitude M = 9.0 at the closest rupture-distance of R = 50 km. The best estimate of the 5% damped spectral acceleration at the degraded period of the dam (i.e., $1.5T_s$ = 1.5 (0.33 s) = 0.5 s) is computed as the average of the median predictions of three GMPEs (e.g., Abrahamson et al. 2016, Atkinson and Boore 2003, and Zhao et al. 2006) for the "rock" site condition for an interface earthquake with M = 9.0 and R = 50 km as S_a(0.5s) = 0.47 g, 0.45 g, and 0.49 g, respectively. Thus, the average value of S_a at the degraded period of sliding mass is 0.47 g, its initial period is 0.33s, and k_y is 0.14.

The probability of "zero" displacement occurring is computed using Equation 2.2 as:

$$P(D=0) = 1 - \Phi\Big(-2.64 - 3.20Ln(0.14) - 0.17\big(Ln(0.14)\big)^2 - 0.49(0.33)Ln(0.14) + 2.09(0.33) + 2.91Ln(0.47)\Big) = 0 \quad (2.10)$$

There is zero probability of negligible displacements occurring for this event. The 16% and 84% exceedance seismic slope displacement values are computed from Equation 2.4 using a standard deviation for the natural logarithm of the displacement of 0.73. The seismic displacement is estimated from Equation 2.4 using the same design parameters with M = 9.0 as:

$$Ln(D) = -6.896 - 3.353Ln(0.14) - 0.390\big(Ln(0.14)\big)^2 + 0.538Ln(0.14)Ln(0.47) + 3.060Ln(0.47) - 0.225\big(Ln(0.47)\big)^2 + 3.081(0.33) - 0.803(0.33)^2 + 0.55(9.0) \pm \varepsilon \quad (2.11)$$

The estimated median seismic slope displacement is: $D = ex(Ln(D)) = exp(2.43) \approx 11\ cm$. The seismic displacement range between the 16% to 84% exceedance levels (by subtracting and adding ε = 0.73, respectively, to the right side of Equation 2.11) is calculated to be 5 cm to 23 cm for the design earthquake scenario. The 16% exceedance displacement value is approximately half of the median estimate and the 84% exceedance displacement value is approximately twice the median estimate, because the standard deviation for the natural logarithm of displacement is 0.73. Thus, one could simply use Equation 2.4 to estimate the median seismic displacement and use a range from half this value to twice this value as the seismic slope displacement estimate range.

The direction of this displacement should be oriented parallel to the direction of slope movement, which will be largely horizontal for this case. For the total crest displacement of the dam, a procedure such as Tokimatsu and Seed (1978) is required to estimate the vertical settlement due to cyclic volumetric compression of the compacted earth fill.

The seismic coefficient to be used in a pseudostatic slope stability analysis of the dam depends greatly on the allowable level of seismic displacement. If the allowable seismic displacement at the 16% exceedance range was judged to be 100 cm for the dam being analyzed, the appropriate seismic coefficient is be 0.07 using Equation 2.8 with the input values of: D_a = 100 cm, T_s = 0.33 s, S_a(0.5s) = 0.47 g, M = 9.0, and ε = 0.73. Use of k = 0.07 is also consistent with a median allowable

displacement level of 50 cm. The seismic coefficient value of 0.07 is applied in a pseudostatic slope stability analysis of the dam for this case, and if the calculated factor of safety is greater or equal to one, the dam is judged to perform satisfactorily based on the selected level of allowable displacement and the other factors.

2.9 CONCLUSIONS

A simplified seismic slope displacement procedure for evaluating earth structures or natural slopes subjected to interface earthquakes in subduction zones is developed. The proposed simplified procedure for estimating shear-induced seismic slope displacements uses the framework of Bray and Travasarou (2007). The fully coupled, nonlinear seismic slope displacement model captures the important influence of the system's yield coefficient k_y, its initial fundamental period T_s, and the ground motion's spectral acceleration at a degraded period of the slope taken as $1.5T_s$. The model separates the probability of "zero" displacement (i.e., < 0.5 cm) from the distribution of "nonzero" displacement, so that low values of calculated seismic displacement do not bias the results. The primary source of uncertainty in assessing the seismic performance of an earth slope or system during an earthquake is the input ground motion.

Therefore, a comprehensive database containing 810 two-component ground motion recordings from subduction zone interface earthquakes was developed and used to compute the seismic slope displacements.

A comparison of the proposed procedure with Bray and Travasarou (2007), which was developed for shallow crustal earthquake settings, shows that the Bray and Travasarou (2007) procedure is conservative when it is used to estimate seismic slope displacements for subduction zone interface earthquakes. There are differences between the ground motion recordings of subduction zone earthquakes and shallow crustal earthquakes. However, the differences are generally minor. The proposed seismic slope displacement model better captures the unique seismic setting of subduction zone interface earthquakes, so it should be used to estimate seismic slope displacements for these types of events.

The proposed simplified seismic slope displacement models are provided at: http://www.ce.berkeley.edu/people/faculty/bray/research. It can be implemented rigorously within a fully probabilistic framework for the evaluation of the seismic displacement hazard, or it may be used in a deterministic analysis. In all cases, however, the estimated range of seismic slope displacement should be considered an index of the expected seismic performance of the earth system. Lastly, care should be exercised if the proposed models are used to evaluate cases outside of the range of the data used to develop them.

Table 2.1. List of earthquakes and number of records used in study.

EQ	Date	Region	M_w	# of Records
(1)	(2)	(3)	(4)	(5)
Tohoku	2011/3/11	Japan	9.0	346
Hokkaido	2003/9/26	Japan	8.1	660
Kushiro-Oki	2004/11/29	Japan	7.1	330
Ofunato	2005/5/12	Japan	6.8	518
Chile85	1985/3/3	Chile	8.0	52
Maule	2010/2/27	Chile	8.8	42
Iquique	2014/4/1	Chile	8.2	46
Tocopilla	2007/11/14	Chile	7.7	28
Hualqui	2008/02/04	Chile	6.2	8
Tarapaca	2009/11/13	Chile	6.4	8
Guerrero	1995/09/14	Mexico	7.4	32
Michoacan	1985/09/19	Mexico	8.0	24
Lima74	1974/10/03	Peru	8.1	4
Lima66	1966/10/17	Peru	8.1	2
Moquegua	2001/06/23	Peru	8.4	14
Pisco	2007/8/15	Peru	7.9	26
CA1	1979/10/27	CA	6.9	4
CA2	1982/7/2	CA	5.9	2
CA3	1990/3/25	CA	7.3	20
CA4	1990/4/28	CA	6.3	4
CA5	1991/03/16	CA	6.3	2
CA6	1996/8/28	CA	5.9	8
CA7	1996/9/4	CA	6.2	10
CA8	2003/1/21	CA	6.4	24
CA9	2004/10/9	CA	6.9	14
CA10	2004/11/20	CA	6.3	14
CA11	1996/3/3	CA	6.6	2

[1] CA= Central America

Table 2.2. Comparison of the estimated seismic slope displacement with the observed displacement

System	EQ[1]	Obs. D_{max} (cm)[2]	k_y	T_s (s)	Site Class	$S_a(1.5T_s)$ (g)	Proposed P (D = "0")	Method[3] Est. Disp (cm)
(1)	(2)	(3)	(4)	(5)	(6)	(7)	(8)	(9)
Coastline Slope[4]	PP	6.0	0.10	0.6	Rock	0.25	0.00	3-12
Dam in the Andes[5]	PP	None	0.27	0.45	Alluvium	0.14	1.00	<1
La Villita dam[6]	S3	1.0	0.20	0.60	Alluvium	0.20	0.80	<1
La Villita dam[6]	S4	1.4	0.20	0.60	Alluvium	0.33	0.30	0-2
La Villita dam[6]	S5	4.0	0.20	0.60	Alluvium	0.41	0.10	1-7
Torata dam[7]	PM	5.0	0.13	0.65	Rock	0.24	0.10	1-7
Esperanza dam[8]	EM	None	0.24	0.40	Alluvium	0.43	0.50	0-2
Tutuven dam[9]	EM	None	0.39	0.15	Alluvium	0.75	0.60	0-2
Nishigo dam[10 to 16]	JT	40	0.26	0.15	Alluvium	1.51	0.00	14-58
Shitoki dam[10 to 16]	JT	None	0.29	0.40	Rock	0.40	0.70	0-1.5
Surikamigawa dam[10 to 16]	JT	None	0.30	0.68	Alluvium	0.22	0.90	<1
Coihueco Dam[9]	CM	~350	0.10	0.25	Alluvium	1.35	0.00	60-260

[1] PP= 2007 Peru/Pisco; PM= 2001 Peru/Moquegua; EM= 2016 Ecuador/Muisne; CM= 2010 Chile/Maule; JT=Japan/Tohoku ; S3, S4, and S5 from Elgamal et al. (1990).

[2] D_{max} = observed maximum displacement due to shear deformation. "None" listed if D is negligible.

[3] P(D=0) from Eqs. (2.2)-(2.3). Zero displacement refers to negligible displacement (i.e., D<0.5 cm). Estimated displacement range is 16% to 84% from Eqs. (2.2)-(2.7).

[4] Sancio et al. (2016), [4,5] Rodriguez-Marek et al. (2007), [5] Macedo (2009), [6] Elgamal et al. (1990), [7] Rodriguez-Marek et al. (2001), [7] CISMID (personal communication), [8] Pestana et al. (1996), [8] Nikolaou et al. (2016), [9] Verdugo et al. (2012), [9] Bray and Frost (2010), [10] Matsumoto (2010), [11] EERI (2011), [12] Yamaguchi et al. (2011), [13]Yamaguchi et al. (2012), [14] Bray (2013), [15] Mr. Matsumoto (personal communication), [16] Mr. Satou of NILIM (personal communication).

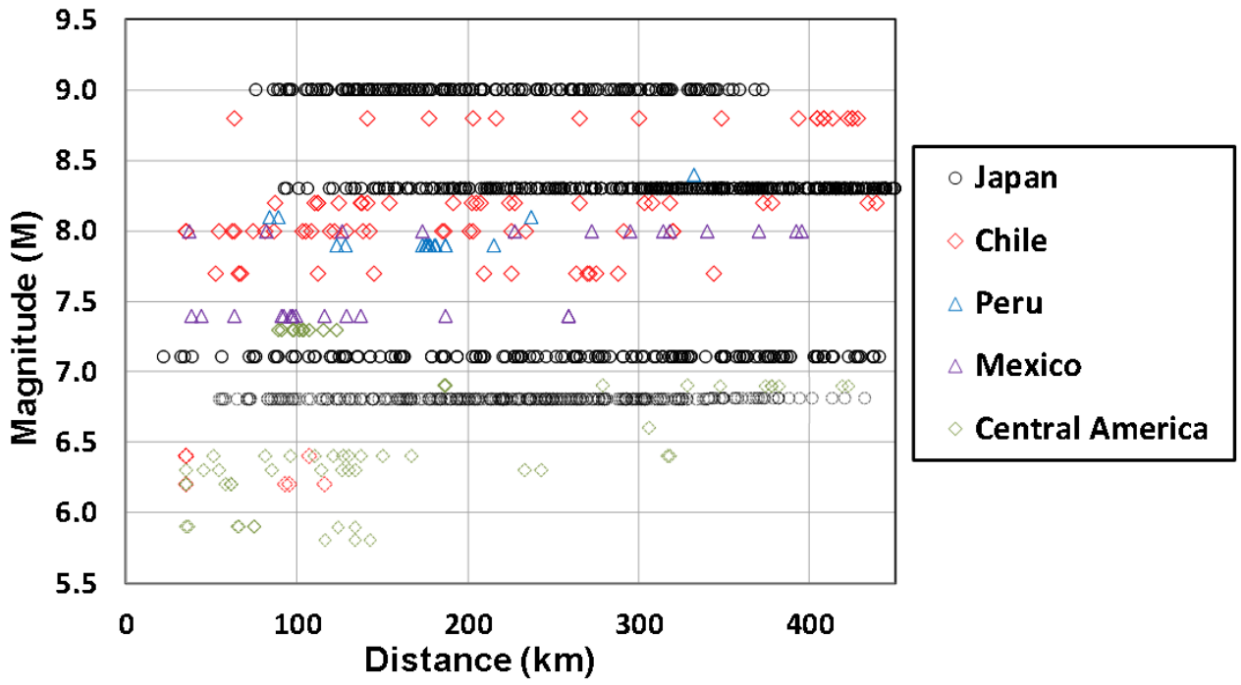

Figure 2.1. Distribution of magnitudes and epicentral distances for the compiled subduction earthquake database.

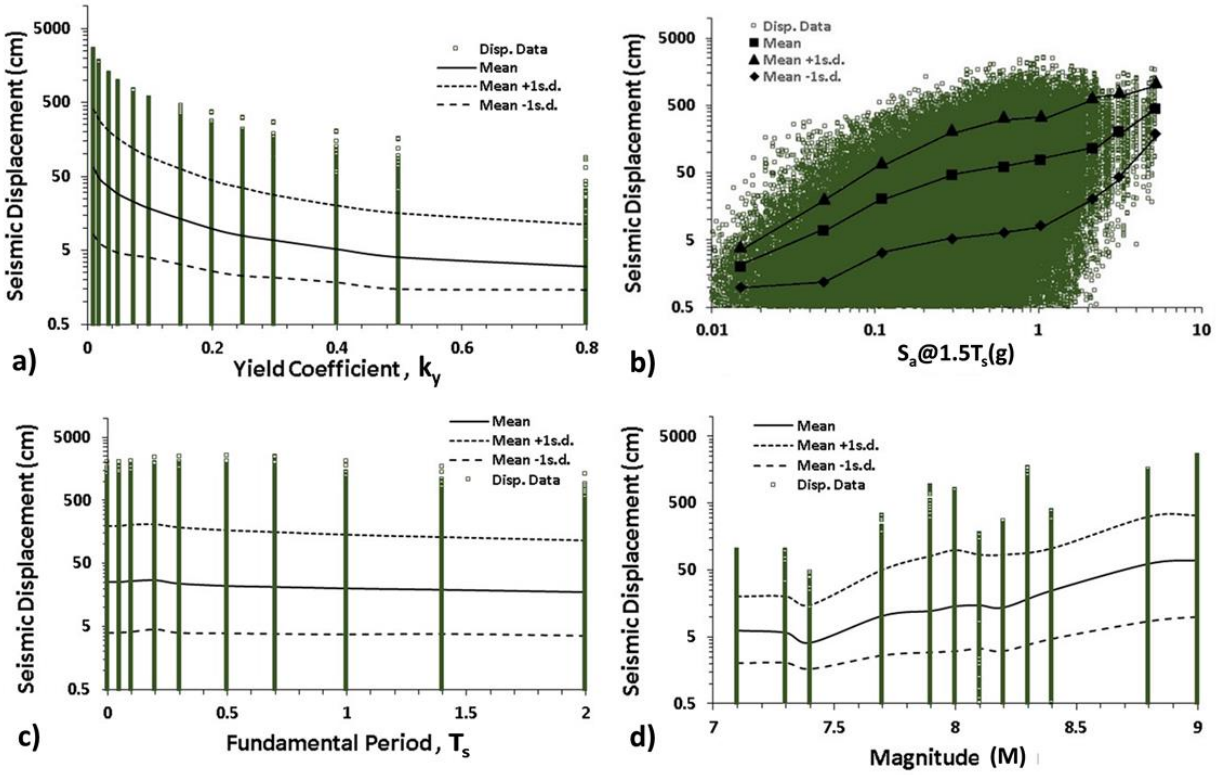

Figure 2.2. Distribution of simulated displacement data for D>0.5 cm with a) yield coefficient, b) spectral acceleration at 1.5 times the initial fundamental period, c) initial fundamental period, and d) moment magnitude.

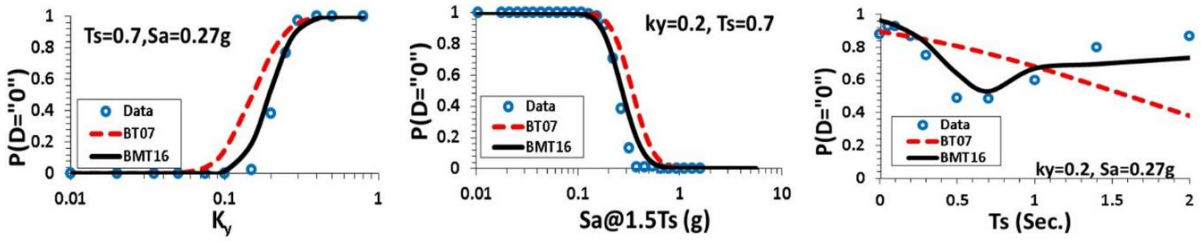

Figure 2.3. Comparison of predicted probability of "zero" displacement (i.e., D≤ 0.5 cm) for the model developed in this study (BMT17) versus the simulated displacement data from subduction zone events considered in this study and the Bray and Travasarou 2007 (BT07) model which was developed using shallow crustal earthquakes along active plate margins records. Comparison for a) yield coefficient, b) spectral acceleration at 1.5 times the initial fundamental period and c) fundamental period.

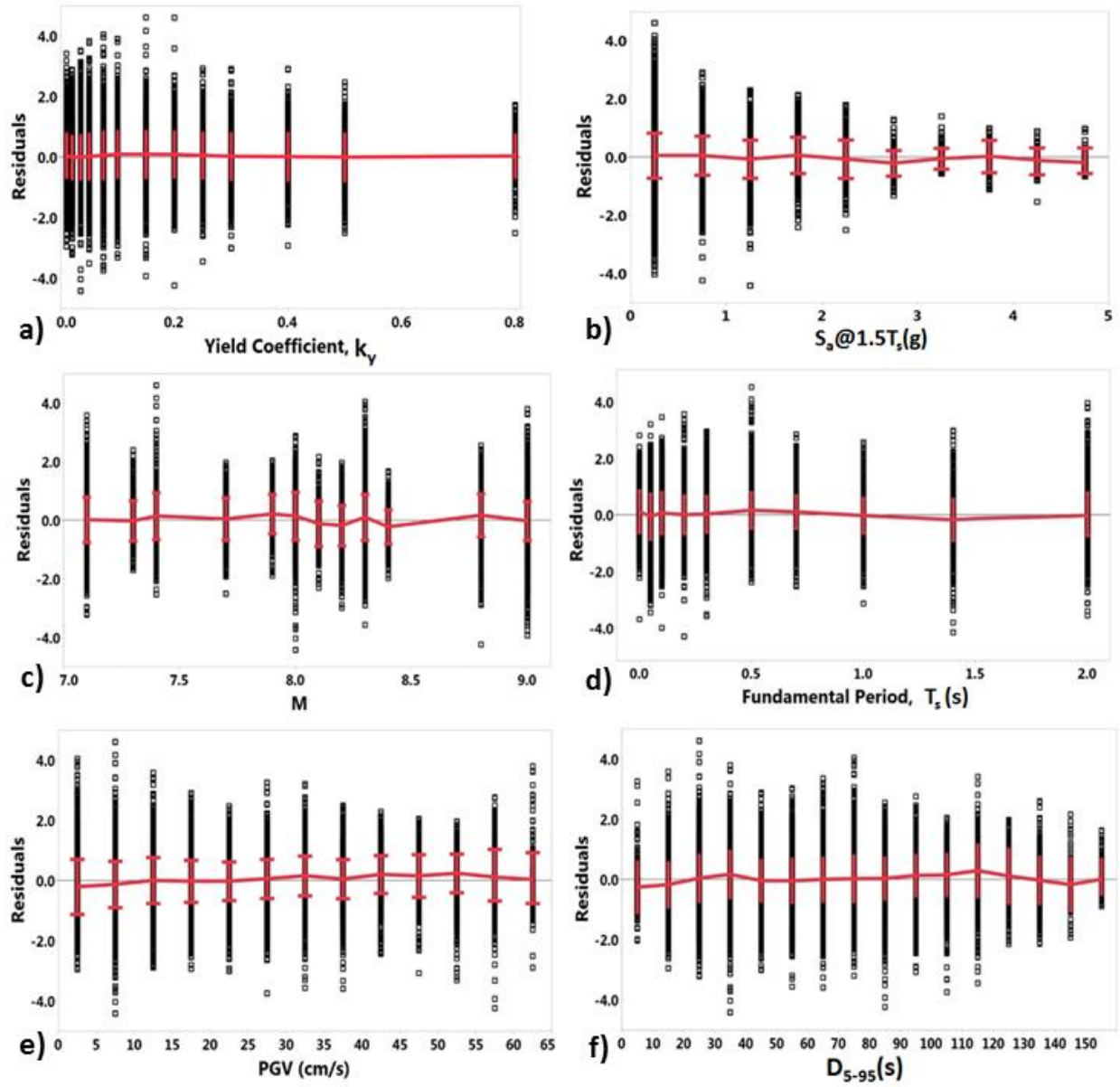

Figure 2.4. Residuals ($Ln(D_{data}) - Ln(D_{Predicted})$) of Equation 2.4 and Equation 2.5 plotted versus a) yield coefficient, b) spectral acceleration, c) moment magnitude, d) fundamental period of sliding mass, e) peak ground velocity, and f) duration.

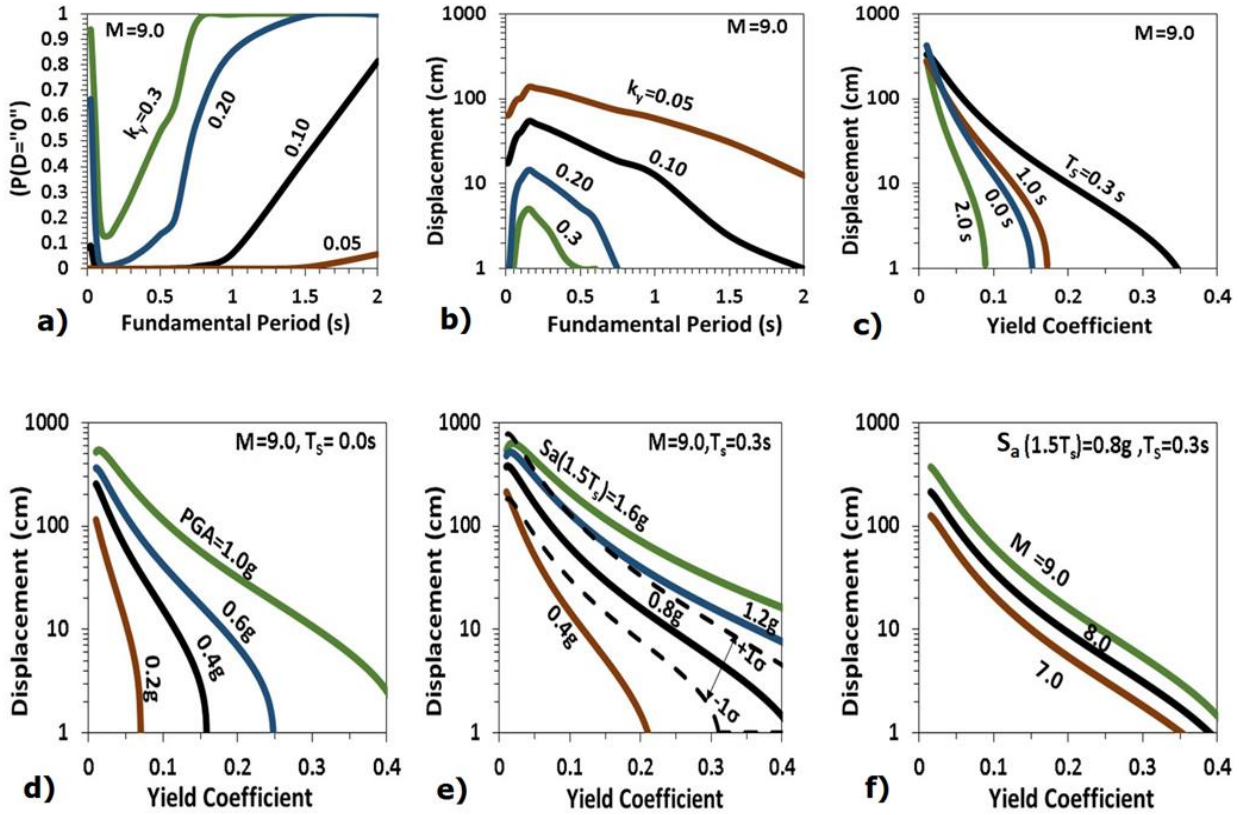

Figure 2.5. Model trends: upper plots are for a M 9.0 interface earthquake at a distance of 35 km and show the dependence of a) the probability of "zero" seismic displacement with respect to the initial fundamental period, b) seismic displacements with respect to the initial fundamental period and c) seismic displacements with respect to yield coefficient. Figures d) and e) are for a M 9.0 interface earthquake. d) seismic displacements with respect to yield coefficient for several *PGA* values, e) seismic displacements with respect to yield coefficient for several $S_a(1.5T_s)$ values. f) effect of earthquake magnitude at a specified ground motion intensity

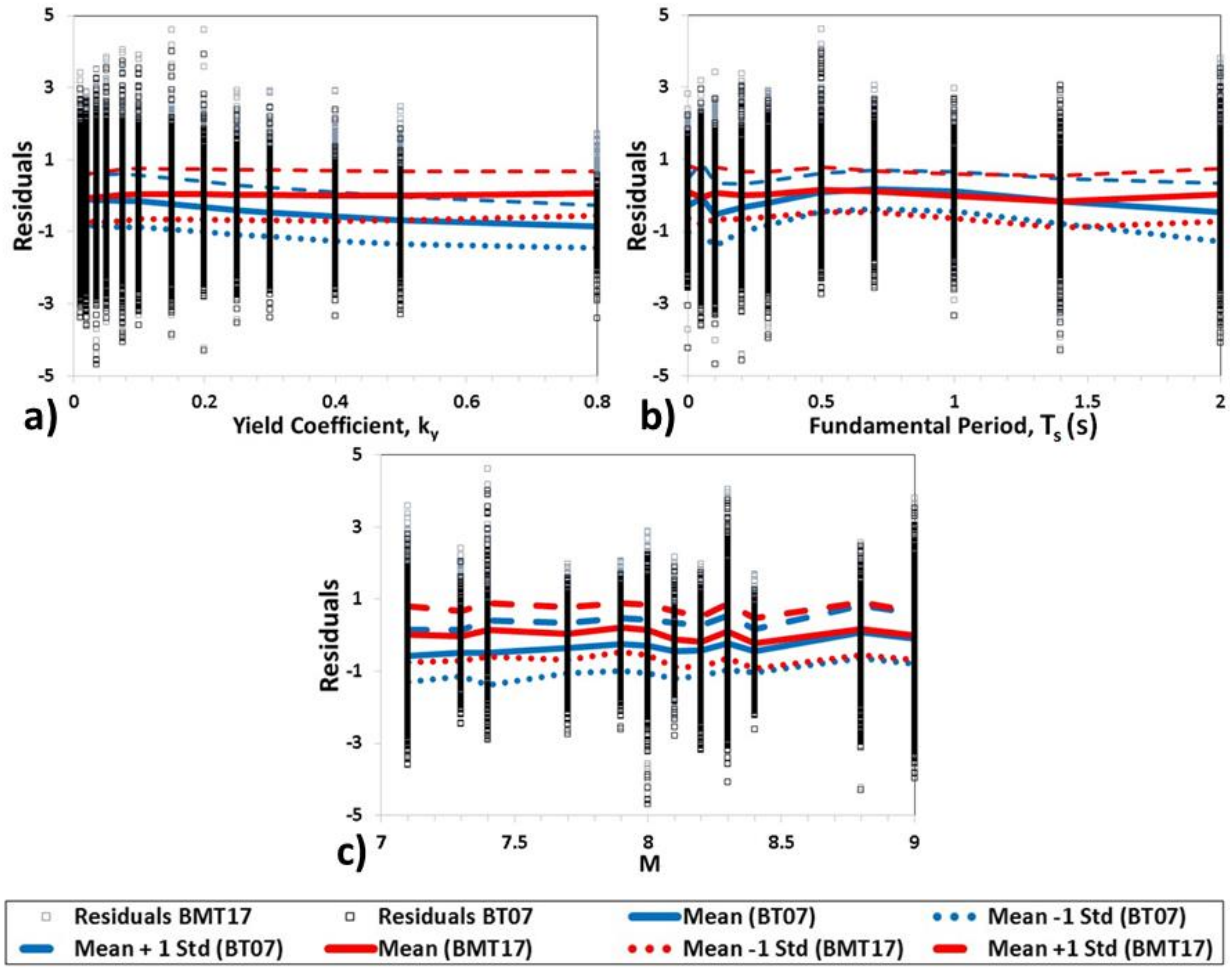

Figure 2.6. Comparison of residuals (i.e. $Ln(D_{data})$ -$Ln(D_{Predicted})$) from the BT07 method versus the proposed BMT17 equations for use in subduction earthquake zones. a) yield coefficient, b) initial fundamental period c) moment magnitude.

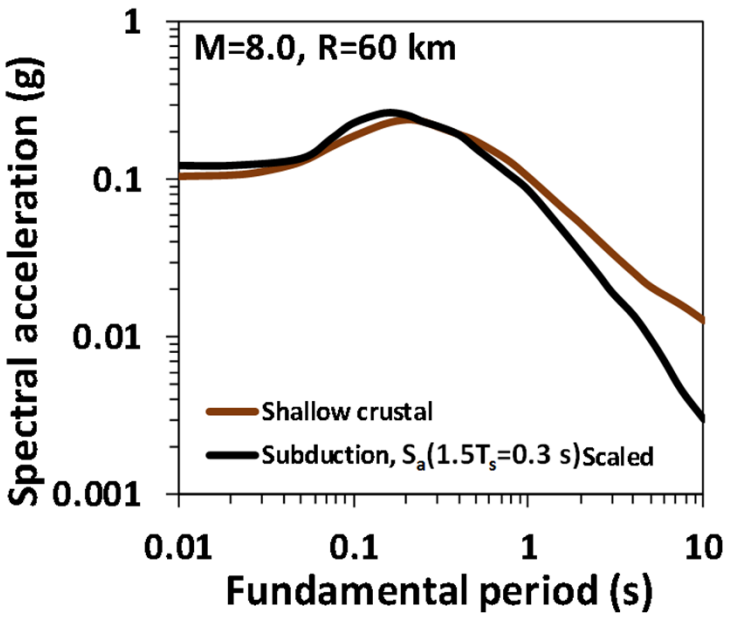

Figure 2.7. Spectral shape comparison for shallow crustal and subduction interface earthquakes for V_{s30} = 760 m/s site condition. $S_a(1.5T_s)$ at a fundamental period of 0.2 sec. is normalized to the value corresponding to the shallow crustal response spectrum for moment magnitude 8.0 and source-to-site distance of 60 km. Spectra were calculated from the Abrahamson et al. (2013) and Abrahamson et al. (2016) GMPEs for shallow crustal and subduction zone earthquakes, respectively.

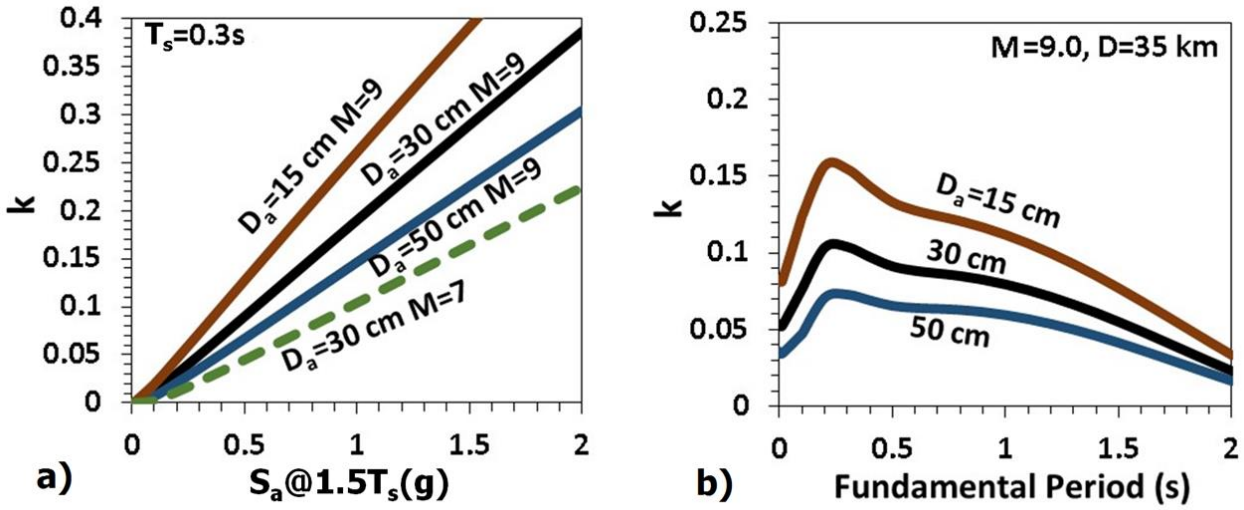

Figure 2.8. Variation of the seismic coefficient as a function of: (a) allowable displacement and seismic demand, and (b) fundamental period of the sliding mass.

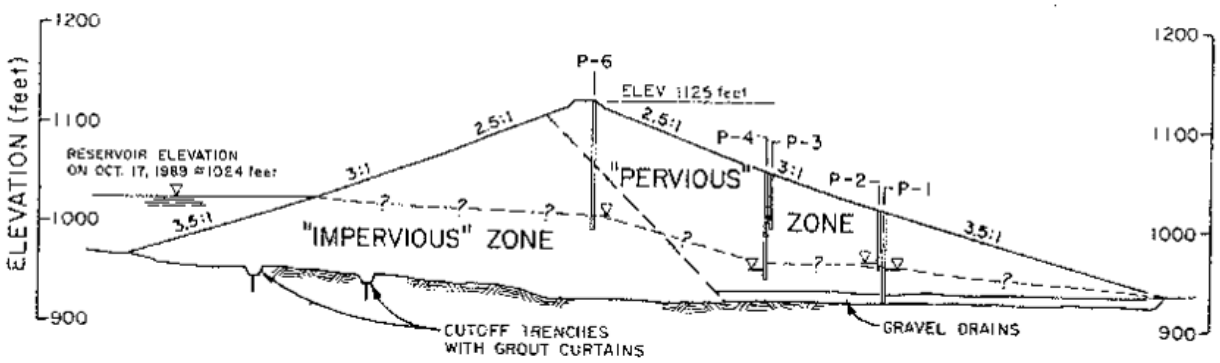

Figure 2.9. Maximum cross section of dam used in illustrative example (from Bray and Travasarou 2007).

CHAPTER 3: PERFORMANCE-BASED SEISMIC SLOPE DISPLACEMENT PROCEDURE

The contents of this chapter are primarily from a journal article submitted to the Earthquake Spectra Journal of the Earthquake Engineering Research Institute (EERI) by Macedo, J., Bray, J.D., Abrahamson, N. and Travasarou, T., entitled: "Performance-based seismic slope displacement procedure", submitted in December 2016, which is under review.

3.1 INTRODUCTION

The seismic performance of an earth/waste system or natural slope is typically assessed through Newmark-type sliding block analyses that provide an estimate of the expected seismic displacement (e.g., Makdisi and Seed 1978, Bray and Travasarou 2007, Saygili and Rathje 2008). Dynamic nonlinear effective stress analyses using finite element or finite difference methods with robust soil constitutive models may be employed for critical earth systems or when strength loss mechanisms such as from soil liquefaction are involved. In many other cases, if dynamic analyses are performed, they are used to calculate the seismic response of the earth system, which is then used to calculate seismic displacements in an approach referred to as the decoupled approximation (i.e., the calculation of seismic displacement is decoupled from the calculation of the seismic response; Lin and Whitman 1983). Even in cases when dynamic analyses are performed, Newmark-type sliding block analyses form the basis for a preliminary assessment of the expected seismic performance of the earth system. Pseudostatic slope stability procedures, wherein a horizontal seismic coefficient is applied to a potential sliding mass in a conventional slope limit equilibrium analysis, are also employed commonly in practice.

Current state of practice simplified seismic slope displacement procedures separate the estimation of the ground motion intensity measure (*IM*) from the calculated seismic displacement (*D*) given the selected *IM* hazard level This approach is referred to in this study as pseudo-probabilistic because the *IM* hazard curve is estimated probabilistically but *D* is estimated based on only a single *IM* value. In this approach, the ground motion *IM* is estimated for a given design hazard level (or return period) though a probabilistic seismic hazard analysis (PSHA), and then, *D* is estimated for that *IM* value. The underlying assumption is the hazard level for *D* is consistent with that of the *IM*. For example, Bray and Travasarou (2007) performed regression analyses of the results of over 55,000 fully coupled deformable sliding block analyses using nearly 700 ground motion records to develop an estimate of the seismic displacement as a function of the yield coefficient of the earth system (k_y, which is the seismic coefficient that results in a pseudostatic factor of safety (*FS*) of one), the 5%-damped spectral acceleration of the ground motion at the base of the potential sliding assuming there is no material above it at its degraded fundamental period, which will be denoted as S_a (the degraded period is taken as 1.5 times the system's initial fundamental period), the initial fundamental period of the sliding mass (T_s), and earthquake moment magnitude (*M*). Each of these parameters are uncertain, with the highest level of uncertainty being commonly associated with the input ground motion. Thus, the mean ground motion *IM*, which in this procedure is S_a, is often estimated considering a design seismic hazard level (e.g., at the 10% probability of exceedance in 50 years level), while the other parameters are assigned best-estimate, median values to develop a 16% to 84% exceedance estimate range of the

seismic displacement given the specified value of S_a.

An alternative is to use a fully probabilistic approach. Whereas a fully probabilistic approach would include all fractals of the *IM* hazard curve, the proposed performance-based assessment of seismic slope displacement uses a single *IM* hazard curve, which is usually the mean hazard curve. The uncertainties associated with the ground motion *IM* parameter are not usually included in the logic tree for the estimation of seismic displacements (*D*) because they have already been taken into account in the ground motion hazard analysis for the *IM* as also pointed out by Wang and Rathje (2015). Only a few of the current available procedures are suitable to be implemented in a performance-based probabilistic seismic slope assessment for slope properties expressed as k_y and T_s (e.g., Travasarou et al. 2004, Bray and Travasarou 2007, Rathje et al. 2014). A performance-based seismic slope assessment is more robust than commonly used procedures and can provide additional insights. However, performance-based seismic slope displacement procedures are rarely used in engineering practice, because they are not easy to use and straightforward, implemented procedures are not available. In this chapter, a straightforward performance-based procedure for the estimation of seismic slope displacement is presented. Additionally, a compatible pseudostatic slope stability procedure is proposed. The proposed procedures are applicable for a wide range of earth systems shaken by shallow crustal earthquakes along active margins (e.g., California) as well as for subduction zone earthquakes (e.g., South America). They are easily implemented in practice using information that an engineer commonly has access to when evaluating the seismic performance of an earth/waste system or natural slope.

3.2 PREVIOUS STUDIES

There are several seismic sliding block displacement procedures available in the literature. Several of these well-known procedures are formulated only for the case of rigid sliding blocks wherein the dynamic response of the potential sliding mass is neglected (e.g., Newmark 1965, Richards and Elms 1979, Lin and Whitman 1986, Watson-Lamprey and Abrahamson 2006, Jibson 2007, and Saygili and Rathje 2008). The rigid sliding block analyses should not be used except in those few cases wherein the potential sliding mass is shallow and stiff, so that its fundamental period is nearly zero, or as a screening tool in regional assessments when there is insufficient information to characterize the actual fundamental period of the potential sliding mass. In all other cases, the dynamic response of what is commonly a "non-rigid" sliding mass should be considered, because the dynamic response of the sliding mass has been shown to be a key factor (Rathje and Bray 1999, 2000). As mentioned previously, many of the seismic slope displacement methods that capture the flexibility of the sliding mass do so by employing the decoupled approximation that assumes no relative displacements during the seismic response analysis, whose results are then used to calculate the seismically induced permanent displacement (e.g., Makdisi and Seed 1978, Bray and Rathje 1998). Due to the inherent limitations of the decoupled approximation, fully coupled stick-slip sliding block analyses are preferred (Rathje and Bray 1999, 2000). There are simplified seismic slope displacement procedures that capture the simultaneous occurrence of the nonlinear dynamic response of the potential sliding mass and the effects of periodic sliding episodes (e.g., Bray and Travasarou 2007, Bray et al. 2017). Few simplified seismic slope displacement procedures are based on the results of two-dimensional (2D) or three-dimensional (3D) dynamic analyses. As mentioned previously, the largest source of uncertainty is typically due to the input earthquake ground motion. Hence, a simpler one-dimensional (1D) model is used with many earthquake ground motions to develop the data to support the development of a simplified seismic slope stability procedure. This assumption is reasonably conservative for most cases

(Rathje and Bray 2001); the exception is for shallow sliding adversely affected by topographic amplification. Lastly, most seismic slope displacement procedures have been formulated only for shallow crustal earthquakes along active plate margins. However, the Bray et al. (2017) procedure has been formulated for subduction earthquake zones.

Figure 3.1 illustrates the different ways sliding block seismic slope displacement procedures are implemented. A deterministic approach first requires the selection of a design earthquake scenario, defined by *M* and distance (*R*) and the selection of the number of standard deviations above the median (ε_{GM}). Several earthquake scenarios should be considered. The IM is estimated based on ground motion prediction equations (GMPE) and the selected ε_{GM} (often arbitrarily set to 0 or 1). Once the *IM* is defined, *D* is estimated using a seismic slope displacement model which is usually formulated in terms of properties of the earth/waste system (e.g., k_y, T_s) and the *IM*. The number of standard deviations below and above the median displacement estimate (ε_d) is used to account for the variability introduced in the calculation of seismic displacement given the specified *IM* and earth system parameters.

In the pseudo-probabilistic approach (Figure 3.1), an *IM* hazard curve that defines the mean annual rate of exceedance (λ_{GM}) for different levels of the *IM* is developed through a PSHA that considers all potential earthquake/ground motion scenarios (*M*, *R*, and ε_{GM}). The design *IM* value is selected from the hazard curve for an acceptable λ_{GM} (or return period). This particular *IM* value is then used to estimate the seismic slope displacement with the physical properties of the earth/waste system (e.g., k_y, T_s). The number of standard deviations (ε_d) in the estimate of *D* given these inputs is used to account for the displacement variability.

In a performance-based approach (Figure 3.1), the variability in the ground motion *IM* and the seismic displacement are considered explicitly through a probabilistic analysis that convolves the *IM* hazard curve with a seismic displacement model and the variability of the system properties used in the model. Several fractals of the *IM* hazard curve may be used, but only the mean *IM* hazard curve is used typically, and different seismic displacement models may also be considered to include this source of epistemic uncertainty, but only one model is used typically. The result is a seismic displacement hazard curve that provides the mean annual rate of exceedance for different levels of seismic displacement (λ_d). The displacement hazard curve can be used to estimate the expected seismic displacements directly related with the design hazard level. It better captures the uncertainty in the estimate of seismic slope displacement. Thus, it is well suited for making engineering decisions.

Pseudostatic slope stability procedures are often used in engineering practice in preliminary assessments, because they are straightforward. However, they are limited unless the parameters utilized in the analysis accurately reflect the potential seismic demand and its impact on the seismic performance of the system. The seismic coefficient that is employed in a pseudostatic slope stability analysis should be selected in a rational manner if this procedure is to form a sound basis for a seismic slope stability assessment (e.g., Bray and Travasarou 2009). The selection of the seismic coefficient employed in the analysis is often based on precedence, regulatory design guidance, and engineering judgment, without due consideration of the seismic displacement that constitutes satisfactory performance for each particular project and without incorporating the vastly different seismic exposure for sites around the world. Commonly used pseudostatic methods are often formulated under the assumption of a fixed maximum level of seismic displacements that can be considered acceptable (e.g., 1 m for earth dams in the Seed 1979 method). These methods usually consider the seismic coefficient as a fixed number based on precedence (e.g., 0.15), or as a fixed fraction of the peak ground acceleration (*PGA*). Several recent efforts relate directly the

selection of the seismic coefficient to be used in pseudostatic slope stability analysis to the allowable level of seismic displacement that the earth/waste system can sustain (e.g., Bray and Travasarou 2009, and Papadimitriou et al. 2014). Although these efforts provide a rational basis for selecting the seismic coefficient based on the allowable level of displacement, they are not formulated in a rigorous probabilistic framework (e.g., they do not consider the entire seismic hazard curve in the selection of the seismic coefficient). A pseudostatic slope stability method based on the performance-based seismic slope displacement procedure developed in this study is also presented in this chapter.

3.3 CRITICAL DESIGN ISSUE

Before discussing the performance-based seismic slope displacement procedure further, it is imperative that a key design issue be addressed. In the evaluation of the seismic performance of an earth/waste system or natural slope, the engineer should first assess if there are materials in the earth structure or its foundation that can lose significant strength as a result of cyclic loading (e.g., soil liquefaction). If so, this should be the primary focus of the evaluation because large displacement flow slides are possible. There is abundant research on this topic, and it is not the focus of this study. This study addresses the seismic performance of earth/waste systems or natural slopes wherein flow slides are not likely (i.e., the post-liquefaction slope stability factor of safety is greater than one).

3.4 PERFORMANCE-BASED ASSESMENT OF SEISMIC DISPLACEMENT

The framework of Bray and Travasarou (2007) is used in this study because it provides an explicit definition of the probability of negligible displacement and the median seismic displacement, it has been formulated based on the fully coupled stick-slip deformable sliding block analysis, its framework has been used to develop procedures for earthquakes in shallow crustal settings and subduction interface settings, and it is used widely in practice. It models seismically induced permanent displacements as a mixed random variable that has a probability mass at "zero" displacement (d_0) and a probability density for finite displacement values greater than d0 (Figure 3.2). Displacements smaller than d_0 are typically not of engineering significance and can for all practical purposes be considered to be negligible (i.e., zero). The values of seismic displacements that are smaller than d_0 are lumped together to d_0. The probability of "zero" displacements ($d \leq d_0$) and the median "non-zero" displacements are estimated based on k_y, T_s, S_a, and M using ground motion recordings from shallow crustal earthquakes. Using this framework, the seismic displacement model for shallow crustal earthquake from Bray and Travasarou (2007), referred to as BT07, has been formulated with and without magnitude dependence, considering d_0 = 1 cm. Bray et al. (2017), referred to as BMT17, used the same framework to develop predictive equations for seismic slope displacement for subduction zone earthquakes, but considered d0 = 0.5 cm.

The goal of a performance-based seismic slope displacement assessment is to develop the seismic displacement hazard curve which defines the annual probability of the seismic displacement exceeding a specified seismic displacement threshold. This probability is given by Equation 3.1 for the case in which the seismic displacement model is not magnitude dependent and by Equation 3.2 for the case in which the model is magnitude dependent.

$$\lambda_d = \sum_{i=1}^{nky} \sum_{j=1}^{nts} \int_0^{\infty} P\,(D > d | S_a, k_{yi}, T_{sj}) \Delta\lambda(S_a) d(S_a) w_{ij} \tag{3.1}$$

$$\lambda_d = \sum_{i=1}^{nky} \sum_{j=1}^{nts} \int_M \int_0^{\infty} P\,(D > d|S_a, M, k_{yi}, T_{sj}) P(M|S_a) \Delta\lambda(S_a) d(S_a) w_{ij} \quad (3.2)$$

Consistent with the PEER performance-based engineering framework (Deierlein et al. 2003), *P* is used for probability and λ is used for annual rate of exceedance. $\Delta\lambda$ represents the rate of occurrence. $P\left(D > d\middle|S_a, k_{yi}, T_{sj}\right)$ in Equation 3.1 is the conditional probability the displacement level d is exceeded given S_a, k_{yi} and T_{sj}, and $\Delta\lambda(S_a)$is the annual probability of occurrence of S_a. In Equation 3.2, $P\,(D > d|S_a, M, k_{yi}, T_{sj})$ is the conditional probability the displacement level d is exceeded given S_a, M, k_{yi} and T_{sj}. $P(M|\,S_a)$ is the probability of occurrence of M given S_a; it represents the contribution to the total hazard S_a from M. The term $P(M|\,S_a)$ can be estimated from the hazard deaggregation for S_a. The uncertainties of k_y and T_s are treated as epistemic, so a logic tree is employed, in which *nky* values for k_y are defined with weighting factors wky_i (i=1: *nky*) and *nts* values for T_s are defined with weighting factors wts_j (j=1: *nts*). The weighting factor for each combination of k_y and T_s is defined as w_{ij}. k_y and T_s may be considered to be represented by a lognormal distribution with its mean and covariance (*cov*) to assign their alternative values and weighting factors (i.e., consider an equal partition in the log space to evaluate the weighting factors). In the case in which the uncertainty of k_y and T_s is not considered, the calculations are performed using the mean values of k_y and T_s with weighting factors equal to 1.

The annual probability of occurrence of a ground motion level S_{ai}, $\Delta\lambda(S_a)$, is equal to the derivative of the hazard curve for S_a (i.e.,$\frac{d(Ha(S_a))}{dS_a}$) evaluated at S_{ai}. Travasarou et al. (2004) used a function that fit approximately the hazard curve at the degraded period of the system to calculate its derivative and then evaluate the required integrals. However, this procedure could lead to inconsistencies especially for low or large values of spectral acceleration. In this study the integrals are estimated based on the "integration by parts" and "rate of occurrence" methods. The integration by parts method does not require approximations and is used by the U.S.G.S. for risk analyses. The rate of occurrence method is an approximation but believed to be sufficiently accurate.

The shallow crustal earthquake seismic slope displacement model without magnitude dependence of Bray and Travasarou (2007) estimates the probability of "zero" displacement and the median value of the "non-zero" seismic displacement with Equations 3.3 and 3.4, respectively.

$$P(D = \text{"0"}) = 1 - \Phi(-1.76 - 3.22Ln\left(k_y\right) - 0.484T_s + 3.52Ln(S_a)) \quad (3.3)$$

$$Ln\left(\hat{d}\right) = -1.10 - 2.83Ln\left(k_y\right) - 0.333\left(Ln\left(k_y\right)\right)^2 + 0.566Ln\left(k_y\right)Ln(S_a) + 3.04Ln(S_a) - 0.244\left(Ln(S_a)\right)^2 + 1.5T_s \quad (3.4)$$

Where Φ is the standard normal cumulative distribution function, and $\hat{d}$ is the median seismic displacement. The first term in Equation 3.4 should be replaced by -0.22 when $T_s < 0.05s$. The first term inside the integral in Equation 3.1 can be evaluated as:

$$P(D > d|\,S_a, k_y, T_s) = \left[1 - P(D = \text{"0"}|\,S_a, k_y, T_s)\right]\left[P(D > d|\,S_a, k_y, T_s, D > \text{"0"})\right] \quad (3.5)$$

Considering a lognormal distribution for seismic displacements (D), the second term is estimated as:

$$P\left(D > d\,\middle|k_y, T_s, S_a, D > \text{"0"}\right) = 1 - \Phi\left(\frac{Ln(d) - Ln(\hat{d})}{\sigma_{LnD}}\right) \quad (3.6)$$

Where $\sigma_{LnD} = 0.67$, which corresponds to the standard deviation of the error in Equation 3.4.

In the "rate of occurrence" approach, the $\Delta\lambda(S_{ai})$term in Equation 3.1 (for a S_{ai} value representative of a spectral acceleration bin from S_{a1} to S_{a2}) can be estimated from the hazard curve in terms of the mean annual rate of exceeding the ground motion levels in the bin, λ_{GM1} and λ_{GM2}, in terms of the rate of occurrence, $RO_i = \lambda_{GM1} - \lambda_{GM2}$, as:

$$\Delta\lambda(S_{ai}) = \left|\frac{dHa}{dS_a}\right|_{S_{ai}} = \frac{\lambda_{GM1}-\lambda_{GM2}}{d_{S_{ai}}} = \frac{RO_i}{d_{S_{ai}}} \tag{3.7}$$

Thus, Equation 3.1 becomes:

$$\lambda_d = \sum_{i=1}^{nky}\sum_{j=1}^{nts}\sum_k P\,(D > d|S_{ak}, k_{yi}, T_{sj})RO_k w_{ij} \tag{3.8}$$

In the integration by parts approach, using the integration by part theorem for the integral in Equation 3.1, the following result is obtained (the detailed derivation is included on the electronic Appendix B.1)

$$I_{Sa} = \int_{-\infty}^{\infty}\left\{3.52PDF1(Ha)\left(1-\Phi\left(\frac{Ln(d)-Ln(d)}{\sigma_{LnD}}\right)\right) + (Ha)\big(\Phi(-1.76-3.22Ln(k_y) - 0.484T_sLn(k_y) + 3.52Ln(S_a))\big)\left(\frac{PDF2}{\sigma_{LnD}}\right)\begin{bmatrix}0.566Ln(k_y)-\\ 0.488Ln(S_a)+3.04\end{bmatrix}\right\}dLn(S_a) \tag{3.9}$$

Equation 3.9 can be used directly in Equation 3.1 to estimate the displacement hazard curve if the best estimated values (e.g. mean) for k_y and T_s are considered (i.e. their weighting factors are set to 1 in Equation 3.1). To account for material inhomogeneity and variability in the strength of the soil, the epistemic variability for the yield coefficient (k_y) and the system's initial fundamental period (T_s) can be considered through a logic tree scheme as previously discussed

Bray and Travasarou (2007) prefer the use of their equation to estimate the median "non-zero" seismic displacements for shallow crustal earthquakes, which includes a magnitude term:

$$Ln(\hat{d}) = -1.10 - 2.83Ln(k_y) - 0.333\left(Ln(k_y)\right)^2 + 0.566Ln(k_y)Ln(S_a) + 3.04Ln(S_a) - 0.244Ln(S_a)^2 + 1.5T_s + 0.278(M-7) \tag{3.10}$$

The probability of "zero" displacement relationship remains as defined previously as Equation 3.3. The probability of a seismic displacement *D* greater than a given value *d* and for given values of k_y, T_s, S_a, and *M*, is estimated from Equation 3.5 with σ_{LnD}equal to 0.66 (which corresponds to the standard deviation of the error term in Equation 3.10).

In the "rate of occurrence" approach, the $\Delta\lambda(S_{ai})$ term in Equation 3.2 (for a S_{a1} value representative of a spectral acceleration bin from S_{a1} to S_{a2}), is estimated using Equation 3.7 as in the previous case and $P(M|S_a)$ can be estimated from the hazard deaggregation for the magnitude term. The seismic slope displacement hazard curve is evaluated by approximating the integrals numerically for weighted values of k_y and T_s as discussed previously. Alternative equations for the "integration by parts" approach are provided in the electronic Appendix B.1.

Bray et al. (2017) provide a predictive equation to estimate the probability of "zero" displacements and the median "non-zero" displacement for subduction interface earthquakes. These equations include a dependence on the magnitude term for the median "non-zero" seismic displacement and can be used in the same way as described before for the predictive equations for

the shallow crustal settings with magnitude dependence. The necessary equations to use the Bray et al. (2017) procedure in a performance-based framework are provided in the electronic Appendix B.1.

3.5 UNCERTAINTY TREATMENT OF SYSTEM PROPERTIES

The uncertainty for the system properties (i.e., ky and Ts) can be treated as epistemic (e.g. Rathje and Saygili 2011, Wang and Rathje 2015). However, their uncertainty has also been considered through probability density functions (PDF) (e.g., Yegian et al. 1991, Travasarou et al. 2004). In the latter case, which is also consistent with the PEER performance-based design framework, Equations 3.1 and 3.2 become:

$$\lambda_d = \int_{T_s}\int_{k_y}\int_0^\infty P(D > d|S_a, k_y, T_s)P(S_a)f(k_y)f(T_s)dS_a dk_y dT_s \quad (3.11)$$

$$\lambda_d = \int_{T_s}\int_{k_y}\int_M\int_0^\infty P(D > d|S_a, M, k_y, T_s)P(M|S_a)(\Delta\lambda(S_a))f(T_s)dS_a dk_y dT_s \quad (3.12)$$

The functions $f(k_y)$ and $f(T_s)$ are the probability density functions for the yield coefficient and the fundamental period, respectively; the other terms were defined previously. Equations 3.11 and 3.12 can be evaluated with the procedures already presented approximating the integrals over k_y and T_s as summations.

The two approaches for categorizing the uncertainty in the system properties are compared considering a system with mean value of k_y=0.15 with *cov*=0.2 and mean value of T_s =0.67 s with *cov*=0.1, which is located in Yerba Buena (YB), California. The hazard curve for the spectral acceleration at the degraded period of the system and the deaggregation information were obtained from the USGS website (https://earthquake.usgs.gov/hazards/interactive/). A lognormal distribution was considered for k_y and T_s in the *PDF* approach. For the case that considers an epistemic treatment for k_y and T_s, 3 alternative k_y and 3 alternative T_s, values are defined through a logic tree with weighting factors consistent with a lognormal distribution. The alternative values of k_y are 0.10, 0.15, and 0.23 with weighting factors of 0.14, 0.72 and 0.14, and the alternative values of T_s are 0.54, 0.67, and 0.83 with weighting factors 0.14, 0.72, and 0.14.

Figure 3.3 shows the comparisons between the two approaches for the system's uncertainty treatment, the different curves from each branch of the logic tree are also included (i.e., 9 curves given the 3 alternative values each for k_y and T_s). The mean slope displacement hazard curve calculated considering the epistemic treatment for k_y and T_s matches the curve calculated using PDF functions for k_y and T_s. Thus, if one only wanted the mean slope displacement hazard curve, either approach could be used. However, the epistemic approach has the advantage of allowing an assessment in the uncertainty of the displacement hazard curve, and it is recommended.

3.6 EPISTEMIC UNCERTAINTY OF *IM* AND *D* MODELS

Usually the uncertainties associated with the ground motion are not included in the logic tree for the estimation of seismic displacements because they have already been taken into account in the ground motion hazard analysis for the *IM* (e.g., Wang and Rathje 2015). However, the epistemic uncertainty in the *IM* may also be integrated into the logic tree for the estimation of *D*. To illustrate the consideration of epistemic uncertainty in the *IM* and *D* predictive models, a simplified PSHA analysis is conducted for 2 seismic sources. The logic tree considered for the PSHA is shown in Figure 3.4. There are 3 possible magnitudes and 2 possible values for the

activity rate for each seismic source, and 2 GMPEs are used to calculate PGA for the rigid sliding block case (i.e., T_s = 0 s). Thus, a total of 72 *IM* hazard curves each one with its respective weighting factor are calculated.

The epistemic uncertainty in the parameter k_y is also considered using values of 0.1, 0.15, and 0.23 with weighting factors of 0.14, 0.72, and 0.14, respectively. The epistemic uncertainty in the seismic displacement model is captured using the BT07 model with a weighting factor of 0.7 and the Saygili and Rathje (2008) scalar model with a weighting factor of 0.3. Each *IM* hazard curve is convoluted with each *D* model for all the realizations of k_y, which produces 432 seismic displacement hazard curves. They are shown in Figure 3.5 with the mean hazard curve and the 10%, 50%, and 90% fractal hazard curves. Figure 3.5 also includes the 10% and 90% fractal hazard curves when only the mean *IM* hazard curve is considered. Including several sources of uncertainty in this simple example illustrates the range of results possible. It is standard practice in performance-based design to use the mean hazard curve to estimate seismic displacement at a specified hazard level.

3.7 DIFFERENT TECTONIC SETTINGS

Sometimes there are significant contributions from seismic sources in more than one tectonic setting (e.g., shallow crustal and subduction zones). Bray et al. (2017) found there were not large differences in the estimates resulting from a shallow crustal earthquake seismic displacement model (BT07) and subduction earthquake zone seismic displacement model (BMT17) if they were both conditioned on the same seismic demand, such as S_a. It is more important to use GMPEs with the appropriate characterization for each tectonic setting to estimate S_a than to use different seismic displacement models. However, as there are some cases in which the secondary effect of using the seismic displacement model appropriate for each tectonic setting is important, recommendations are presented.

In those cases, the *IM* hazard curve from each tectonic setting should be convoluted with their respective representative displacement model, and their annual rates of exceedance summed up to produce the total seismic displacement hazard curve. Figure 3.6a shows the spectral acceleration hazard curves from shallow crustal and subduction earthquake zones for a system with T_s = 0.67 s and k_y = 0.1 located in Washington, which has contributions from two seismic settings. A PSHA provides the hazard curves for S_a and the deaggregation information, which for this example is obtained from the USGS website (https://earthquake.usgs.gov/hazards/interactive/). The website provides the deaggregation by GMPE which can be used to estimate the deaggregation for the seismic sources in each tectonic setting. The shallow crustal S_a hazard curve was convoluted with the BT07 model, and the subduction S_a hazard curves (i.e., slab and interface) were convoluted with the BMT07 model. Figure 3.6b shows the total seismic displacement hazard curve and the contributions from each tectonic setting.

3.8 METHODOLOGY IMPLEMENTATION

The proposed procedures for developing the seismic slope displacement hazard curve in shallow crustal earthquake and subduction interface tectonic settings are implemented in the electronic Appendix B.2, which contains excel spreadsheets and executables files to perform the necessary calculations. They can be readily used in engineering practice after the engineer defines the required inputs, which are:

1) Estimate the mean value of the yield coefficient (k_y) and fundamental period (T_s) of the

potential sliding mass as described by Bray (2007). The uncertainty of these variables may be included by estimating their coefficient of variation and defining alternative values with corresponding weights in a logic tree scheme. The engineer can evaluate the mean and *cov* values for k_y and T_s using available information (e.g., Travasarou et al. 2004), and use these parameters to define the alternative values and weighting factors which are consistent with a lognormal distribution. In cases where uncertainty in these variables is not judged to be significant, the calculations are computed at the mean values of k_y and T_s with weighting factors equal to 1.

2) Compute the seismic hazard curve for S_a (the spectral acceleration at 1.5 times the fundamental period of the system) and the deaggregation information for magnitude bins at different values of S_a in the hazard curve. In general, this can be done through a site-specific probabilistic seismic hazard analysis. For the United States, the seismic hazard curve and deaggregation may be obtained from: https://earthquake.usgs.gov/hazards/interactive/, or using the *nshmp-haz* software from: https://github.com/usgs/nshmp-haz/. Interpolated values may be used to define the S_a seismic hazard curve at periods not available at these websites.

3) Specify a list of seismic displacement values used for the estimation of the seismic displacement hazard curve. The provided tools will estimate the annual rate of exceedance (i.e., λ_d) for each value in the list.

4) Define a target hazard level (or return period, e.g., 475 years) for the estimation of the seismic displacement.

Figure 3.7 illustrates the use of the spreadsheets and executable files in the electronic Appendix B.2 (the diagram is for the shallow crustal case, but it is similar for other cases). The spreadsheets in the Appendix B.2 also contain explanatory notes for their use. In this straightforward application of performance-based seismic slope displacement hazard calculations, the engineer can focus on the estimation of the spectral acceleration hazard curve with its deaggregation information and the system properties defined by k_y and T_s and their variability.

3.8.1 Illustrative example

The anticipated performance of a representative earth dam is evaluated in terms of seismically-induced permanent slope displacement. Return periods of 475 and 2475 years are considered. The calculations are performed with the files provided in electronic Appendix B.2. The geometry and properties of the dam are identical to the example used by Bray and Travasarou (2007). The maximum cross-section of the 57 m-high rolled earth-fill dam, which is founded on rock, is shown in Figure 3.8.

Step 1: The analysis is performed with best-estimate (mean) values of k_y and T_s to evaluate a deep slide through the dam. For the case of base sliding at the maximum height of this triangular-shaped potential sliding mass, the best estimate of its initial fundamental period is:

$$T_s = \frac{2.6\,H}{V_s} = \frac{2.6(57m)}{450m/s} \approx 0.33 \text{ s}, \qquad \text{therefore, } 1.5\,T_s \approx 0.5 \text{ s} \tag{3.13}$$

where V_s is the mean value of the shear wave velocity of the sliding mass. The yield coefficient for a deep failure surface was estimated to be 0.14 from a pseudostatic slope stability analyses. The stability analysis was performed with the total stress strength properties of c = 14 kPa and $\phi = 21°$ based on undrained triaxial compression tests. The mean values of k_y and T_s are entered in the Input sheet of the *Input Crustal.xls* spreadsheet with *cov* = 0 for this example.

Step 2: The dam is assumed to be at GPS coordinates N37.81 W122.36 in Northern California, where there is negligible contribution to the seismic hazard from subduction earthquakes. The hazard curve for the spectral acceleration at the degraded period of the dam (0.5 s) and the deaggregation information are obtained using the *nshmp-haz* software. Different combinations of return period were entered to develop the seismic hazard curve shown in Figure 3.9a. The corresponding deaggregation information is pasted on the Input sheet of the *Input Crustal.xls* spreadsheet (i.e., the grey cells).

Step 3: A list of seismic displacements for their annual rate of exceedance is needed. 23 values between 1 and 100 cm are considered and entered in the *Input Sheet of the Input Crustal.xls*.

Step 4: The design hazard levels are defined in this example for return periods of 475 and 2475 years.

With this information, the files in the electronic Appendix B.2 are used to develop the seismic slope displacement hazard curve shown in Figure 3.9b. The estimated seismic slope displacement for the 475 and 2475 years return periods are approximately 20 cm and 63 cm, respectively.

In a pseudo-probabilistic analysis using the BT07 procedure, first the spectral accelerations for the return periods of interest are estimated, and these values are used in the procedure with the properties of the sliding mas (T_s and k_y) and a magnitude value which can be obtained from the deaggregation at each return period. From Figure 3.9a, the spectral accelerations for 475 and 2475-year return periods are 0.63 g and 1.0 g, respectively, and the modal magnitude is 8.0 in both cases. With these input values, the median seismic slope displacements from the BT07 model are estimated to be 20 cm and 52 cm, respectively. For this case, the use of a spectral acceleration that corresponds to 2475-year return period in the pseudo-probabilistic approach yields a seismic slope displacement value (52 cm) with approximately a return period of 1750 years (Figure 3.9b). Conversely, the performance-based approach enables the seismic slope displacement at each return period to be estimated directly. As illustrated with this example, the return period of the seismic slope displacement does not necessarily correspond with the return period of the ground motion intensity measure. The seismic slope displacement hazard should be used to evaluate the seismic performance of an earth/waste system or natural slope.

3.8.2 Comparison of performance-based analyses

Performance-based seismic slope displacement hazard assessments are compared for earth systems located at 3 different sites in the United States. The sites are selected to represent areas with different seismic activity and tectonic settings. Figure 3.10 shows a comparison of seismic slope displacement hazard curves, considering the "integration by parts" and the "rate of occurrence" methods as well as with magnitude and no magnitude dependence. The curves are shown for a system with a fundamental period T_s = 0.67 s located in Yerba Buena Island (YB), California (N37.81 W122.36), a system with a fundamental period T_s = 0.33 s located in Salt Lake City (SL), Utah (N40.75 W111.88), and two systems with fundamental periods equal to T_s = 0.33 s and T_s = 0.67 s located west of Seattle (S1 and S2, respectively), Washington (N47.42 W123.56). The sites in YB and SL have contributions primarily from crustal seismic sources; whereas, the site west of Seattle has contribution primarily from the subduction seismic sources.

The USGS website (https://earthquake.usgs.gov/hazards/interactive/) and *nshmp-haz* software provide the hazard curves for the spectral acceleration at the system's degraded period and magnitude deaggregation information. Mean values of k_y (i.e., 0.04, 0.1, 0.2, and 0.3) and T_s were

used in the analyses. However, sensitivity analyses were performed using *cov* values of 0.2 and 0.5 for k_y, and *cov* values of 0.1 and 0.25 for T_s. As described previously, weighting factors were applied to three alternative values of each parameter to capture a lognormal distribution. The selected values of k_y cover the range found typically in practice. The selected *cov* values represent typical lower and upper ranges (e.g. Travasarou et al., 2004).

The results for the cases shown in Figure 3.10 indicate the "integration by parts" and "rate of occurrence" methods provide consistent results for the estimation of the seismic slope displacement hazard curve. Also, the inclusion of the magnitude dependence term in the predictive equations for median seismic displacements for the cases analyzed in the shallow crustal earthquake setting does not affect greatly the seismic slope displacement hazard curve. The different slopes of the seismic slope displacement hazard curves for these cases (Figure 3.10b, 3.10d, 3.10e, and 3.10f) generally follow the trends of the slopes of the spectral acceleration hazard curves (Figure 3.10a) with the YB site displaying the steepest slope and the SL site displaying the flattest slope over the return periods examined in this study. The inclusion of the uncertainty of k_y and T_s did not affect significantly the estimated seismic displacements for the cases with the lower *cov* values of 0.2 and 0.1 for k_y and T_s, respectively (Figure 3.10c). However, use of the higher *cov* values of 0.5 and 0.25 for k_y and T_s, respectively, influenced considerably the estimated seismic slope displacements.

Table 3.1 compares the results obtained using the conventional pseudo-probabilistic approach and the proposed performance-based approach to estimate seismic slope displacements for the cases discussed previously. The pseudo-probabilistic approach underestimates the seismic slope displacement value estimated with the performance-based approach at both return periods for the YB case. The pseudo-probabilistic approach overestimates the seismic slope displacement value estimated with the performance-based approach at the 475-year return period for the SL case. Results are consistent at the 2475-year return period. These results occur because of the higher recurrence of earthquakes in California relative to the recurrence of earthquakes in Utah, which implies that the slope of the seismic hazard curve in YB is steeper than the slope of the hazard curve in SL. Thus, the rate of occurrence of spectral acceleration values is higher in YB than in SL causing more contribution to the annual rate of exceedance for a given seismic displacement. For the Seattle cases, the pseudo-probabilistic approach overestimates the seismic slope displacement value estimated with the performance-based approach at the 475-year return period and underestimates the seismic slope displacement values at the 2475-year return period. This result can be explained by considering the activity rate of earthquakes in the Cascadia zone (~1/600 per year). For a median ground motion (i.e., its probability of exceedance is 0.5) and a simple seismic source, the annual rate of exceedance for the median ground motion will be about 1/1200 per year (i.e., 0.5 x 1/600). Thus, a negative value for delta (the difference between the performance-based and the pseudo-probabilistic estimations) would be expected for the first return period (associated with a rate of 1/475 per year), and a positive value for delta would be expected for the second return period (associated with a rate of 1/2475 per year). A performance-based seismic slope displacement hazard analysis is not in general more or less conservative than a pseudo-probabilistic analysis. There may be systematic differences in the same region and the same return period, but ultimately the comparison depends on the seismo-tectonic setting for the site and the return period.

Engineers often use the ground motion associated with a specified hazard level to calculate seismic slope displacements (i.e., pseudo probabilistic approach) with the implicit assumption that the hazard level associated with the seismic slope displacement is the same as the hazard level

associated with the ground motion parameter being used. However, this is not generally valid (as shown in Table 3.1). Similar inconsistencies with the pseudo-probabilistic approach were found by Rathje and Saygili (2011), Kramer and Mayfield (2007), and Franke et al. (2016). The engineer should target directly the hazard levels associated with the calculated seismic slope displacements, because ultimately the potential seismic performance of an earth/waste system or natural slope depends on seismic slope displacement and not on a particular ground motion intensity measure.

3.9 PROBABILISTIC EVALUATION OF SEISMIC COEFFICENT

The proposed performance-based seismic slope displacement hazard procedure can be reformulated to estimate a hazard-compatible seismic coefficient (k) to be used in a pseudostatic slope stability analysis using these steps:

1. In consultation with the client and regulators define the allowable level of seismic slope displacement of the earth/waste system to achieve the desired performance level.
2. Select the appropriate return period for the allowable seismic slope displacement. Several values may be selected, each with their respective return period.
3. Develop a best-estimate mean value of the fundamental period of the potential sliding mass (T_s). Assign an appropriate co-variance value of its uncertainty if epistemic uncertainty is to be modeled. Typically, this is not required, because a majority of the uncertainty is in the seismic demand parameter.
4. Assume an initial mean value of the system's yield coefficient (k_y). The uncertainty of k_y could also be modeled using an appropriate co-variance value of this variable. Calculate an initial displacement hazard curve following the procedures described previously.
5. Iterate using different values of k_y to recalculate the seismic slope displacement hazard until the seismic slope displacement hazard curve passes through the intersection of the horizontal line that goes through the annual frequency of exceedance defined in Step 2 and the vertical line that goes through the tolerable level of seismic displacement defined in Step 1. The corresponding k_y value is the seismic coefficient (k) compatible with the tolerable level of seismic slope displacement and the specified return period. This procedure is implemented in the files included in the electronic Appendix B.2 to automate the iterative procedure.
6. The calculated k value is applied to the potential sliding mass in a pseudostatic slope stability analysis, and if $FS \geq 1.0$, the seismic slope displacement is at or below the tolerable level of seismic slope displacement for the specified return period.

Figure 3.11 shows the results of the probabilistic estimation of the pseudostatic seismic coefficient for the sites described previously for a tolerable seismic slope displacement of 15 cm. Table 3.2 provides a comparison (including also the case where tolerable seismic slope displacement is set at 30 cm) of the estimated seismic coefficients using the proposed performance-based method and the median values estimated based on a pseudo-probabilistic method. The estimation based on a pseudo-probabilistic method is performed by inverting the Equations 3.10 and B.2(Appendix B.1) and solving for k_y. The inversion of the Equation 3.9 is performed for shallow crustal settings (as recommended by Bray and Travasarou 2009) and the inversion of Equation B.2 for subduction interface earthquakes (as recommended by Bray et al. 2017). In general, the estimation of the seismic coefficient using the performance-based and pseudo-probabilistic methods are consistent (the highest difference is in the order of 30%), but the performance-based method is preferred because it incorporates more rationally the uncertainties of the variables and the influence of the selected hazard level.

3.10 CONCLUSIONS

Performance-based procedures are presented for the straightforward assessment of the seismic performance of earth/waste systems or natural slopes in shallow crustal and subduction earthquake settings. Deterministic or pseudo-probabilistic simplified seismic slope displacement procedures are typically used in engineering practice. However, performance-based procedures are preferred because they consider more completely the actual uncertainty in the ground motion intensity measure and earth system properties. Moreover, a performance-based procedure provides seismic slope displacement estimates that are consistent with design hazard levels. Performance-based procedures are not commonly used because they are thought to be too complicated to be used for non-critical projects. The proposed procedures enable the straightforward development of the seismic slope displacement hazard or hazard-compatible seismic coefficient through the files provided in the electronic Appendix B.2. Thus, they may be readily used in engineering practice.

The seismic slope displacement models of Bray and Travasarou (2007) for shallow crustal earthquakes and Bray et al. (2017) for subduction interface earthquakes are incorporated in the proposed probabilistic procedure. Consistent results are obtained with these models whether the seismic slope displacement hazard curve is estimated using "integration by parts" or "rate of occurrence" approaches. The integration by parts approach is more fundamental if the analytical derivatives of the displacement models can be calculated (as it is the case for BT07 or BMT17). It has been used to confirm the accuracy of the local approximations in the "rate of occurrence" approach. The results of a sensitivity study indicate that the choice of the governing earthquake magnitude value is not critically important. It is sufficient to use the modal magnitude from the seismic hazard deaggregation in the magnitude-dependent model.

The performance-based seismic slope displacement hazard procedure does not necessarily provide higher or lower values than the commonly used pseudo-probabilistic procedure. Their relative values depend on the particular seismo-tectonic setting and the design hazard level. The performance-based method provides seismic slope displacement estimates that are directly compatible with the target design levels. Hence, it should be used, because the hazard is developed based on a relevant index of seismic performance, which is the calculated seismic slope displacement, and not on an indirect index of performance such as a ground motion intensity measure. Other alternatives to be used as an index of seismic performance, such as the measure of damage (DM in the PEER approach) or decision variables in loss analyses (DV in the PEER approach) may also be considered in the performance-based framework.

The proposed performance-based seismic slope displacement hazard procedure was recast to estimate a hazard-compatible seismic coefficient to be used in a pseudostatic slope stability analysis. The value of the seismic coefficient is a function of the selected threshold of allowable seismic slope displacement, among other factors. Thus, the design seismic coefficient value is estimated in a rational manner. The procedure relies on the estimation of the displacement hazard curve and uses standard information that is currently used in practice so it can be readily implemented. A comparison with conventionally employed pseudo-probabilistic procedures for selecting the seismic coefficient (i.e., Bray and Travasarou 2009) indicates that the results of performance-based procedure can differ by up 30%. However, the trends in the results from both procedures are consistent. The performance-based procedure is recommended because it addresses directly the selected hazard level and the associated uncertainties.

Table 3.1. Comparison pseudo- probabilistic and performance-based approaches to estimate seismic slope displacements for selected cases at 475 and 2475-year return periods (k_y = 0.1)

Site	$1.5T_S$ (s)	Spectral Accel. (g)		Pseudo-Prob. D (cm)		Perf.-Based D (cm)		Δ_d	
		475 years	2475 years	475 Years	2475 years	475 years	2475 years	475 years	2475 years

YB	1.0	0.33	0.58	15	50	16	57	0.07	0.13
SL	0.5	0.30	1.10	6	76	5	76	-0.18	0.00
S1	0.5	0.47	1.03	25	100	16	106	-0.44	0.06
S2	1.0	0.25	0.60	11	64	7	70	-0.45	0.09

T_s is the initial fundamental period of the system, Δ_d is defined as *Ln(Perf.-Based)-Ln(Pseudo-Prob.)*, YB= Yerba Buena, SL= Salt Lake, and S1, S2= Seattle.

Table 3.2. Comparison pseudo- probabilistic and performance-based approaches to estimate a pseudostatic coefficient for selected cases at 475 and 2475-year return periods. (D_a=15cm)

Site.	$1.5T_S$ (s)	D_a (cm)	Spectral Accel. (g)		Pseudo-Prob. k		Perf-Based k	
			475 years	2475 years	475 years	2475 years	475 years	2475 years
YB	1.0	15	0.33	0.58	0.103	0.184	0.100	0.200
YB	1.0	30	0.33	0.58	0.070	0.127	0.080	0.140
SL	0.5	15	0.30	1.10	0.057	0.280	0.060	0.270
S1	0.5	15	0.47	1.03	0.133	0.280	0.100	0.270
S2	1.0	15	0.25	0.60	0.090	0.200	0.070	0.210

T_s: fundamental period of the system, k: seismic coefficient, D_a: tolerable level of displacements, YB= Yerba Buena, SL= Salt Lake, and S1, S2= Seattle. For YB, D_a=15 and 30 cm for comparison purposes.

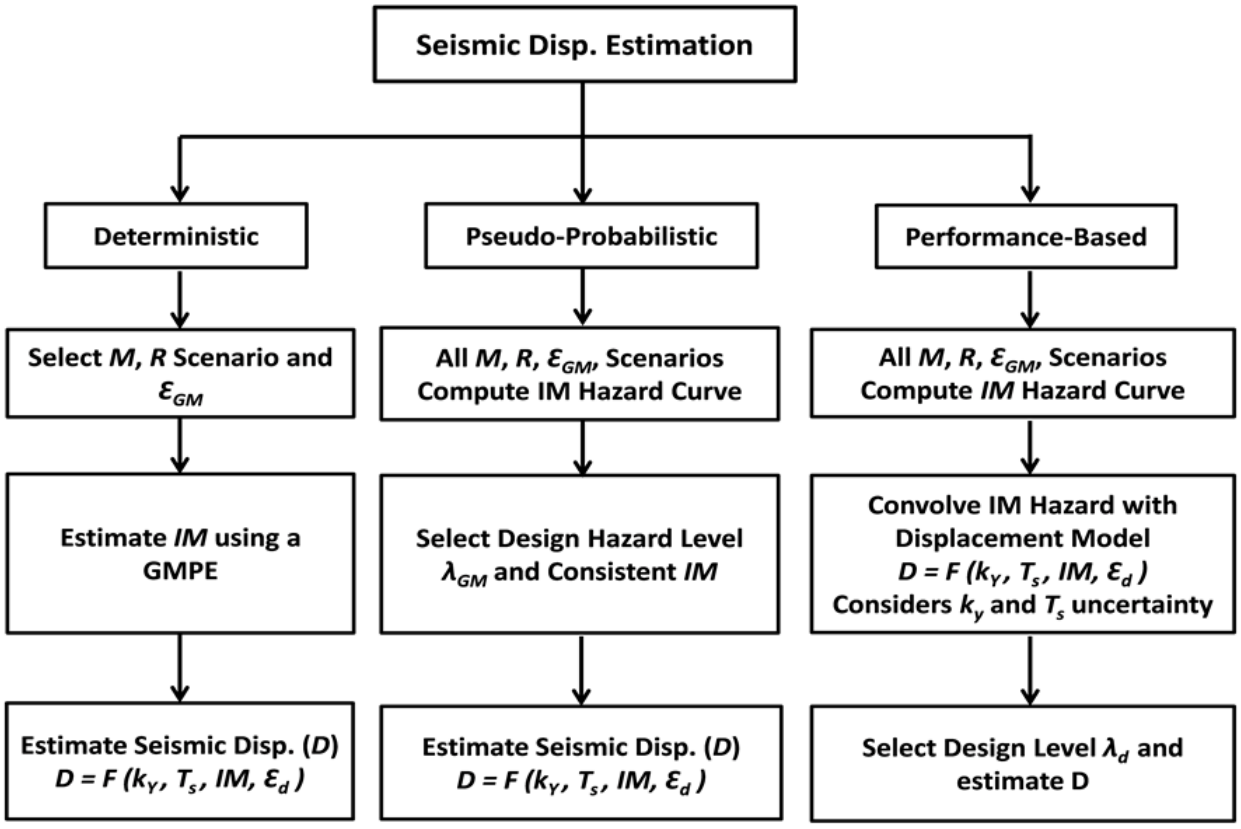

Figure 3.1. Different approaches for the estimation of Newmark-based seismic slope displacements.

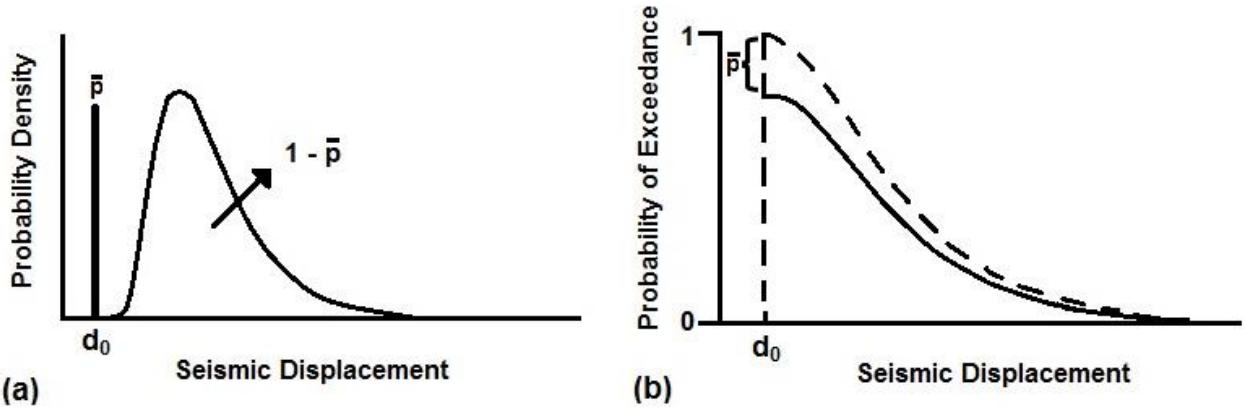

Figure 3.2. a) Probability density function for a mixed random variable and b) probability of exceedance for a mixed (solid line) and a continuous (dotted line) random variable (after Bray and Travasarou 2007).

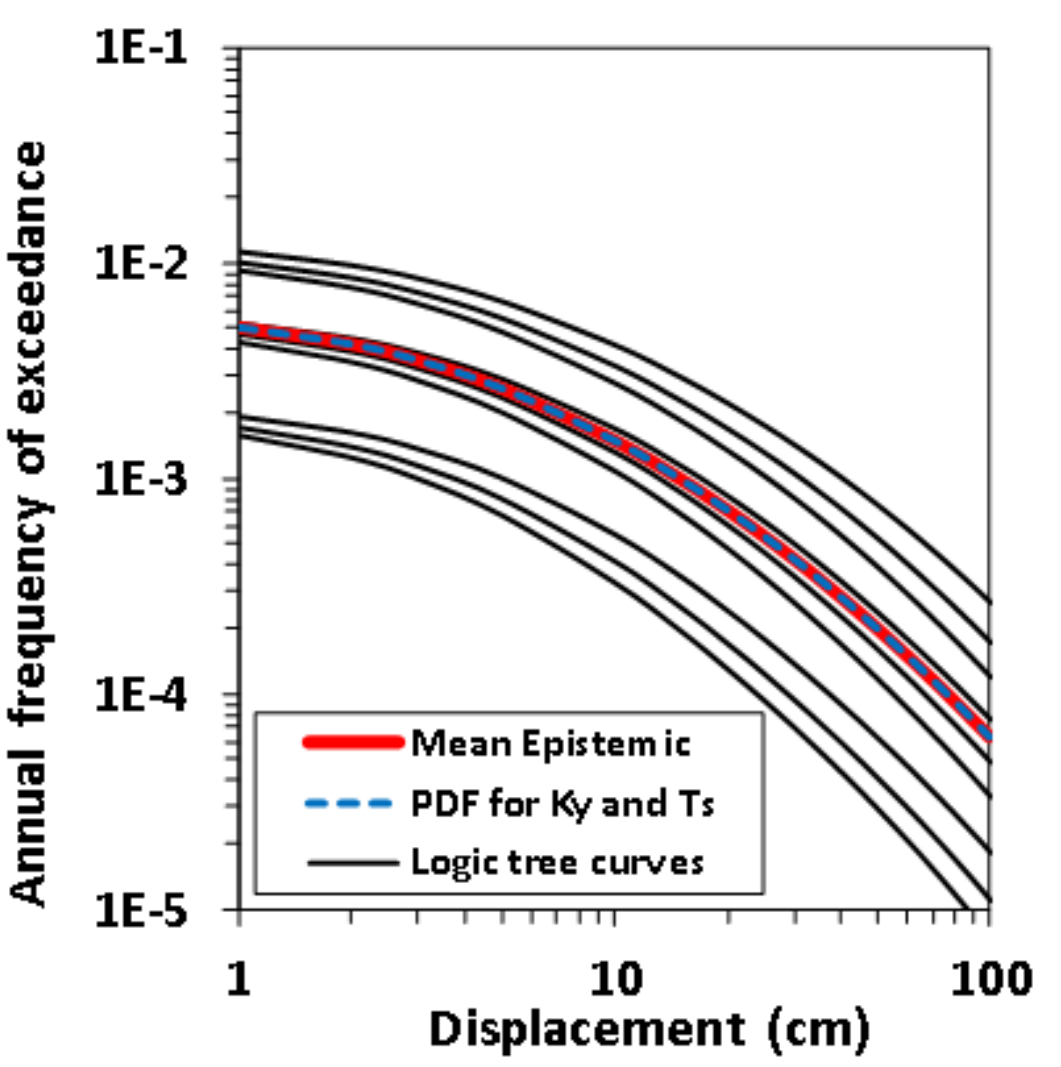

Figure 3.3. Comparison between the mean hazard displacement curve considering an epistemic uncertainty for k_y and T_s and the hazard displacement curve considering PDFs for k_y and T_s.

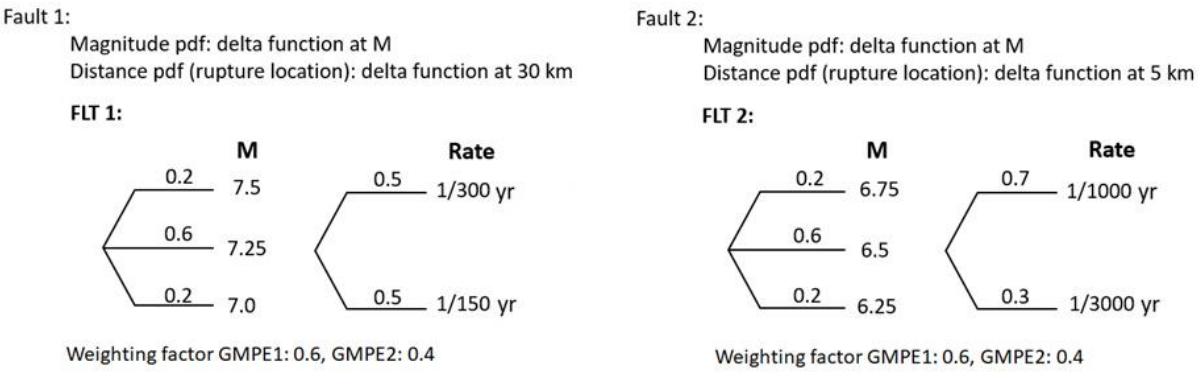

Figure 3.4. Illustrative logic tree for PSHA analysis.

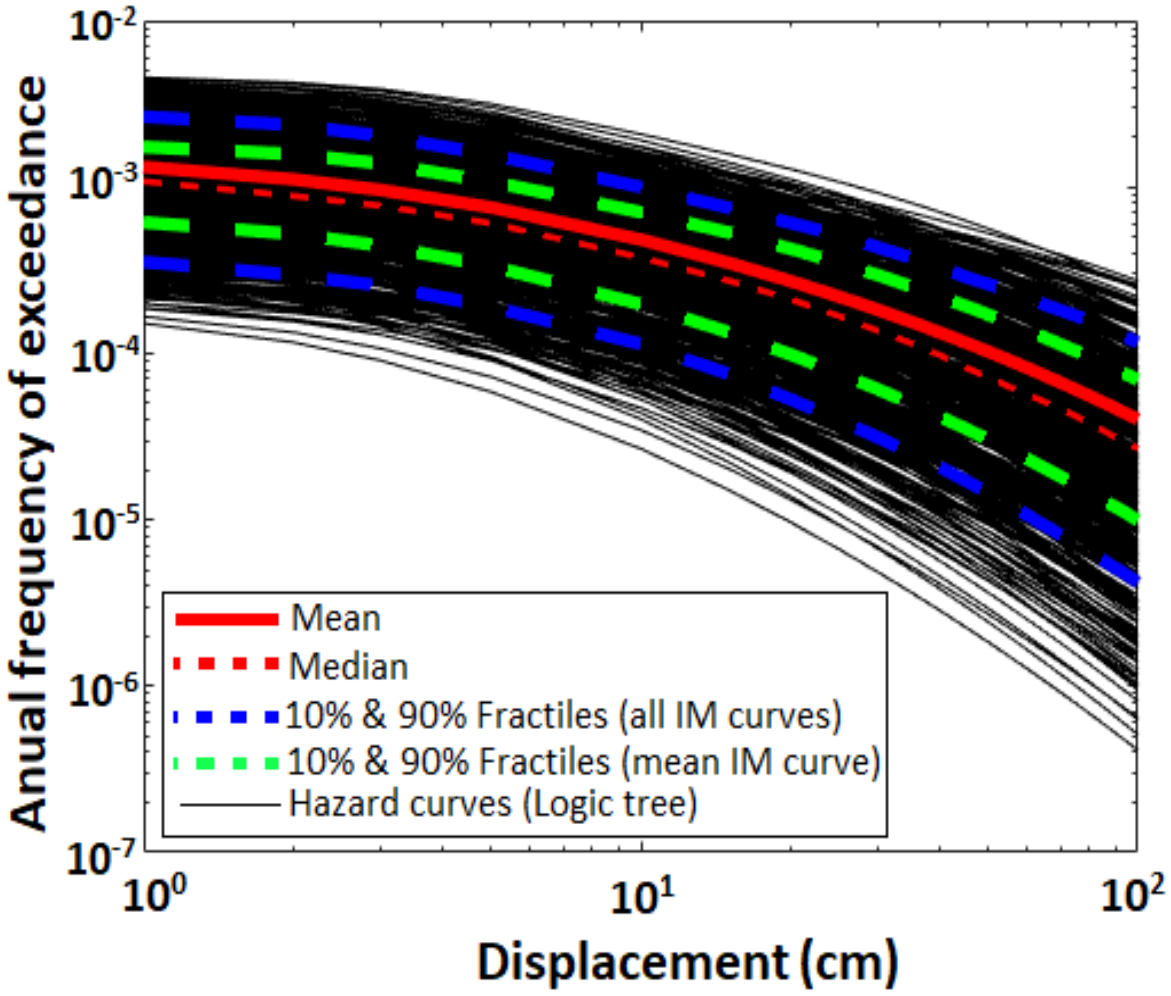

Figure 3.5. Mean, median, and 10-90% percentiles seismic displacement hazard curves.

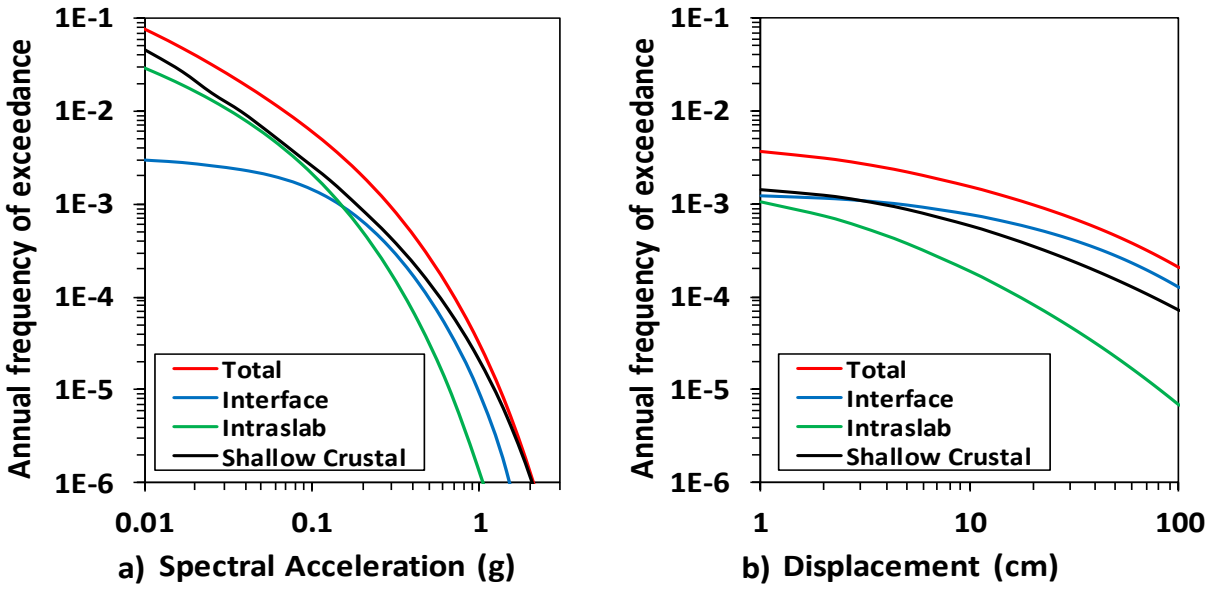

Figure 3.6. a) Spectral acceleration hazard curves by tectonic settings, $1.5T_s$=1.00 s b) Total displacement hazard curve and components by tectonic setting.

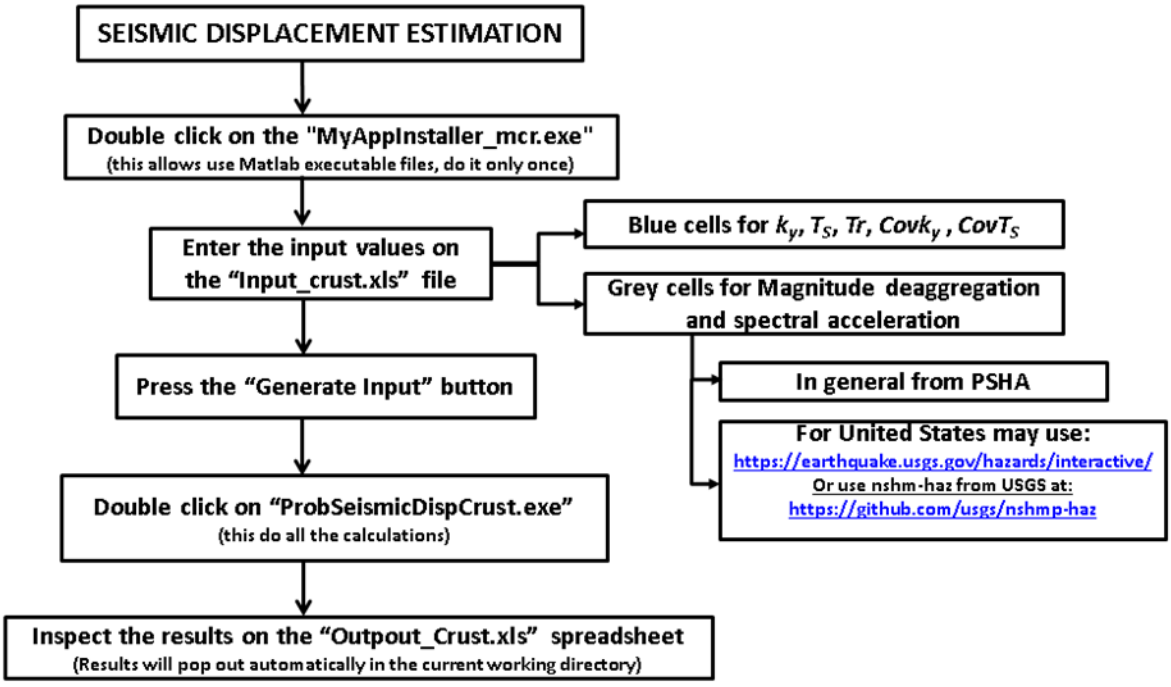

Figure 3.7. Flow diagram for the performance-based estimation of seismic slope displacements.

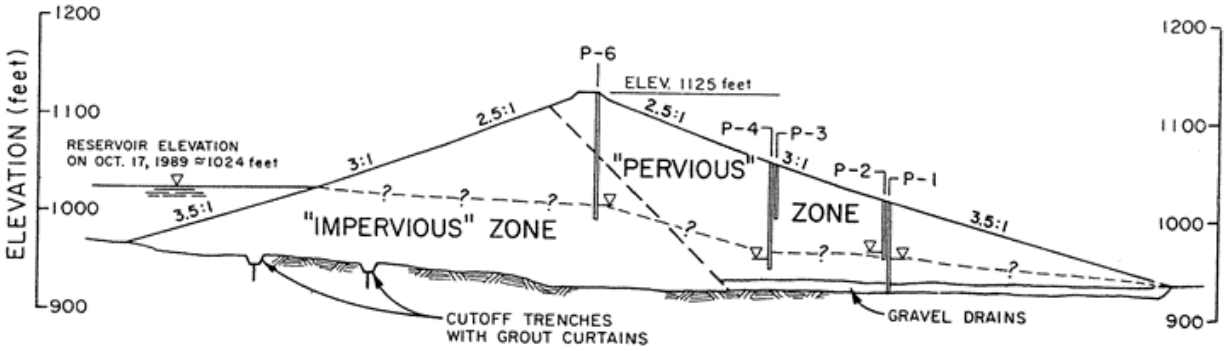

Figure 3.8. Cross section of dam used in illustrative example (from Bray and Travasarou 2007).

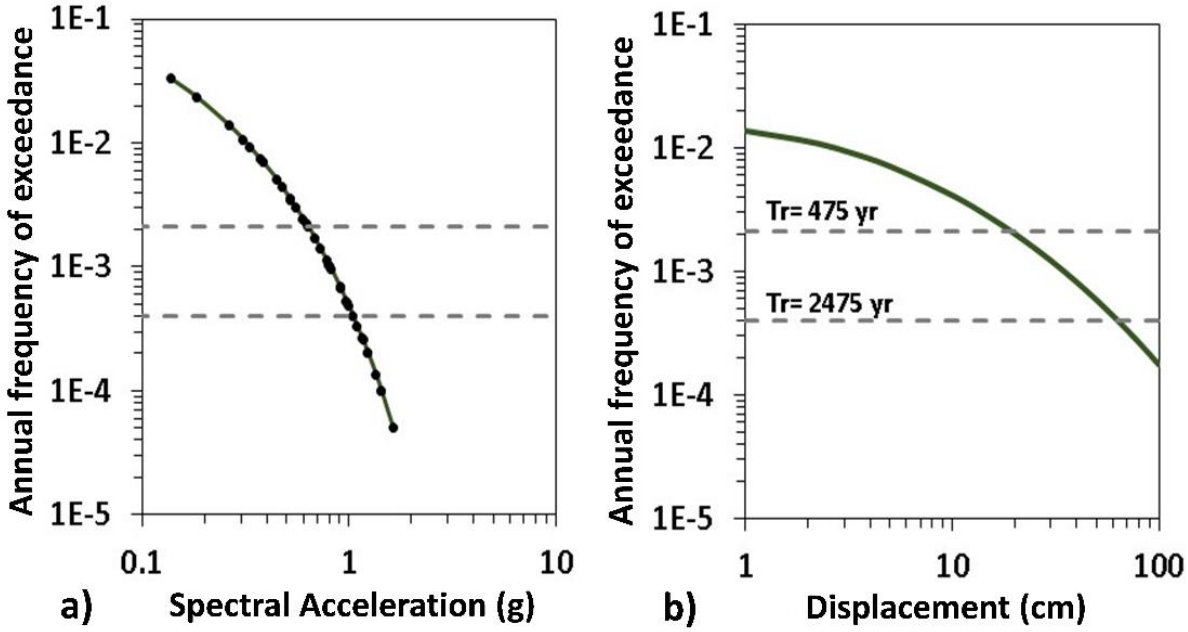

Figure 3.9. Illustrative example: (a) Spectral acceleration hazard curve, and b) Seismic Slope displacement hazard curve.

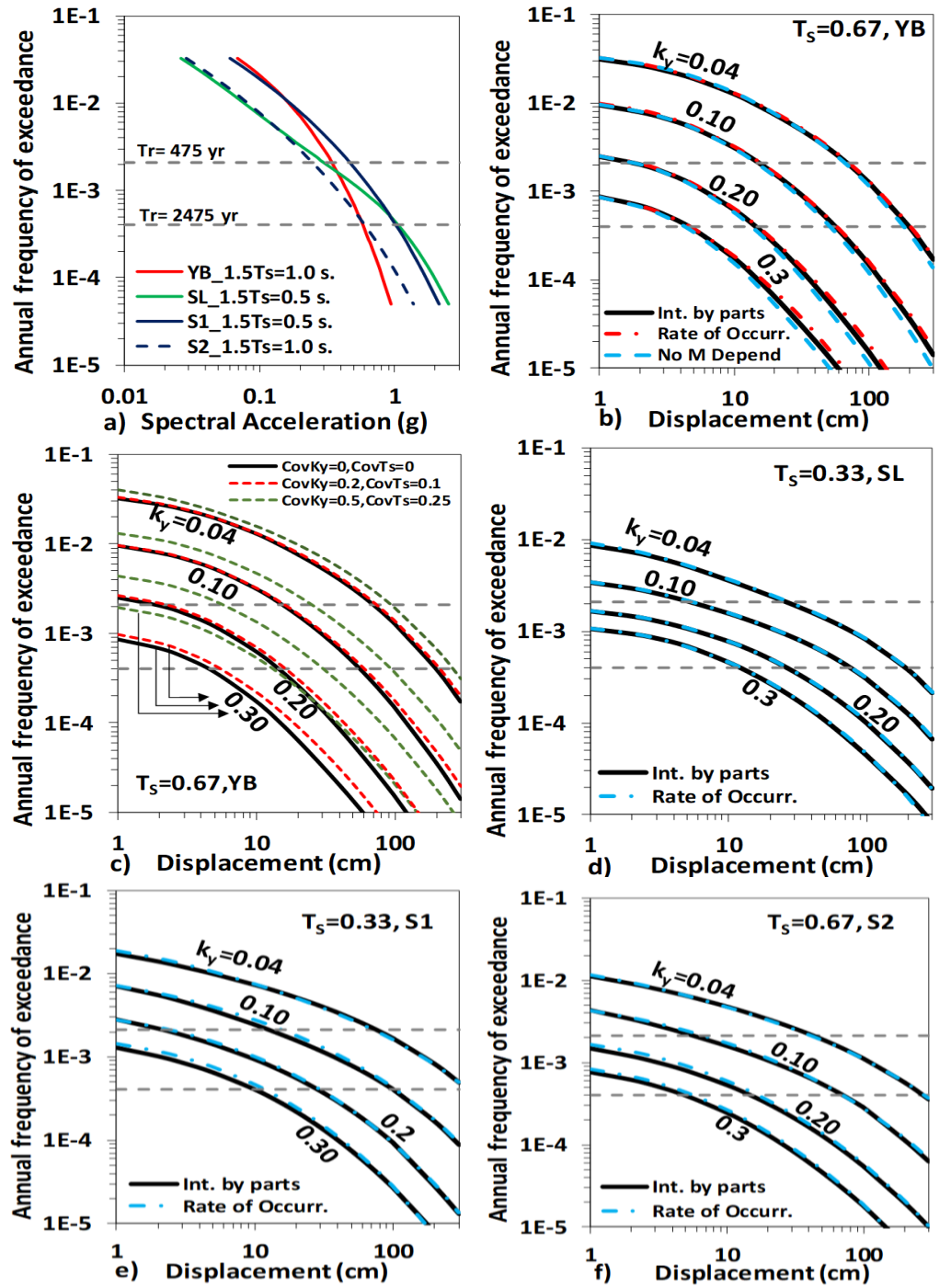

Figure 3.10. (a) Spectral acceleration hazard curves: YB= Yerba Buena, SL= Salt Lake, S1, S2= Seattle; b) Comparison of "integration by parts", "rate of occurrence" methods and examination of magnitude dependence for YB site; c) Sensitivity analyses in terms of *cov* values of k_y and T_s, considering magnitude dependence for YB site; results are for the mean weighted hazard curve; d-f) Comparison of "integration by parts" and "rate of occurrence" methods for SL, S1, and S2 cases; horizontal dashed lines represent hazard levels for return periods of 475 and 2475 years.

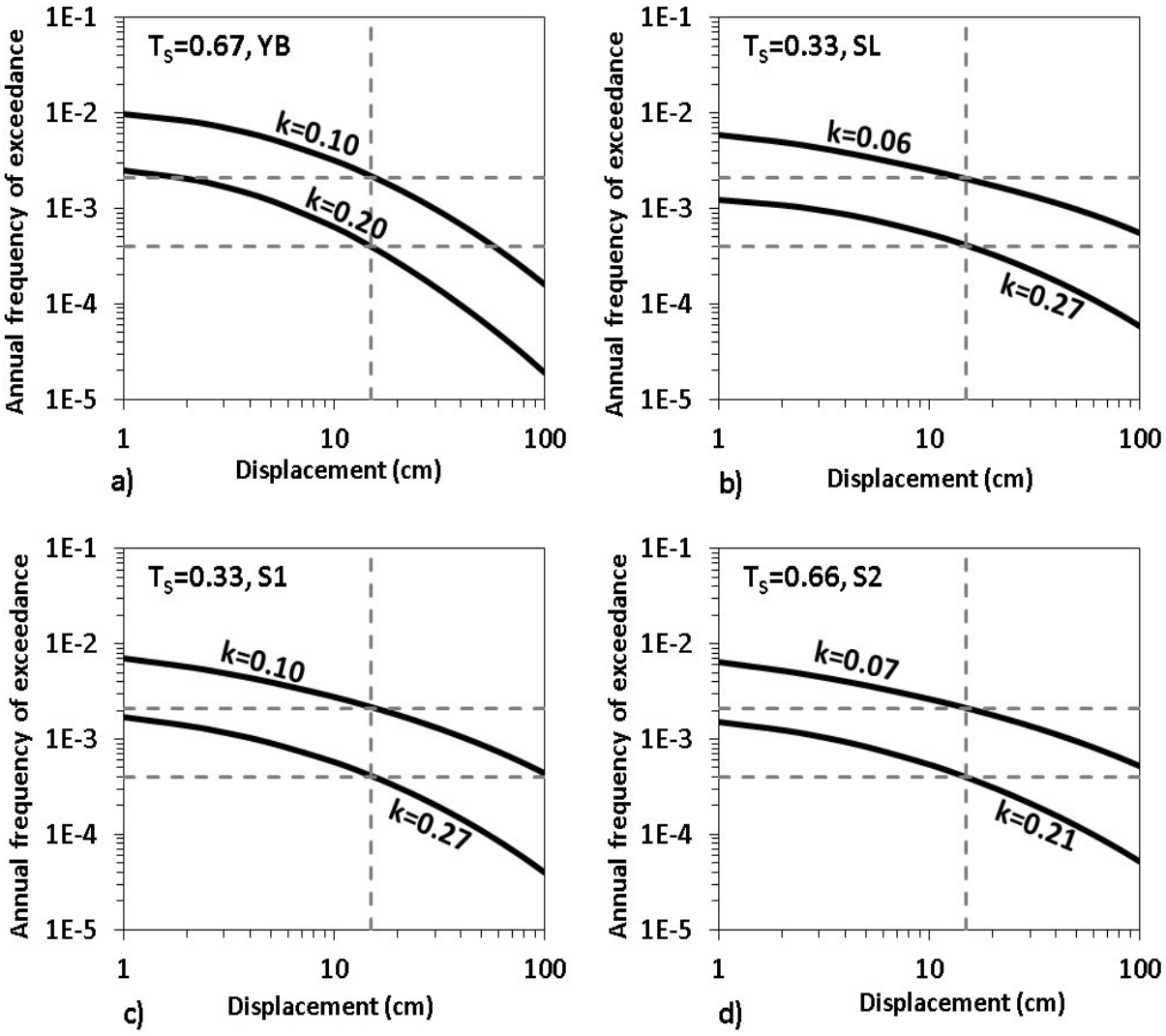

Figure 3.11. Probabilistic estimation of seismic coefficient. Horizontal lines represent return periods of 475 and 2475 years. Allowable displacement (vertical line) of 15 cm (a) Probabilistic estimation of seismic coefficient YB site. (b) Probabilistic estimation of seismic coefficient SL site. (c) Probabilistic estimation of seismic coefficient S1 site. (d) Probabilistic estimation of seismic coefficient S2 site.

CHAPTER 4: KEY TRENDS IN LIQUEFACTION-INDUCED BUILDING SETTLEMENT

The contents of this chapter are primarily from a journal article submitted to the Journal of Geotechnical and Geoenvironmental Engineering from the American Society of Civil Engineers (ASCE) by Macedo, J. and Bray, J.D. entitled: "Key trends in liquefaction-induced building settlement", submitted in July 2017, which is under review.

4.1 INTRODUCTION

Liquefaction-induced settlement of shallow founded buildings has damaged many buildings during major earthquakes. It is informative to categorize liquefaction-induced ground movements as ejecta-induced, shear-induced, or volumetric-induced deformations (Bray and Dashti 2014). When a significant amount occurs, the removal of materials beneath a structure due to the formation of sediment ejecta is often the dominant factor. In many other cases, building settlement is controlled primarily by shear-induced ground deformations as a result of soil-structure-interaction (SSI)-induced ratcheting and bearing capacity-type movements. Volumetric-induced ground deformations resulting from localized partial drainage, sedimentation, and post-liquefaction reconsolidation can also produce significant building settlement.

Nonlinear dynamic SSI effective stress analyses, using a soil constitutive model and numerical method shown to capture field case history observations and experimental data, can provide salient insights regarding shear-induced and volumetric-induced liquefaction building settlement mechanisms (Bray et al. 2017). However, volumetric-induced liquefaction building settlement can also be estimated with simplified empirical procedures developed to estimate post-liquefaction, one-dimensional (1D) reconsolidation settlement in the free-field without the effects of structures (e.g., Ishihara and Yoshimine 1992; Zhang et al. 2002). Established procedures for estimating shear-induced liquefaction building settlement are not widely available. Ejecta-induced building settlement cannot be captured with continuum-based analyses. Considerably more work is required before methods for estimating ejecta-induced settlement can be used with confidence. Instead, it is best to use liquefaction ground failure indices (e.g., LSN; van Ballegooy et al. 2014), the Ishihara (1985) design chart, and case histories (e.g., Bray and Sancio 2009) to develop rough estimates of ejecta-induced building settlement.

Nonlinear dynamic SSI nonlinear effective stress analyses have been used by researchers to replicate the measured responses of the ground or structures during physical experiments (i.e., commonly centrifuge tests). Popescu and Prevost (1993), Elgamal et al. (2005), Popescu et al. (2006), Lopez-Caballero and Farahmand-Razavi (2008), Shakir and Pak (2010), Andrianopoulos et al. (2010), Dashti and Bray (2013), and Karimi and Dashti (2016a,b) performed nonlinear dynamic SSI effective stress analyses to capture the response of buildings on top of a soil deposits that include a liquefiable soil layer. A few studies have back-analyzed field case histories. Travasarou et al. (2006) and Luque and Bray (2015, 2017) performed numerical back-analyses of buildings that suffered liquefaction-induced damage in the 1999 Kocaeli and 2011 Christchurch earthquakes with success. Their analyses capture many of the key aspects of the soil and building responses well. Thus, there is confidence that nonlinear dynamic SSI effective stress analyses can

be used to investigate the important shear-induced liquefaction building settlement mechanism. This is the aim of this study.

4.2 OVERVIEW OF NUMERICAL PARAMETRIC STUDY

4.2.1 Analytical Procedure

The nonlinear dynamic SSI effective stress analyses are performed using the program FLAC Version 7.0 (Itasca 2011). The widely used finite difference method code is capable of modeling coupled stress-flow problems under dynamic loading conditions. The PM4Sand Version 3 user-defined constitutive model (Boulanger and Ziotopoulou 2015) is employed to capture the cyclic response of saturated sand. The constitutive model PM4Sand is a stress-ratio controlled, critical state compatible, bounding surface plasticity model developed primarily for earthquake engineering applications.

The PM4Sand model has three primary input parameters: relative density (D_r), shear modulus coefficient (G_o), and the contraction rate parameter (h_{po}). The value of D_r is specified based on the soil conditions for the case being analyzed. The stress-dependent elastic shear modulus (G) is defined as (Boulanger and Ziotopoulou 2015):

$$G = G_o P_a \left(\frac{\sigma_m}{P_a}\right)^{0.5} \tag{4.1}$$

where P_a is the atmospheric pressure (101.3 kPa), σ_m is the mean effective confining pressure, and G_o is calculated in this study as (Boulanger and Ziotopoulou 2015):

$$G_o = 167\sqrt{46{D_r}^2 + 2.5} \tag{4.2}$$

Element tests are analyzed with the PM4Sand model in FLAC to set the value of h_{po} to obtain the cyclic resistance ratio (CRR) at 15 cycles estimated by the Boulanger and Idriss (2016) simplified liquefaction triggering procedure for the specified relative density. Default values calibrated by Boulanger and Ziotopoulou (2015) are used for the 18 secondary model parameters.

The structures modeled in the SSI analyses are typical frame structures founded on a mat with a sufficient number of floors to capture the important modes of shaking. FLAC models the response of structural components through beam elements that can sustain axial force, shear force, and bending moment. Luque and Bray (2015, 2017) showed that the primary aspects of the dynamic response of a 3D system in terms of liquefaction-induced building settlement can be captured in 2D analyses by using tributary mass and stiffness with the primary goal being to capture the mass and stiffness, and hence, the correct fundamental period of the structural system as well as the contact pressure transmitted to the foundation system. The flexural stiffness (EI) of the beam, column, and mat elements is set to 340 MN-m^2, 450 MN-m^2, and 1100 MN-m^2, respectively, and their density is adjusted to obtain the desired contact pressure at the foundation level as well as a reasonable fundamental period for the structure, which varied from 0.17 s to 0.6 s. A compliant base is used in FLAC (i.e., quiet absorbing viscous boundary developed by Lysmer and Kuhlemeyer (1969) consisting of two sets of dashpots attached independently to the mesh in the normal and shear direction element). The seismic excitation is applied as a shear stress-time history to elastic bedrock, consistent with the outcrop acceleration-time history used as input,

following the recommendations of Mejia and Dawson (2006). Lateral boundaries are sufficiently far away from the building so that moving them does not influence the results. Their respective nodes at each depth were tied together to capture free-field conditions.

4.2.2 Analytical Models

Sensitivity analyses are performed to investigate the influence of different soil conditions, building configurations, and ground motion characteristics on the magnitude of liquefaction-induced building settlement. The baseline analytical model is shown in Figure 4.1. The ground consists of 3 soil layers: a nonliquefiable crust layer of thickness *HC*, a liquefiable soil layer of thickness *HL* with relative density D_r, and a nonliquefiable base soil layer of thickness *HB*. The water table is set at the base of the nonliquefiable crust layer. The building is defined by its width *B*, height *H*, and foundation contact pressure *Q*. The range of ground conditions and building configurations considered in the sensitivity analyses as well as the baseline case values of the aforementioned parameters are given in Table 4.1. Importantly, the liquefiable soil layer's relative density varies from 35% to 90%, and its thickness varies from as thin as 1 m to as much as 18 m. The depth of the top of the liquefiable layer is varied through changing *HC* from 1 to 6 m. Typical 2-story to 8-story buildings are modeled with *Q* varying from 20 to 240 kPa, *H* varying from 6 to 24 m, and *B* varying from 6 to 24 m. Through varying each parameter as noted in Table 4.1, a total of 105 different models are analyzed.

4.2.3 Earthquake Ground Motions

The characteristics of the earthquake ground motions affect greatly the seismic response of the ground and structure. Hence, the input ground motions play a significant role in the amount of liquefaction-induced building settlement. Twelve recorded acceleration-time histories from shallow crustal earthquakes along active plate margins are employed to perform primary analyses of each of the 105 analytical models discussed previously (i.e., a total of 1,260 analyses were performed with the primary suite of 12 ground motions). A suite of 24 additional earthquake ground motions are applied to a subset of the SSI models considered in this study to explore the influence of a wider range of ground motions. Ground motions 13 to 24 include amplitude-scaled ground motion records from the primary suite of ground motion records to examine the influence of variations in ground motion intensity on the amount of liquefaction-induced building settlement. Ground motions 25 to 36 include ground motions of lower intensity compared to the other suites of motions to explore the influence of less intense motions. The 36 acceleration-time histories listed in Table 4.2 are used in this study. Considering all cases analyzed, 1,308 nonlinear dynamic SSI effective stress analyses were performed.

Earthquake ground motions are characterized using dozens of parameters, including: PGA: peak ground acceleration (*g*), *PGV*: peak ground velocity (cm/s), I_a: Arias intensity (m/s), CAV_{dp}: standardized cumulative velocity (*g-s*), $D_{5\text{-}95}$: significant duration (*s*), SIR: shake intensity rate (m/s/s), T_m: mean period (*s*), S_a1: 5%-damped spectral acceleration at T = 1 s (*g*), and S_aT: 5%-damped spectral acceleration at T = the fundamental period of the structure (*g*) (Arias 1970, Campbell and Bozorgnia 2011, Trifunac and Brady 1978, Dashti et al. 2010, Rathje et al. 2004). The newer ground motion intensity parameter CAV_{dp} is used extensively in this chapter, so its definition is provided as (Campbell and Bozorgnia 2011):

$$CAV_{dp} = \sum_{i=1}^{N}(H(PGA_i - 0.025)\int_{i-1}^{i}|a(t)|dt) \quad (4.3)$$

where N is the number of discrete 1-s time intervals, PGA_i is the value of the peak ground acceleration (g) in time interval i (inclusive of the first and last values), and $H(x)$ is the Heaviside Step Function ($H(x)$=0 for x<0 and $H(x)$=1 for $x \geq 1$). CAV_{dp} is taken as 0 if CAV_{dp} is less than or equal to 0.16 g-s or the maximum value of the spectral acceleration in the period range from 0.1 to 0.5 s is less than or equal to 0.20 g.

For the 12 primary earthquake ground motion (i.e., ground motions 1 to 12 in Table 4.2), PGA varies from 0.15 to 0.65 g, *PGV* varies from 8 to 65 cm/s, I_a varies from 0.6 to 6 m/s, and CAV_{dp} varies from 0.5 to 3 g-s. Ground motions 13 to 24 has *PGA* values from 0.27 to 1.2, *PGV* values from 15 to 110 cm/s, I_a values from 0.9 to 13 m/s, and CAV_{dp} values from 0.5 to 3.2 g-s. Ground motions 25 to 36 have *PGA* values from 0.15 to 0.4 g, *PGV* values from 8 to 25 cm/s, I_a values from 0.35 to 0.85 m/s, and CAV_{dp} values from 0.22 to 0.52 g-s to explore the influence of less intense motions. The analytical models are subjected to a wide range of earthquake ground motions, with a deliberate bias toward ground motions of sufficient intensity to produce significant liquefaction-induced building settlement.

4.3 RESULTS OF THE PARAMETRIC STUDY

4.3.1 Insights from Analytical Results

Before examining trends in the results, insights from examining detailed results of the dynamic SSI effective stress analyses are shared. Excess pore water pressure generated by the PM4Sand model and the resulting total head in the soil profile for a representative case are shown in Figure 4.2. As shown in Figures 4.2a and 4.2b, pore water pressures increase significantly near the start of intense shaking. The generated pore water pressures under the building are higher during strong shaking due to the confinement imposed by the building, which increases the capacity for pore water pressure generation and enhances the sand's contractive response. Pore water pressures are transient and affect soil response as illustrated by the acceleration peak in Figure 4.2a at approximately 12 s, which coincides with a drop in the pore water pressure in Figure 4.2b. Figure 4.2c shows the distribution of the total head at 11 s of the seismic excitation; the distribution of total head forms a more chaotic pattern at this early time in the record. In the middle of strong shaking (i.e., t =15 s; Figure 4.2d), high total head values are localized within the top of the liquefiable soil layer under the building; water flows outward from underneath the building at this time. After strong shaking subsides (i.e., t = 40 s; Figure 4.2e), water flows primarily upward, as excess pore water pressures dissipate and largely volumetric strains occur. High, transient hydraulic gradients develop underneath the building during strong shaking and water flow patterns vary significantly.

Similar observations were found during centrifuge tests (e.g., Dashti et al., 2010).

Figure 4.3 shows the change in frequency content of the ground motion as it is propagated from the base of the model (Figure 4.3c) to its surface (Figure 4.3a). The change in frequency content is seen clearly through the use of a Stockwell transform (Stockwell et al. 1996). Comparing the surface motion Stockwell transform of Figure 4.3b to that for the base motion in Figure 4.3d, the frequency content peaks are shifted to higher periods at approximately 12 s when the most intense part of the ground motion occurs which increased dramatically the excess pore pressure as shown previously in Figure 4.2b. The increased excess pore water pressure reduces the soil stiffness

which in turn shifts the motion to higher periods. Similar observations were made for ground motions recorded at liquefied sites by using the Stockwell transform (e.g., Kramer et al. 2016).

The development of shear strains and volumetric strains within the liquefiable layer and the resulting building settlement are shown in Figure 4.4. As suggested by Dashti et al. 2010, the rate of building settlement follows the shape of the Arias intensity-time history as shown in Figure 4.4a. However, the shape of the building settlement vs. time curve matches the shape of the normalized standardized cumulative accumulated velocity of the input base ground motion even more closely. Building settlement initiates as CAV_{dp} starts to increase at about 12 s. The rate of building settlement is highest during that part of the earthquake shaking with the highest rate of increase of CAV_{dp}. As the rate of increase of CAV_{dp} decreases, so does the rate of building settlement. Some additional building settlement occurs after 100% of the record's CAV_{dp} is reached, which is largely due to post-liquefaction volumetric strain. However, shear strains largely govern building response during strong shaken as shown in Figures 4.4c and 4.4d. The magnitudes of shear strains and volumetric strains developed along a profile at the edge of the building are shown for two times: during strong shaking at t=15 s and after strong shaking at t=46 s in Figure 4.4c. Shear strains are larger than volumetric strains within the liquefiable layer. As shown in Figure 4.4d, the ratio of shear strain rate to volumetric strain rate is high during strong shaking, indicating they govern building response during this period. However, after strong shaking the ratio of shear strain rate to the volumetric strain rate decreases.

As shown in Figure 4.4b, large shear strains develop under the edge of the building during strong shaking. The importance of the shear-induced liquefaction building settlement mechanisms can also be seen clearly in examining the deformed meshes at the end of the analyses of two models shaken by different ground motions, as shown in Figure 4.5. The liquefied soil is pushed laterally from underneath the building by primarily liquefaction-induced shear mechanisms, which in turn leads to the large part of the building settlement during strong shaking.

The accumulation of shear strains and volumetric strains within the soil profile produce vertical strains that when integrated produce building settlement. The vertical strain profile in the sand beneath a shallow foundation is the basis of Schmertmann et al. (1978) static sand settlement estimation procedure wherein incremental settlement contributions are calculated using the strain influence factor within each layer, which depends on the shape of vertical strain variation with depth. Thus, it is insightful to examine the vertical strain profiles produced during earthquake shaking. Figure 4.6 shows the variation of vertical strains under the building for two representative analytical models undergoing the 12 primary earthquake motions of Table 4.2. Vertical strain profiles and normalized vertical strain profiles are shown on the left and right sides of Figure 4.6, respectively. The vertical strains calculated for the baseline case shown in Figure 4.1 are shown at the top of Figure 4.6, and the vertical strains calculated for a similar model, but with HL = 6 m are shown at the bottom. The magnitude of the vertical strains developed in the liquefied soil layer depend significantly on the characteristics of each ground motion (see left plots of Figure 4.6). The cases with higher verticals strains are associated with the ground motions with higher CAV_{dp} or I_a values.

The normalized vertical strain profiles shown on the right side of Figure 4.6 illustrate characteristic shapes that develop in the liquefied soil layer as a result of the response of the soil and overlying structure. For the 3-m thick liquefied soil layer, the shape of the normalized vertical strain profile resembles the triangular shape, starting at zero at surface and increasing until reaching a maximum value in the liquefiable layer and then decreasing with depth, similar to that used in the Schmertmann et al. (1978) procedure. The normalized vertical strain profile is less

triangular for cases with larger liquefiable layer thicknesses (i.e., see lower right plot in Figure 4.6 for the case where *HL* = 6 m). In these cases, the vertical strain profile more resembles a trapezoid. Similar typical shapes for the variation of normalized vertical strains with depth were observed in other models with similar thicknesses of the liquefiable layer. Thus, for cases involving uniform liquefiable soil layers as shown Figure 4.1, either triangular or trapezoidal strain influence diagrams could be used within a calculation scheme to estimate liquefaction-induced building settlement. However, for cases where the soil profile is not uniform, the vertical strain profiles are expected to be more complex and a more sophisticated approach would likely be necessary.

Figure 4.7 shows the variation of liquefaction-induced building settlements versus the maximum vertical strain induced within the liquefiable soil layer for all of the analytical models considered in this study for the case with ground motion 4 (Nishi-Akashi/000 component of the 1995 Kobe earthquake). As would be expected, liquefaction-induced building settlement is well correlated to the maximum vertical strain developed for each particular ground motion ($R^2 = 0.80$). Thus, a key to estimating liquefaction-induced building settlement is estimation of the maximum induced vertical strain, which in turn depends on several key parameters, such as the relative density of the liquefiable soil layer and the CAV_{dp} of the input ground motions, as will be discussed in the following sections of this chapter.

4.3.2 Key Trends for Liquefaction-Induced Building Settlements

It is informative to examine the key trends in the results of the large set of dynamic SSI effective stress analyses performed in this study. Initially, the variation of the calculated liquefaction-induced building settlement as each of the ground and building parameters of Table 4.1 are varied is examined to gain insight using the primary suite of earthquake ground motions (i.e., motions 1-12 of Table 4.2). Later, the variation of liquefaction-induced building settlements in terms of ground motion parameters is explored. Volumetric-induced settlement largely occur after strong shaking and can be estimated readily with available simplified procedures, so the analyses are stopped after strong shaking to focus on the period when a majority of building settlement occurs and to minimize computational effort. There is likely some coupled shear- and volumetric-induced settlement that occurs during strong shaking, but as discussed previously, the majority of the liquefaction-induced building settlement is shear-induced. Lastly, as noted previously, these continuum analyses cannot capture ejecta-induced settlement, which must be estimated separately. Thus, the trends explored in this study are for liquefaction-induced building settlement that occurs during strong shaking, which are largely a result of shear-induced mechanisms.

Figure 4.8 shows representative typical trends for building settlement versus the relative density of the liquefiable soil layer considering ground motion records 1-12 for a subset of the analyses. Liquefaction-induced building settlement decrease significantly as the liquefiable soil layer's relative density increases, as expected. The reduction in building settlement is more pronounced for medium density sands (i.e., D_r increasing from 50% to 75%) than for low density sands (e.g., D_r increasing from 35% to 50%). The amount of liquefaction-induced settlement is significantly lower when the liquefiable layer is dense (i.e., D_r = 90%), but importantly, it is often not zero. The shape of the curves depicted in Figure 4.8 look similar to that of the strain-dependent shear modulus reduction curve of a sandy soil based on a hyperbolic relationship between shear stress and strain.

Figure 4.9 shows representative typical trends for building settlement versus the thickness of the liquefiable soil layer considering ground motion records 1-12 for a subset of the analyses. Liquefaction-induced building settlement increase as the thickness of the liquefiable layer

increases at a diminishing rate of increase as *HL* continues to increase. There is eventually a point, which depends on the width of the building foundation, where further increases of HL do not increase building settlement substantially. The shape of the curves shown in Figure 4.9 resemble a hyperbolic tangent shape.

The distribution of shear strains induced by earthquake shaking for the analytical results shown in Figure 4.9a for ground motion 4 are shown in Figure 4.10 to explore further the effects of increasing the thickness of the liquefiable soil layer. A limitation of these FLAC analyses is the inability to capture a water film and highly concentrated shear strains within a thin layer that could develop at the top of the liquefiable layer under a low permeability crust. If a thin water film developed, building settlements larger than those calculated in these analyses could develop. For a relatively thin liquefiable layer (i.e., *HL* = 1 m; Figure 4.10a), the maximum shear strains are concentrated in the liquefiable layer, and they are considerably less than those developed when the thickness of the liquefiable is increased to 3 m (i.e., Figure 4.10b). However, if the thickness of the liquefiable layer increases further, the shear strains spread out over the thicker layer, so that the maximum shear strain when *HL* =12 m (Figure 4.10d) is less than with the case when *HL*= 6 m (Figure 4.10c). Thus, the amount of liquefaction-induced buildings settlement is not proportional to the thickness of the liquefiable layer.

Figure 4.11 shows a comparison of the results of this study in terms of normalized liquefaction-induced building settlements with the results from previous studies. The results of the dynamic SSI effective stress analyses for the cases that have a thin liquefiable layer are consistent with the results from the centrifuge tests performed by Dashti et al. (2010). As noted previously, contrary to what the proposed normalization suggests, the amount of liquefaction-induced buildings settlement is not proportional to the thickness of the liquefiable layer. If there is a sufficient thickness of liquefiable soil present under the building foundation, significant liquefaction-induced building settlement can occur that is not proportional to the thickness of the liquefying layer. Liquefaction-induced building settlements in these cases are governed by shear strains, as emphasized previously. Building settlement is not governed by volumetric strains. These results indicate that normalizing building settlement by the thickness of the liquefiable layer is misleading in understanding the response of different structures founded on relatively thin, shallow deposits of saturated granular soils. Therefore, following the recommendations of Bray and Dashti (2014), this type of plot should not be used in engineering practice. Liquefaction-induced settlements depend on the thickness of the liquefiable layer (*HL*) and the width of the foundation (*B*), but in a more complex way than depicted in the normalized plot shown in Figure 4.11.

Representative typical trends for building settlement versus the crust thickness considering ground motion records 1-12 for a subset of the analyses are shown in Figure 4.12. Liquefaction-induced building settlement decreases if the liquefiable layer is not directly beneath the foundation, then settlements decrease only slightly for increasing values of the crust thickness up to a point. If crust thickness increases further, there is a point that causes an additional decrease in settlements. The depth that this occurs appears to be between *B*/4-*B*/3 below the foundation, where *B* is the width of the foundation. Thus, if the seat of settlement due to the building load is largely in the crust, buildings settlement due to the deeper liquefiable layer diminish significantly.

Figure 4.13 shows representative typical trends for building settlement versus the building contact pressure considering ground motion records 1-12 for a subset of the analyses. Building settlement initially increases roughly proportionally with increasing *Q* from low to medium values of *Q* (i.e., 20 kPa to 80 kPa). At higher *Q* values, however, the rate of increase of building settlement decreases as *Q* continues to increase. There appears to be a point for the cases examined

in this study where increasing Q does not cause the building settlement to increase significantly. In fact, in some cases liquefaction-induced building settlement may actually decrease slightly with increasing Q values. Similar results were obtained in centrifuge model tests shown by Dashti et al. (2010). This result may be due to the higher confinement and reduced stress reversal for cases with heavy, wide buildings. Additionally, this result may be due to reduced levels of pore water pressure ratio (i.e., $r_u = u_e/\sigma'_{vo}$) generated by the earthquake under the heavily loaded building. Although higher excess pore water pressures (u_e) may be generated for the case of heavily loaded buildings, they are significantly less than the initial vertical effective stress (σ'_{vo}). Thus, building settlement does not necessarily continue to increase as building contact stress increases as the confining stress induced by the building also increases. However, these analyses ignore the potentially deleterious effects of particle breakage and crushing at high confining stresses, which would increase soil compressibility and potentially lead to higher excess pore water pressures and greater building settlement.

Figures 4.14a and 4.14b show representative typical trends for building settlement versus the width of the building foundation considering ground motion records 1-12 for a subset of the analyses. Liquefaction-induced building settlement decrease moderately in a nearly linear manner as the width of the building foundation (B) increases. Thus, foundation width is another important parameter to be considered in estimating liquefaction-induced building settlement. Figure 4.14c and Figure 4.14d show the influence of building height (H). Figures 4.14c shows the variation of liquefaction-induced settlement when the building height is increased, but the contact pressure (Q) also increases as H is increased for these cases. To separate the coupled influence of building height and contact pressure, a set of analyses is performed wherein H varies while keeping Q constant. The results from these analyses shown in Figure 4.14d indicate there is only a minor increase on building settlement when H is increased alone for the 2-story to 8-story buildings analyzed in this study. Building height could be more important for taller buildings with additional rocking tendencies. For the cases modeled herein, building height is already captured sufficiently through the building's foundation contact pressure (i.e., as H increases so does Q).

The effects of the input earthquake ground motion is examined next. Figure 4.15 shows representative trends for liquefaction-induced building settlement versus a few of the most promising ground intensity measure (IM) parameters (i.e., IMs that correlate best with the liquefaction-induced building settlements calculated in this study). The optimal IMs are CAV_{dp}, I_a and S_a1, which are shown in Figures 4.15a, 4.15b, and 4.15c, respectively. Liquefaction-induced building settlement increases systematically as each of these IMs increase. An example of an IM that does not correlate well with liquefaction-induced building settlement is $D_{5\text{-}95}$ (i.e., significant duration between 5 and 95 percent of the arias intensity), which is shown in Figure 4.15d. In summary, the characteristics of the earthquake ground motions influence greatly the magnitude of liquefaction-induced building settlement. It is difficult to capture all facets of their characteristics with one simple parameter such as PGA or PGV or S_a1. IMs that describe the intensity, frequency content, and duration of shaking more completely are preferred, with CAV_{dp} and I_a being the most efficient.

Previous work (e.g., Bray et al. 2014, and Bray et al. 2017) highlighted the importance of the calculated post-liquefaction bearing capacity factor of safety (FS) as a useful index of the seismic performance for buildings with shallow foundations situated atop liquefiable soils. For the cases analyzed in this study, the static bearing capacity FS was calculated using the procedure developed for a two-layer cohesive soil deposit (Meyerhof and Hanna, 1978), using these equations to calculate the ultimate bearing capacity of the foundation:

$$q_u = 5.14C_2 + 2\frac{C_a D_1}{B} + \gamma_1 D_f \leq 5.14C_1 + \gamma_1 D_f \quad (4.4)$$

$$C_a = C_1\left(-0.58\left(\frac{C_2}{C_1}\right)^2 + 0.96\left(\frac{C_2}{C_1}\right) + 0.612\right) \quad (4.5)$$

where the average shear strength of the non-liquefied crust (C_1) represents the top layer with thickness of D_1 and unit weight of γ_1; the post-liquefaction residual shear strength of the liquefied soil layer (C_2) represents the bottom layer; B is the foundation width; and D_f, the embedment depth of the foundation. The post-liquefaction residual shear strength (C_2) is estimated using empirical relations (e.g., Idriss and Boulanger 2008) based on the relative density of the liquefiable soil layer. The thickness of the liquefiable layer is ignored in this two layer closed-form solution to estimate the post-liquefaction bearing capacity factor of safety: $FS = q_u/Q$.

The amount of liquefaction-induced building settlement are plotted against the post-liquefaction bearing capacity factor of safety in Figure 4.16 for a subset of the dynamic SSI effective stress analyses for four of the primary ground motion records. Liquefaction-induced building settlements are not large until the post-liquefaction bearing capacity *FS* is below 1.5. As the calculated *FS* decreases below 1.0, the liquefaction-induced building settlement can increase significantly. Large settlements are not calculated for all cases. The data points shown in Figure 4.16 with $FS < 1$ and small settlements (i.e., lesser than 100 mm) correspond to cases where there is either a small thickness of the liquefiable layer (i.e., HL = 1.0 m), or a higher relative density of the liquefiable layer (i.e., $D_r \geq 50\%$) combined with a large contact pressure (i.e., Q = 160 kPa). However, the potential for large building settlement clearly increases when the post-liquefaction bearing capacity *FS* falls below one. Thus, it is prudent to calculate the post-liquefaction bearing capacity *FS*, and exercise judgment when it is below 1.5, and be cautious when *FS* is below 1.0. In the latter case, large liquefaction-induced building settlements are possible.

4.4 CONCLUSIONS

Liquefaction-induced building settlement results from ejecta-induced, shear-induced, and volumetric-induced displacement mechanisms. The shear-induced mechanism is an important component of the settlement of shallow-founded structures, especially when significant ejecta do not occur. Nonlinear dynamic SSI effective stress analyses can capture the shear-induced mechanisms of liquefaction building settlement. Over 1300 analyses are performed to investigate how key parameters affect the shear-induced liquefaction mechanism of building settlement.

Examination of the results from the dynamic SSI effective stress analyses show that typically higher excess pore water pressures are generated under the building compared to the free-field during the intense part of earthquake shaking. However, due to larger initial vertical effective stress under the building, the excess pore water pressure ratio may be lower under the building than in the free-field. Regardless, water tends to flow laterally from underneath the building towards the free-field during strong shaking, due to higher pore water pressures and hence higher total head under the building. Although there are overall systematic outward flow patterns, the instantaneous hydraulic gradients induced by the earthquake loading are highly variable. Importantly, the building is shown to create significant shear-induced ground movements underneath it during intense earthquake shaking, and the shear-induced mechanism is dominant relative to the volumetric-induced mechanism during strong shaking. As strong shaking subsides, the volumetric-induced mechanism becomes increasingly significant and may eventually produce significant building settlements. Whereas there are procedures for estimating volumetric-induced liquefaction

settlements, there are not well-established procedures for estimating shear-induced building settlements resulting from liquefaction.

The results of the large number of dynamic SSI effective stress analyses performed in the parametric analyses of this study identified several key parameters affecting shear-induced liquefaction building settlement. The relative density of the liquefiable layer is a critically important parameter, especially when transitioning from medium dense to dense sands wherein liquefaction-induced building settlement decrease significantly. Building settlement is less sensitive to variations of the liquefiable layer's relative density when it was in the ranges of very loose to loose, or dense to very dense. In the former case, building settlement is large, and in the latter case, it is small. Liquefaction-induced building settlement increases as the thickness of the liquefiable soil layer increases up to a point where increasing it further does not cause significantly more settlement. Analytical results show that methods that assume a directly proportionality between liquefaction-induced settlements and the thickness of the liquefiable layer are not satisfactory, especially for cases with thin liquefiable layers. More complex functional forms and the inclusion of other parameters are needed. A thick non-liquefiable crust suppresses building settlement due to liquefaction of a deeper layer. Liquefaction-induced building settlement increases dramatically if the liquefiable layer is directly beneath the building foundation.

Building contact pressure is an important structural factor to consider when evaluating liquefaction-induced building settlement. However, there is a point wherein the magnitude of liquefaction-induced settlement does not continue to increase for increasing values of the applied building pressure. This result, which has also been observed in centrifuge experiments, is likely due the higher confinement of a heavy building. The width of the building is also an important structural parameter. Building height is a potentially important parameter but its effect on settlement for the cases studied is correlated with building contact pressure, which captures the key aspects of the building performance better. A low post-liquefaction bearing capacity factor of safety indicates when large building settlements are possible.

The characteristics of the earthquake ground motions influence greatly the magnitude of liquefaction-induced building settlement. The ground motion intensity measures that correlate best with liquefaction-induced building settlement are CAV_{dp}, I_a and S_a1. Liquefaction-induced building settlement increases systematically as each of these *IMs* increase. It is difficult to capture all aspects of the ground motions with a simple parameter such as *PGA*. An *IM* that describes the intensity, frequency content, and duration of shaking more completely is preferred. For the cases examined in this study, CAV_{dp} is the preferred due to its better predictability compared to Ia. The results of this study provide useful insights regarding those characteristics of the ground, structure, and earthquake shaking that are most important to consider when evaluating liquefaction-induced building settlement.

Table 4.1. Parameters Considered in Sensitivity Study

Parameter	Description	Values Used	Baseline Case
HC	non-liquefiable layer thickness (m)	1, 2, 4, 6	2
HL	liquefiable layer thickness (m)	1, 2, 3, 6, 12, 18	3
HB	thickness below liquefiable layer (m)	20-HL-HC	15
D_r	liquefiable layer relative density (%)	35, 50, 60, 75, 90	50
B	building width (m)	6, 12, 24	12
H	building height (m)	6, 12, 24	12
Q	foundation contact pressure (kPa)	20, 40, 80, 160, 240	80

Table 4.2. Earthquake Ground Motions Used in the SSI Analyses (12 Primary Earthquake Ground Motion Records Are Listed First; NGA# Is from PEER NGA-West2 Database)

#	NGA#	arthquake	Site/Component	M_w	R_{rup} (km)	Amplitude Scale Factor
1	4455	Montenegro	Herceg Novi/000	7.1	26	2.2
2	6928	Darfield	LPCC/080	7.0	26	1.0
3	1787	Northridge	LA 00/000	7.1	10	1.5
4	1111	Kobe	Nishi-Akashi/000	6.9	7	1.25
5	164	Imperial V	Cerro Prieto/147	6.5	15	1
6	1787	Hector Mine	Hector/000	7.1	10	1
7	2111	Denali	R109/090	7.9	43	3
8	830	Mendocino	Shelter Cove Airport/000	7.0	29	1
9	952	Northridge	Beverly Hills/035	6.7	18	1.3
10	1512	Chi-Chi	TCU/078	7.6	8	1
11	164	Imperial V	Cerro Prieto/147	6.5	15	2
12	1787	Hector Mine	Hector/000	7.1	10	1.5
13	3750	Mendocino	Loleta Fire Station/270	7.0	24	1
14	448	Morgan Hill	Anderson Dam/340	6.2	3	1
15	6928	Darfield	LPCC/170	7.0	26	2
16	1012	Northridge	LA 00/090	6.7	19	3
17	1111	Kobe	Nishi-Akashi/090	6.9	7	2.4
18	1162	Kocaeli	Goynuk/000	7.5	32	3
19	164	Imperial V	Cerro Prieto/237	6.5	15	2
20	1787	Hector Mine	Hector/090	7.1	10	2
21	265	Victoria	Cerro Prieto/045	6.3	14	1
22	753	Loma Prieta	Corralitos/000	6.9	4	1
23	830	Mendocino	Shelter Cove Airport/000	7.0	29	2
24	952	Northridge	Beverly Hills/125	6.7	18	2.3
25	690	Whittier N	San Gabriel/180	6.0	15	1
26	1612	Duzce	Lamont 1059/000	7.1	4	1
27	26220	Chi-Chi	TCU071/000	6.2	17	1
28	33	Parkfield	Temblor pre/205	6.2	16	1
29	3943	Tottori	SMN015/000	6.6	9	1
30	4132	Parkfield	Parkfield/000	6.0	5	1
31	4457	Montenegro	Ulcinj/000	7.1	4	1
32	4477	L'Aquila	Gran Sasso /000	6.3	6	1
33	1078	Northridge	Santa Susana Ground/360	6.7	17	1
34	125	Friuli	Tolmezzo/000	6.5	16	1
35	1618	Duzce	Lamont 531/531	7.1	8	1
36	587	NZ-02	Matahina Dam/083	6.6	16	1

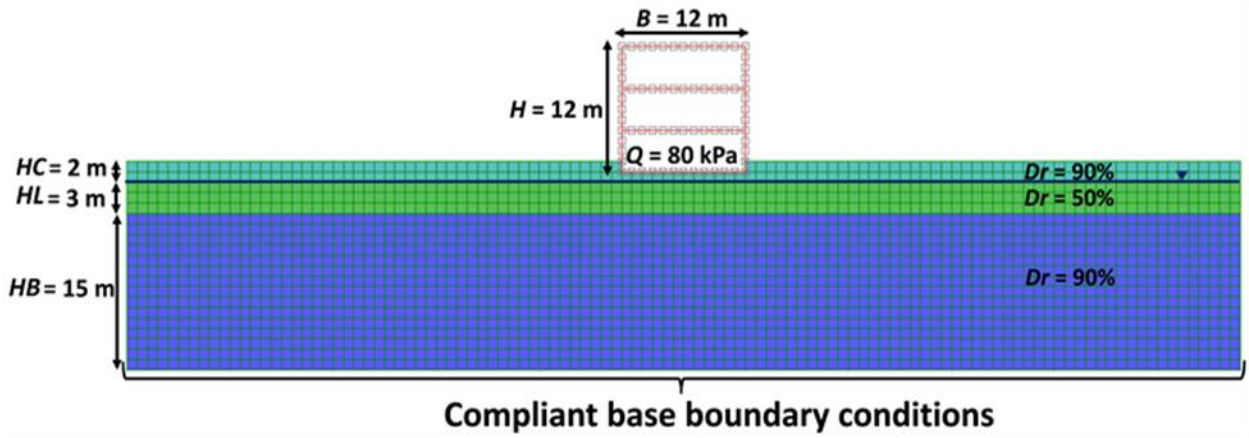

Figure 4.1. Baseline case model. The water table depth is 2 m. Lateral node boundaries are attached to represent free-field conditions.

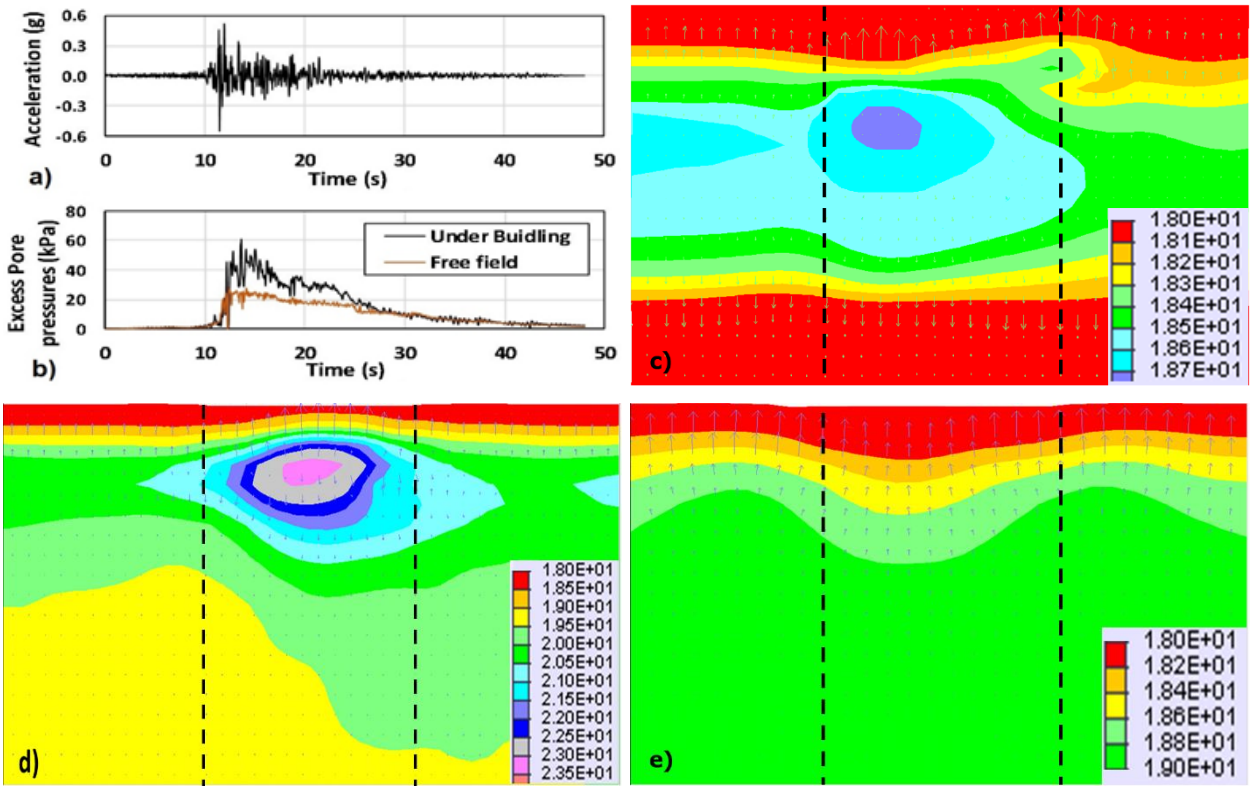

Figure 4.2. Groundwater response to cyclic loading from ground motion 1 for baseline case: a) free-field ground surface acceleration-time history, b) excess pore water pressure-time history in middle of the liquefiable layer under the building and in free-field, c) total head distribution at *t*=11 s, d) Total head distribution at *t*=15 s, and e) total head distribution at *t*=40 s. The vertical dotted lines indicate the outer edges of the building.

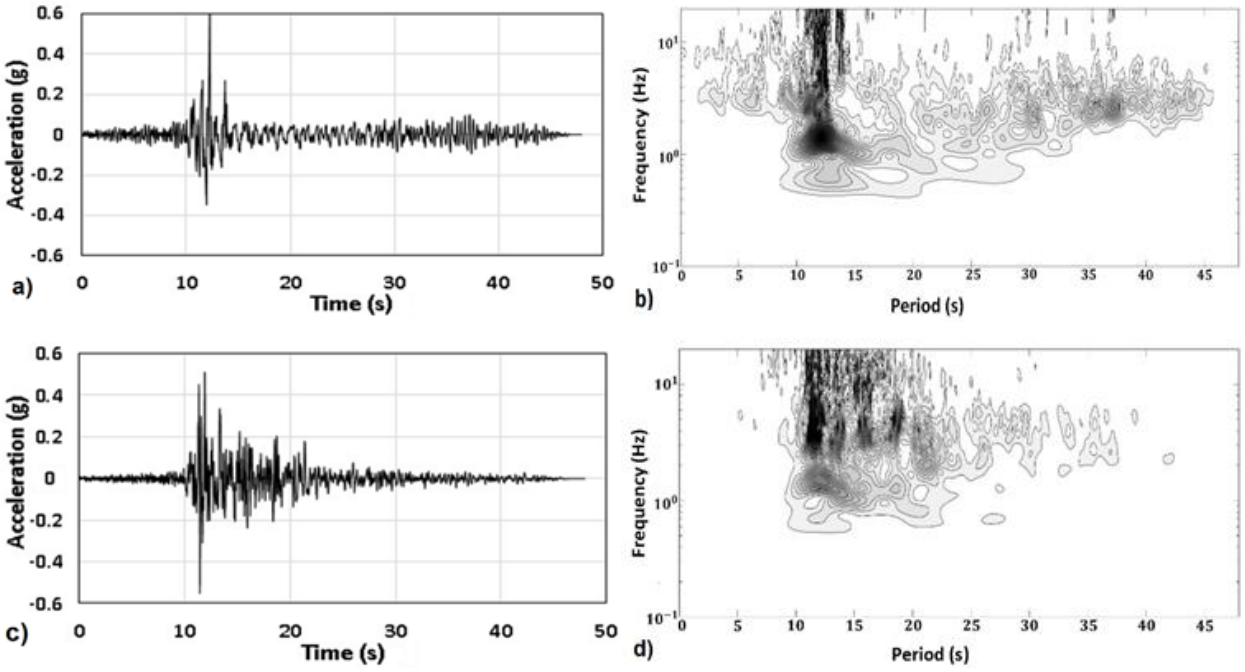

Figure 4.3. Frequency content change of ground motion 1 due to propagation through baseline case soil deposit: a) free-field ground surface acceleration-time history, b) Stockwell transform of free-field acceleration-time history, c) base acceleration-time history, and d) Stockwell transform of base acceleration-time history.

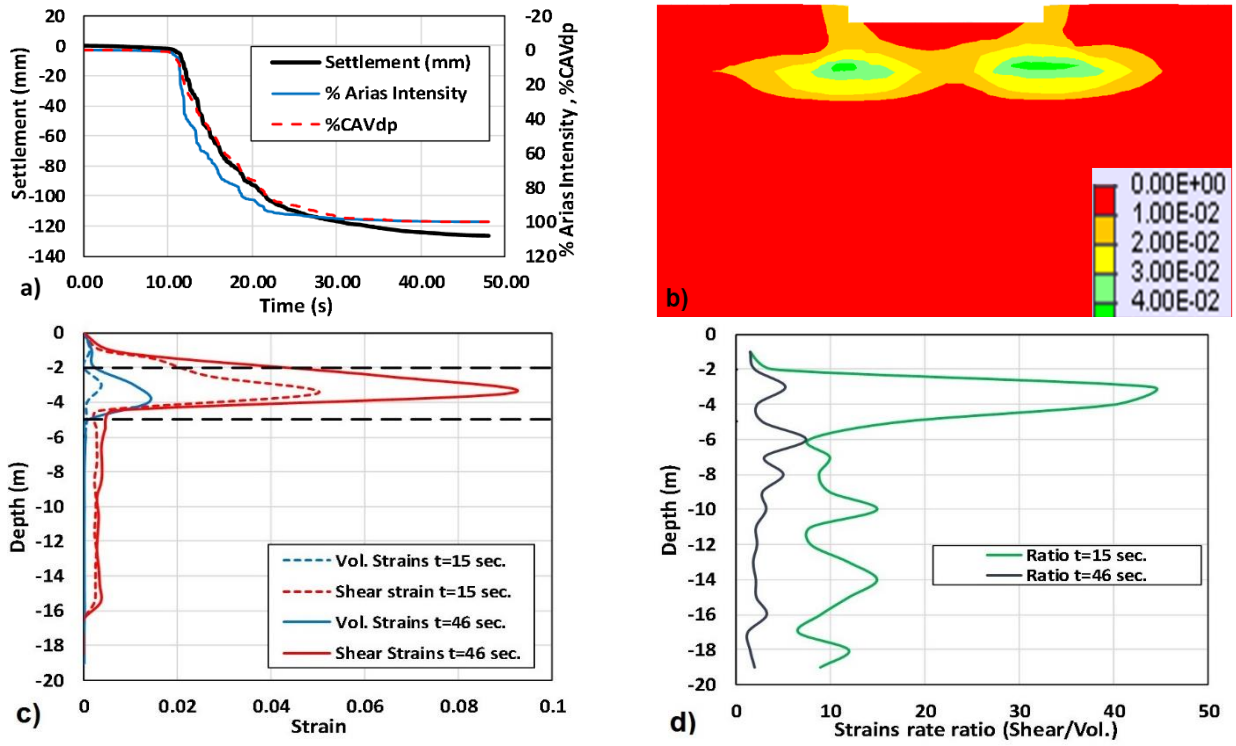

Figure 4.4. Shear and volumetric strain patterns for ground motion 1 for the baseline case: a) liquefaction induced building settlement-time history with %Arias intensity and % CAV_{dp} time histories of base motion, b) shear strain distribution at t = 15 s, c) volumetric and shear strain profiles under the building edge at different times during the seismic excitation, and d) variation of shear/volumetric strain rates ratio under the building at different times during the seismic excitation.

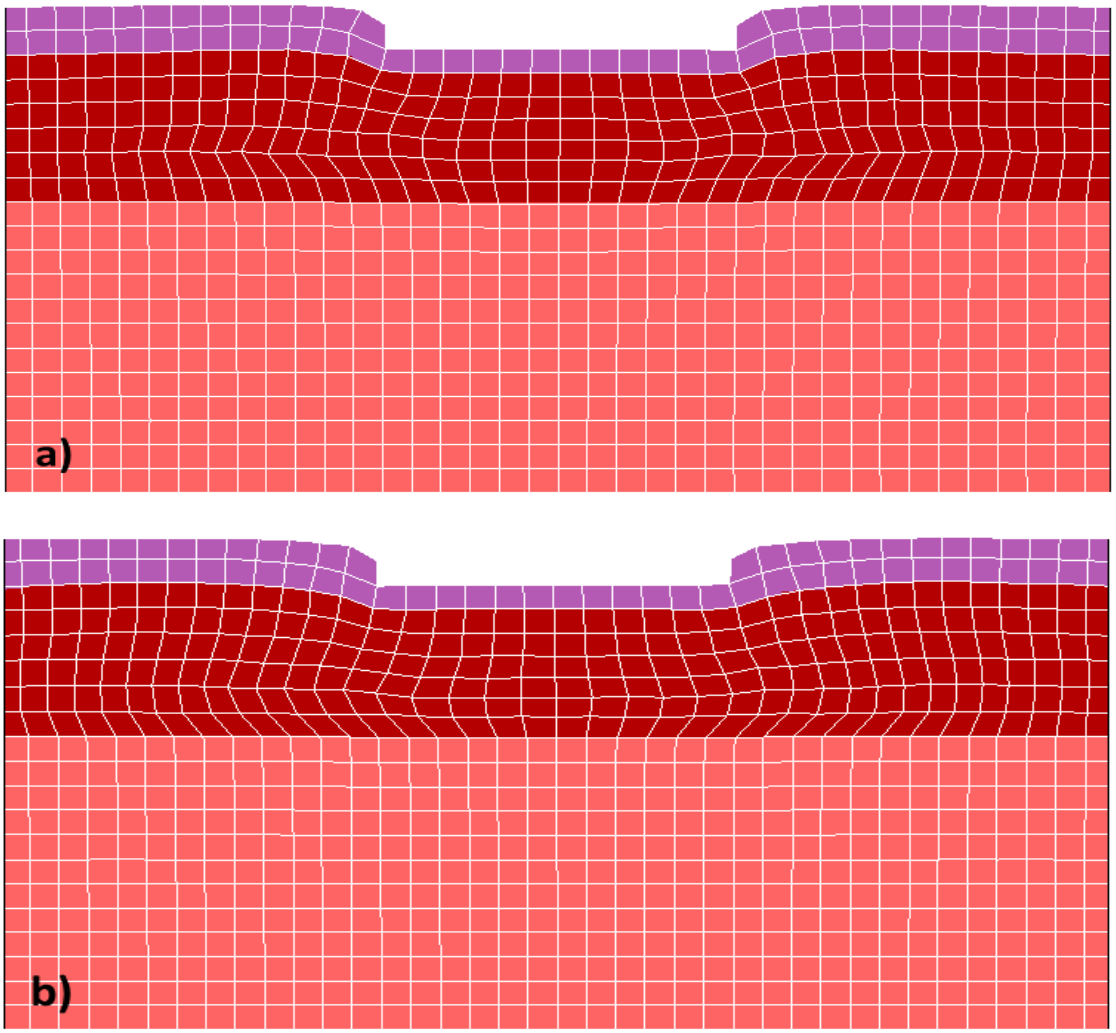

Figure 4.5. Deformed meshes at the end of seismic excitation: (a) model with D_r(liquefiable layer)=35% *HL*=6 m, *Q*=80 kPa, *B*=12 m, *H*=12 m, and *HC*= 2m for ground motion 4 at *t* = 64 s, and (b) model with D_r(liquefiable layer)=50%, *HL*=6 m, *Q*=80 kPa, *B*=12 m, *H*=12 m, and *HC*= 2m for ground motion 12 at *t* = 45 s (see Table 4.2 for description of ground motion record).

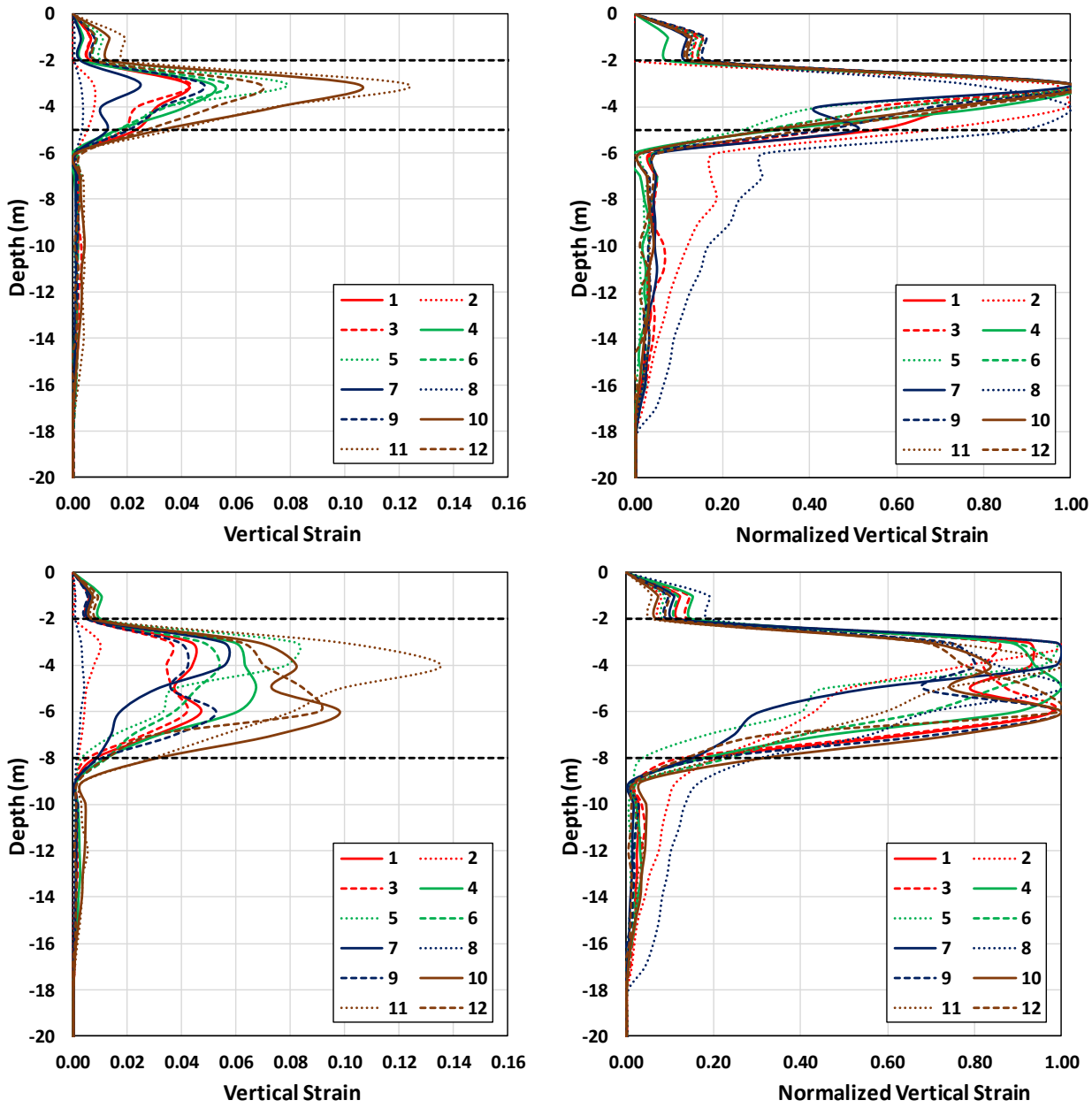

Figure 4.6. Vertical strain (left) and normalized vertical strain (right) profiles at edge of foundation for two cases analyzed with D_r(liquefiable layer)=50%, Q=80 kPa, B=12 m, H=12 m, and HC= 2m: (top) model has HL = 3m, and (bottom) model has HL = 6 m. Vertical strain profiles calculated at end of record. Horizontal dotted lines delineate top and bottom of liquefiable layer.

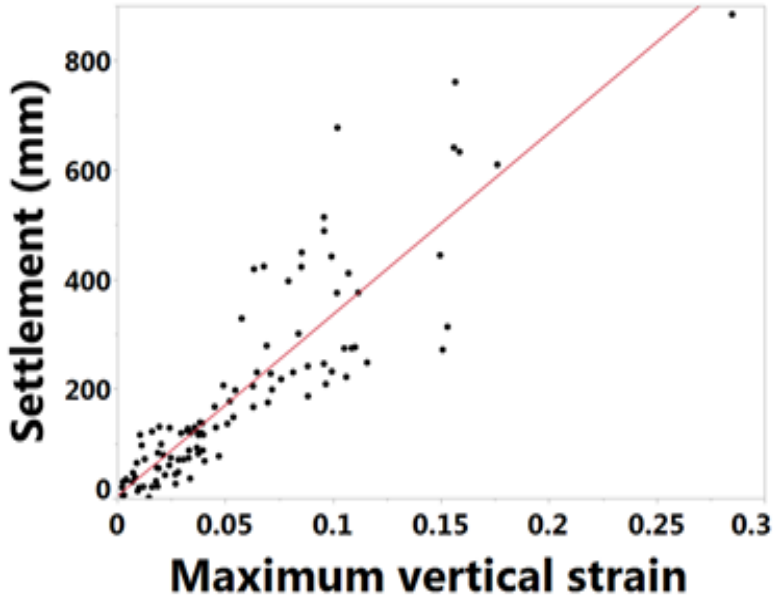

Figure 4.7. Dependence of liquefaction-induced building settlements on the maximum vertical strain developed within the soil deposit for ground motion 4 (R^2=0.80).

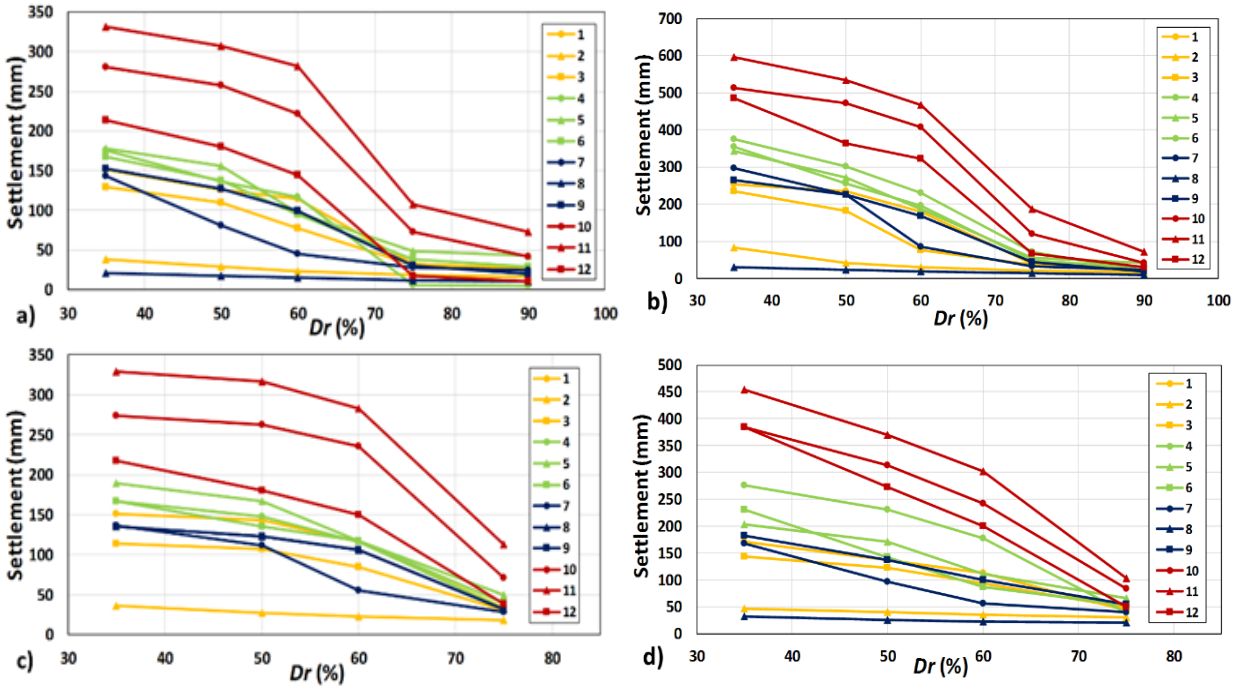

Figure 4.8. Building settlement (mm) versus relative density (D_r) for ground motions 1-12 (Table 4.2): a) model with *HL*=3 m, *Q*=80 kPa, *B*=12 m, *H*= 12m, and *HC*=2 m; b) model with *HL*=6 m, *Q*=80 kPa, *B*=12 m *H*= 12m, and; *HC*=2 m c) model with *HL*=3 m, *Q*=80 kPa, *B*=12 m, *H*= 12m and *HC*=4 m d) model with *HL*=3 m, *Q*=160 kPa, *B*=12 m, *H*=12m and *HC*=2 m.

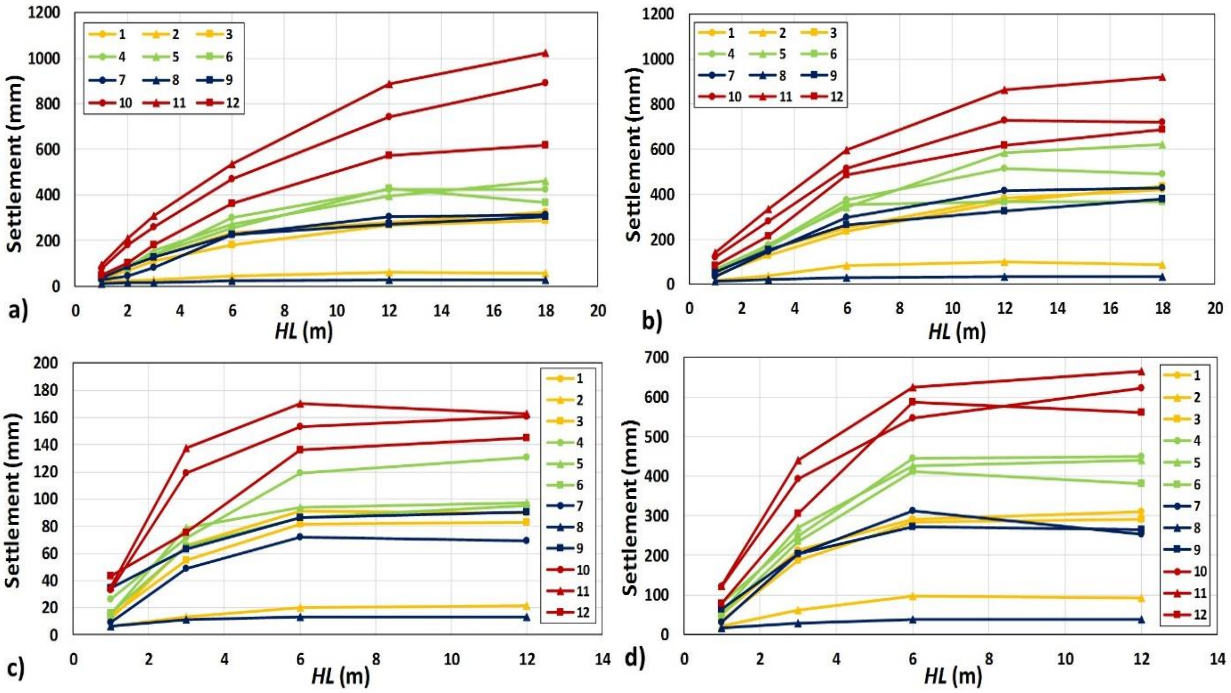

Figure 4.9. Building settlement (mm) versus thickness of the liquefiable layer (*HL*) for ground motions 1-12 (Table 4.2): a) model with D_r (liquefiable layer) =50%, *Q*=80 kPa, *B*=12 m, *H*=12 m, and *HC*= 2m; b) model with *Dr* (liquefiable layer) =35%, *Q*=80 kPa, *B*=12 m, *H*=12 m, and *HC*= 2m; c) model with *Dr* (liquefiable layer) =50%, *Q*=40 kPa, *B*=6 m, *H*=6 m, and *HC*= 2m; and d) model with *Dr* (liquefiable layer) =35%, *Q*=80 kPa, *B*=6 m, *H*=12 m, and *HC*= 2m.

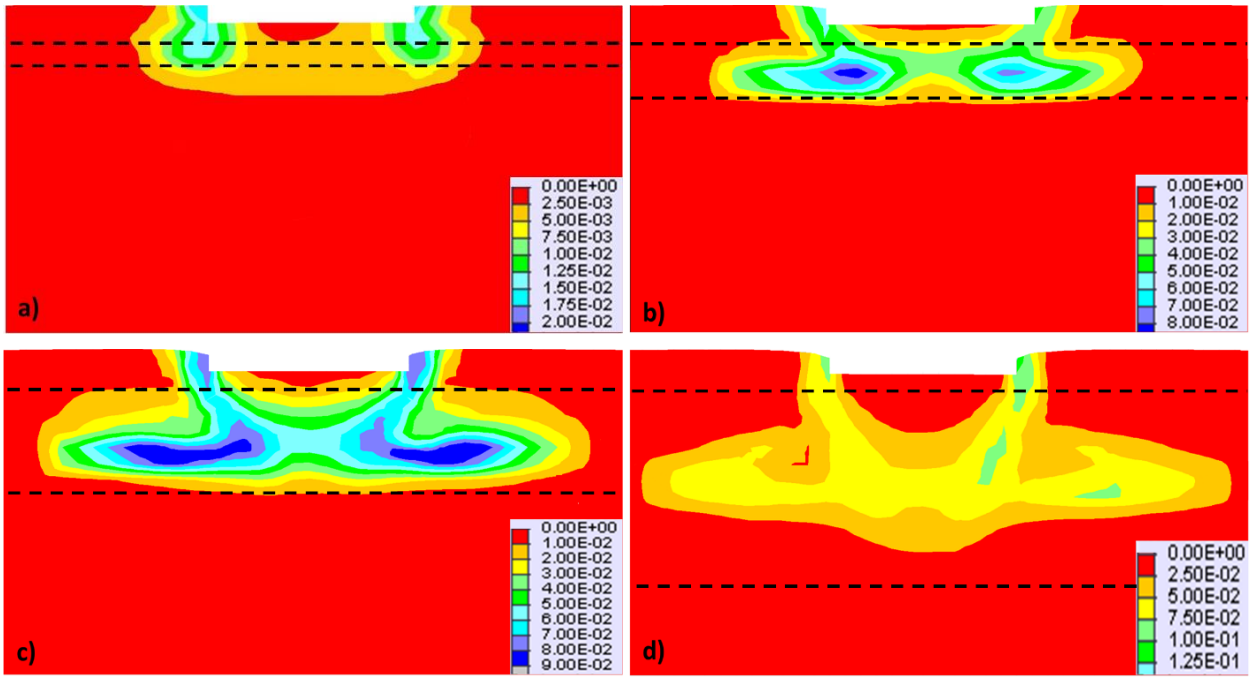

Figure 4.10. Shear strain distribution calculated for models with differing liquefiable layer thickness for ground motion 4 (Table 4.2) for case with D_r (liquefiable layer)=50%, Q=80 kPa, B=12 m, H=12 m, and HC= 2m: a) HL = 1 m, b) HL = 3 m, c) HL = 6 m, and d) HL = 12 m. The horizontal dotted lines indicate the top and bottom of the liquefiable layer.

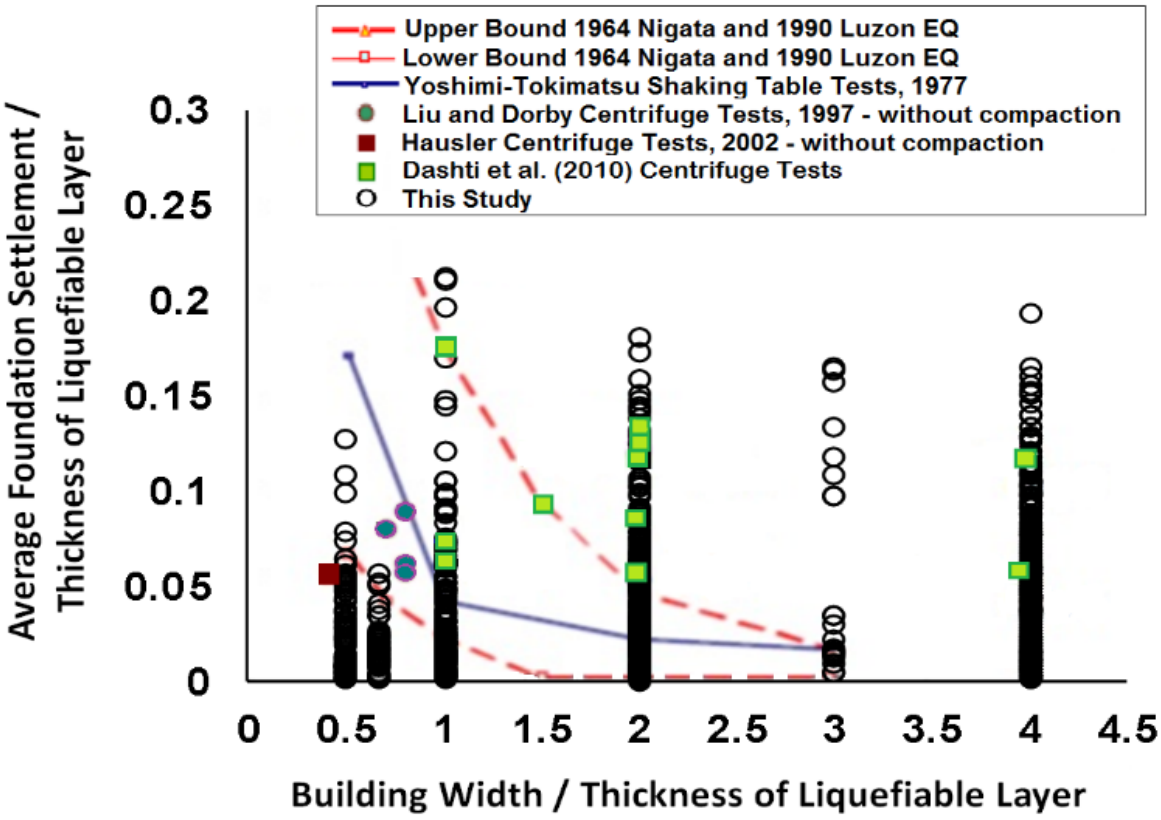

Figure 4.11. Normalized foundation settlements obtained from SSI analyses performed in this study compared with available case histories and results from centrifuge tests (data included from Yoshimi and Tokimatsu 1977, Liu and Dobry 1997, Hausler 2002, and Dashti et al. 2010).

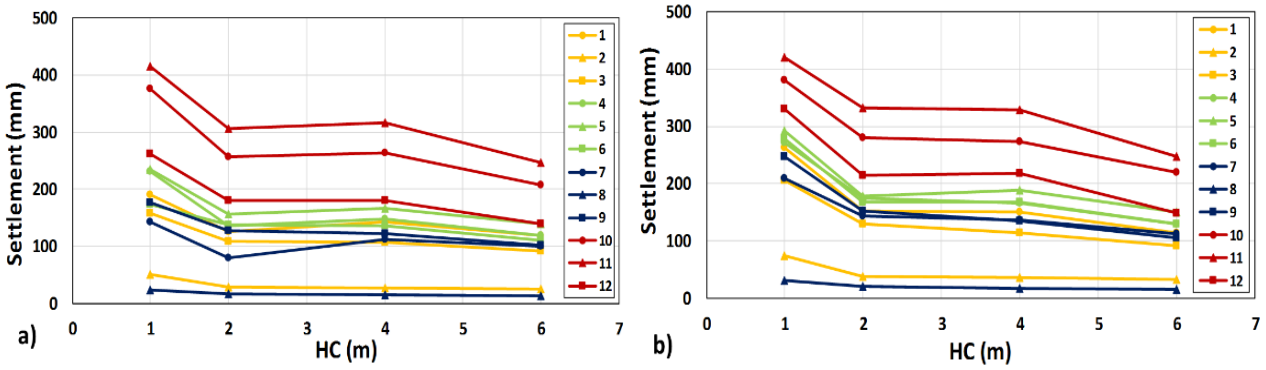

Figure 4.12. Building settlement (mm) versus crust thickness (HC) for ground motions 1-12 (Table 4.2): a) model with D_r(liquefiable layer) =50%. *HL*=3 m, *Q*= 80 kPa, *B*=12 m, and *H*=12 m; and b) model with D_r(liquefiable layer) =35%. *HL*=3 m, *Q*= 80 kPa, *B*=12 m, and *H*=12 m.

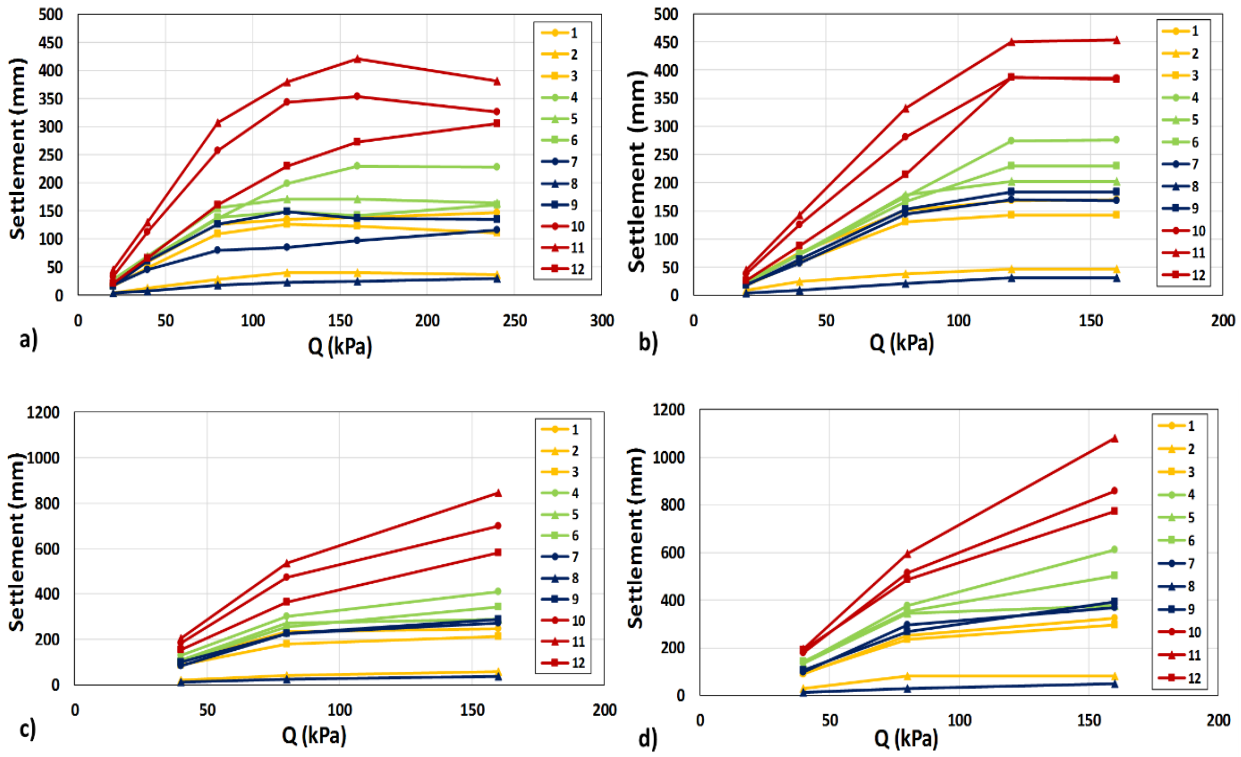

Figure 4.13. Building settlement (mm) versus building contact pressure (Q) for ground motions 1-12 (Table 4.2): a) model with D_r(liquefiable layer)=50%, HL=3 m, B=12 m, H=12 m, and HC= 2m; b) model with D_r(liquefiable layer) =35%, HL=3 m, B=12 m, H=12 m, and HC= 2m; c) model with D_r(liquefiable layer) =50%, HL=6 m, B=12 m, H=12 m, and HC= 2m; and d) model with D_r(liquefiable layer) =35%, HL=6 m, B=12 m, H=12 m, and HC= 2m.

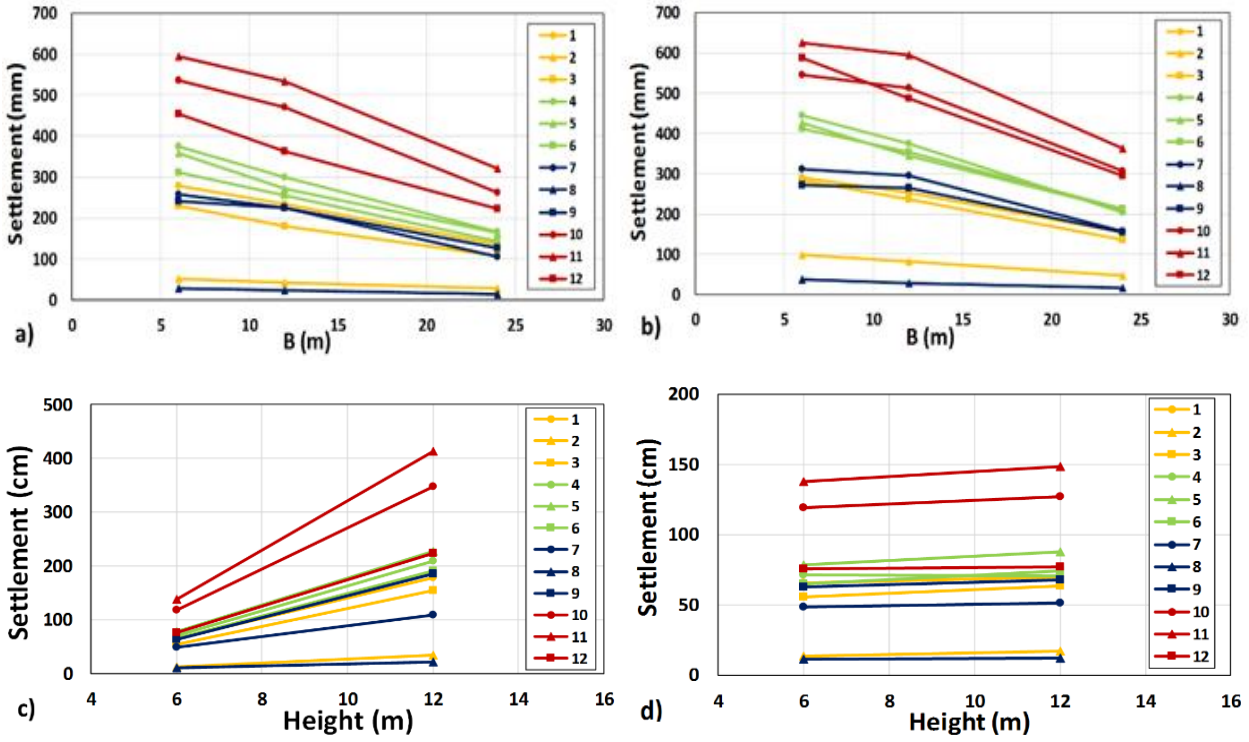

Figure 4.14. Building settlement (mm) versus foundation width (*B*) and building height (*H*) for ground motions 1-12 (Table 4.2), ground motion numbers are indicated in the legend of each figure: a) model with D_r(liquefiable layer)=50%, *HL*=6 m, *Q*=80 kPa, *B*=variable, *H*=12 m, and *HC*=2 m, b) model with D_r(liquefiable layer)=35%, *HL*=6 m, *Q*=80 kPa, *B*=variable, *H*=12 m, and *HC*=2 m, c) model with D_r(liquefiable layer) =50%, *HL*=3 m, *Q*= variable (from 40 to 80 kPa), *B*=6 m, *H*=variable, and *HC*=2m, and d) model with D_r(liquefiable layer) =50%, *HL*=3 m, *Q*= 80 kPa, *B*=6 m, *H*=variable, and *HC*=2 m.

T

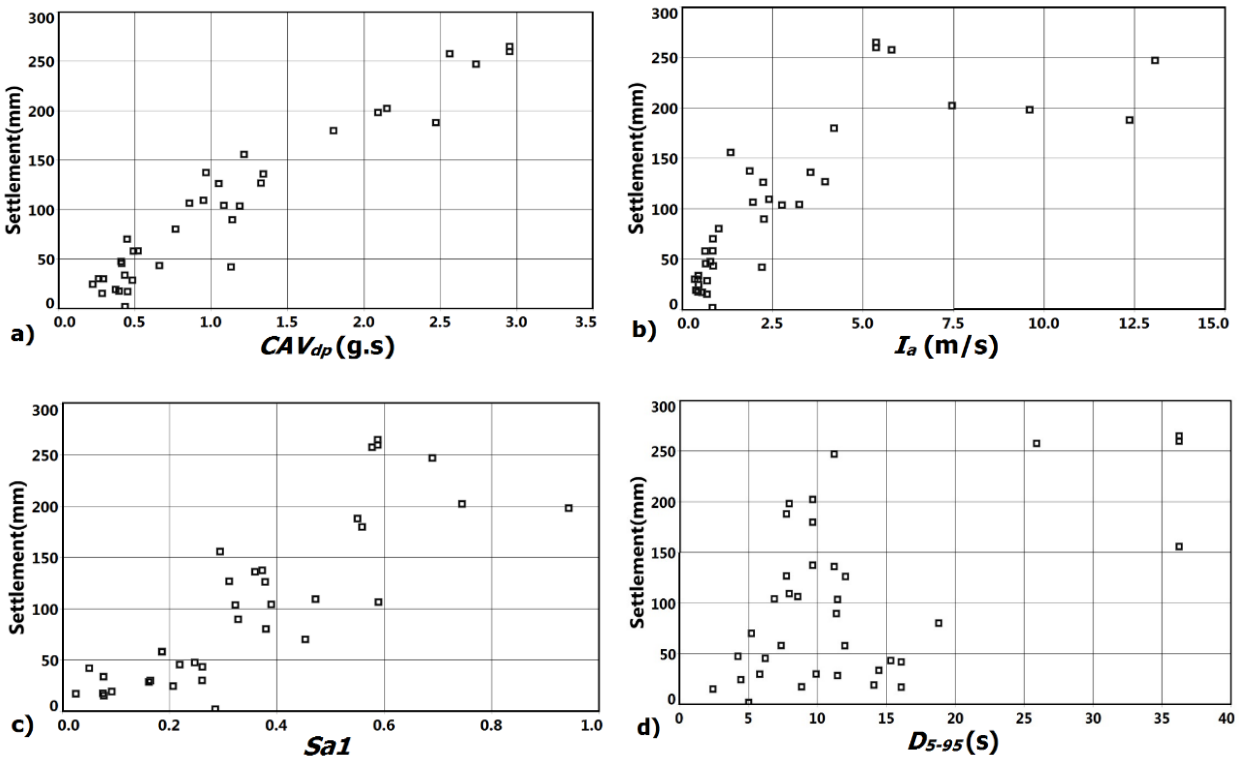

Figure 4.15. Liquefaction-induced building settlement (mm) versus selected ground motion parameters: a) CAV_{dp}, b) I_a, c) S_a1 and d) D_{5-95} for the baseline model configuration (Figure 4.1) and the ground motions considered in this study (Table 4.2).

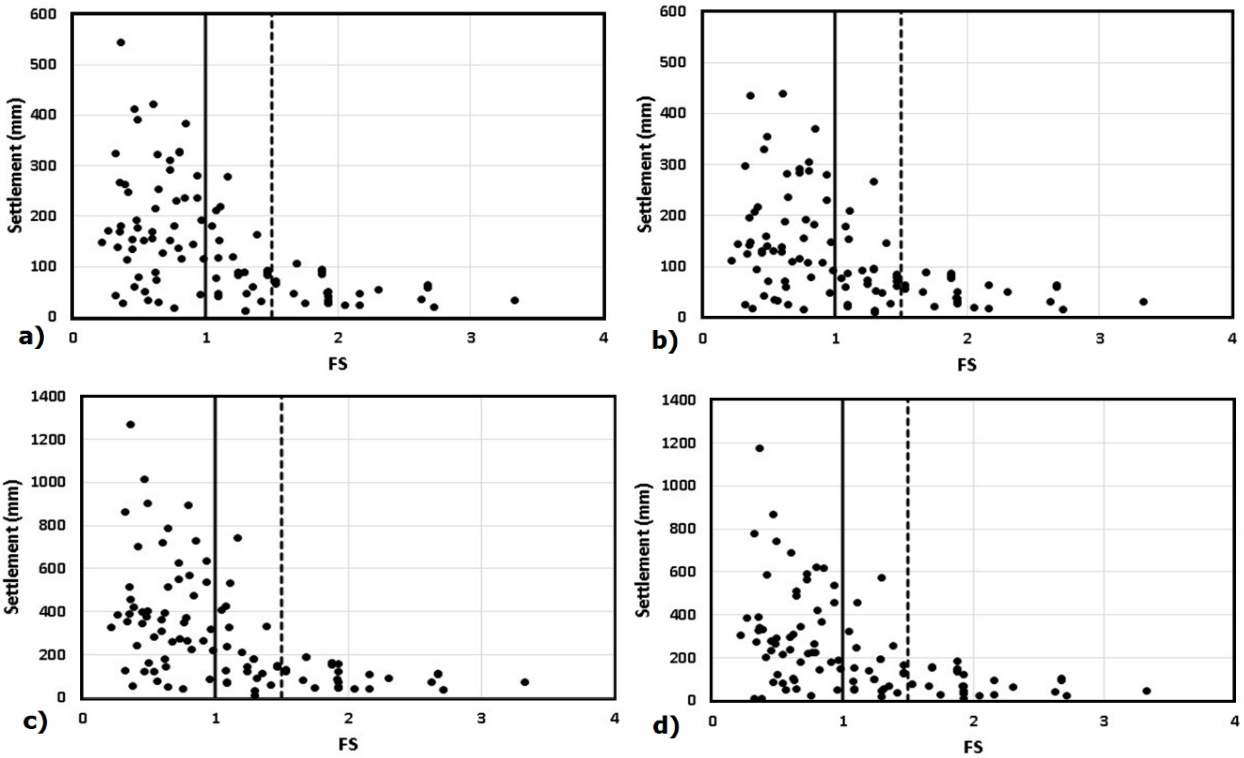

Figure 4.16. Liquefaction-induced building settlement (mm) versus post-liquefaction bearing capacity factor of safety (*FS*) for four ground motions (Table 4.2): a) ground motion 1, b) ground motion 3, c) ground motion 10, and d) ground motion 12. Dark vertical solid line corresponds to *FS*=1.0, and dark vertical dashed line corresponds to *FS*=1.5.

CHAPTER 5: SIMPLIFIED PROCEDURE FOR ESTIMATING LIQUEFACTION-INDUCED BUILDING SETTLEMENT

The contents of this chapter are primarily from a journal article submitted to the Journal of Soil Dynamics and Earthquake Engineering by Bray, J.D. and Macedo, J., entitled: "Simplified procedure for estimating liquefaction-induced building settlement", which has been accepted.

5.1 INTRODUCTION

Liquefaction of the soils supporting a shallow-founded structure can produce significant building settlement and damage. Empirical procedures are available to estimate post-liquefaction, one-dimensional (1D) consolidation settlement in the free-field without the effects of structures (e.g., Ishihara and Yoshimine 1992). In addition to considering volumetric-induced liquefaction ground deformation, the engineer should consider shear-induced ground deformation and ejecta-induced ground deformation (e.g., Bray and Dashti 2014). Effective evaluation of building performance requires a thorough understanding of all key mechanisms involved in the phenomenon and identification of the parameters governing performance. Nonlinear dynamic soil structure interaction (SSI) effective stress analyses can provide salient insights (e.g., Bray and Dashti 2014). However, before performing such analyses, it is useful to have a sense of how much liquefaction-induced building settlement is likely.

Simplified procedures that capture shear-induced liquefaction building settlement are currently lacking. However, liquefaction-induced building settlement is often controlled primarily by shear-induced ground deformations as a result of SSI-induced ratcheting and bearing capacity-type movements (e.g., Bray and Dashti 2014). Volumetric-induced ground deformations resulting from localized partial drainage, sedimentation, and post-liquefaction reconsolidation can also contribute to liquefaction-induced building settlement in addition to the removal of materials beneath a structure due to the formation of sediment ejecta. The previously mentioned 1D empirical procedures can only capture settlement as a result of the cumulative effect of volumetric strains related to sedimentation and post-liquefaction reconsolidation mechanisms. A simplified procedure that captures the important shear-induced ground deformation mechanisms involved in liquefaction-induced building settlement and provides an assessment consistent with the results of advanced SSI analyses and data from field case histories is presented in this chapter.

5.2 PREVIOUS WORK

Numerical analyses have been used by researchers to replicate the measured responses of the ground or structures during physical experiments (i.e., commonly centrifuge tests). Popescu and Prevost (1993), Elgamal et al. (2005), Popescu et al. (2006), Lopez-Caballero and Farahmand-Razavi (2008), Shakir and Pak (2010), Adrianopoulos et al. (2010), Dashti and Bray (2013), and Karimi and Dashti (2016a,b) performed nonlinear dynamic SSI effective stress analyses to capture the response of model buildings on top of a soil deposits that commonly include a liquefiable soil layer. A few studies have back-analyzed field case histories. Travasarou et al. (2006) and Luque and Bray (2015, 2017) performed numerical analyses of buildings damaged by liquefaction in the 1999 Kocaeli and 2011 Christchurch earthquakes and captured the observed performance well. There has been much learned, but there remains significant uncertainty in analyzing this problem.

No validated, widely accepted simplified method exists for estimating liquefaction-induced building settlement.

Heavily loaded structures on shallow foundations at liquefied sites typically settle more than the surrounding ground (e.g., Bray and Dashti 2014). Liquefaction-induced settlement of shallow foundations on liquefied soil have been found to be related to the contact pressure and width of the foundation and the thickness of the liquefied soil layer, among other factors (e.g., Yoshimi and Tokimatsu 1977, Liu and Dobry 1977, Dashti et al. 2010a,b, Karimi and Dashti 2016a,b, and Bray et al. 2017). Researchers have also used shaking table and centrifuge tests to investigate the seismic performance of rigid, shallow model foundations situated atop deep, uniform deposits of saturated, loose-to-medium dense, clean sand (e.g., Yoshimi and Tokimatsu 1977, Liu and Dobry 1977, and Dashti et al. 2010a,b). A majority of the measured foundation settlement occurred during strong shaking in these experiments. Settlement after strong shaking was relatively minor in comparison. Foundations settled in an approximately linear manner with increasing time during earthquake strong shaking, and they commonly settled more than the free-field soil. As a result, the structure's inertial forces were identified as another important factor (Liu and Dobry 1997).

5.3 MECHANISMS OF LIQUEFACTION-INDUCED BUILDING MOVEMENTS

Cyclically-induced pore water pressure generation and liquefaction may produce several mechanisms of building movement. Several of the key mechanisms of liquefaction-induced building settlement are illustrated in Figure 5.1. It is useful to categorize movements as ejecta-induced, shear-induced, or volumetric-induced deformations (Bray and Dashti 2014).

When it occurs, ejecta-induced deformations (ε_e) can govern building settlement (Figure 5.1a). Soil that was supporting the shallow foundations of a building can be transported from underneath the building to the ground surface. This mechanism physically removes soil that was below a building foundation. The resulting impacts can be devastating and lead to large settlement.

Shallow-founded structures exert shear stresses in the underlying soil that can produce liquefaction-induced settlement, wherein the building punches into the surrounding ground. Partial bearing capacity failure under the static load of structures due to cyclic softening/strength loss in the foundation soil can result in punching settlements or tilting of the structure ($\varepsilon_{q\text{-}BC}$) (Figure 5.1b). Cumulative ratcheting foundation displacement due to SSI-induced cyclic loading near the edges of the foundation ($\varepsilon_{q\text{-}SSI}$) (Figure 5.1c) can be especially damaging, as soil cannot sustain tension, and loading the soil downward after an upward loading is particularly disruptive to the soil structure.

Volumetric-induced displacement mechanisms can be important as well. Localized volumetric strains may occur due to partially drained cyclic loading ($\varepsilon_{p\text{-}DR}$) induced by the high transient hydraulic gradients that may occur during cyclic loading. Downward displacement of the building due to sedimentation or solidification after liquefaction or soil structure break-down ($\varepsilon_{p\text{-}SED}$) occurs when a high pore water pressure ratio is reached (Figure 5.1d). Consolidation-induced volumetric strains ($\varepsilon_{p\text{-}CON}$) occur as excess pore water pressures dissipate and the soil's effective stress increase (Figure 5.1e). This mechanism is present anytime some amount of excess pore water pressure is generated. This mechanism and the sedimentation mechanism are captured by most free-field post-liquefaction reconsolidation methods (e.g., Ishihara and Yoshimine 1992).

The differing responses of the adjacent buildings shown in Figure 5.2 illustrate further some of the key mechanisms of liquefaction-induced building settlement. The March 11, 2011 (M_w=9.0) Tohoku, Japan earthquake devastated areas of Japan. Comprehensive studies (e.g., Tokimatsu et

al. 2011) have documented many cases of liquefaction-induced building movement. This particular case occurred in Urayasu, near Tokyo.

Widespread, severe liquefaction occurred in the loose sandy hydraulic fills in Urayasu as a result of the Tohoku earthquake. The building to the left in Figure 5.2 is supported on piles, and it appears to have not displaced vertically. A building that is supported adequately on piles with their neutral plane below the liquefied soil does not undergo significant settlement. The adjacent ground settled about 300 mm relative to the pile-supported building. This amount of liquefaction-induced ground settlement was pervasive in the free-field in this area of Urayasu. The volumetric-induced ground deformation mechanisms of sedimentation and reconsolidation produced the free-field ground settlement (i.e., $\varepsilon_{p\text{-}SED}$ and $\varepsilon_{p\text{-}CON}$). The 3-story building supported on a shallow mat foundation, which is to the right of the pile-supported structure shown in Figure 5.2, punched into the ground and displaced 400 mm into the surrounding ground, so that it displaced downward 700 mm relative to the pile-supported structure. Thus, liquefaction of the soils in the vicinity of the 3-story shallow-founded structure produced about 300 mm of settlement of the ground surface in the free-field condition, and liquefaction of the soils underlying the 3-story building produced an additional 400 mm of foundation punching settlement due to largely shear-induced ground deformations (i.e., $\varepsilon_{q\text{-}BC}$ and $\varepsilon_{q\text{-}SSI}$). These observations clearly show that buildings supported by shallow foundations displace downward more than the 1D volumetric reconsolidation liquefaction-induced settlement for the free-field, level ground case. Shear-induced mechanisms should be considered when estimating liquefaction-induced building settlement.

5.4 SSI ANALYTICAL MODELS

Sensitivity analyses were performed to investigate the influence of different ground motion characteristics, site conditions, and building configurations on the amount of liquefaction-induced building settlement. The site conditions and building configurations considered for the sensitivity analyses are listed in Table 5.1, and the baseline case analytical model is shown in Figure 5.3. The groundwater table was always at the base of the non-liquefiable crust layer, the building was always embedded 1 meter, and the relative density of the non-liquefiable soil layers was 90%. In total, 105 different models were analyzed. The thickness of the liquefiable layer (*HL*) was varied from 1 to 18 meters, and its relative density (D_r) varied from 35% to 90%. The depth of the liquefiable layer was varied through varying the thickness of the non-liquefiable crust layer (*HC*) from 1 to 6 meters. The building contact pressure (*Q*) ranged from 20 to 240 kPa with building heights (*H*) of 6 to 24 meters and building widths (*B*) of 6 to 24 meters. Conventional 2-story to 8-story buildings were thus captured.

The nonlinear dynamic SSI effective stress analyses were performed using the program FLAC Version 7.0 (Itasca 2011). The widely used finite difference method program is capable of modeling coupled stress-flow problems under static and dynamic loading conditions. The *PM4Sand* Version 3 user-defined constitutive model (Boulanger and Ziotopoulou 2015) was employed to capture the cyclic response of saturated sand. The constitutive model *PM4Sand* is a stress-ratio controlled, critical state compatible, bounding surface plasticity model developed primarily for earthquake engineering applications.

The *PM4Sand* model has three primary input parameters: relative density (D_r), shear modulus coefficient (G_o), and contraction rate parameter (h_{po}). The value of D_r was first specified based on the soil conditions for the case being analyzed. The value of G_o was calculated using Equation 5.1, which is recommended by Boulanger and Ziotopoulou (2015):

$$G_o = 167\sqrt{46(D_r/100\%)^2 + 2.5} \quad (5.1)$$

and the stress dependent elastic shear modulus (G) is given by:

$$G = G_o P_a \left(\frac{\sigma_m}{P_a}\right)^{0.5} \quad (5.2)$$

where P_a is the atmospheric pressure (101.3 kPa), and σ_m is the mean effective confining pressure in the units of the parameter P_a. Element tests were analyzed with the *PM4Sand* model in *FLAC* to set the value of h_{po} to obtain the cyclic resistance ratio (CRR) at 15 cycles estimated by the Boulanger and Idriss (2016) simplified deterministic liquefaction triggering procedure for the specified relative density. The 18 secondary model parameters retained the default values recommended by Boulanger and Ziotopoulou (2015).

The structures modeled in these SSI analyses were typical frame structures founded on a mat with a sufficient number of floors to capture several modes of shaking. FLAC can model the equivalent-linear-perfectly-plastic response of structural components through beam elements that can sustain axial force, shear force, and bending moment. Luque and Bray (2015), Luque (2017), and Luque and Bray (2017) showed that the primary aspects of the dynamic response of a three-dimensional (3D) system in terms of liquefaction-induced building settlement can be captured in two-dimensional (2D) analyses by using tributary mass and stiffness with the primary goals being to capture the mass and stiffness, and hence the correct fundamental period of the structural system for one-directional shaking as well as the contact pressure transmitted to the foundation system. The flexural stiffness (EI) of the beam, column, and mat elements is set to 340 MN-m^2, 450 MN-m^2, and 1100 MN-m^2, respectively and their density is adjusted to obtain the desired contact pressure at the foundation level as well as a reasonable fundamental period for the structure, which varied from 0.17 s to 0.6 s. The seismic excitation is applied as a shear stress-time history to elastic bedrock, consistent with the outcrop acceleration-time history used as input. Lateral boundaries are sufficiently far away from the building so that moving them does not influence the results. Their respective nodes at each depth were tied together to capture free-field conditions.

Additionally, nonlinear total stress seismic site response analyses were performed for a 1D column representing free-field conditions in each model to calculate the ground motions at the ground surface for the no-liquefaction case. These analyses provided the seismic demand at the ground surface for the free-field no-liquefaction case similar to what is done when using existing simplified liquefaction triggering procedures. Surface ground motions were calculated using the input "rock" ground motions described in the next section. The seismic site response analyses were performed using the *GQ/H* model implemented in *Deepsoil* V 6.1 (Groholski et al. 2015). The *GQ/H* model can capture an initial shear modulus at zero shear strain as well as a limiting shear strength at large shear strains.

5.5 EARTHQUAKE GROUND MOTIONS

The characteristics of the earthquake ground motion largely determine the seismic response of the ground and structure, and hence, play a significant role in the amount of liquefaction-induced building settlement that occurs. Twelve recorded acceleration-time histories from shallow crustal earthquakes along active plate margins were initially selected for performing analyses of the 105 SSI analytical models discussed previously (i.e., a total of 1,260 analyses were performed). A suite of 24 additional earthquake ground motions were applied to a subset of the SSI models considered

in this study to explore the influence of a wider range of ground motions. Some of them were modified through amplitude-scaling to examine the influence of the intensity of the ground motion on the amount of liquefaction-induced building settlement. A total of 36 acceleration-time histories were used (see Table 5.2). Considering all cases analyzed, 1,308 nonlinear dynamic SSI effective stress analyses were performed in this study.

Figure 5.4 shows the distribution of the peak ground acceleration (PGA), peak ground velocity (*PGV*), Arias Intensity (I_a), and a standardized version of the cumulative absolute velocity (CAV_{dp}) for the 12 primary earthquake ground motion records used in the sensitivity analyses (i.e., ground motions 1 to 12 in Table 5.2). I_a is defined in Arias (1970), and CAV_{dp} is defined in Campbell and Bozorgnia (2011) as:

$$CAV_{dp} = \sum_{i=1}^{N}(H(PGA_i - 0.025) \int_{i-1}^{i} |a(t)|\, dt) \tag{5.3}$$

where N is the number of discrete 1-s time intervals, PGA_i is the value of the peak ground acceleration (g) in time interval i (inclusive of the first and last values), and $H(x)$ is the Heaviside Step Function ($H(x)$=0 for x<0 and $H(x)$=1 for $x \geq 1$). CAV_{dp} is taken as 0 if CAV_{dp} is less than or equal to 0.16 g-s or the maximum value of the spectral acceleration in the periods range from 0.1 to 0.5 s is less than or equal to 0.20 g. Ground motions 13 to 24 included amplitude-scaled ground motion records from the primary suite of ground motion records to examine the influence of variations in ground motion intensity on the amount of liquefaction-induced building settlement. Ground motions 25 to 36 included ground motions of lower intensity compared to the other sets (i.e., I_a < 1.0 m/s, *PGA* < 0.4 g and *PGV* < 25 cm/s) to explore the influence of less intense motions.

5.6 TRENDS IN ANALYTICAL RESULTS

The results of the large number of dynamic SSI effective stress analyses performed as part of this study identify important parameters and key trends of shear-induced liquefaction building settlement (i.e. chapter 4). These continuum analyses could not capture the ejecta-induced settlement (Figure 5.1a). Volumetric-induced settlement largely occur after strong shaking and can be estimated with available simplified procedures, so the analyses are stopped after strong shaking to minimize computational effort. There is likely some coupled shear-induced and volumetric-induced settlement that occurs during strong shaking, but the majority of the settlement is shear-induced (chapter 4). Assuming all of the liquefaction-induced settlement calculated during earthquake strong shaking is shear-induced is conservative for most cases, as volumetric-induced free-field ground settlement is computed separately and added later to estimate the total building settlement.

The relative density of the liquefiable soil layer (D_r) and its thickness (*HL*) are identified as key site parameters through examination of the analytical results (chapter 4). Figure 5.5 shows representative trends for liquefaction-induced building settlement versus these site parameters for a subset of the analyses. Liquefaction-induced building settlement decreases significantly as the liquefiable soil layer's relative density increases (Figure 5.5a). The reduction in building settlement is more pronounced for medium density sands (i.e., D_r increasing from 50% to 75%) than for low density sands (i.e., D_r increasing from 35% to 50%) or high density sands (i.e., D_r increasing from 75% to 90%). Although the amount of liquefaction-induced settlement is modest when the liquefiable layer is dense, it is often not zero. The shape of the curves depicted in Figure 5.5a looks similar to that of the strain-dependent shear modulus reduction curve of a sandy soil based on a hyperbolic relationship between shear stress and strain. Liquefaction-induced building

settlement increases as the thickness of the liquefiable layer increases at a diminishing rate of increase as *HL* continues to increase (Figure 5.5b). There is eventually a point, which depends on the width of the building foundation, where further increases of *HL* do not increase building settlement substantially. The shape of the curves shown in Figure 5.5b resembles a hyperbolic tangent shape.

The depth of the liquefiable layer, which is defined by the thickness of the non-liquefiable crust (*HC*), is another potentially important site parameter. Figure 5.6 shows representative trends for liquefaction-induced building settlement versus this site parameter for a subset of the analyses. For values of *HC* in the lower range of the values considered in this study (Table 5.1), its influence is modest, except when increasing *HC* moves the liquefiable layer down from being directly beneath the foundation. Liquefaction-induced building settlement increases significantly in the cases where the liquefiable layer is directly beneath the building foundation. As *HC* increases further, there is a point, which is at a depth of about *B*/3 below the base of the foundation of width (*B*) for the cases studied, where building settlement decreases significantly as the *HC* increases. This is due to the liquefiable layer moving increasingly below the seat of settlement of the shallow-founded structure. Thus, the parameter *HC* can influence greatly liquefaction-induced building settlement.

The building foundation contact pressure (*Q*) and building width (*B*) are identified as key structural parameters through examination of the analytical results (chapter 4). Figure 5.7 shows representative trends for liquefaction-induced building settlement versus these structural parameters for a subset of the analyses. Building settlement initially increases roughly proportionally with increasing *Q* from low to medium values of *Q* (i.e., 20 kPa to 80 kPa), as shown in Figure 5.7a. At higher *Q* values, the rate of increase of building settlement decreases as *Q* continues to increase. There is a point for the cases examined in this study where increasing *Q* does not cause the building settlement to increase significantly. In some cases, building settlement actually decreases slightly with increasing *Q* values. This result may be due to the higher confinement and reduced stress reversal for cases with heavy buildings. Additionally, this result may be due to reduced levels of pore water pressure ratio (i.e., $r_u = u_e/\sigma'_{vo}$) generated by the earthquake under the heavily loaded building. Although higher excess pore water pressures (u_e) may be generated for the case of heavily loaded buildings, they are significantly less than the initial vertical effective stress (σ'_{vo}). Importantly, however, these analyses ignore the potentially deleterious effects of particle breakage and crushing at high confining stresses, which would increase soil compressibility and potentially lead to higher excess pore water pressures and greater building settlement.

Liquefaction-induced building settlement decreases moderately in a nearly linear manner as the width of the foundation increases for the cases analyzed in this study (Figure 5.6b). Thus, foundation width is an important parameter to capture in the development of a predictive equation for liquefaction-induced building settlement. Conversely, building height (*H*) is already captured partially through the building's foundation contact pressure (*Q*), i.e., as H increases so does *Q*. The results from a set of analyses wherein *H* varies while keeping *Q* constant indicate there is only a minor increase of building settlement when H is increased alone for the 2-story to 8-story buildings analyzed in this study (chapter 4). Building height could be more important for taller buildings with additional rocking tendencies. However, *H* need not be considered separately for the building configurations studied (i.e., 2-story to 8-story buildings), because *Q* already captures much of its effect.

Previous work (e.g., Bray and Sancio 2009, Bray et al. 2014, and Bray et al. 2017) highlighted the importance of the calculated post-liquefaction bearing capacity factor of safety (*FS*) as an

important index of the seismic performance of buildings with shallow foundations situated atop liquefiable soils. For the cases analyzed in this study, the static bearing capacity *FS* was calculated using the procedure developed by Meyerhof and Hanna 1978 for a two-layer cohesive soil deposit. The post-liquefaction bearing capacity factor of safety is calculated using: $FS = q_u/Q$, where the ultimate bearing capacity of the foundation (q_u) is calculated as:

$$q_u = 5.14C_2 + 2\frac{C_a D_1}{B} + \gamma_1 D_f \leq 5.14C_1 + \gamma_1 D_f \quad (5.4)$$

$$C_a = C_1\left(-0.58\left(\frac{C_2}{C_1}\right)^2 + 0.96\left(\frac{C_2}{C_1}\right) + 0.612\right) \quad (5.5)$$

where the average shear strength of the non-liquefied crust (C1) represents the top layer with thickness of D_1 and unit weight of γ_1; the post-liquefaction residual shear strength of the liquefied soil layer (C_2) represents the bottom layer; *B* is the foundation width; and D_f, the embedment depth of the foundation. The post-liquefaction residual shear strength (C_2) is estimated using empirical relations (e.g., Idriss and Boulanger 2008) based on the relative density of the liquefiable soil layer. The thickness of the liquefiable layer is assumed to be substantial in this two layer closed-form solution, and thus its influence is ignored in the calculation of the post-liquefaction bearing capacity factor of safety.

Results are shown for a subset of the SSI analyses for four ground motion records in Figure 5.8. Liquefaction-induced building settlements are not large until the post-liquefaction bearing capacity *FS* is below 1.5. As the *FS* decreases below 1.0, the liquefaction-induced building settlement may increase significantly. Thus, it is prudent to calculate the post-liquefaction bearing capacity *FS* and be cautious when it is below 1.5. When *FS* is below 1.0, extreme care is warranted as bearing capacity failure is possible with large building movements. The data points shown in Figure 5.8 with $FS < 1$ and small displacements (i.e., lesser than 100 mm) correspond to cases where there is either a small thickness of the liquefiable layer (i.e., *HL*=1.0 m), or a higher relative density (i.e., $D_r \geq 50\%$) combined with a large contact pressure (i.e., *Q*= 160 kPa).

Lastly, several important earthquake ground motion parameters are identified through examination of the results of the analyses, as well as observing key trends (chapter 4). The relative importance of the ground motion parameters are best explored through regression analyses of models based on different combinations of ground motion parameters, which is discussed in the next section of this chapter.

5.7 REGRESSION ANALYSIS OF ANALYTICAL RESULTS

5.7.1 Selection of independent variables and functional form

Based on concepts in liquefaction-induced deformation and building performance, and interrogation of the results from the SSI analyses described previously, several trial functional forms were investigated to represent the shear-induced building settlement due to liquefaction. One of the more promising functional forms is:

$$Ln(Ds) = a1 + a2 * Ln(Q) + a3 * Ln(Q)^2 + a4 * Dr + a5 * Ln\left(Tanh\left(\frac{HL}{a6}\right)\right) + a7 * B + a8 * HC + a9 * Ln(IM1) + a10 * Ln(IM2) \quad (5.6)$$

where *Ds* is the shear-induced liquefaction building settlement (mm), *IM1* and *IM2* represent intensity ground motion parameters, a1 to a10 are coefficients, and the other variables have been defined previously (e.g., Table 5.1). Regression analyses were performed using the functional form of Equation 5.6 using the analytical results considering different candidates for the intensity measure parameters (when considering only one *IM*, *a10*=0). The results of these analyses are shown in Figure 5.9b for outcrop "rock" ground motion parameters as well as for ground motion parameters for the motion calculated at the free-field ground surface in the nonlinear total stress seismic site response analyses in Figure 5.9a.

The preferred *IM* parameters to estimate Ds have the highest higher R^2 values in Figure 5.9. The preferred *IM* parameters are standardized cumulative absolute velocity (CAV_{dp}), Arias Intensity (I_a), and S_a1, the spectral acceleration at a period equal to 1 s ($S_a(T=1\ s)$). Arias Intensity and cumulative absolute velocity have been proposed previously as informative ground motion intensity measures that incorporate the cumulative effects of ground motion intensity, frequency content, and duration on the seismic response of structural and geotechnical systems (e.g., Dashti et al. 2010b, Kramer and Mitchell 2006). However, the ground motion predictive equations (GMPE) for Arias Intensity exhibit a greater aleatory uncertainty than standardized cumulative absolute velocity (Campbell and Bozorgnia 2012). Additional regression analyses are performed exploring the robustness of using the ground motion intensity parameters of CAV_{dp}, I_a, and S_a1, independently (i.e., setting a10=0) or using combinations of them (i.e., I_a & S_a1, or CAV_{dp} & S_a1).

The regression performed considering CAV_{dp} and S_a1 for the outcrop "rock" motion calculated these model coefficients for Equation 5.6: a1= -4.63, a2= 4.70, a3= -0.43, a4= -0.03, a5= 0.98, a6= 6.0, a7= -0.02, a8= -0.07, a9= 0.74, and a10= 0.41. The shear-induced liquefaction building settlement estimated with this model was compared to the building settlement calculated by Karimi and Dashti (2017) during strong shaking for several cases analyzed in a comprehensive study by them. Karimi and Dashti (2017) performed a large set of 3D dynamic SSI effective stress analyses using a different computational platform (i.e., OpenSees finite element analysis program), a different constitutive model (i.e., PDMY02; Elgamal et al. 2002; Yang et al. 2003), and a different suite of ground motions. The comparison of shear-induced building settlement estimated using Equation 5.6 with the coefficients listed above and the building settlement calculated by Karimi and Dashti (2017) during strong shaking are shown in Figure 5.10. The Equation 5.6 model estimates are reasonable when compared with the numerical results from Karimi and Dashti (2017). There are only significant systematic inconsistencies between the values estimated using Equation 5.6 and those calculated by Karimi and Dashti (2017) for cases where small liquefaction-induced building settlements were calculated (i.e., $D < 5$ mm). Equation 5.6 underestimates the calculated building settlement for these few cases. However, overall, Equation 5.6 captures the observed trends in the analytical results over the range of building settlements that are of engineering importance.

5.7.2 Liquefaction-induced building settlement (LBS) index

Liquefaction-induced building settlement during strong shaking is related primarily to the level of shear strain induced in the foundation soils (chapter 4). Consequently, a liquefaction-induced building settlement index (*LBS*) is proposed as:

$$LBS = \int W * \frac{\varepsilon_{shear}}{z}\, dz \tag{5.7}$$

where z (m) is the depth measured from the ground surface, which must be greater than 0, W is a foundation-weighting factor wherein $W = 0.0$ for z less than D_f, which is the embedment depth of the foundation, and $W = 1.0$ otherwise. The shear strain parameter in Equation 5.7 (ε_{shear}) is the liquefaction-induced free-field shear strain (in %) estimated using the Zhang et al. (2004) CPT-based procedure, which is based on the work of Ishihara and Yoshimine [1]. It is calculated based on the estimated D_r of the liquefied soil layer and the calculated safety factor against liquefaction triggering (FS_L). The relative density of the liquefied soil layer is defined in each case analyzed (Table 5.1), and the simplified liquefaction triggering procedure of Boulanger and Idriss (2016) is used to estimate FS_L. The integral of Equation 5.7 is approximated as the summation of increments of liquefaction-induced shear strain divided by the depth of the midpoint of the sublayer over the soil profile depth to calculate *LBS*. The use of the reciprocal of depth as the depth-weighting function for *LBS* emphasizes the relative importance of liquefaction of soil layers close to the foundation.

Several other depth-weighting functions were examined (e.g., linearly decreasing with increasing depth, and one similar to that used in the Schmertmann et al. (1978) procedure for estimating static settlement). However, the reciprocal of depth captured the trends in the data best and was straightforward. Several other liquefaction damage indices were also explored. The use of *LBS* was compared to other liquefaction indexes such as *LPI* (Iwasaki et al. 1982), *LSN* (van Ballegooy et al. 2015), and *LPIish* (Maurer et al. 2015). *LBS* is better correlated with the profile density distribution in the analyses, provides the smallest standard deviation in the regressions, and performs better for the field cases histories analyzed in this study, which are presented later.

5.7.3 Model for estimating liquefaction-induced building settlement

It is standard practice in earthquake engineering to perform simplified liquefaction triggering evaluations using the estimated free-field no-liquefaction ground surface PGA to represent the seismic demand. Moreover, the seismic performance of a site should be more influenced by the characteristics of the ground motions at the ground surface than those for the outcropping "rock" site condition. Therefore, the ground motion intensity parameters corresponding to the surface ground motions are preferred in the proposed simplified procedure for estimating shear-induced liquefaction building settlement. As discussed previously, nonlinear total stress seismic site response analyses were employed to calculate the ground surface acceleration-time histories for the cases examined in this study. The functional form considered going forward (where *b1*-*b10* are coefficients and *IMs* are estimated for the free-field no-liquefaction case) is:

$$Ln(Ds) = b1 + b2 * Ln(Q) + b3 * Ln(Q)^2 + b4 * LBS + b5 * Ln\left(Tanh\left(\frac{Hl}{b6}\right)\right) + b7 * B + b8 * HC + b9 * Ln(IM1) + b10 * Ln(IM2) \quad (5.8)$$

The regression analyses using Equation 5.8 indicated the HC term can be eliminated once the parameter *LBS* is included, because *LBS* carries descriptive information related to *HC*. Additionally, there is a bias in the residuals with respect to D_r for values greater than 60%. Accordingly, dummy variables are used for *LBS* values less than or equal to 16 (which correspond to the range of D_r, where the residuals were observed), which led to a different set of coefficients for *b1* and *b4* in Equation 5.8. Lastly, there are not considerable differences for the models that used the pair of I_a and S_a1 or the pair of CAV_{dp} and S_a1 as *IM1* and *IM2*. Given the better predictability of CAV_{dp} compared to I_a, CAV_{dp} is preferred. Models with only one *IM* were also

tested, but these models exhibited bias in terms of residuals for *IM*s that were not considered in the models. The final form of the recommended equation to estimate shear-induced liquefaction building settlement (*Ds* in mm) is:

$$Ln(Ds) = c1 + 4.59 * Ln(Q) - 0.42 * Ln(Q)^2 + c2 * LBS + 0.58 * Ln(Tanh\left(\frac{HL}{6}\right) - 0.02 * B + 0.84 * Ln(CAVdp) + 0.41 * Ln(Sa1) + \varepsilon \quad (5.9)$$

where *c1* = -7.48 and *c2* = 0.014 for *LBS* > 16 and *c1* = -8.35 and *c2* = 0.072 for *LBS* ≤ 16. *LBS* is calculated with Equation 5.7. *HL* is the cumulative thickness of layers with $FS_L \leq 1.0$ in the units of m. *Q* is the foundation contact pressure in the units of kPa, and *B* is its width in m. The intensity measures, CAV_{dp} in units of *g*-s and S_a1 in units of *g*, are estimated for free-field ground motions at the site. The uncertainty in the estimate of building settlement given the input parameters is defined by ε, which is a normal random variable with zero mean and 0.50 standard deviation in *Ln* units. Figure 5.11 show the plots of residuals for several ground motion, site, and building parameters.

5.8 SIMPLIFIED PROCEDURE FOR ESTIMATING LIQUEFACTION-INDUCED BUILDING SETTLEMENT

Shallow foundations at sites with liquefiable layers within its seat of settlement can undergo shear-induced ground settlement as well as settlement due to volumetric-induced mechanisms and settlement due to the removal of soil from beneath foundation elements through the formation of sediment ejecta. Shear-induced mechanisms are not captured and hence cannot be estimated using 1D post-liquefaction volumetric reconsolidation procedures, which only capture free-field ground settlement. Instead, a separate procedure that considers the important shear-induced building settlement mechanism is required.

The proposed simplified procedure for estimating liquefaction-induced building settlement involves these steps:

1. Perform a liquefaction triggering assessment for the free-field conditions, and calculate the safety factor against liquefaction triggering (FS_L) for each potentially liquefiable soil layer, preferably using a CPT-based method (e.g., Boulanger and Idriss 2016).
2. Calculate the post-liquefaction bearing capacity safety factor (FS) using the two-layer solution of Meyerhof and Hanna (1978) (i.e., Equations 5.4 and 5.5), where the average shear strength of the non-liquefied crust layer represents the top layer and the post-liquefaction residual shear strength of the liquefied soil layer (estimated using empirical procedures, e.g. Idriss I, and Boulanger R. 2008) represents the bottom layer. If the post-liquefaction bearing capacity *FS* is less 1.0 for light or low buildings or less than 1.5 for heavy or tall buildings, large movements are possible, and the potential seismic building performance can often be judged to be unsatisfactory.
3. Estimate the likelihood of sediment ejecta developing at the site by using the Ishihara (1985) ground failure design chart or ground failure indices such as *LSN* (van Ballegooy, S. et. al. 2015) or *LPI* (Iwasaki, T. et. al. 1982). If the amount of sediment ejecta is significant, estimate the amount of building settlement as a direct result of loss of ground due to the formation of sediment ejecta (*De*). This can best be done using relevant case histories to estimate the amount of ejecta and then assuming that the ejecta has been removed below the building foundation.
4. Estimate the amount of volumetric-induced building settlement (*Dv*) preferably using a CPT-based method (e.g., Zhang et al. 2002).

5. Estimate the shear-induced building settlement (*Ds*) due to liquefaction below the building using Equation 5.9, which is repeated below:

$$Ln(Ds) = c1 + 4.59 * Ln(Q) - 0.42 * Ln(Q)^2 + c2 * LBS + 0.58 * Ln\left(Tanh\left(\frac{HL}{6}\right)\right) - 0.02 * B + 0.84 * Ln(CAVdp) + 0.41 * Ln(Sa1) + \varepsilon \quad (5.9)$$

where *Ds* is in mm, *c1* = -7.48 and *c2* = 0.014 for *LBS* > 16, and *c1* = -8.35 and *c2* = 0.072 for *LBS* ≤ 16. *LBS* is calculated with Equation 5.7. *HL* is the cumulative thickness of layers with $FS_L \leq 1.0$ in the units of m. *Q* is the foundation contact pressure in the units of kPa, and *B* is its width in m. The intensity measures, CAV_{dp} in units of *g*-s and S_a1 in units of *g*, are estimated for free-field ground motions at the site. ε is a normal random variable with zero mean and 0.50 standard deviation in *Ln* units.

6. Estimate the total liquefaction-induced building settlement (*Dt*) by adding each component of settlement (i.e., results of steps 3, 4, and 5):

$$Dt = De + Dv + Ds \quad (5.10)$$

7. Use engineering judgment. There are important limitations of the proposed simplified procedure. Equation 5.9 was developed using a subset of potential building configurations and earthquake ground motions. The structures considered are regular (e.g., uniformly loaded) and have heights no greater than 24 m. The non-liquefiable crust does not have defects (e.g., utility trenches that could provide preferential paths for ejecta). Some volumetric-induced liquefaction building settlement occurs during strong shaking, but this procedure categorizes all of the settlement that occurs during strong shaking as being due to the shear-induced mechanism. Case histories and previous experience are important to consider in developing the final engineering assessment of this complex problem. For important projects, perform nonlinear dynamic SSI effective stress analyses to refine estimates of liquefaction-induced building settlement and to gain insight (Bray et al. 2017).

5.9 VALIDATION OF PROPOSED SIMPLIFIED PROCEDURE

5.9.1 Comparison with centrifuge experimental results

Results from centrifuge tests performed by Dashti (2009), Allmond and Kutter (2012), Zupan et al. (2013), and Hayden et al. (2014) are used to compare the estimates from Equation 5.9 with the measured liquefaction-induced settlements during strong shaking in the centrifuge tests. Nonlinear total stress site response analyses with the *GQ/H* model implemented in *Deepsoil* V6.1 and the ground motions used as input excitations for the experiments were used to estimate the ground motion parameters at the model surface. Liquefaction triggering analyses using the Boulanger and Idriss (2016) procedure were performed to estimate the safety factor for liquefaction triggering, and the Zhang et al. (2004) procedure was used to estimate the cyclic shear strains induced in the soil profile. With this information, *LBS* was estimated for each case using Equation 5.7. A total of 102 cases were analyzed. Figure 5.12 shows the comparison between the centrifuge experiments results and the estimated settlements, including 24 cases where the settlement is small (i.e., < 11 mm). Most of the cases are within the lines with slopes 1H:2V and 2H:1V. Thus, the proposed equation produces reasonable results when compared to the centrifuge tests considered in this study.

5.9.2 Comparison with observations from field case histories

The performance of the proposed methodology has been tested for several well documented field cases histories after the Kocaeli earthquake (17 AUG 1999 M_w 7.5) and the 2010-2011 Canterbury earthquake sequence (Christchurch event: 22 FEB 2011 M_w 6.2, Darfield event: 4 SEP 2010 M_w 7.1, and the June event: 13 JUN 2011 M_w 6.0). Table 5.3 shows the comparison of observed shear-induced liquefaction building settlements for nineteen field case histories with the values estimated using the proposed simplified procedure. The observed shear-induced building settlements (D1-CPT1 and D2-CPT2) were measured or estimated from well documented field case histories near the location of two CPTs (i.e., CPT1 and CPT2). The data from those same CPTs, the free-field ground motion *IMs*, and the building characteristics (i.e., *Q* and *B*) were used to estimate the 16% and 84% values of shear-induced building settlement using Equation 5.9 (i.e., a range of expected settlement is provided).

The Canterbury earthquake sequence ground motion parameters S_a1 and CAV_{dp} were estimated from the ground motion recordings within the Christchurch Central Business district (CBD). The average of the ground motion parameters calculated from the ground motion recordings was used given the close proximity to the buildings to the recording sites and their similar soil conditions. For the considered cases after the Kocaeli earthquake, S_a1 was estimated from the Abrahamson et al. (2013) GMPE for the Turkey region and CAV_{dp} from the Campbell and Bozorgnia (2011) GMPE. LBS is estimated from Equation 5.7 using available CPT results. For the shear strain potential estimation of the site, the Zhang et al. (2004) procedure is used where the safety factor against liquefaction is estimated from Boulanger and Idriss (2016) and the "clean sand" equivalent relative density is estimated from a combination of three correlations presented in Idriss and Boulanger (2008), Kulhawy and Mayne (1990) and Jamiolkowski et al. (2001) with 0.4, 0.3 and 0.3 weights, respectively.

The FTG-7 building was a 7-floor steel frame structure that was supported on reinforced concrete (RC) strip footings. Details of the ground conditions, building, and its performance during the Canterbury earthquake sequence are provided in Zupan (2014) and Bray et al. (2014). Luque and Bray (2017) performed SSI analyses to estimate numerically the shear-induced liquefaction settlements in the building using the PM4Sand model. Table 5.3 values for this case are their best assessment of the observed shear-induced liquefaction building settlements.

The shear-induced building settlements due to liquefaction from the Christchurch earthquake are estimated using Equation 5.9 to be 100-270 mm with a median estimate of 160 mm for the SW corner (CPT1) whereas the best estimate from the field case history was about 150 mm. For the SE corner (CPT2), the shear-induced building settlement was about 170-210 mm, whereas the estimation based on the proposed simplified procedure was 120 to 310 mm with a median estimate of 190 mm. For the NW corner (CPT3; Footnote 3 of Table 5.3), the estimated shear settlements are in the range of 90 to 240 mm with a median estimate of 150 mm whereas the field values were in the range of 90 to 130 mm. For the Darfield event, the proposed procedure's estimates are greater than the negligible observed displacements, but the estimates are small (on the order of 50 mm for the median value). The conservatism in the estimate of liquefaction-induced building settlement for the Darfield event has been also observed with the application of simplified liquefaction triggering procedures for this event (Bray et al. 2014). For the June event, the median estimates are about 40-60 mm whereas the best estimate of observed settlements are 10-20 mm for the NW corner and 30-40 mm for the SE corner. Luque and Bray (2017) report measured total building settlements over the 2010-2011 Canterbury earthquake sequence for the NW and SE corners of the building based on field surveys and LiDAR data. The total settlements are reported

as 400-450 mm for the NW corner and 550-600 mm for the SE corner. Using the proposed procedure to estimate shear-induced settlement, using Luque and Bray (2017) to estimate ejecta-induced settlement, and using Zhang et al. (2002) to estimate volumetric-induced settlement, the estimated total liquefaction-induced building settlements over the Canterbury earthquake sequence are 340-790 mm for the NW corner and 440-970 mm for the SE corner. The estimated values are reasonable considering the conservatism of the liquefaction triggering assessments of the Darfield and June events.

The FTG-4 was a four-story RC framed structure located adjacent to the FTG-7 Building. Details of the site conditions, building, and its performance during the 2010-2011 Canterbury earthquake sequence are provided in Zupan (2014) and Bray et al. (2014). During the Christchurch event, more settlement was observed on the west side of the building compared to its east side. The ground floor slab settled approximately 160 mm more at the building's northwest corner than at its northeast corner. The difference of volumetric settlements estimated by Zupan (2014) between the west and east sides is around 100 mm. Based on the proposed simplified liquefaction-induced building settlement procedure, shear-induced settlements on the east side (CPT1 in Table 5.3 for the SE corner and CPT2 in Table 5.3 for the NE corner) are about 100 to 120 mm (median values). The median shear-induced settlement on the west side can be estimated from CPT2 in FTG7 (Table 5.3), and it is about 190 mm. Thus, the differential shear-induced settlement is on the order of 70 to 90 mm. The median estimate of the total differential settlements is on the order of 170 to 190 mm, which is only slightly above the reported differential settlement of 160 mm.

The CTUC Building was a six-story RC frame structure with RC core walls and block in-fill walls with its roof supported by steel framing. Details of the site conditions, building, and its performance during the Canterbury earthquake sequence are provided in Zupan (2014) and Bray et al. (2014). Luque and Bray (2017) estimated the shear-induced liquefaction building settlements presented in Table 5.3. Their best estimates of the shear-induced settlements for the Christchurch earthquake are 100-200 mm for the SE corner and 60 mm for the NE corner. Using the proposed simplified procedure, these estimates are 110-290 mm with a median value of 180 mm for the SE corner (CPT1 in Table 5.3) and 40-120 mm with a median estimate of 70 mm for the NE corner. The total building pressure over its full width and the contact pressure and width for individual footings were used in two calculations with Equation 5.9, and the results averaged because the footings of this building are poorly connected. In terms of total settlements, using the procedure proposed in this study, the Zhang et al. (2002) procedure for volumetric settlements and the sediment ejecta settlement estimates from Luque and Bray (2017), the estimated total settlements are in the range of 330 to 690 mm for the SE corner and 140 to 320 mm for the NE corner. The observed total settlements from Luque and Bray (2017) are 320 to 600 mm for the SE corner and 160 to 260 mm for the NE corner.

For the Darfield event, the displacements estimated with the proposed simplified procedure are conservative with a median estimate of 80 mm for the SE corner and 10 mm for the NE corner. The estimates correspond to minor levels of settlements, but the observed level of settlements during the Darfield event was considered negligible. As mentioned previously, simplified liquefaction triggering procedures were generally conservative for the Darfield event in the CBD. For the June event the median estimated settlements are about 70 mm for the SE corner and 10 mm for the NE corner. These estimations can be considered consistent with the minor level of settlements observed after the June event. It is also important to mention that the soils that liquefied after the June event had already liquefied extensively during the Christchurch earthquake. Thus,

their age and fabric were likely more susceptible to liquefaction triggering and liquefaction-induced building settlement in the June 2011 event.

The CTH building is located in the northwest quadrant of the CBD, with the meandering Avon River to its immediate south. The facility is composed of several independent structures. This study refers to the auditorium located at the west end of the facility. The foundation system for the auditorium consists of an outer ring of rectangular shallow RC spread footings and an inner ring of square shallow RC spread footings. Details of the site conditions, building, and its performance during the Canterbury earthquake are provided in Zupan (2014). The field observations at the CTH building are complicated by lateral spreading-induced settlements. The entire facility moved laterally towards the river with decreasing severity of lateral movements to the north of the building. Luque (2017) provides estimates of the observed settlement based on LiDAR data for the CTH building, field measurements, and advanced SSI analyses. Table 5.3 shows their best estimate of the shear-induced liquefaction building settlement. For the Christchurch event, the observed settlements are 50-210 mm for the southern part of the building and 40-140 mm for its northern part. Using the proposed simplified procedure (e.g., Equation 5.9), the shear-induced settlements are estimated to be 70 to 180 mm with a median estimate of 110 mm for the southern part of the building and 40 to 120 mm with a median estimate of 70 mm for the northern part of the building.

For the Darfield event, the median estimates of the shear-induced settlements for the CTH auditorium are about 50 mm and 35 mm for the south and north sides of the building, respectively. Similar to previous cases for the Darfield earthquake, these estimates are greater than the observed settlements of 0-20 mm, but they do correspond to the minor observed building settlements. For the June event, the median estimates of the shear induced settlements are about 40 mm and 20 mm for the north and south of the building, respectively. The best estimate of the observed settlements is 30 mm for the south side and 20 mm for the north side. In terms of total settlements (from LiDAR data), the observed settlements are in the range of 350 to 800 mm for the south part of the building and 250 to 550 mm for the north part of the building (Luque 2017). Using the proposed simplified procedure for shear-induced settlements, the Zhang et al. (2002) procedure for volumetric settlements, and the sediment ejecta and lateral spreading settlement estimations from Luque (2017), the estimated total settlements are 410-850 mm and 260-560 mm for the southern and northern parts of the building, respectively.

The PWC building was a 21-story reinforced-concrete (RC) structure with one-story basement. The basement foundation consisted on a RC mat with variable thickness. Details of the site conditions, building, and its performance during the Canterbury earthquake sequence are provided in Zupan (2014). Luque (2017) provide estimations of the observed total and shear-induced settlements based on LiDAR data, field measurements, and advanced SSI analyses. Their estimates of shear-induced building settlement are provided in Table 5.3. For the Christchurch event, the observed settlements are 80-140 mm for the southern part of the building and 30-70 mm for the northern part of the building. Using the proposed simplified procedure, the shear-induced liquefaction building settlements are 40 to 110 mm with a median estimate of 70 mm for the southern part of the building, and 30 to 80 mm with a median estimate of 50 mm for the northern part of the building. The estimates for the settlements in the southern part are in the lower range of the observed settlements possibly due to the presence of a thick gravel layer below the foundation (Zupan 2014).

For the Darfield event, the median estimates of the shear-induced liquefaction settlements of the PWC building are approximately 20 mm and 10 mm for the southern and northern parts of the

building, respectively. The observed shear-induced settlements are in the range of 0 to 10 mm. For the June event, the median estimated shear-induced building settlements are 10 mm for both parts of the building. The observed shear-induced building settlements are in the range of 0 to 20 mm. In terms of total settlements from LiDAR data, the estimated settlements are 160-350 mm for the southern part of the building and 130-300 mm for the northern part of the building (Luque 2017). Using the proposed simplified procedure for shear-induced settlements, the Zhang et al. (2002) procedure for volumetric-induced settlements, and the sediment ejecta and lateral spreading settlement estimations from Luque (2017), the estimated total settlements in this study are 140 to 340 mm and 140 to 300 mm for the southern and northern parts of the building, respectively.

The SA Building was located about 200 m northwest of the Avon River and was a two-story RC frame structure with concrete infilled walls, interior timber framed walls, and exterior strip footings. Details of the soil conditions, building, and its performance during the Canterbury earthquake sequence are described in Zupan (2014) and Bray et al. (2014). According to Bray et al. (2014), the building settled approximately 250 mm at its southeast corner and approximately 100–200 mm at its northwest corner largely due to shear-induced punching and ejecta-induced mechanisms. In the southern part of the building (CPT1, Table 5.3), the estimated shear-induced settlements for the Canterbury earthquake sequence are about 120-310 mm with a median estimate of 190 mm; whereas, for the northern part of the building (CPT2, Table 5.3), the estimated shear-induced building settlements are 15-50 mm. The volumetric-induced settlements for the Canterbury earthquake sequence are estimated by Bray et al. (2014) as 170 mm and 10 mm for the southern and northern parts of the building, respectively.

There was sediment ejecta observed around the SA building perimeter during the Darfield, Christchurch, and June events, with considerable more ejecta found after the Christchurch event. Hence, it is likely the sediment ejecta mechanism is also important for this case history. This is consistent with the existence of a shallow liquefiable layer directly beneath the building foundation. Considering this mechanism, a sediment ejecta-induced settlement of 70 to 150 mm is estimated for the southern part of the building based on similar cases in Christchurch (Luque and Bray 2017). For the northern part of the building, the estimate is 30 to 90 mm. Considering all mechanisms, the total estimated settlements are 360 to 630 mm and 55 to 150 mm for the southern and northern parts of the building, respectively. Given the uncertainties in this case history, the estimations are considered reasonable.

Buildings C2 and C3 are located in Adapazari, Turkey (Bray et al. 2004). The height, width, and length of these regular structures are approximately 13.7 m, 19.5 m, and 20.1 m, respectively. The structural design and construction of these buildings are similar, but they have different soil conditions below their foundation. Details of the site conditions, buildings, and their performance during the 1999 Kocaeli earthquake are provided in Bray et al. (2004) and Sancio (2003). The observed settlements for these buildings are reported as 350 mm for Building C2 and negligible for C3. For Building C2, the median estimate of shear-induced settlement is 150 mm with a range from 90 to 250 mm. A significant part of the observed building settlement was due to sediment ejecta surrounding the edges of the building (i.e., about 50%). Accordingly, the observed shear-induced settlement is estimated to be about 175 mm (i.e., about half of the observed punching building settlement), which is consistent with that estimated. For Building C3, the estimated shear-induced settlement has a median value of 40 mm with a range of 20 to 70 mm. Thus, in this case, the shear-induced building settlement is overestimated slightly, but as the estimated building settlement is relatively minor, the comparison is judged to be reasonable.

Building F1 is a 4-story, reinforced concrete apartment building located in Adapazari (Bray et al. 2004). The foundation of this structure consists of a 400-mm thick RC mat strengthened with 1.20-m deep grade beams. Details of the soil conditions, building, and its performance during the Kocaeli earthquake are provided in Bray et al. (2004) and Sancio (2003). The observed building punching settlement, which was due to primarily shear-induced and ejecta-induced settlement mechanisms, is reported to be 900 mm. The median estimate of shear-induced building settlement is 370 mm with a range from 220 to 600 mm. Given the presence of liquefiable soils directly beneath the foundation and the large amount of sediment ejecta observed at the site, it is estimated that about half of the measured settlement was due to sediment ejecta and half due to shear-induced settlement. Thus, the median estimate of 370 mm compares well to the observed settlement estimate of about 450 mm.

5.10 ILLUSTRATIVE EXAMPLE

The proposed simplified liquefaction-induced building settlement procedure is applied to an example problem to illustrate its use. The building selected to illustrate the procedure is the FTG-7 building, which was considered as one of the field case histories described in the previous section. The liquefaction-induced building settlement is assessed for the Christchurch earthquake. Figure 5.13 shows the plan view of the building and Section A-A' with the soil profile under the building. Liquefaction-induced settlements are estimated for the southwest corner of the building (from CPT Z1-B3 shown in Figure 5.13) and for the southeast corner of the building (from CPT Z1-B4 shown in Figure 5.13).

The groundwater depth was estimated to be 2.0 m for the Christchurch event. As described in Luque and Bray (2017), there is a 1-1.5-m thick fill at the ground surface, which is underlain by a shallow sandy silt/silty sand (SM/ML) layer with variable fines content (FC) and soil behavior type index (I_c) generally between 2.2–2.4, which extends down to a depth of 7–8.5 m. Below this layer, a medium dense sand (SP/SM, Ic ≈ 1.8 and 2.1) is found, which extends down to a depth of around 14-16.5 m. The loose SM/ML layer below the groundwater table and soil units in the SP/SM layer are likely to liquefy when strongly shaken. Below the medium dense sand, very dense sand (SP) is encountered. The CPT typically reaches refusal in this unit. The estimated depth for the dense Riccarton Gravel unit is 22 m based on a soil boring near the SE corner of the FTG-7 building. A 1-2-m thick clayey silt (ML/MH) layer with some organics overlies the Riccarton Gravel.

PGA and S_a1 are estimated from an appropriate GMPE. The NGA-West2 GMPEs are appropriate for shallow crustal earthquake events such as the Christchurch earthquake. Excel files with the implementation of these GMPE can be downloaded from: http://peer.berkeley.edu/ngawest/nga_models.html. CAV_{dp} is estimated from the Campbell and Bozorgnia (2011) GMPE, which has a similar set of input parameters as the NGA-West2 GMPEs. With the earthquake parameters (e.g., rupture distance, magnitude, and fault type) and site conditions (e.g., V_{S30}) appropriate for this site and the Christchurch event, median values of *PGA*, S_a1, and CAV_{dp} are estimated. In this case, nearby ground motion recordings are available, so the values of *PGA* = 0.45 g, S_a1 = 0.90 g and CAV_{dp} = 1.00 g-s from these recordings are used. The foundation system of stiff footings connected with stiff grade beams is robust so it is judged to respond as a unit. Hence, the foundation width (B) is 29 m. Its contact pressure (Q) is about 100 kPa (Luque and Bray 2017).

Following the simplified procedure for estimating liquefaction-induced building settlement delineated in Section 8 of this chapter, these steps are carried out:

1. The safety factor against liquefaction triggering (FS_L) is calculated for the site conditions shown in Figure 5.13 using the CPT-based Boulanger and Idriss (2016) procedure. The colored soil layers have FS_L values less than 1.0. The thickness of the liquefiable soil layers (*HL*) are estimated as the summation of the layers with safety factor against triggering lesser than 1.0. *HL* is estimated to be approximately 12 m for the SW corner and 13 m for the SE corner of the building.
2. The post-liquefaction bearing capacity safety factor (*FS*) is calculated to be 1.1 using the Meyerhof and Hanna (1978) method with a post-liquefaction residual strength of the liquefied soil layer of 12 kPa (based on Idriss and Boulanger 2008) and using an average shear strength of the non-liquefied crust layer of 35 kPa. As the post-liquefaction bearing capacity *FS* is close to 1.0, significant liquefaction-induced building settlement may occur. The calculation is continued to develop a rough estimate of the potential liquefaction-induced building settlement for this case.
3. The *LSN* value at the SW corner is 41 and *LPI* is 34; whereas at the SE corner, *LSN* is 45 and *LPI* is 40. Considering the relatively high *LSN* and *LPI* values at the SW and SE corners of the building and considering the Ishihara (1985) ground failure design chart, ejecta are assumed to occur near both corners of the building. An average estimate of about 60 mm of sediment ejecta-induced settlement (*De*) is assumed to occur with an estimated range of 40 mm to 80 mm, based on observations after case histories (i.e., Bray et al. (2014), and Luque and Bray 2014).
4. The 1D post-liquefaction volumetric-induced building settlement (*Dv*) of the soil profile is estimated using the Zhang et al. (2002) procedure. *Dv* is estimated to be 170-310 mm for the SE corner and 150-290 mm for the SW corner of the building.
5. LBS is estimated from Equation 5.7 using the Zhang et al. (2002) procedure with the FSL values for each layer estimated previously. The "clean sand" equivalent relative density is estimated from a combination of three correlations presented in Idriss and Boulanger (2008), Kulhawy and Mayne (1990), and Jamiolkowski et al. (2001) with 0.4, 0.3 and 0.3 weights, respectively. *LBS* is estimated as 71 and 82 for the SW and SE corners of the building, respectively. The shear-induced building settlement (*Ds*) due to liquefaction is estimated using Equation 5.9 with these input parameters for the SW corner calculation: S_a1= 0.90 g, CAV_{dp} = 1.0 g-s, *B*= 29 m, *Q*= 100 kPa, *HL*= 12 m, and *LBS*= 71, and for the SE corner calculation: S_a1= 0.90 g, CAV_{dp}= 1.0 g-s, *B*= 29 m, *Q*= 100 kPa, *HL*= 13 m, and *LBS*= 82. The estimated shear-induced building settlements (*Ds*) are 100-270 mm with a median estimate of 160 mm for the SW corner and 120-310 mm with a median estimate of 190 mm for the NE corner.
6. The median estimate of the total liquefaction-induced building settlement (*Dt*) of the SW building corner is:

Dt = *De* + *Dv* + *Ds* = 60 mm + 220 mm + 160 mm = 440 mm, with *Dt* ranging from 290 mm to 640 mm.

The median estimate of the total liquefaction-induced building settlement of the SE building corner is:

Dt = *De* + *Dv* + *Ds* = 60 mm + 240 mm + 190 mm = 490 mm, with *Dt* ranging from 330 mm to 700 mm.

7. Considering the results of the analyses presented above, the estimated total liquefaction-induced building settlements of the SW and SE corners of the FTG-7 building as a result of the 2011 Christchurch earthquake are 290-640 mm and 330-700 mm, respectively. The estimated median differential settlement across the southern edge of the building is 50 mm (i.e., 490 mm – 440 mm). A survey of the ground floor of the FTG-7 building measured about 30 mm of

differential settlement across its southern edge (Zupan 2014; Luque and Bray 2017). The estimated total building settlements are also consistent with those observed (e.g., the total liquefaction-induced settlement at the SE corner was judged to be 380-600 mm; Luque and Bray 2017). The simplified procedure for estimating liquefaction-induced building settlement provides estimated values of settlement that are consistent with the observed seismic performance of the FTG-7 building.

5.11 CONCLUSIONS

A simplified procedure for estimating liquefaction-induced building settlements is proposed. It is based on the results of over 1,300 nonlinear dynamic SSI effective stress analyses using the program *FLAC* with the robust *PM4Sand* model. It has been validated using centrifuge experiments, the results of SSI analyses by other researchers, and nineteen field case histories.

The results of the large number of nonlinear dynamic analyses performed in this study exhibit important trends that highlight the importance of several parameters. The standardized cumulative absolute velocity and 5%-damped one-second spectral acceleration capture optimally the earthquake ground motion characteristics. Arias intensity is also a useful ground motion parameter, but the GMPEs used to estimate it has higher aleatory variability than those used to estimate standardized cumulative absolute velocity.

The relative density and thickness of the liquefiable layer are important soil profile parameters. The influence of the site conditions could largely be captured by a new liquefaction-induced building settlement index parameter referred to as *LBS*. This parameter is based on the work of Ishihara and Yoshimine (1992) as presented in the Zhang et al. (2004) CPT-based lateral spreading procedure that focuses on earthquake-induced shear strain. *LBS* can be calculated readily using the Zhang et al. (2004) equations that estimate the maximum shear strain induced cyclically as a function of the relative density of the liquefiable layer and its safety factor against liquefaction triggering. Building contact pressure and width are important structural properties.

The primary mechanisms of liquefaction-induced settlements of structures are ejecta-induced, shear-induced, and volumetric-induced ground deformation. Regression analyses of the results of the nonlinear dynamic SSI effective stress analyses are used to develop the form of the equation and its coefficients (i.e., Equation 5.9) to estimate shear-induced liquefaction building settlement. The form the equation is also based on widely accepted foundation engineering and earthquake engineering concepts. There are methods already available to capture the volumetric-induced settlement mechanism (e.g., Zhang et al. 2004). The continuum based analyses cannot capture the loss of ground due to the development of sediment ejecta. Hence, case histories and judgment should be used to evaluate the settlement potential from the ejecta-induced building settlement mechanism.

The proposed simplified method is applied to several field case histories and shown to provide estimates of settlement consistent with those observed. It also captures well the results of centrifuge experiments and provides estimates of building settlement consistent with those calculated by Karimi and Dashti (2017b) who performed comprehensive SSI analyses with a different computational program, a different soil constitutive model, and a different suite of earthquake ground motions.

The proposed simplified procedure provides a rational approach for estimating liquefaction-induced building settlement. The estimated values are consistent with those calculated using more advanced analyses for general conditions. However, the proposed procedure is a simplification of

an inherently complex phenomenon. The proposed procedure is based on the results of dynamic SSI effective stress analyses performed for a particular suite of earthquake ground motions (i.e., shallow crustal earthquakes) and a limited set of building and ground conditions, which do not have highly variable soil conditions nor highly irregular building configurations. Thus, care is warranted in its use, especially for cases not considered in this study. Further research and calibrations are warranted. Moreover, the use of the proposed simplified procedure should be complemented with the results of project-specific nonlinear dynamic SSI effective stress analyses on important projects.

Table 5.1. Parameters Considered in Sensitivity Study

Parameter	Description	Values Used	Baseline Case
HC	non-liquefiable layer thickness (m)	1, 2, 4, 6	2
HL	liquefiable layer thickness (m)	1, 2, 3, 6, 12, 18	3
HB	thickness below liquefiable layer (m)	20-HL-HC	15
D_r	liquefiable layer relative density (%)	35, 50, 60, 75, 90	50
B	building width (m)	6, 12, 24	12
H	building height (m)	6, 12, 24	12
Q	foundation contact pressure (kPa)	20, 40, 80, 160, 240	80

Table 5.2. Earthquake Ground Motions Used in the SSI Analyses (12 Primary Earthquake Ground Motion Records Are Listed First; NGA# Is from PEER NGA-West2 Database)

#	NGA#	arthquake	Site/Component	M_w	R_{rup} (km)	Amplitude Scale Factor
1	4455	Montenegro	Herceg Novi/000	7.1	26	2.2
2	6928	Darfield	LPCC/080	7.0	26	1.0
3	1787	Northridge	LA 00/000	7.1	10	1.5
4	1111	Kobe	Nishi-Akashi/000	6.9	7	1.25
5	164	Imperial V	Cerro Prieto/147	6.5	15	1
6	1787	Hector Mine	Hector/000	7.1	10	1
7	2111	Denali	R109/090	7.9	43	3
8	830	Mendocino	Shelter Cove Airport/000	7.0	29	1
9	952	Northridge	Beverly Hills/035	6.7	18	1.3
10	1512	Chi-Chi	TCU/078	7.6	8	1
11	164	Imperial V	Cerro Prieto/147	6.5	15	2
12	1787	Hector Mine	Hector/000	7.1	10	1.5
13	3750	Mendocino	Loleta Fire Station/270	7.0	24	1
14	448	Morgan Hill	Anderson Dam/340	6.2	3	1
15	6928	Darfield	LPCC/170	7.0	26	2
16	1012	Northridge	LA 00/090	6.7	19	3
17	1111	Kobe	Nishi-Akashi/090	6.9	7	2.4
18	1162	Kocaeli	Goynuk/000	7.5	32	3
19	164	Imperial V	Cerro Prieto/237	6.5	15	2
20	1787	Hector Mine	Hector/090	7.1	10	2
21	265	Victoria	Cerro Prieto/045	6.3	14	1
22	753	Loma Prieta	Corralitos/000	6.9	4	1
23	830	Mendocino	Shelter Cove Airport/000	7.0	29	2
24	952	Northridge	Beverly Hills/125	6.7	18	2.3
25	690	Whittier N	San Gabriel/180	6.0	15	1
26	1612	Duzce	Lamont 1059/000	7.1	4	1
27	26220	Chi-Chi	TCU071/000	6.2	17	1
28	33	Parkfield	Temblor pre/205	6.2	16	1
29	3943	Tottori	SMN015/000	6.6	9	1
30	4132	Parkfield	Parkfield/000	6.0	5	1
31	4457	Montenegro	Ulcinj/000	7.1	4	1
32	4477	L'Aquila	Gran Sasso /000	6.3	6	1
33	1078	Northridge	Santa Susana Ground/360	6.7	17	1
34	125	Friuli	Tolmezzo/000	6.5	16	1
35	1618	Duzce	Lamont 531/531	7.1	8	1
36	587	NZ-02	Matahina Dam/083	6.6	16	1

Table 5.3. Case history parameters and observed and estimated shear-induced liquefaction building settlement

Case	*Building*	*EQ*[1]	*B*	*Q*	*Sa1*	*CAVdp*	*HL*[2]*(m)*		*LBS*[2]	
			(m)	*(kPa)*	*(g)*	*(g-s)*	*CPT1*	*CPT2*	*CPT1*	*CPT2*
1[3]	*FTG7*	*C*	*29*	*100*	*0.9*	*1.0*	*12.0*	*13.0*	*71*	*82*
2[3]	*FTG7*	*D*	*29*	*100*	*0.3*	*0.9*	*3.5*	*4.5*	*51*	*65*
3[3]	*FTG7*	*J*	*29*	*100*	*0.5*	*0.6*	*4.0*	*5.0*	*50*	*61*
4	*FTG4*	*C*	*15*	*60*	*0.9*	*1.0*	*10.0*	*10.0*	*62*	*51*
5	*CTUC*	*C*	*20*[6]	*70*[6]	*0.9*	*1.0*	*5.0*	*6.0*	*57*	*10*
6	*CTUC*	*D*	*20*[6]	*70*[6]	*0.3*	*0.9*	*3.0*	*1.0*	*47*	*2*
7	*CTUC*	*J*	*20*[6]	*70*[6]	*0.5*	*0.6*	*4.0*	*1.5*	*47*	*1*
8	*CTH*	*C*	*47*	*150*	*0.9*	*1.0*	*10.0*	*6.0*	*52*	*30*
9	*CTH*	*D*	*47*	*150*	*0.3*	*0.9*	*5.0*	*3.0*	*40*	*20*
10	*CTH*	*J*	*47*	*150*	*0.5*	*0.6*	*5.0*	*3.0*	*39*	*20*
11	*PWC*	*C*	*38*	*210*	*0.9*	*1.0*	*6.0*	*4.0*	*14*	*11*
12	*PWC*	*D*	*38*	*210*	*0.3*	*0.9*	*2.0*	*1.0*	*8*	*5*
13	*PWC*	*J*	*38*	*210*	*0.5*	*0.6*	*2.0*	*1.0*	*6*	*4*
14	*SA*	*C*	*1.5*	*80*	*0.9*	*1.0*	*7.0*	*0.5*	*35*	*10*
15	*SA*	*D*	*1.5*	*80*	*0.3*	*0.9*	*3.0*	*0.25*	*12*	*2*
16	*SA*	*J*	*1.5*	*80*	*0.5*	*0.6*	*3.5*	*0.3*	*10*	*2*
17	*C2*	*K*	*20*	*80*	*0.5*	*1.6*	*5.0*	*-*	*68*	*-*
18	*C3*	*K*	*20*	*80*	*0.5*	*1.6*	*1.5*	*-*	*15*	*-*
19	*F1*	*K*	*8*	*75*	*0.7*	*1.7*	*13.0*	*-*	*90*	*-*

Case	*FS*	*Observed Ds (mm)*[4,5]		*Estimated Ds -CPT1(mm)*		*Estimated Ds -CPT2(mm)*	
		D1	*D2*	*D16*	*D84*	*D16*	*D84*
1[5]	*1.1*	*150*	*170-210*	*100*	*270*	*120*	*310*
2[5]	*-*	*-*	*0*	*30*	*80*	*40*	*120*
3[5]	*-*	*-*	*30-40*	*30*	*70*	*30*	*90*
4	*1.5*	*-*	*110-150*	*70*	*190*	*60*	*160*
5	*0.9*	*100-200*	*60*	*110*[6]	*290*[6]	*40*[6]	*120*[6]
6	*-*	*-*	*-*	*50*[6]	*140*[6]	*10*[6]	*20*[6]
7	*-*	*-*	*-*	*40*[6]	*120*[6]	*10*[6]	*20*[6]
8	*0.8*	*50-210*	*40-140*	*70*	*180*	*40*	*120*
9	*-*	*0-20*	*0-20*	*30*	*70*	*20*	*50*
10	*-*	*10-30*	*20-40*	*20*	*60*	*10*	*40*
11	*1.1*	*80-140*	*30-70*	*40*	*110*	*30*	*80*
12	*-*	*0-10*	*0-10*	*10*	*30*	*10*	*20*
13	*-*	*0-20*	*0-20*	*10*	*20*	*0*	*10*
14	*0.6*	*100-180*	*50-100*	*80*	*220*	*10*	*40*
15		*-*	*-*	*20*	*50*	*2*	*6*
16		*-*	*-*	*20*	*40*	*3*	*6*
17	*0.7*	*175*	*-*	*90*	*250*	*-*	*-*
18	*1.7*	*0*	*-*	*20*	*70*	*-*	*-*
19	*0.6*	*450*	*-*	*220*	*600*	*-*	*-*

Notes:

1. C= Christchurch M 6.2 EQ, D= Darfield M 7.1 EQ, J= June M 6.0 EQ, and K= August 1999 Kocaeli *EQ*.
2. CPT data from Zupan (2014) and Bray et al. (2004) used for estimation of *HL* and *LBS*. For FTG7: CPT1=Z1B3, CPT2=Z1B4. For FTG4: CPT1=Z1-3, CPT2=,Z1-8. For CTUC: CPT1=Z4-5, CPT2=Z4-7. For CTH: CPT1=Z5-11, CPT2=Z5-8. For PWC: CPT1=Z2-21, CPT=Z2-19. For SA: CPT1=Z8-6, CPT2=Z8-14. For C2: CPT1=CPTC4. For C3: CPT1=CPTC1. For F1: CPT1=CPTF1.
3. Two additional CPT were considered for FTG7 building, with CPT data from Zupan (2014). CPT3=Z1-B1 in the NW corner and CPT4=Z1-B2 in the NE corner. HL ~12m for CPT3 and CPT4 for the C event, HL ~3.5m for CPT3 and CPT4 for the D event, HL ~4.0m for CPT3 and CPT4 for the J event. For CPT3, LBS is 64, 50 and 47 for the C, D and J events, respectively. For CPT4, LBS is 76, 45 and 43 for the C, D and J events, respectively.
4. Estimates of shear-induced settlements are available for FTG7, FTG4, CTUC, CTH, PWC. Shear-induced settlements estimated for SA, C1, C2 and F1. For FTG 7 from Luque and Bray (2017); for FTG4 from Bray et al. (2014); for CTUC from Luque and Bray (2017); for CTH from Luque (2017); for PWC from Luque (2017); for SA from Bray et al. (2014): for C2, C3, F1 from Bray et al. (2004).
5. Observed shear-induced settlements from Luque and Bray (2017) for FTG7 building at CPT3 are from 90 to 130 mm for C event, 0 mm for D event and from 10 to 20 mm for J event. Estimated shear-induced settlements at CPT3 are from 90 to 240 mm for C event, from 30 to 80 mm for D event and from 30 to 70 mm for J event. At CPT4 shear-induced estimated settlements are from 110 to 290 mm for C event, from 30 to 80 mm for D event, and from 20 to 60 mm for J event.
6. The individual footings of CTUC are not tied together well; settlements were estimated as the average of: 1) B=20 m, Q=70 kPa, and 2) B=1 m, Q=200 kPa.

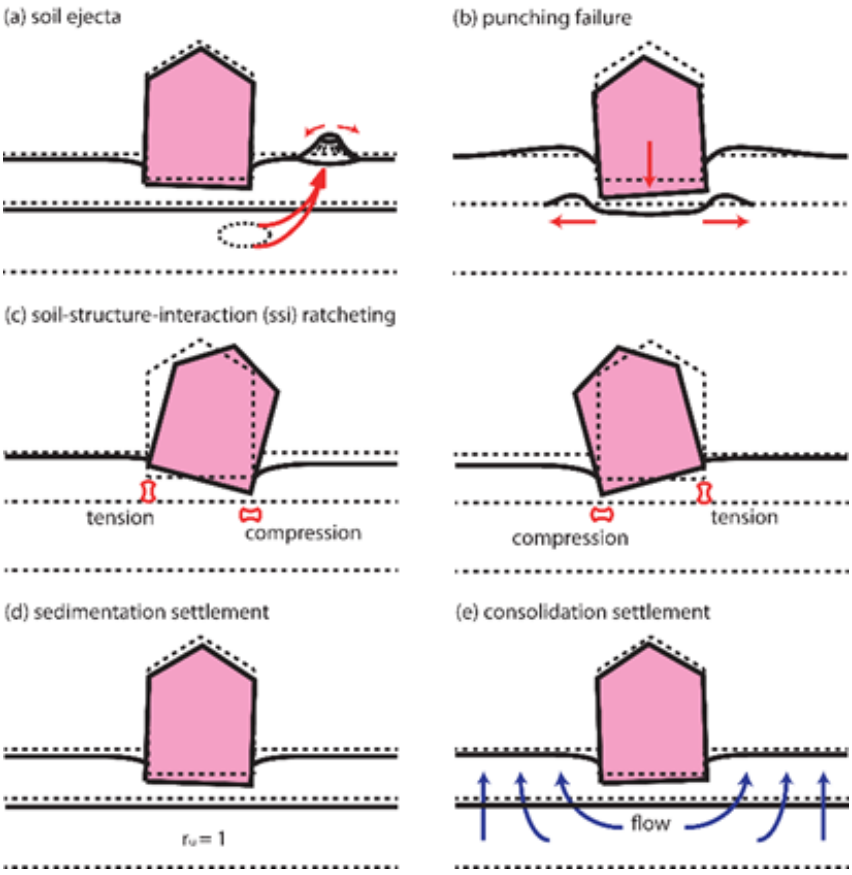

Figure 5.1. Liquefaction-induced building displacement mechanisms: (a) ground loss due to soil ejecta; shear-induced settlement from (b) punching failure, or (c) soil-structure-interaction (SSI) ratcheting; and volumetric-induced settlement from (d) sedimentation or (e) post-liquefaction reconsolidation (modified from Bray and Dashti 2014).

Figure 5.2. Differing responses of pile-supported building (left) and shallow-founded building (right) relative to free-field ground (from Ashford et al. 2011).

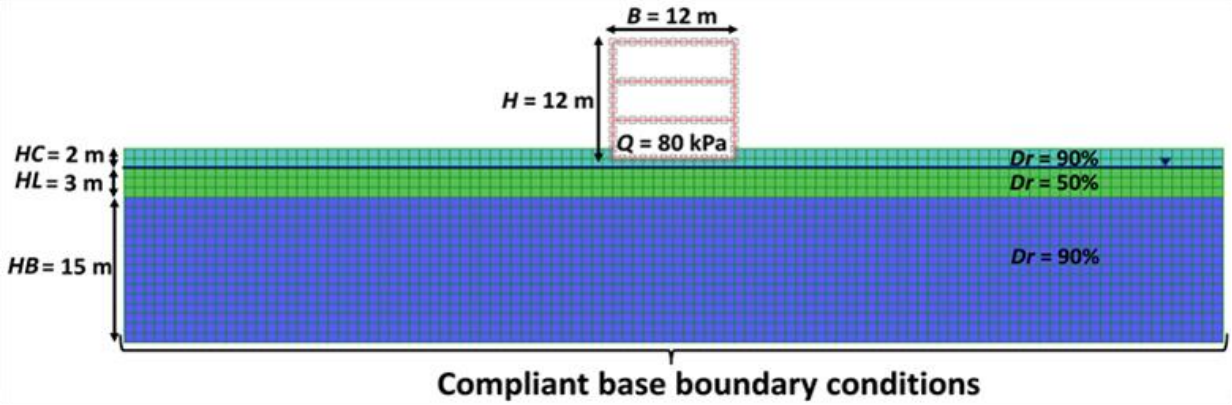

Figure 5.3. Baseline case analytical model. The water table depth is 2 m. The side boundaries are connected to represent free-field conditions.

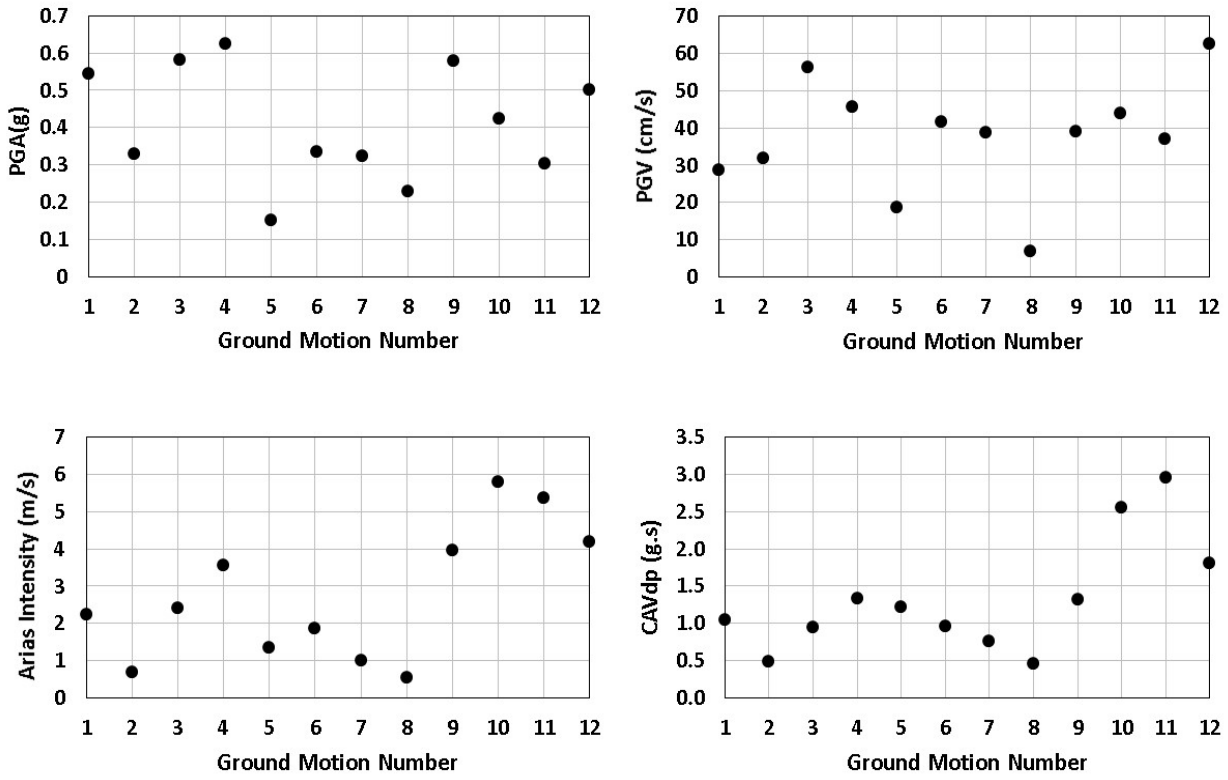

Figure 5.4. Distribution for the *PGA*, *PGV*, I_a, and CAV_{dp} for the primary earthquake ground motions records.

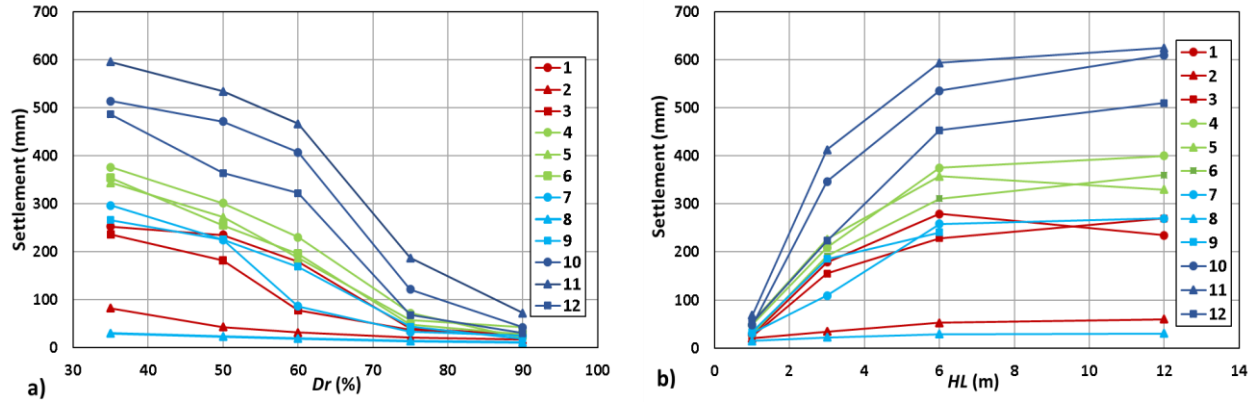

Figure 5.5. Effects of liquefiable layer on building settlement (mm) for ground motions 1-12 (Table 5.2): (a) relative density (D_r) for case with: *HL*=6m, *B*=12m, *Q*=80 kPa, *H*=12m, and *HC*=2m, and (b) thickness of liquefiable layer (*HL*) for D_r=50%, *B*=6m, *Q*=80 kPa, *H*=12m, and *HC*=2m.

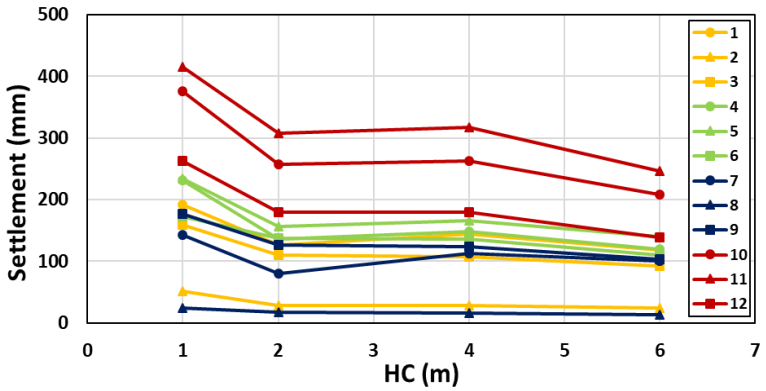

Figure 5.6. Effects of crust thickness (*HC*) on building settlement (mm) for ground motions 1-12 (Table 5.2) for case with: D_r of liquefiable layer = 50%, *HL* = 3 m, *Q* = 80 kPa, *B* = 12 m, and *H* = 12 m.

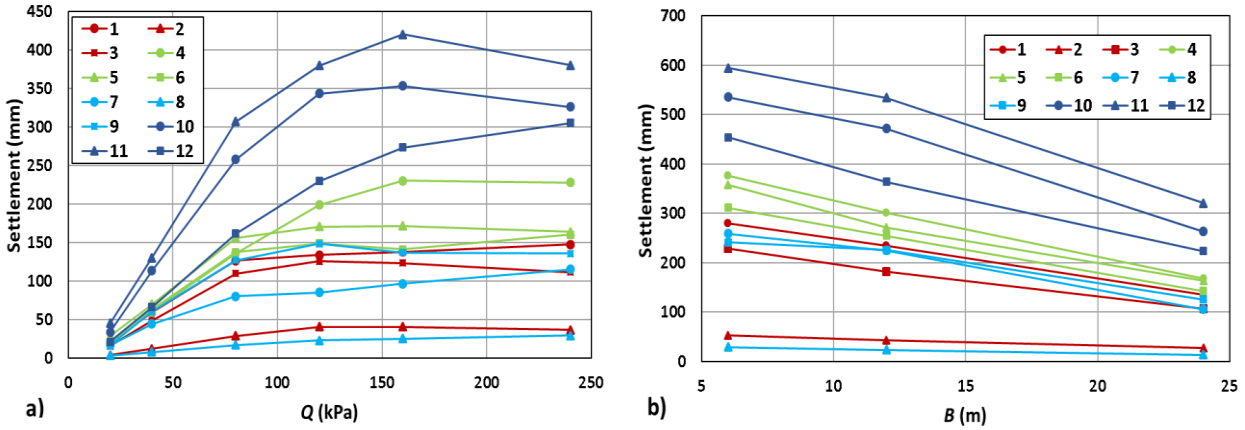

Figure 5.7. Effects of structure on building settlement (mm) for ground motions 1-12 (Table 5.2): (a) foundation contact pressure (*Q*) for D_r=50%, *HL*=3 m, *B*=12m, *H*=12m, and *HC*=2m, and (b) foundation width (*B*) for D_r=50%, *HL*=6 m, *Q*=80 kPa, *H*=12m, and *HC*=2m.

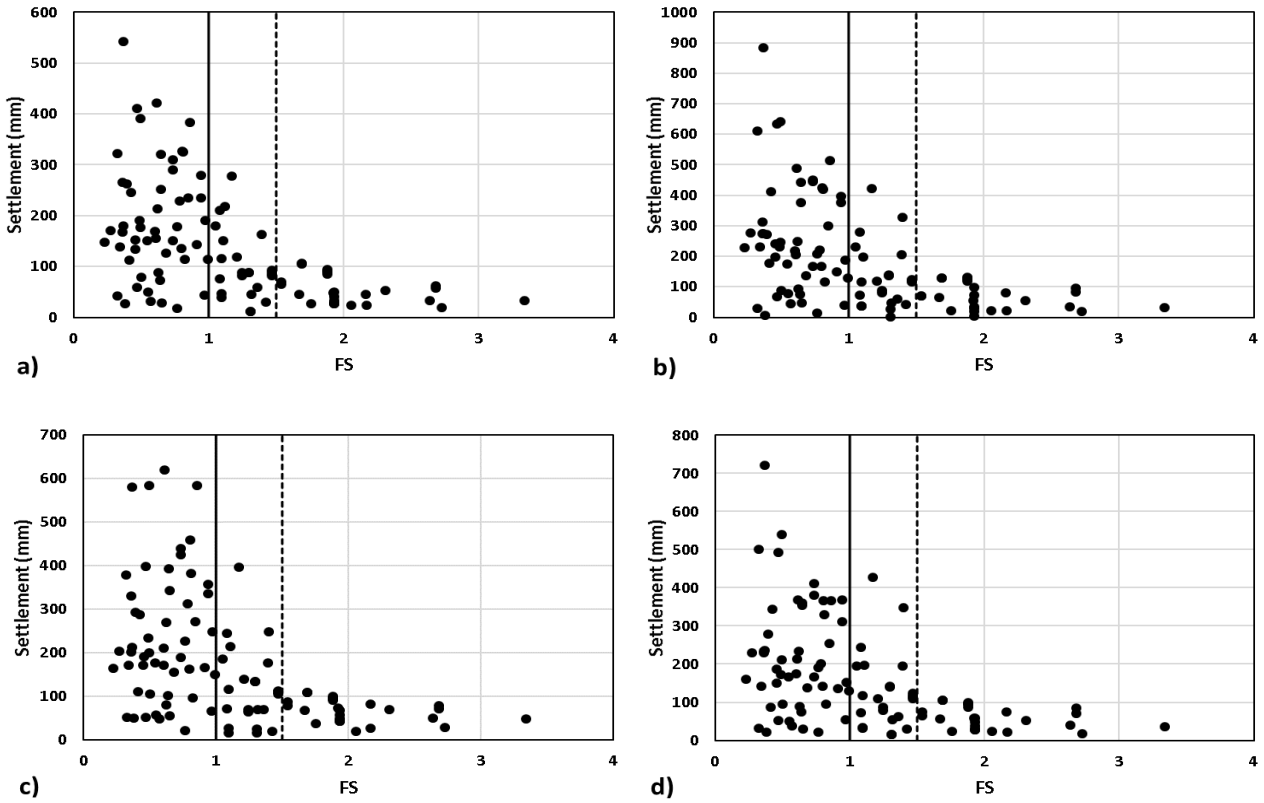

Figure 5.8. Liquefaction-induced building settlement (mm) versus post-liquefaction bearing capacity factor of safety (FS) for: (a) Ground Motion 1, (b) Ground Motion 4, (c) Ground Motion 5, and (d) Ground Motion 6. Dark vertical solid line corresponds to FS = 1.0, and dark vertical dashed line corresponds to FS = 1.5.

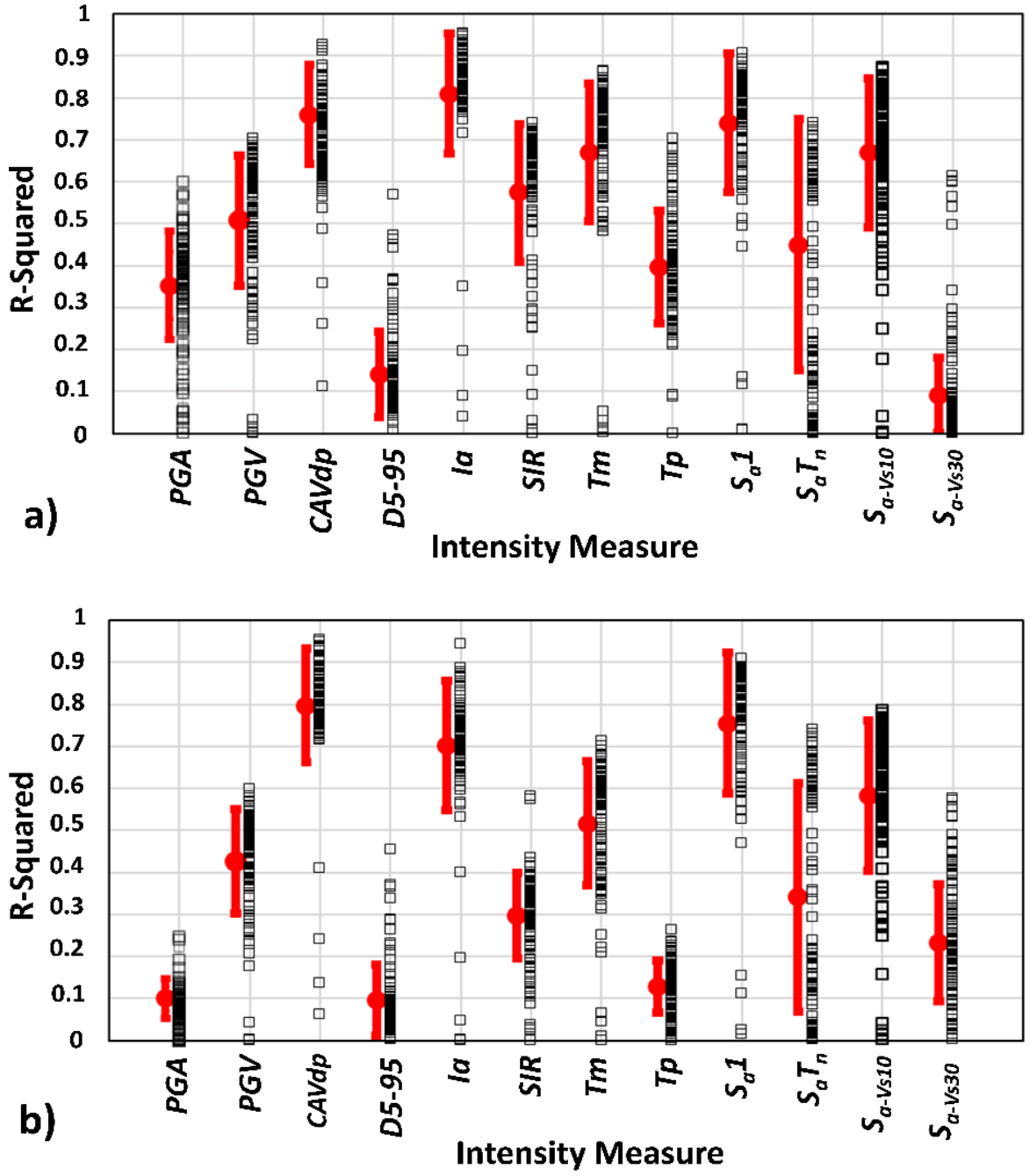

Figure 5.9. R^2 values for different *IMs* for: (a) free-field motions calculated at the ground surface, and (b) outcrop "rock" motions. The error bars indicate mean and mean +/- 1 standard deviation values for the models. *PGA*: peak ground acceleration (*g*), *PGV*: peak ground velocity (cm/s), CAV_{dp}: standardized cumulative velocity (*g*-s), $D_{5\text{-}95}$: significant duration (s), I_a: Arias intensity (m/s), *SIR*: shake intensity rate (m/s/s), T_m: mean period (s), T_P: predominant period (s), S_a1: spectral acceleration at T = 1 s (*g*), S_aT_n: spectral acceleration at T_n = the natural period of the structure (*g*), $S_{a\text{-}Vs10}$: spectral acceleration at $T = 4(10\text{m})/V_{s10}$ (*g*), and $S_{a\text{-}Vs30}$: spectral acceleration at $T = 4(30\text{m})/V_{s30}$ (g).

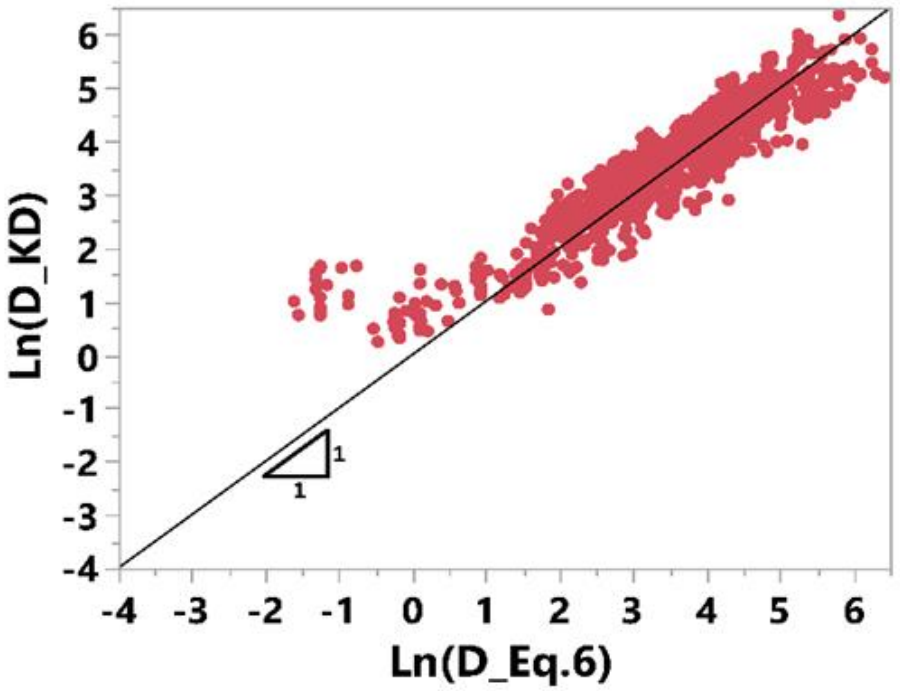

Figure 5.10. Comparison of liquefaction-induced building settlement (mm) estimated using Equation 5.6 (*Ln(D_Eq.6)*) and calculated analytically through 3D dynamic SSI finite element analyses by Karimi and Dashti (2017) (*Ln(D_KD)*). R^2=0.83.

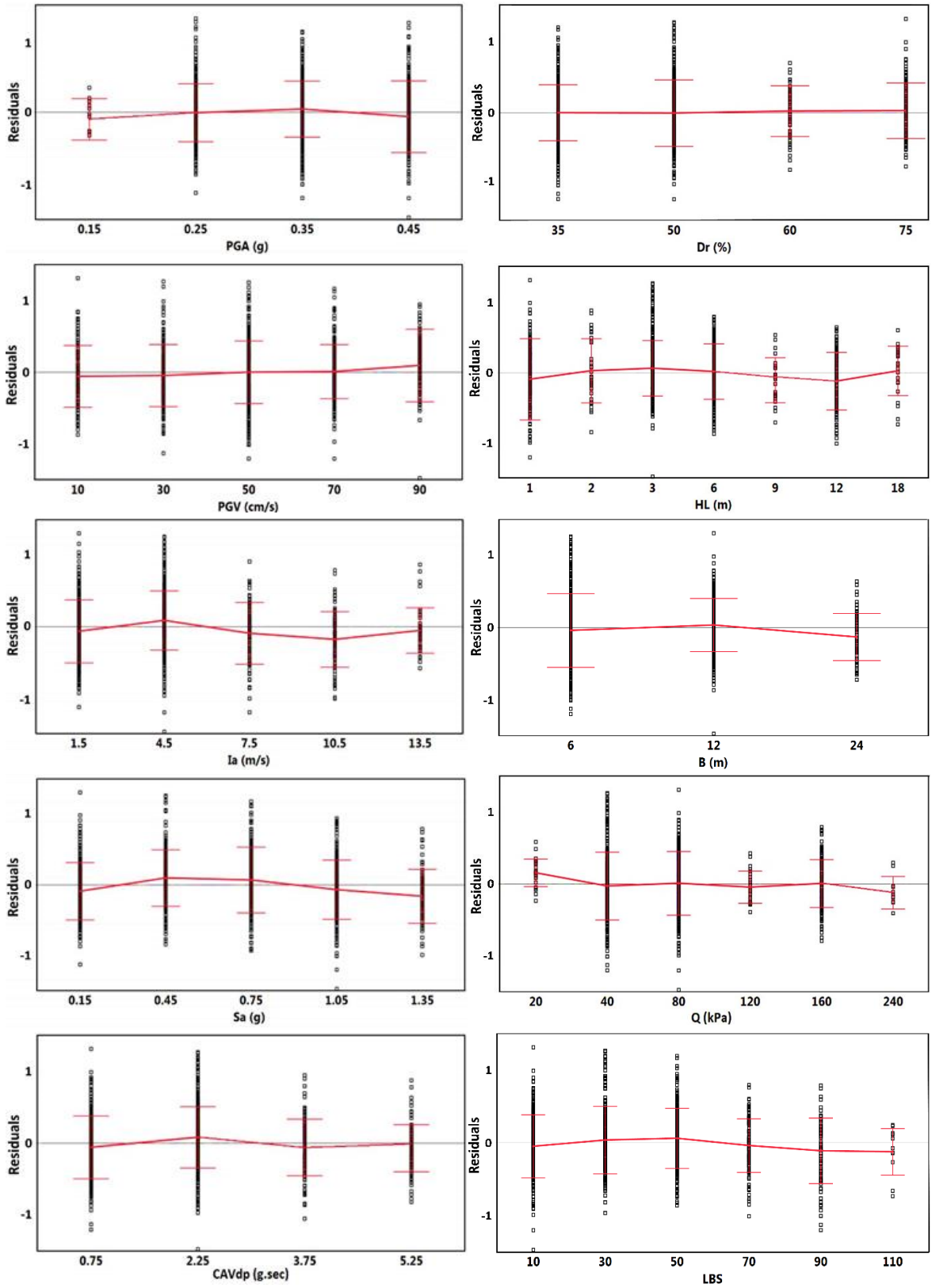

Figure 5.11. Residual plots for several earthquake ground motion, site, and building parameters.

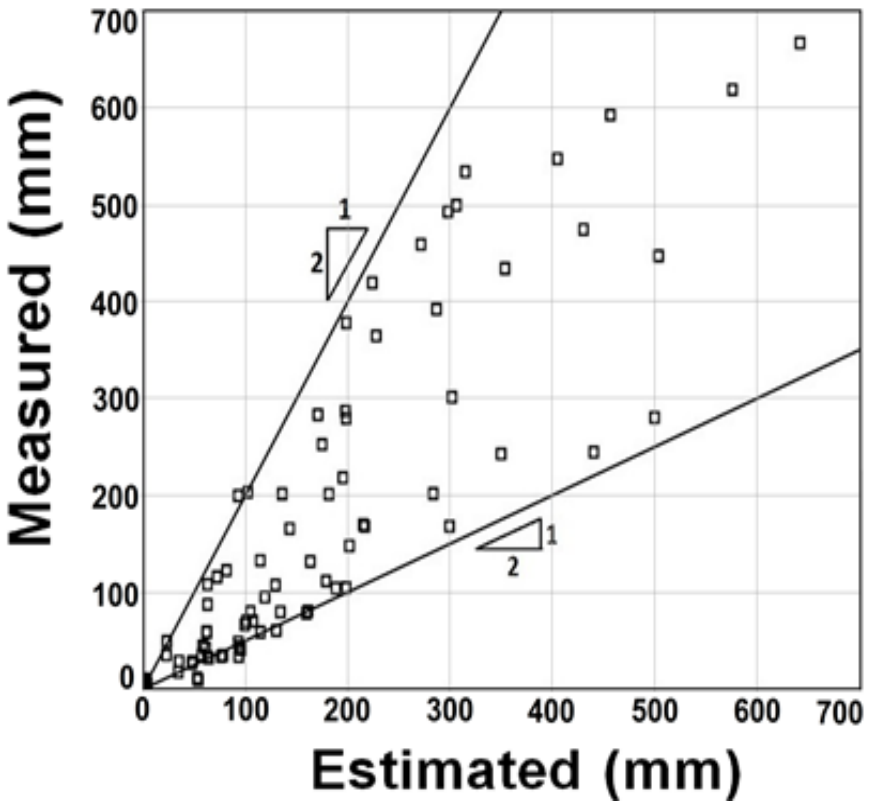

Figure 5.12. Comparison of liquefaction-induced model building settlements measured during centrifuge tests by Dashti (2002), Allmond and Kutter (2012), Zupan et al. (2013) and Hayden et al. (2014) with estimated liquefaction-induced settlements with the proposed procedure.

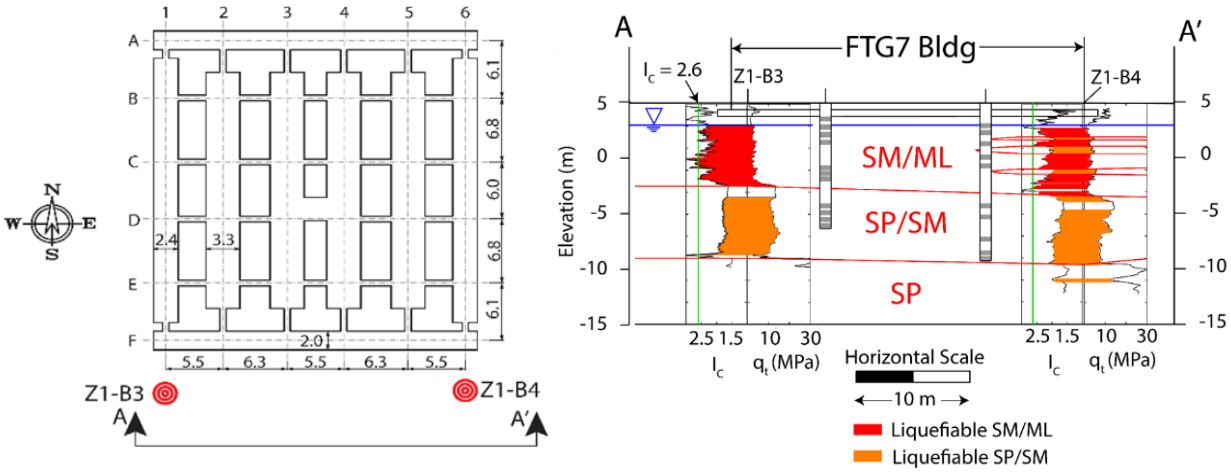

Figure 5.13. Plan view (top) and Section A-A' (bottom) of the FTG-7 building (Zupan 2014).

CHAPTER 6: CONCLUSIONS

6.1 SUMMARY

This research develops new, robust simplified procedures to estimate shear-induced displacements of earth/waste structures or natural slopes and to estimate shear-induced settlement of structures founded atop liquefiable soils. Evaluating the effects of seismically-induced displacements in slopes and liquefaction-induced building settlement is a key area of performance based earthquake engineering (PBEE). The damage caused by seismically-induced displacements in slopes of geotechnical systems and the damage caused by liquefaction-induced settlement of buildings during recent large earthquakes has highlighted the importance of developing procedures for evaluating the seismic performance of these geosystems.

This study identifies the lack of robust simplified procedures to estimate seismically-induced slope displacements in subduction zones, and proposes a simplified seismic slope displacement procedure for evaluating earth/waste structures or natural slopes subjected to interface earthquakes in subduction zones. The proposed simplified procedure uses the framework of Bray and Travasarou (2007). The fully coupled, nonlinear seismic slope displacement model captures the important influence of the system's yield coefficient k_y, its initial fundamental period T_s, and the ground motion's spectral acceleration at a degraded period of the slope taken as 1.5 T_s. The model separates the probability of "zero" displacement (i.e., < 0.5 cm) from the distribution of "nonzero" displacement, so that low values of calculated seismic displacement do not bias the results. The primary source of uncertainty in assessing the seismic performance of an earth slope or system during an earthquake is the input ground motion. Therefore, a comprehensive database containing 810 two-component ground motion recordings from subduction zone interface earthquakes was developed and used to compute the seismic slope displacements. The proposed procedure has been validated using observations of 12 case histories of seismic slope performance during recent earthquakes, including the 2011 Moquegua, 2007 Pisco, 2010 Maule, 2011 Tohoku, and 2016 Muisne earthquakes. A comparison of the proposed procedure with the procedure proposed by Bray and Travasarou (2007), which was developed for shallow crustal earthquake settings, shows that the Bray and Travasarou (2007) procedure is conservative when it is used to estimate seismic slope displacements for subduction zone interface earthquakes. There are differences between the ground motion recordings of subduction zone earthquakes and shallow crustal earthquakes. However, the differences are not as significant as might have been conjectured. The proposed seismic slope displacement model better captures the unique seismic setting of subduction zone interface earthquakes, so it should be used to estimate seismic slope displacements for these types of events. The proposed simplified procedure is also used to provide a rational basis for the estimation of a calibrated seismic coefficient that can be employed in pseudostatic slope stability analyses.

Another important issue is currently the estimation of seismic displacements is based primarily on procedures that do not incorporate the uncertainty in the properties of the slope system (i.e., k_y and T_s) and they rely on a single value of the ground motion intensity parameter (*IM*). However, uncertainty is present in every step of the evaluation starting with the inherent variability in the properties of the slope system to the variability of the *IMs*. In this research, easily implemented performance-based procedures that consider the uncertainty in the slope's properties and earthquake ground shaking *IM* are presented for the straightforward assessment of the seismic performance of earth/waste systems or natural slopes in shallow crustal (based on the model

developed by Bray and Travasarou, 2007) and subduction earthquake settings (based on the model developed in this study). Deterministic or pseudo-probabilistic simplified seismic slope displacement procedures are typically used in engineering practice. However, performance-based procedures are preferred because they better capture the actual uncertainty in the ground motion intensity measure and earth system properties. Moreover, a performance-based procedure provides seismic slope displacement estimates that are consistent with design hazard levels. The performance-based seismic slope displacement hazard procedure does not necessarily provide higher or lower values than the commonly used pseudo-probabilistic procedure. Their relative values depend on the particular seismo-tectonic setting and the design hazard level. Finally, the proposed performance-based seismic slope displacement hazard procedure was recast to estimate a hazard-compatible seismic coefficient to be used in a pseudostatic slope stability analysis.

Dynamic SSI effective stress analyses are performed to identify key trends in the settlement of buildings with shallow foundations affected by soil liquefaction. Over 1,300 dynamic SSI effective stress analyses are performed by systematically varying subsurface conditions and building properties while applying 36 earthquake motions. Examination of the results from the dynamic SSI effective stress analyses show that the building is shown to create significant shear-induced ground movements underneath it during intense earthquake shaking, and the shear-induced mechanism is dominant relative to the volumetric-induced mechanism during strong shaking. As strong shaking subsides, the volumetric-induced mechanism becomes increasingly significant and may eventually produce significant building settlements. The analytical results provide salient insights regarding the key parameters controlling liquefaction-induced building settlement. The relative density of the liquefiable layer is the key soil property, and its thickness is an important soil profile characteristic. Building contact pressure is the most important building parameter, and building width is also important. The ground motion intensity parameters that correlate best with building settlement are standardized cumulative absolute velocity, Arias intensity, and spectral acceleration at 1 s. The post-liquefaction bearing capacity factor of safety indicates when large building settlements are possible.

The primary mechanisms of liquefaction-induced settlements of structures are ejecta-induced, shear-induced, and volumetric-induced ground deformation. Regression analyses of the results of the nonlinear dynamic SSI effective stress analyses are used to develop a procedure to estimate shear-induced liquefaction building settlement. A new index, referred to as the liquefaction building settlement index (*LBS*), is proposed. *LBS* captures the influence of earthquake-induced shear strains within liquefiable layers and hence shear-induced liquefaction building settlement. The form of the equation is also based on widely accepted foundation engineering and earthquake engineering concepts. There are methods already available to capture the volumetric-induced settlement mechanism (e.g., Zhang et al., 2002). The continuum based analyses cannot capture the loss of ground due to the development of sediment ejecta. Hence, case histories and judgment should be used to evaluate the settlement potential from the ejecta-induced building settlement mechanism.

The proposed simplified method is applied to several field case histories and shown to provide estimates of settlement consistent with those observed. It also captures well the results of centrifuge experiments. The proposed simplified procedure provides a rational approach for estimating liquefaction-induced building settlement. The estimated values are consistent with those calculated using more advanced analyses for general conditions. However, the proposed procedure is a simplification of an inherently complex phenomenon. The proposed procedure is based on the results of dynamic SSI effective stress analyses performed for a particular suite of

earthquake ground motions (i.e., shallow crustal earthquakes) and a limited set of building and ground conditions, which do not have highly variable soil conditions nor highly irregular building configurations. Thus, care is warranted in its use, especially for cases not considered in this thesis. Further research and calibrations are warranted. Moreover, the use of the proposed simplified procedure should be complemented with the results of project-specific nonlinear dynamic SSI effective stress analyses on important projects.

6.2 FINDINGS

This thesis presents the development of simplified procedures to estimate seismically-induced displacements of earth/waste structures or natural slopes and to estimate liquefaction-induced settlement of buildings with shallow foundations affected by soil liquefaction. As a result of this study, these key findings were developed:

- A comprehensive database containing 810 two-component ground motion recordings from subduction zone interface earthquakes was developed through this research. The interface earthquake ground motion database is required to develop empirically based models such as one to estimate seismic slope displacement in subduction earthquake zones.
- A new, robust simplified procedure for estimating seismically-induced slope displacements in areas affected by subduction zone interface earthquakes was developed. The fully coupled, nonlinear seismic slope displacement model captures the important influence of the system's yield coefficient k_y, its initial fundamental period T_s, and the ground motion's spectral acceleration at a degraded period of the slope taken as 1.5 T_s. The model separates the probability of "zero" displacement (i.e., < 0.5 cm) from the distribution of "nonzero" displacement, so that low values of calculated seismic displacement do not bias the results.
- A comparison of the proposed procedure for subduction settings, referred as BMT17 with the Bray and Travasarou (2007) procedure, referred as BT07, which was developed for shallow crustal earthquake settings, shows that the BT07 procedure is conservative when it is used to estimate seismic slope displacements for subduction zone interface earthquakes. There are differences between the ground motion recordings of subduction zone earthquakes and shallow crustal earthquakes. However, the differences are not as significant as might have been conjectured. The proposed seismic slope displacement model better captures the unique seismic setting of subduction zone interface earthquakes, so it should be used to estimate seismic slope displacements for these types of events.
- Considering that the amount of seismic displacement is most influenced by the long period energy, it is consistent with empirical observations that for a given earthquake magnitude, distance and site conditions the ground motion records from shallow crustal settings tend to have a stronger long period content energy compared with ground motion records from subduction interface settings and then may cause higher seismically-induced slope displacements.
- The BT07 predictive equations are biased in terms the residuals of seismic slope displacement as a function of earthquake magnitude. The residuals using the BT07 equations are more negative than the residuals derived in this study at intermediate and lower magnitudes. The BT07 residuals become less negative as magnitude increases and tend to zero for M = 9 earthquakes. The magnitude scaling term for the BT07 and BMT17 methods are 0.278 and 0.550, respectively. The higher magnitude scaling coefficient in the BMT17 relationship for subduction earthquakes is consistent with what has been observed for ground motion prediction equations (GMPE) for spectral acceleration for subduction earthquakes (e.g., Abrahamson et al. 2016)

compared with shallow crustal earthquakes (e.g., Abrahamson et al. 2014). The higher magnitude scaling coefficient in the BMT17 relations may also be due to the longer duration of subduction earthquake records relative to records from shallow crustal earthquakes of similar magnitude.

- The BT07 residuals of the subduction zone earthquake-induced displacement data when plotted against yield coefficient are more negative compared to the residuals using the equations derived in this study for subduction zone earthquakes (i.e., BMT17). However, the residuals do not show significant bias for lower (more common) values of k_y. There is significant bias only for higher values of yield coefficient. This is likely due in part to the wider range of k_y values employed in the present study (i.e., values up to 0.8) relative to the range used in the BT07 study (i.e., k_y values up to only 0.4). A conservative extrapolation of the BT07 predictive equations to higher k_y values is likely the primary cause of the bias and not a seismological difference between subduction zone and shallow crustal earthquakes.
- The residuals of the BT07 model versus the simulated subduction zone earthquake seismic displacement data are slightly more negative compared with the residuals of the BMT17 model derived in this study for periods less than 0.5 s. For higher periods, the residuals of the BT07 predictive equations do not differ significantly from those of the proposed BMT17 predictive equations. Thus, there is no significant effect of the slope fundamental period due to the different ground motion databases.
- The proposed simplified procedure developed in this study for subduction earthquake zones is used to provide a rational basis for selecting a seismic coefficient (k) in subduction earthquake zones for use in a pseudostatic slope stability analysis by requiring it to provide a seismic assessment that is consistent with the results of the seismic slope displacement analysis. To estimate a consistent rational seismic coefficient, the engineer needs to define the maximum allowable seismic displacements for the system, the system properties (i.e. the initial fundamental period) and the seismic demand (i.e. the spectral acceleration at the degraded period).
- Deterministic or pseudo-probabilistic simplified seismic slope displacement procedures are typically used in engineering practice. However, performance-based procedures should be preferred because they consider more completely the actual uncertainty in the ground motion intensity measure and earth system properties. Moreover, a performance-based procedure provides seismic slope displacement estimates that are consistent with design hazard levels. There is a shift of the engineering state-of-practice towards probabilistic approaches and the evolution of performance-based engineering. Thus, it is expected that performance-based procedures will become the state-of-practice in evaluating seismic slope displacements.
- Consistent results are obtained with the BT07 and BMT17 models whether the seismic slope displacement hazard curve is estimated using "integration by parts" or "rate of occurrence" approaches. The integration by parts approach is more fundamental if the analytical derivatives of the displacement models can be calculated (as it is the case for the BT07 or BMT17 models). It provides a closed-form solution for the cases with no magnitude dependence. It has been employed in this research to confirm the accuracy of the local approximations in the more commonly used "rate of occurrence" approach.
- For the shallow crustal earthquake cases studied, the seismic slope displacement hazard curve was not highly sensitive to the use of predictive equations with or without the earthquake magnitude term. The results of a sensitivity study indicate that the choice of the governing earthquake magnitude value is not critically important. It is sufficient to use the modal magnitude from the seismic hazard deaggregation in the magnitude-dependent model, which is the preferred model.

- The uncertainty treatment of the properties in a slope system (i.e. k_y and T_s) has been categorized by previous researchers as aleatory through the use of probability density functions (PDF) or as epistemic through the use of alternative values and corresponding weights in a logic tree approach. Comparisons between the two approaches for categorizing the uncertainty in the properties of a slope system shows that the mean hazard curve considering an epistemic treatment for k_y and T_s is equivalent to the hazard curve calculated using PDF functions for k_y and T_s, given that the weighting factors used for the logic tree are consistent with the PDF distributions assumed for k_y and T_s. If only the mean displacement hazard curve needs to be estimated either approach could be used. However, the epistemic approach has the advantage of allowing an assessment in the uncertainty of the displacement hazard curve, and its use is recommended.
- The performance-based seismic slope displacement hazard procedure does not necessarily provide higher or lower values than the commonly used pseudo-probabilistic procedure. Their relative values depend on the particular seismo-tectonic setting and the design hazard level. The performance-based method provides seismic slope displacement estimates that are directly compatible with the target design levels. Hence, it should be used, because the hazard is developed based on a relevant index of seismic performance, which is the calculated seismic slope displacement, and not on an indirect index of performance such as a ground motion intensity measure.
- The proposed performance-based seismic slope displacement hazard procedure was recast to estimate a hazard-compatible seismic coefficient to be used in a pseudostatic slope stability analysis. The value of the seismic coefficient is a function of the selected threshold of allowable seismic slope displacement, among other factors. A comparison with conventionally employed pseudo-probabilistic procedures for selecting the seismic coefficient (i.e., Bray and Travasarou 2009) indicates that the results of performance-based procedure can differ by up 30%. The performance-based procedure is recommended because it addresses directly the selected hazard level and the associated uncertainties.
- Liquefaction-induced building settlement results from ejecta-induced, shear-induced, and volumetric-induced displacement mechanisms. The shear-induced mechanism is an important component of the settlement of shallow-founded structures, especially when significant ejecta do not occur. Nonlinear dynamic SSI effective stress analyses can capture the shear-induced mechanisms of liquefaction building settlement.
- Examination of the results from the dynamic SSI effective stress analyses show that typically higher excess pore water pressures are generated under the building compared to the free-field during the intense part of earthquake shaking. However, due to larger initial vertical effective stress under the building, the excess pore water pressure ratio may be lower under the building than in the free-field. Regardless, water tends to flow laterally from underneath the building towards the free-field during strong shaking, due to higher pore water pressures and hence higher total head under the building. Although there are overall systematic outward flow patterns, the instantaneous hydraulic gradients induced by the earthquake loading are highly variable.
- Examination of the results from the dynamic SSI effective stress analyses show that the building creates significant shear-induced ground movements underneath it during intense earthquake shaking, and the shear-induced mechanism is dominant relative to the volumetric-induced mechanism during strong shaking. As strong shaking subsides, the volumetric-induced mechanism becomes increasingly significant and may eventually produce significant building settlements.

- The relative density of the liquefiable layer is a critically important parameter, especially when transitioning from medium dense to dense sands wherein liquefaction-induced building settlement decrease significantly. Building settlement is less sensitive to variations of the liquefiable layer's relative density when it was in the ranges of very loose to loose, or dense to very dense. In the former case, building settlement is large, and in the latter case, it is small.
- Liquefaction-induced building settlement increases as the thickness of the liquefiable soil layer increases up to a point where increasing it further does not cause significantly more settlement. A thick non-liquefiable crust suppresses building settlement due to liquefaction of a deeper layer. Liquefaction-induced building settlement increases dramatically if the liquefiable layer is directly beneath the building foundation.
- Building contact pressure is an important structural factor to consider when evaluating liquefaction-induced building settlement. However, there is a point wherein the magnitude of liquefaction-induced settlement does not continue to increase for increasing values of the applied building pressure. This result, which has also been observed in centrifuge experiments, is likely due the higher confinement of a heavy building.
- The width of the building is also an important structural parameter. Building height is a potentially important parameter but its effect on settlement for the cases studied is correlated with building contact pressure, which captures the key aspects of the building performance better.
- A low post-liquefaction bearing capacity factor of safety indicates when large building settlements are possible. Liquefaction-induced building settlements are not large until the post-liquefaction bearing capacity *FS* is below 1.5. As the calculated *FS* decreases below 1.0, the liquefaction-induced building settlement can increase significantly.
- Analytical results show that methods that assume a directly proportionality between liquefaction-induced settlements and the thickness of the liquefiable layer are not satisfactory, especially for cases with thin liquefiable layers. More complex functional forms and the inclusion of other parameters are needed.
- The characteristics of the earthquake ground motions influence greatly the magnitude of liquefaction-induced building settlement. The ground motion intensity measures that correlate best with liquefaction-induced building settlement are CAV_{dp}, I_a and S_a1. Liquefaction-induced building settlement increases systematically as each of these *IMs* increase. For the cases examined in this study, CAV_{dp} is the preferred due to its better predictability compared to I_a.
- A new index, referred as liquefaction building settlement index (LBS), is proposed. LBS captures the influence of earthquake-induced shear strains within liquefiable layers and hence shear-induced liquefaction building settlement.
- Regression analyses of the results of the nonlinear dynamic SSI effective stress analyses are used to propose a new simplified procedure to estimate shear-induced liquefaction building settlement. There are methods already available to capture the volumetric-induced settlement mechanism. The continuum based analyses cannot capture the loss of ground due to the development of sediment ejecta. Hence, case histories and judgment should be used to evaluate the settlement potential from the ejecta-induced building settlement mechanism.
- Based on the results of this study, a simplified procedure for estimating liquefaction-induced building settlement is developed. It provides estimates of building settlement consistent with those of 19 field case histories. It also provides estimates of liquefaction-induced building settlement consistent with those measured in geotechnical centrifuge experiments.

6.3 FUTURE RESEARCH

This research provides robust simplified procedures to estimate seismically-induced slope displacement and liquefaction-induced building settlement. As a result of this work, research opportunities related to these problems have been identified, including:

- Future research should examine the development of analytical models capable to capture both the stick-slip sliding accumulation of shear strains and the accumulation of volumetric strains at the same time. This will enable the subsequent development of simplified procedures able to estimate total permanent seismically-induced deformations including shear and volumetric components in a unified and consistent manner.
- This research considers the seismically-induced slope displacement, which is an engineering demand parameter, as an index of seismic performance. Other alternatives to be used as an index of seismic performance, such as the measure of damage (*DM* in the PEER approach) or decision variables in loss analyses (*DV* in the PEER approach) may also be considered in the performance-based earthquake engineering framework.
- The current model proposed for seismic slope displacement prediction needed to have a magnitude term to account for the insufficiency of $SA(1.5T_s)$ to represent the duration of the strong ground motion. Rather than adding a magnitude term, another way of account for this insufficiency of $SA(1.5T_s)$ would be to use a vector intensity measure. However, this entails the use of probabilistic seismic hazard results for vectors of ground motion parameters which are not readily available by appropriate agencies and would require additional effort from the engineer to perform the vector seismic hazard evaluation. Recent efforts support the performance of vector hazard analyses in practice (e.g., studies of cross correlation coefficients between different *IMs* with robust databases). However, this information has not been implemented by appropriate agencies and often is not familiar among engineers in practice. Future research should consider the examination and implementation of vector models for the estimation of seismically-induced displacements and compare the advantages or disadvantages against scalar models.
- Nonlinear dynamic SSI effective stress analyses considering the aleatory and spatial variability in the soil foundation properties should be performed in future research. The analyses performed in this thesis considered soil layers with uniform properties; however, the soil properties often change considerably even within the same geological unit. Performing many simulations with variable soil properties is becoming feasible with the development of high performance computing and parallel computing.
- Additional nonlinear dynamic SSI effective stress analyses using different numerical methods and different constitutive models should be performed to identify key trends in liquefaction-induced settlement. Comparison of the results of different nonlinear dynamic SSI effective stress analyses will provide important insights, develop confidence in the methods examined, and importantly will enable consideration of the epistemic uncertainty that exist in the estimation of liquefaction-induced building settlement.
- The potential for important 3D effects of building response considering the combined effect of all seismic excitation components should be investigated. The nonlinear dynamic SSI parametric effective stress analyses in this research, considered 2D sections representative of critical sections of buildings and soil profiles then the analyses were performed under plane strain conditions. 2D analyses have shown to capture reasonably well the performance of buildings

observed after recent case histories; however, more insight can be developed using 3D analyses, such as evaluating the influence of drainage in the out-of-plane direction. Further research is warranted which considers more complex conditions (e.g., highly irregular buildings or buildings in dense urban areas that are affected by structure-soil-structure interaction). The potential benefits of 3D analyses need to be weighed against the limitations of knowledge of the true variability of ground and whether important aspects of the 3D system can be captured reasonably well.

- The effects that soil ejecta have on building settlement and seismic performance has been observed to be important for some of the case histories examined in this study. The occurrence of soil ejecta depends on many factors such as geologic environment, characteristics of the crust layer, and the depth and thickness of the liquefiable layer, among others, which are often difficult to characterize. Research in this area is highly encouraged to advance the profession. A better estimation of ejecta induced settlements will allow refinement of the proposed simplifed procedure to estimate liquefaction-induced building settlement.
- Any robust simplified method to estimate seismically-induced displacements in slopes or shallow-founded buildings situated atop liquefiable soils should be validated against field case histories. The collection of detailed measurements, photos, LiDAR data, slope displacements, tilting measurements in buildings, ground motion data in different locations of interest (i.e. base and crest in case of earth dams, or free field and foundation level in case of a building), in-situ testing, laboratory testing, etc. after an earthquake produces well-documented case histories that provide invaluable opportunities to gain insight and to identify key deformation mechanisms through back-analysis. Therefore, continued and improved efforts to capture systematically perishable data after major earthquakes are encouraged.

REFERENCES

Abrahamson, N., Silva, W., Kamai, R. (2013). Update of the AS08 Ground-Motion Prediction Equations. PEER 2013/04 Report.

Abrahamson, N., Gregor, N., Addo, K. (2016). BC Hydro Ground Motion Prediction Equations for Subduction Earthquakes. *Earthquake Spectra (EERI)*, V. 32(1), 23-44.

Allmond, J., Kutter, B. L., (2012). Centrifuge Testing of Rocking Foundations on Saturated and Submerged Sand. Centrifuge Data Report for JDA01, UCD/CGMDR-12/01, Univ. of Calif., Davis, CA.

Andrianopoulos, K.I., Papadimitriou, A.G., Bouckovalas, G.D. (2010). Bounding Surface Plasticity Model for the Seismic Liquefaction Analysis of Geostructures. *Soil Dynamics and Earthquake Engineering (SDEE)*, V. 30, 895-911.

Ancheta T.D., Darragh R.B., Stewart J.P., Seyhan E., Silva W.J., Chiou B.-S.J., Wooddell K.E., Graves R.W., Kottke A.R., Boore D.M., Kishida T., Donahue J.L. (2013). PEER NGA-West2 database, PEER Report No. 2013/03, Pacific Earthquake Engineering Research Center, Univ. of California, Berkeley.

Arias, A. (1970). A Measure of Earthquake Intensity. Seismic Design for Nuclear Power Plants, R. J. Hansen, ed., MIT Press, Cambridge, Mass.

Ashford, S. A., Sitar, N. (2002). Simplified Method for Evaluating Seismic Stability of Steep Slopes. *Journal Geotechnical and Geoenvironmental Engineering (ASCE)*, V. 128(2), 119–128.

Ashford, S., Boulanger, R., Donahue, J., Stewart, J. (2011). Geotechnical Quick Report on the Kanto Plain Region during the March 11, 2011, Off Pacific Coast of Tohoku earthquake, Japan. GEER quick report, April 5.

Atkinson, G., Boore, D. (2003). Empirical Ground-Motion Relations for Subduction-Zone Earthquakes and their Application to Cascadia and Other Regions. *Bulletin of the Seismological Society of America*, V. 93(4), 1703-1729.

Boulanger, R.W., Ziotopoulou, K. PM4Sand (Version 3) (2015). A Sand Plasticity Model for Earthquake Engineering Applications. Report No. UCD/CGM-15/01, Center for Geotechnical Modeling, Department of Civil and Environmental Engineering, Univ. of California, Davis, CA; 108 pp.

Boulanger, R.W., Idriss, I.M. 2016. CPT- Based Liquefaction Triggering Procedures. *Journal Geotechnical and Geoenvironmental Engineering (ASCE)*, V.142(2), 04015065.

Bray, J. D. (2007). Chapter 14: Simplified Seismic Slope Displacement Procedures. Earthquake Geotechnical Engineering, 5th International Conference on Earthquake Geotechnical Engineering Invited Lectures, in Geotechnical, Geological, and Earthquake Engineering Series, Pitilakis, Kyriazis D., Ed., Springer, Vol. 6, 327-353.

Bray, J. (2013). Seismic Performance Considerations for Dams and Reservoirs. Presentation for Institution of Professional Engineers, New Zealand.

Bray, J., Cubrinovski, M., Zupan, J., Taylor, M. (2014). Liquefaction Effects on Buildings in the Central Business District of Christchurch. *Earthquake Spectra (EERI)*, V.30(1), 85-109.

Bray, J.D., Dashti, S. 2014. Liquefaction-Induced Building Movements. *Bulletin of Earthquake Engineering, Springer*, V. 12(3), 1129-1156, DOI: 10.1007/s10518-014-9619-8.

Bray, J.D., Frost, J.D. (2010). Geo-Engineering Reconnaissance of the February 27, 2010 Maule, Chile Earthquake. GEER Association Report No. GEER-022.

Bray, J. D., Macedo, J.L., Travasarou, T., (2017). Simplified Procedure for Estimating Seismic Slope Deviatoric Displacements in Subduction Zones. *Journal Geotechnical and Geoenvironmental Engineering (ASCE)*, accepted for publication.

Bray, J.D., Markham, C.S., Cubrinovski, M. (2017). Liquefaction Assessments at Shallow Foundation Building Sites in the Central Business District Of Christchurch, New Zealand. *Soil Dynamics and Earthquake Engineering (SDEE)*, V. 92, 153-164, DOI: 10.1016/j.soildyn.2016.09.049.

Bray, J.D., Rathje, E.R., (1998). Earthquake - Induced Displacements of Solid-Waste Landfills. *Journal Geotechnical and Geoenvironmental Engineering (ASCE)*, V.124(3), 242–253.

Bray, J.D., Sancio, R.B. (2009). Performance of Buildings in Adapazari during the 1999 Kocaeli, Turkey Earthquake, in Earthquake Geotechnical Case Histories for Performance Based Design, Kokusho, T, Ed., TC4 Committee, ISSMFE, CRC Press/Balkema, The Netherlands, pp. 325-340 & Data on CD-ROM.

Bray, J., Sancio, R., Durgunoglu, T., Onalp, A., Youd, T., Stewart, J., Seed, R., Cetin, O., Bol, E., Baturay, M., Christensen, C., Karadayilar, T. (2004). Subsurface Characterization at Ground Failure Sites in Adapazari, Turkey. *Journal Geotechnical and Geoenvironmental Engineering (ASCE)*, V. 130 (7), pp. 673–685.

Bray, J. D., Travasarou, T., (2007). Simplified Procedure for Estimating Earthquake-Induced Deviatoric Slope Displacements. *Journal Geotechnical and Geoenvironmental Engineering (ASCE)*, V. 133(4), 381–392.

Bray, J. D., Travasarou, T., (2009). Pseudostatic Coefficient for Use in Simplified Seismic Slope Stability Evaluation. *Journal Geotechnical and Geoenvironmental Engineering (ASCE)*, V. 135(9).

Campbell, K. W., Bozorgnia, Y. (2011). Predictive Equations for the Horizontal Component Of Standardized Cumulative Absolute Velocity As Adapted for Use in the Shutdown of U.S. Nuclear Power Plants. *Nuclear Engineering and Design*, V. 241, 2558–2569.

Campbell, K. W., Bozorgnia, Y. (2012). A Comparison of Ground Motion Prediction Equations for Arias Intensity and Cumulative Absolute Velocity Developed Using a Consistent Database and Functional Form. *Earthquake Spectra (EERI)*, V. 28(3), 931-941.

Chopra, A.K., Zhang, L. (1991). Base Sliding Response of Concrete Gravity Dams to Earthquakes. Earthquake Engineering Research Center, Univ. of California, Berkeley, Report No. UCB/EERC-91/05.

Darendeli, M.B. (2001). Development of A New Family of Normalized Modulus Reduction and Material Damping Curves. Ph.D. dissertation, Univ. of Texas at Austin.

Dashti, S. (2009). Toward Evaluating Building Performance on Softened Ground (Appendices 473 I–IV), Ph.D. Thesis, University of California, Berkeley.

Dashti, S., Bray, J.D., Pestana, J.M., Riemer, M.R., Wilson, D. (2010). Mechanisms of Seismically-Induced Settlement of Buildings With Shallow Foundations on Liquefiable Soil. *Journal Geotechnical and Geoenvironmental Engineering (ASCE)*, V. 136(1).

Dashti, S., Bray, J.D., Pestana, J.M., Riemer, M.R. and Wilson, D. (2010). Centrifuge Testing to Evaluate and Mitigate Liquefaction-Induced Building Settlement Mechanisms. *Journal Geotechnical and Geoenvironmental Engineering (ASCE),* V.136(7), 918-929.

Dashti, S., Bray, J.D. (2013). Numerical Simulation of Building Response on Liquefiable Sand. *Journal Geotechnical and Geoenvironmental Engineering (ASCE)*, V. 139(8), 1235-1249.

Deierlein, G., Krawinkler, H., Cornell, C., (2003). A Framework for Performance-Based Earthquake Engineering, Paper No. 140, in Proceedings., Pacific Conference on Earthquake Engineering, 2003, Christchurch, New Zealand.

Elgamal, A., Lu, J., and Yang, Z. (2005). Liquefaction-Induced Settlement of Shallow Foundations and Remediation: 3D Numerical Simulation. *Journal and Earthquake Engineering*, V. 9, Special Issue, 17-45.

Elgamal, A.W., Scott, R., Succarieh, M., and Yan, L. (1990). La Villita Dam Response During Five Earthquakes Including Permanent Deformations. *Journal Geotechnical and Geoenvironmental Engineering (ASCE)*, V. 116(10), 1443–1462.

Elgamal, A., Yang, Z., and Parra, E. (2002). Computational Modeling of Cyclic Mobility And Post-Liquefaction Site Response. Soil Dynamics and Earthquake Engineering, V. 22(4), 259–271.

EERI (2011). Geotechnical Effects of the Mw 9.0 Tohoku, Japan, Earthquake of March 11, 2011. EERI Special Earthquake Report.

Franke, K.W., Ulmer, K.J., Ekstrom, L.T., Meneses, J.F., (2016). Clarifying the Difference Between Traditional Liquefaction Hazard Maps and Probabilistic Liquefaction Reference Parameter Maps. *Soil Dynamics Earthquake Engineering*, V. 90, 240-249.

Greene, W. (2003). Econometric analysis. 5th Ed., Prentice-Hall, Englewood Cliffs, N.J.

Groholski, D.R., Hashash, YMA., Kim, B., Musgrove, M., Harmon, J., Stewart, JP. (2015). Simplified Model for Small-Strain Nonlinearity And Strength in 1d Seismic Site Response Analysis. *Journal Geotechnical and Geoenvironmental Engineering (ASCE)*, V.142(9):04016042. doi:10.1061/(ASCE)GT.1943-5606.0001496.

Hausler, E. (2002). Influence of Ground Improvement on Settlement and Liquefaction: a Study Based on Field Case History Evidence and Dynamic Geotechnical Centrifuge Tests. Ph.D., Univ. of Calif., Berkeley, CA.

Hayden, C.P., Allmond, J.D., Rawlings, I.A., Kutter, B. L., Bray, J.D., Hutchinson, T.C., Fiegel, Zupan, J.D., and Whittaker, A.S. (2014). Seismic Performance Assessment in Dense Urban Environments, Centrifuge Data Report for Test-6, University of California, Davis.

IBC (2012). International Building code.

Idriss I, Boulanger R. (2008). Soil Liquefaction during Earthquakes. Earthquake Engineering Research Institute (EERI), MNO-12, Oakland, CA.

Ishihara, K. (1985). Stability of Natural Deposits During Earthquakes. In Proceedings of the 11th International Conference on Soil Mechanics and Foundation Engineering, San Francisco, 1:321-376.

Ishihara, K., and Yoshimine, M. (1992). Evaluation of Settlements in Sand Deposits Following Liquefaction During Earthquakes. *Soils Foundations*, V 32(1), 173–188.

Itasca (2011). FLAC – Fast Lagrangian Analysis of Continua, Version 7.0. Itasca Consulting Group, Inc., Minneapolis, MN.

Iwasaki, T., Arakawa, T., Tokida, K. (1982). Simplified Procedures for Assessing Soil Liquefaction During Earthquakes. In Proceedings of Conference on Soil Dynamics & EQ Engineering. Southampton, 925-939.

Jamiolkowski, M., LoPresti, D.C.F., Manassero, M. (2001). Evaluation of Relative Density and Shear Strength of Sands from Cone Penetration Test and Flat Dilatometer Test, Soil Behavior and Soft Ground Construction (GSP 119), American Society 689 of Civil Engineers, Reston, VA, 201 – 238.

Jibson, R.W. (2007). Regression Models for Estimating Coseismic Landslide Displacement. *Engineering Geology*, V. 91(2-4), 209–218.

Karimi, Z., Dashti, S. (2016a). Numerical and Centrifuge Modeling of Seismic Soil-Foundation-Structure Interaction on Liquefiable Ground. *Journal Geotechnical and Geoenvironmental Engineering (ASCE)*, V.142(1), 04015061.

Karimi, Z., Dashti, S. (2016b). Seismic Performance of Shallow-Founded Structures on Liquefiable Ground: Validation of Numerical Simulations Using Centrifuge Experiments. *Journal Geotechnical and Geoenvironmental Engineering (ASCE)*, V.142(6).

Karimi, Z., Dashti, S. (2017). Ground Motion Intensity Measures to Evaluate II: The Performance of Shallow-Founded Structures on Liquefiable Ground, *Earthquake Spectra (EERI)*, 33(1), 277-298.

Kramer, S.L., Mayfield, R.T., (2007). Return Period of Soil Liquefaction. *Journal of Geotechnical and Geoenvironmental Engineering, (ASCE)*, V. 133(7): 802-813.

Kramer, S. L., and Mitchell, R. A. (2006). Ground Motion Intensity Measures for Liquefaction Hazard Evaluation. *Earthquake Spectra (EERI),* V.22, 413–438.

Kramer, S., Sideras, S., Greenfield, M. (2016). The Timing of Liquefaction and its Utility in Liquefaction Hazard Evaluation. *Soil Dynamics and Earthquake Engineering (SDEE),* V. 91, 133–146.

Kulhawy, F.H. and Mayne, P.H. (1990). Manual on Estimating Soil Properties for Foundation Design. Electric Power Research Institute, August, 1990.

Lin, J.S., and Whitman, R.V. (1983). Decoupling Approximation to the Evaluation of Earthquake-Induced Plastic Slip in Earth Dams. EESD, V. 11(5), 667–678.

Lin, J.-S., Whitman, R.V., 1986. Earthquake Induced Displacements of Sliding Blocks. *Journal of Geotechnical Engineering,* V.112(1), 44–59.

Liu L., Dobry R. (1997). Seismic Response of Shallow Foundation on Liquefiable Sand. *Journal Geotechnical and Geoenvironmental Engineering (ASCE),* V.123(6), 557–567.

Lopez-Caballero, F., and Farahmand-Razavi A.M. (2008). Numerical Simulation of Liquefaction Effects on Seismic SSI. *Soil Dynamics and Earthquake Engineering (SDEE),* V.49, 2-38.

Luque, R. (2017). Analysis of Liquefaction-Induced Building Settlement. Ph.D. Dissertation, University of California, Berkeley.

Luque, R., and Bray, J. (2015). Dynamic Analysis of a Shallow-Founded Building in Christchurch During the Canterbury Earthquake Sequence. 6th International Conference on Earthquake Geotechnical Engineering, 1-4 November, Christchurch, New Zealand.

Luque, R., and Bray, J. (2017). Dynamic Analyses of Two Buildings Founded on Liquefiable Soils During the Canterbury Earthquake Sequence. *Journal Geotechnical and Geoenvironmental Engineering (ASCE),* In press.

Lysmer, J. and Kuhlemeyer, R.L. (1969). Finite Difference Model for Infinite Media. *Journal of Engineering Mechanics Division,* V. 95, 859-877.

Macedo, J.L. (2009). Dynamic Analysis of Yuracmayo Earth Dam. Thesis, National Univ. of Engineering, Lima, Peru.

Makdisi, F., Seed, H., 1978. Simplified Procedure for Estimating Dam and Embankment Earthquake Induced Deformations. *Journal of Geotechnical Engineering,* V.104(7), 849–867.

Matsumoto, N. (2010). The Recent Earthquakes and Dam Safety in Japan. ICOLD Europe 2010.

Maurer, B.W., Green, R.A., Cubrinovski, M., Bradley, B.A. (2015). Assessment of CPT-Based Methods for Liquefaction Evaluation in a Liquefaction Potential Index (LPI) framework. *Geotechnique,* V.65(5):328–36.

Mejia, L. H., and Dawson, E. M. (2006). Earthquake Deconvolution for FLAC. In Proc, 4th International FLAC Symp. Num. Mod. In Geotechnics, Madrid, Spain, May 2006, 10 pp.

Meyerhof, G. G., and Hanna, A. M. (1978). Ultimate Bearing Capacity of Foundations on Layered Soil Under Inclined Load. *Canadian Geotechnical Journal*, V. 15(4), 565-572.

Newmark, N., (1965). Effects of Earthquakes on Dams and Embankments. *Geotechnique*, V.15(2), 139–160.

Nikolaou, S. et al. (2016). Geo-Engineering Reconnaissance of the April 16, 2016 Muisne, Ecuador Earthquake. GEER Association Report No. GEER-049.

Papadimitriou, A.G., Bouckovalas, G.D., Andrianopoulos, K.I., 2014. Methodology for Estimating Seismic Coefficients for Performance-Based Design of Earth Dams and Tall Embankments. *Soil Dynamics and Earthquake Engineering (SDEE)*, V.56, 57–73.

Pestana, J.M., D'Orazio, T.B., Espinoza, R.D., Bray, J.D., Hunt, C.E., Lok, T.M., and Marstall, K. (1996). Stress and Deformation Analysis of La Esperanza Dam Using GeoFEAP and CONSWELL," in IV Inter. Benchmark Workshop on Numerical Analysis of Dams, ICOLD, Madrid, Spain, Theme B2, 14 pp.

Popescu, R. and Prevost, J.H. (1993). Centrifuge Validation of a Numerical Model for Dynamic Soil Liquefaction. *Soil Dynamics and Earthquake Engineering*, V.12, 73-90.

Popescu, R., Prevost, J.H., Deodatis, G., and Chakrabortty, P. (2006). Dynamics of Nonlinear Porous Media with Applications to Soil Liquefaction. *Soil Dynamics and Earthquake Engineering (SDEE)*, V.26, 648-655.

Rathje, E.M., and Antonakos, G. (2011). A Unified Model for Predicting Earthquake-Induced Sliding Displacements of Rigid and Flexible Slopes. *Engineering Geology*, V.122, 51–60.

Rathje, E.M., Bray, J.D., 1999. An Examination of Simplified Earthquake Induced Displacement Procedures for Earth Structures. *Canadian Geotechnical Journal*, V.36(1), 72–87. doi:10.1139/t98-076.

Rathje, E.M., Bray, J.D., (2000). Nonlinear Coupled Seismic Sliding Analysis of Earth Structures. *Journal Geotechnical and Geoenvironmental Engineering (ASCE)*, V.126(11), 1002–1014.

Rathje, E. M., Bray, J. D., (2001). One- and Two-Dimensional Seismic Analysis of Solid-Waste Landfills. *Canadian Geotechnical Journal*, V. 38(4), 850–862.

Rathje, E.M., Faraj, F., Russell, S., and Bray, J.D. (2004). Empirical Relationships for Frequency Content Parameters of Earthquake Ground Motions. *Earthquake Spectra (EERI)*, V.20(1), 119-144.

Rathje, E.M., Saygili, G., (2008). Probabilistic Seismic Hazard Analysis for the Sliding Displacement of Slopes: Scalar And Vector Approaches. *Journal Geotechnical and Geoenvironmental Engineering (ASCE)*, V.134(6), 804–814.

Rathje, E.M., Saygili, G. (2011). Pseudo-Probabilistic Versus Fully Probabilistic Estimates of Sliding Displacements of Slopes. *Journal Geotechnical and Geoenvironmental Engineering (ASCE)*, V.137(3), 208-217.

Rathje, E.M., Wang, Y., Stafford, P., Antonakos, G., Saygili, G. (2014). Probabilistic Assessment of the Seismic Performance of Slopes. *Bulletin of Earthquake Engineering*, V.12(3), 1071-1090.

Richards, R., Elms, D.G., 1979. Seismic Behavior of Gravity Retaining Walls. *Journal Geotechnical and Geoenvironmental Engineering (ASCE)*, V.105(4), 449–64.

Rodriguez-Marek, A., et al. (2001). Geotechnical Earthquake Engineering Reconnaissance of the June 23, 2001, Southern Peru Earthquake: A Preliminary Report. GEER Association Report No. GEER-006.

Rodriguez-Marek, A., et al. (2007). Preliminary Reconnaissance Report on the Geotechnical Engineering Aspects of the August 15, 2007 Pisco, Peru Earthquake. GEER Association Report No. GEER-012.

Saygili, G., Rathje, E.M., (2008). Empirical Predictive Models for Earthquake-Induced Sliding Displacements of Slopes. *Journal Geotechnical and Geoenvironmental Engineering (ASCE)*, V.134(6), 790–803.

Sancio, R. B. (2003). Ground Failure and Building Performance in Adapazari, Turkey. PhD thesis, Univ. of California at Berkeley, Berkeley, Calif.

Sancio, R., Rice, A., Been, K., and Villet, W. (2015). Seismic Stability Performance of a Coastline Slope beneath a Pipeline: A Case History of Onshore Observations for Offshore Application. Proc., Offshore Technology Conf., Houston, Texas.

Schmertmann, J.H., Hartmann, J.P. and Brown, P.R. (1978). Improved Strain Influence Factor Diagrams. *Journal of the Geotechnical Engineering Division*, V.104 (GT8), 1131-1135.

Seed, H.B., (1979). Considerations in the Earthquake-Resistant Design of Earth and Rockfill Dams. *Geotechnique*, V.29(3), 215-263.

Shakir, H. and Pak, A. (2010). Estimating Liquefaction-Induced Settlement of Shallow Foundations by Numerical Approach. *Computer and Geotechnics*, V.37(3), 267-279.

Song, J., and Rodriguez- Marek, A. (2014). Sliding Displacement of Flexible Earth Slopes Subject to Near- Fault Ground Motions. *Journal Geotechnical and Geoenvironmental Engineering (ASCE)*, V.141(3), DOI:10.1061/(ASCE)GT.1943- 5606.0001233.

Stockwell, R., Mansinha, L., Lowe RP (1996). Localization of the Complex Spectrum: The S transform. *IEEE Trans Signal Process*, V. 44(4), 998–1001.

Travasarou, T., Bray, J. D., Der Kiureguian, A., 2004. A Probabilistic Methodology for Assessing Seismic Slope Displacements, Paper No. 2326, in Proceedings, 13th World Conference on Earthquake Engineering, 2004, Vancouver, B.C., Canada.

Travasarou, T., Bray, JD., Sancio, RB. (2006). Soil–Structure Interaction Analyses of Building Responses During the 1999 Kocaeli Earthquake. Proceedings of the 8th US National Conference on Earthquake Engineering, 100th Anniversary Earthquake Conference Commemorating the 1906 San Francisco Earthquake. EERI, April, Paper 1877.

Trifunac, M.D. and Brady, A.G. (1975). A Study for the Duration of Strong Earthquake Ground Motions. *Bulletin of the Seismological Society of America*, V.65, 584-626.

Tokimatsu, K., and Seed, H.B. (1987). Evaluation of Settlements in Sands Due to Earthquake Shaking. *Journal Geotechnical and Geoenvironmental Engineering (ASCE)*, V.113(8), 861–878.

Tokimatsu, K., et al. (2011). Quick Report on Geotechnical Problems in the 2011 Tohoku Pacific Ocean Earthquake. Research Reports on Earthquake Engineering, CUEE, Tokyo Institute of Technology, #118, 21-47 (in Japanese).

Urzúa, A., and Christian, J.T. (2013). Sliding Displacements Due to Subduction-Zone Earthquakes. *Engineering Geology*, V.166, 237–244.

van Ballegooy S, Lacrosse V, Simpson J, Malan P. (2015). Comparison of CPT-Based Simplified Liquefaction Assessment Methodologies Based on Canterbury Geotechnical Dataset. In: Proceedings of the 12th Australia-New Zealand Conference on Geomechanics. Wellington, New Zealand: NZGS & AGS; 2015. p. 618–25.

van Ballegooy S, Malan P, Lacrosse V, Jacka ME, Cubrinovski M, Bray JD, et al. (2014). Assessment of Liquefaction-Induced Land Damage for Residential Christchurch. *Earthquake Spectra (EERI)*, V. 30(1), 31–55.

Verdugo, R., Sitar, N, Frost, J.D., Bray, J.D., Candia, G., Eldridge, T., Hashash, Y., Olson, S.M., and Urzua, A. (2012). Seismic Performance of Earth Structures: Dams, Levees, Tailings Dams and Retaining Walls. *Earthquake Spectra (EERI)*, V.28(S1), S75-S96.

Wang, Y. and Rathje, E. (2015). Probabilistic Seismic Landslide Hazard Maps Including Epistemic Uncertainty. *Engineering Geology*, V.196, 313-324.

Wartman, J., Bray, J. D., and Seed, R. B. (2003). Inclined Plane Studies of the Newmark Sliding Block Procedure. *Journal Geotechnical and Geoenvironmental Engineering (ASCE)*, V.129(8), 673–684.

Watson-Lamprey, J., Abrahamson, N., 2006. Selection of Ground Motion Time Series and Limits on Scaling. *Soil Dynamics and Earthquake Engineering (SDEE)*, V.26 (5), 477–482.

Yamaguchi, Y., Kondo, M., Kobori, T., and Mitsuishi, S. (2011). Effects on Dams due to the 2011 off the Pacific Coast of Tohoku Earthquake. PWRI report.

Yamaguchi, Y., Kondo, M., and Kobori, T. (2012). Safety Inspections and Seismic Behavior of Embankment Dams During the 2011 off The Pacific Coast of Tohoku Earthquake. *Soils and Foundations*, V.52(5), 945–955.

Yang, Z., Elgamal, A., and Parra, E. (2003). Computational Model for Cyclic Mobility and Associated Shear Deformation. *Journal Geotechnical and Geoenvironmental Engineering*, 10.1061/*(ASCE)*1090-0241(2003)129:12(1119), 1119–1127.

Yegian, M. K., Marciano, E. A., Ghahraman, V. G., (1991). Earthquake-Induced Permanent Deformations: Probabilistic Approach. *Journal of Geotechnical Engineering*, V.117, 35–50.

Yoshimi, Y. and Tokimatsu, K. (1977). Settlement of Buildings on Saturated Sand During Earthquakes. *Soils and Foundations*, V.17 (1), 23-38.

Zhang, G., Robertson, P.K., and Brachman, R.W.I. (2002). Estimating Liquefaction-Induced Ground Settlements from CPT for Level Ground. *Canadian Geotechnical Journal*, V. 39, 1168-1180.

Zhang, G., Robertson, P.K., Brachman, R.W.I. (2004). Estimating Liquefaction induced Lateral Deformations from SPT and CPT. *Journal Geotechnical and Geoenvironmental Engineering (ASCE)*, V.130(8), 861-871.

Zhao, J. X., Zhang, J., Asano, A., Ohno, Y., Oouchi, T., Takahashi, T., Ogawa, H., Irikura, K., Thio, H. K., Somerville, P. G., Fukushima, Y. (2006). Attenuation Relations of Strong Ground Motion in Japan Using Site Classification Based on Predominant Period. *Bulletin Seismological Society of America*, V. 96(3), 898–913.

Zupan, JD. (2014). Seismic Performance of Buildings Subjected to Soil Liquefaction. Ph.D. Dissertation, University of California, Berkeley.

Zupan, J.D., Trombetta, N.W., Puangnak, H., Paez, D., Bray, J.D., Kutter, B. L., Hutchinson, T. C., Fiegel, G. L., Bolisetti, C., and Whittaker, A. S. (2013). Seismic Performance Assessment in Dense Urban Environments, Centrifuge Data Report for Test-5, University of California, Davis.

APPENDIX A: VALIDATION OF THE SIMPLIFIED SLOPE DISPLACEMENT PROCEDURE FOR SUBDUCTION ZONES

This appendix examines the ability of the proposed semi-empirical model in chapter 2, to estimate the observed seismically-induced slope displacements on geotechnical systems that were shaken by subduction zone interface earthquakes. 12 case histories were used for the validation. The case histories include nine earth dams (one dam underwent three events) and a coastline slope beneath a pipeline. The observations from these case histories were only used to validate the proposed procedure and were not included in the dataset for the estimation of the coefficients of the model.

Table A.1 lists the 12 case histories, along with the information from the corresponding earthquake events, and the observed maximum permanent displacements. In all cases the maximum observed displacement is the portion of the permanent displacement attributed to stick-slip type movement and distributed deviatoric shear within the deformable mass. Ground movement resulting from volumetric compression has been subtracted from the total observed permanent displacement when appropriate, since a Newmark-type model, as the model proposed in this study, does not capture the mechanisms that result in volumetric compression. The Tokimatsu and Seed (1987) procedure has been used to estimate the seismically-induced displacements associated to volumetric mechanisms when considered appropriate.

Table A.1. Comparison of the estimated seismic slope displacement with the observed displacement.

System	Earthquake	Date	Mw	Site Class	Rrup (km)	Obs.Dmax (cm)[1]
(1)	(2)	(3)	(4)	(5)	(6)	(7)
Coastline Slope	Pisco	8/15/2007	8.0	Rock	40	6.0
Dam in the Andes	Pisco	8/15/2007	8.0	Alluvium	125	None
La Villita dam	S3[a]	3/14/1979	7.4	Alluvium	121	1.0
La Villita dam	S4[a]	10/25/1981	7.2	Alluvium	31	1.4
La Villita dam	S5[a]	9/21/1985	8.0	Alluvium	58	4.0
Torata dam	Moquegua	6/23/2001	8.4	Rock	100	5.0
Esperanza dam	Muisne	4/16/2016	7.8	Alluvium	50	None
Tutuven dam	Maule	2/27/2010	8.8	Alluvium	40	None
Nishigo dam	Tohoku	11/3/2011	9.0	Alluvium	90	40
Shitoki dam	Tohoku	11/3/2011	9.0	Rock	52	None
Surikamigawa dam	Tohoku	11/3/2011	9.0	Alluvium	90	None
Coihueco Dam	Maule	2/27/2010	8.8	Alluvium	20	~350

[1] D_{max} = observed maximum displacement due to shear deformation. "None" listed if D is negligible.

[a] from Elgamal et al. (1990)

The coastline slope system corresponds to the development of an LNG export facility in Peru during early 2006, which included the excavation of a Quarry Haul Road and a pipeline Sleeper Way from the Plant Site (excavated to Elev. +125 m) down through the coastal cliffs to the lower levels near the sea shore where construction staging platforms were built (Sancio et al. 2016). In addition, surface stripping and grade leveling activities were carried out at the Plant Site in preparation for the construction of the LNG processing train and storage tanks. Excavation totaled approximately 860,000 m3. A large portion of the stripped material was bulldozed over the cliff onto the existing colluvial materials in the undercliff area at different locations.

The Sleeper Way was built as a path for the LNG cryogenic pipeline to traverse the topographic relief of about 130 m over a distance of about 300 m from the Storage Area to the Beach Area. A

1.5-km long marine jetty would then carry the pipeline to an LNG carrier berthing area for export. The details of the coastline slope are provided in Sancio et al. (2016). The slope was shaken by the 15 August 2007 Mw 8.0 Pisco, Peru earthquake. Information for the deviatoric seismically-induced displacements was obtained from instrumentation installed on the slope that recorded the seismically-induced displacements by Sancio et al. (2016). The yield coefficient is provided by Sancio et al. (2016) and the initial fundamental period was estimated from the shear wave velocity information provided by Sancio et al. (2016). The spectral acceleration at the degraded period of the system was estimated from the Abrahamson et al. (2016) ground motion prediction equation. The parameters estimated for the coastline slope are shown in Table A.1.

The "dam in the Andes" system corresponds to an earth dam located in the Junín province of Peru, approximately 170 kilometers east of Lima. The dam is used for water regulation, it is 567 m in length and 56 m in height, with upstream and downstream slopes of 2.5H: 1V and 1.72H: 1V, respectively. The dam site is located in a complex, geologically active region east of a major plate boundary where numerous damaging historical earthquakes have occurred. Peru, as with most of western South America, is situated along the western edge of the convergent plate boundary between the South America plate in the east and Nazca plate to the west. The eastern edge of the oceanic Nazca plate in this region is marked by the deep Peru-Chile Trench (PCT) offshore. The western edge of the continental South America plate is marked by broad, high mountains of the Western and Eastern Cordillera of Peru, and the numerous folds and faults that mark the eastern boundary of the Andes Range. Two accelerometers were installed in the dam, one of them in an inspection tunnel at bedrock level and the other one in the crest. Detailed information about the dam is provided by Macedo (2009). The dam was shaken by the 15 August 2007 Mw 8.0 Pisco, Peru earthquake. Information for the deviatoric seismically-induced displacements was obtained from the instrumentation installed on the dam (Macedo 2009). The yield coefficient of the dam and the initial fundamental period is provided by Macedo (2009), the spectral acceleration at the degraded period was estimated using the Abrahamson et al. (2016) ground motion equation prediction. The parameters estimated for the "dam in the Andes" system, are shown in Table A.1.

The case history of La Villita Dam in Mexico has been documented by Elgamal et al. (1990) and has been also used by Bray and Travasarou (2007) as a case history to evaluate the performance of their procedure, formulated for shallow crustal settings, on subduction zones. La Villita dam It is an earth/rockfill dam that has been subjected to six major subduction zone earthquakes since its construction in 1968, three of which are back analyzed in terms of deformations in the current study. These events, referred to as 53, S4, and S5 occurred at March 14, 1979, October 25, 1981, and September 19, 1985, respectively. Bray and Travasarou (2007), based on the inclinometers records during the seismic events, provide estimates for the observed deviatoric seismically-induced displacements. Estimations for the yield acceleration for the dam, the initial fundamental period of the dam and the spectral accelerations at the degraded period of the dam are provided by Bray and Travasarou (2007). The parameters estimated for La Villita dam are shown in Table A.1.

The Torata dam is a 110-meter high concrete face rockfill dam (CFRD) that is owned and operated by Southern Copper Corporation, SCC, (formerly called Southern Peru Copper Corporation SPCC), located approximately 4 km upstream from the town of Cuajone. It has a crest length of about 450 meters, a 1.6H:1V upstream slope (concrete face) and 1.4H:1V downstream slope. The dam was completed in 2001 and creates a freshwater reservoir with a capacity of approximately 16 million cubic meters. The dam was shaken by the 23 June 2001 Mw 8.4 Moquegua, Peru earthquake. The deviatoric seismically-induced displacements caused by the

seismic event was obtained from the instrumentation installed on the dam (CISMID-personal communication, Rondinel, 2010), subtracting the seismic displacements associated with volumetric compression which were estimated based on the Tokimatsu and Seed (1987) method. Information about the dam is provided by Rondinel (2010). Figure A.1 show the estimation of the yield coefficient. The Initial fundamental period of the dam is provided by Rondinel (2010), and was estimated from ground motion recordings in the dam for small events, and shear wave velocity measurements. The spectral acceleration at the degraded dam period was estimated using the Abrahamson (2016) ground motion prediction equation, and nearby ground motion recordings during the earthquake. The parameters estimated for the Torata dam are shown in Table A.1.

La Esperanza dam is a zoned embankment, 47 meters high, with a crest length of 700 m. The embankment has silty sand shells and a clay core. The dam was shaken by the 16 April 2016 Mw 7.8 Muisne, Ecuador earthquake. The post-event reconnaissance efforts reported negligible seismically-induced displacements for the dam (Nikolaou et al. 2016). Information about the dam is provided by Pestana et al. (1996). Figure A.2 show the estimation of the yield coefficient. The initial fundamental period of the dam was estimated from the material stiffness properties provided by Pestana et al. (1996). The spectral acceleration at the degraded period of the dam was estimated from the Abrahamson et al. (2016) ground motion prediction equation. The parameters estimated for la Esperanza dam are shown in Table A.1.

The Tutuven dam was built in 1951 as a homogenous dam and was repaired in 1979 due to serious damage caused by a flood. Its crest length is about 1000 m, and its maximum height is 17 m. The dam was shaken by the 27 February 2010 Mw 8.8 Maule, Chile earthquake, without observed damage. Verdugo et al. (2012) provide a description of the dam materials that was used to estimate the initial fundamental period. Figure A.3 show the estimation of the yield coefficient. The spectral acceleration at the degraded period of the dam was estimated from the Abrahamson et al. (2016) ground motion prediction equation. The parameters estimated for the Tutuven dam are shown in Table A.1.

The case histories consider 3 dams shaken by the 11 March 2011 Mw 9.0 Tohoku, Japan earthquake. The dams are the Nishigo dam, the Shitoki dam and the Surikamigawa dam. The material properties of these dams, geometric configurations, initial fundamental period, and observations for their performance after the Tohoku earthquake are provided by Matsumoto (2010), EERI (2011), Yamaguchi et al. (2011), Yamaguchi et al. (2012), 14 Bray (2013), Mr. Matsumoto (personal communication), Mr. Satou of NILIM (personal communication). Figure A.4 shows the estimation of the yield coefficient for the Nishigo dam. Figure A.5 shows the estimation of the yield coefficient for the Shitoki dam and Figure A.6 shows the estimation of the yield coefficient for the Surikamigawa dam. The parameters estimated for the Japanese dams considered in this study are shown in Table A.1.

The Nishigo dam is a 32.5 m high earthfill dam completed in 1955. According to Bray (2013) the Tohoku earthquake caused 30-45 cm of maximum downslope displacements in the upstream shell and 20 cm of settlements. Considering that approximately 10 cm of the induced settlements are due to shear-induced displacements, the maximum deviatoric seismically-induced displacement is approximately 40 cm. The spectral acceleration at the degraded period has been estimated from the ground motions recorded in nearby stations and the Abrahamson et al. (2016) ground motion equation prediction.

The Shitoki dam is a 83.5 m high rock fill dam completed in 1984. EERI (2011) reports only some minor local cracking with maximum deviatoric seismically-induced displacements lesser

than 1 cm. The spectral acceleration at the degraded period has been estimated from the Abrahamson et al. (2016) ground motion equation prediction.

The Surikamigawa dam, is a central earth-core type rockfill dam (ECRD) with a height of 105.0 m completed in 2006. As a result of the detailed investigation, after the Tohoku earthquake, it was concluded that there was no threat to the safety of the dam (Yamaguchi, et al. 2012). The observed deviatoric seismically-induced displacements after removing the volumetric induced displacements as estimated using the Tokimatsu and Seed (1987) procedure is negligible. The spectral acceleration at the degraded period has been estimated from the Abrahamson et al. (2016) ground motion equation prediction.

The Coihueco dam was built in 1970, it is located approximately 28 km east of Chillán, Chile. It is a zoned earthfill dam that has a crest length of 1,040 m long and a maximum height of 31 m. The dam was shaken by the 27 February 2010 Mw 8.8 Maule, Chile earthquake. Following the earthquake, a portion of the upstream slope experienced a failure that generated significant deformations and cracks as shown in Figure A.7. Maximum vertical displacements of the upstream slope were observed towards the left abutment, reaching values close to 4 m (Verdugo et al. 2012). From the total observed seismically-induced displacements, approximately 3.5 m are associated with deviatoric seismically-induced displacements. The fundamental period of the dam and the yield coefficient were estimated from the information provided by Verdugo et al. (2012). Figure A.8 shows the estimation of the yield coefficient. The spectral acceleration at the degraded period has been estimated from the ground motions recorded in nearby stations and the Abrahamson et al. (2016) ground motion equation prediction. The parameters estimated for the Coihueco dam are shown in Table A.1.

The comparison of the proposed model estimates of seismic displacement with the maximum observed seismic permanent displacement is shown in Table A.2. For this comparison, only mean or median values of the slope's yield coefficient, initial fundamental period, and the spectral acceleration at 1.5 times the initial fundamental period are considered. The computed seismic displacement range is for values that the probability of exceeding is 84% and 16%, which is computed using Equation 2.6 by solving d for $P(D>d) = 0.84$ and 0.16, respectively. The displacement range is due to the variability in the seismic displacement given the values of the slope properties and the seismic load (i.e., $\sigma = 0.73$ from Equation 2.4). Overall, the proposed model provides reasonable estimates of the observed seismic performances of the 12 earth system case histories examined in this study.

There are five case histories in which the observed seismic slope displacement was noted as being "None." The proposed method estimates high probabilities of "zero" displacement (i.e., 100% that $D \leq 0.5$ cm) for the dam in the Andes, Shitoki dam, and Surikamigawa dam. There is a 50% probability of "zero" displacement and a seismic displacement range of 0–2 cm for Esperanza dam, which is consistent with the negligible displacement observed at this earth dam after the 2016 Muisne, Ecuador earthquake. Lastly, there is a 65% probability of "zero" displacement and a seismic displacement range of 0–2 cm for Tutuven dam, which is also consistent with the negligible displacement observed at this dam after the 2010 Maule, Chile earthquake. Thus, the proposed method's assessment of seismic performance is consistent with the good seismic performance observed of these earth structures

There are two case histories with observed seismic displacements of a few centimeters (i.e., 5 cm for Torata dam and 6 cm for the coastline slope in Peru). The proposed model is able to capture the observed seismic displacements for these cases. The estimated seismic displacement range is 1 to 7 cm for the Torata dam and 3 to 12 cm for the coastline slope. Good seismic performance

was also observed for the La Villita Dam in Mexico (Elgamal et al. 1990). Its performance during three earthquake events is well-documented with increasing levels of the observed seismic displacements from Events S3, S4, and S5. The proposed model develops estimates of seismic displacement with the same trends. There is a high probability of "zero" displacements (80%) for Event S3 where the maximum observed displacement was 1 cm, which is considered a negligible level of displacement for an earth dam. There is a relatively low probability of "zero" displacement (10%) with a range of estimated seismic displacement from 1 to 7 cm, which encompasses the observed value of 4 cm for Event S5.

Table A.2. Comparison of the estimated seismic slope displacement with the observed displacement

System	Obs. D_{max} (cm)[1]	k_y	T_s (s)	$S_a(1.5T_s)$ (g)	Proposed Method[2] P (D = "0")	Proposed Method[2] Est. Disp (cm)
(1)	(2)	(3)	(4)	(5)	(6)	(7)
Coastline Slope[3]	6.0	0.10	0.6	0.25	0.00	3-12
Dam in the Andes[4]	None	0.27	0.45	0.14	1.00	<1
La Villita dam[5]	1.0	0.20	0.60	0.20	0.80	<1
La Villita dam[5]	1.4	0.20	0.60	0.33	0.30	0-2
La Villita dam[5]	4.0	0.20	0.60	0.41	0.10	1-7
Torata dam[6]	5.0	0.13	0.65	0.24	0.10	1-7
Esperanza dam[7]	None	0.24	0.40	0.43	0.50	0-2
Tutuven dam[8]	None	0.39	0.15	0.75	0.60	0-2
Nishigo dam[9 to 15]	40	0.26	0.15	1.51	0.00	14-58
Shitoki dam[9 to 15]	None	0.29	0.40	0.40	0.70	0-1.5
Surikamigawa dam[9 to 15]	None	0.30	0.68	0.22	0.90	<1
Coihueco Dam[9]	~350	0.10	0.25	1.35	0.00	60-260

[1] D_{max} = observed maximum displacement due to shear deformation. "None" listed if D is negligible.

[2] P(D=0) from Eqs. (2.2)-(2.3). Zero displacement refers to negligible displacement (i.e., D<0.5 cm). Estimated displacement range is 16% to 84% from Eqs. (2.2)-(2.7).

[3] Sancio et al. (2016), [3,4] Rodriguez-Marek et al. (2007), [4] Macedo (2009), [5] Elgamal et al. (1990), [6] Rodriguez-Marek et al. (2001), [6] CISMID (personal communication), [7] Pestana et al. (1996), [7] Nikolaou et al. (2016), [8] Verdugo et al. (2012), [8] Bray and Frost (2010), [9] Matsumoto (2010), [10] EERI (2011), [11] Yamaguchi et al. (2011), [12] Yamaguchi et al. (2012), [13] Bray (2013), [14] Mr. Matsumoto (personal communication), [15] Mr. Satou of NILIM (personal communication).

The proposed model's estimates are intermediate for Event S4, which is consistent with the observed seismic performance of the dam for this event. Thus, the proposed method provides seismic displacement estimates that are consistent with the trends of the observed seismic performance of La Villita Dam for these earthquake events.

There is one case of moderate seismic displacement, which corresponds to the Nishigo dam shaken by the 2011 Tohoku Earthquake. Nishigo dam underwent approximately 40 cm of seismic displacement due to shear-induced deformation in this event. The proposed method estimates essentially no chance of "zero" displacement occurring for this case and a range of expected seismic slope displacement (i.e., 14-58 cm) that includes the observed shear-induced seismic slope displacement of 40 cm.

For the Coihueco dam case history the proposed method estimates that there is a negligible chance of "zero" displacement occurring. The calculated shear-induced seismic slope

displacement range is from 60 cm to 260 cm, which is indicative of large displacements likely occurring. The observed seismic slope displacement value is above the 84% seismic displacement estimate, but it is within 1.5 standard deviations of the median estimate of seismic slope displacement. Importantly, the proposed method is capable of predicting the unsatisfactory seismic performance of an earth dam, as it is unlikely that an engineer would accept the design of a dam that could undergo over 3 m of total seismic displacement (with up to 2.6 m of shear-induced displacement) for a reasonable earthquake scenario in this area of Chile.

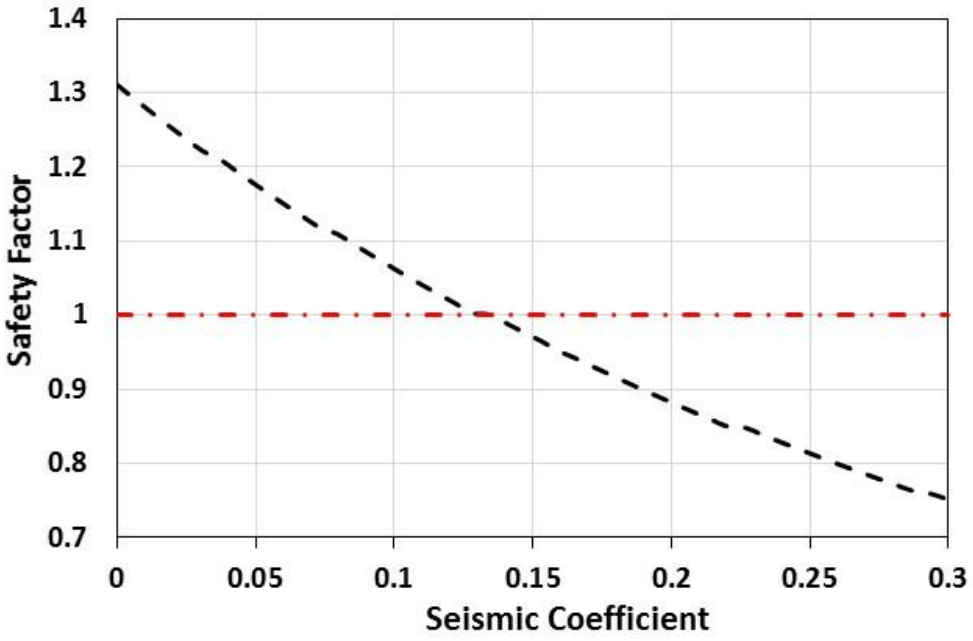

Figure A.1. Estimation of the yield coefficient for the Torata dam (k_y=0.13).

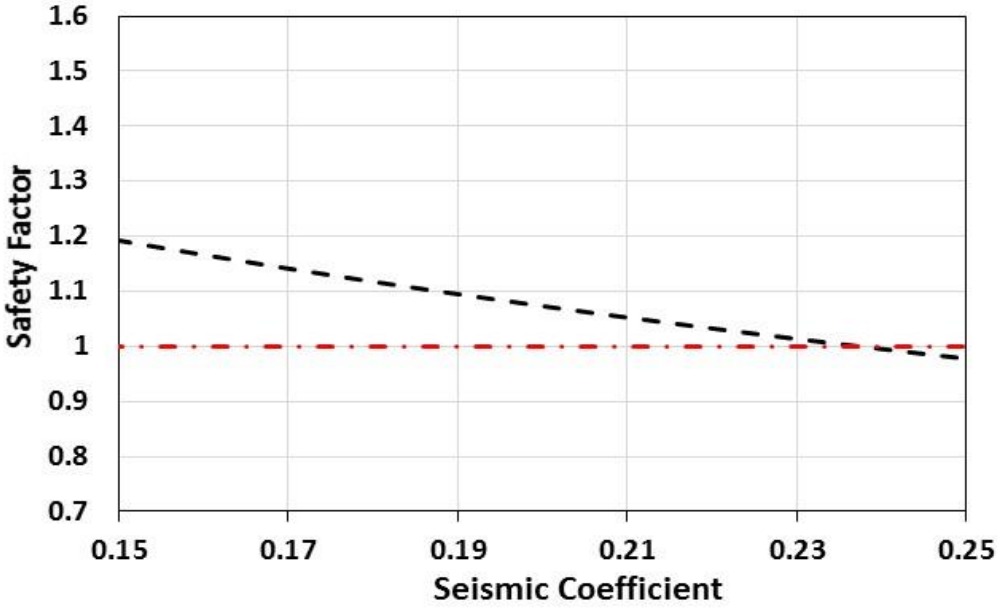

Figure A.2. Estimation of the yield coefficient for the Esperanza dam (k_y=0.24).

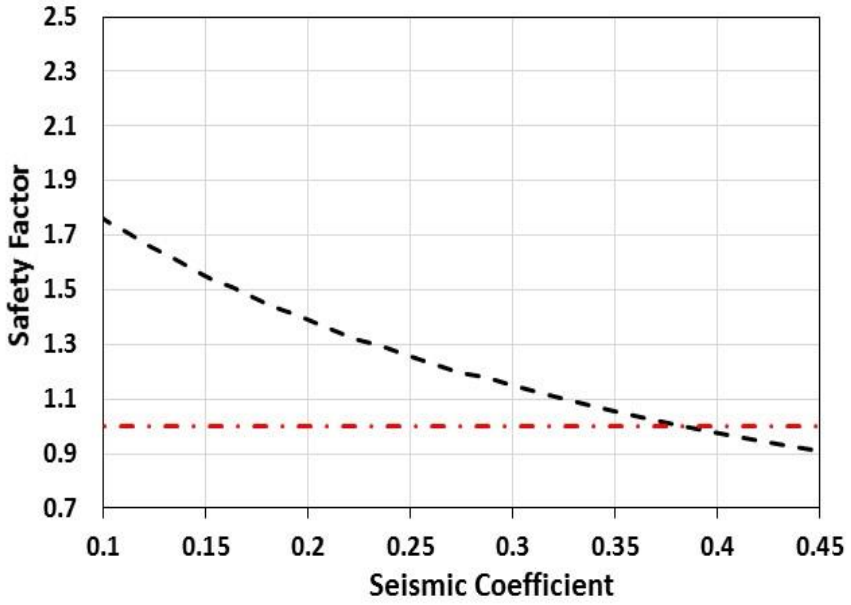

Figure A.3. Estimation of the yield coefficient for the Tutuven dam (k_y=0.39).

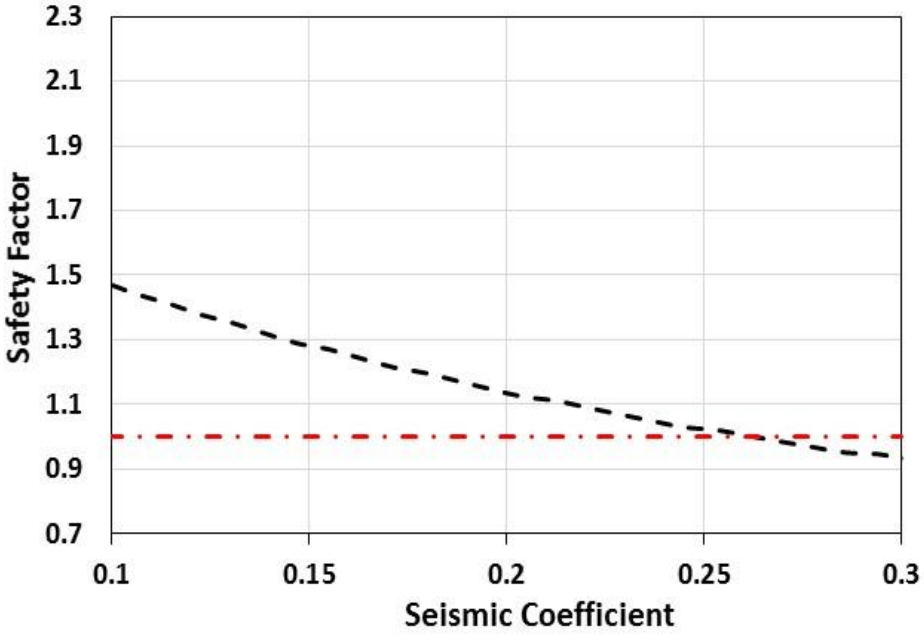

Figure A.4. Estimation of the yield coefficient for the Nishigo dam (k_y=0.26).

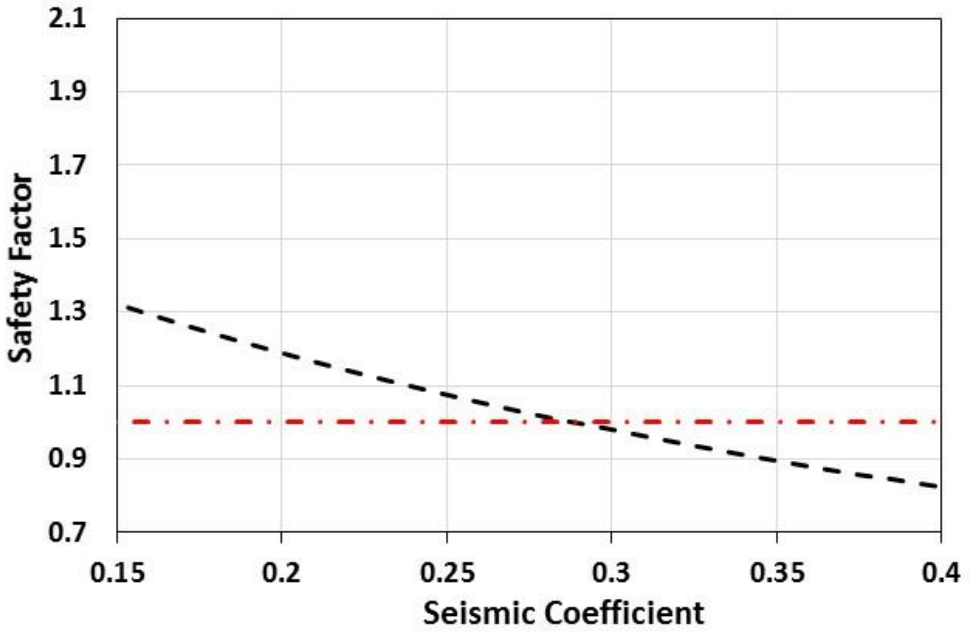

Figure A.5. Estimation of the yield coefficient for the Nishigo dam (k_y=0.29).

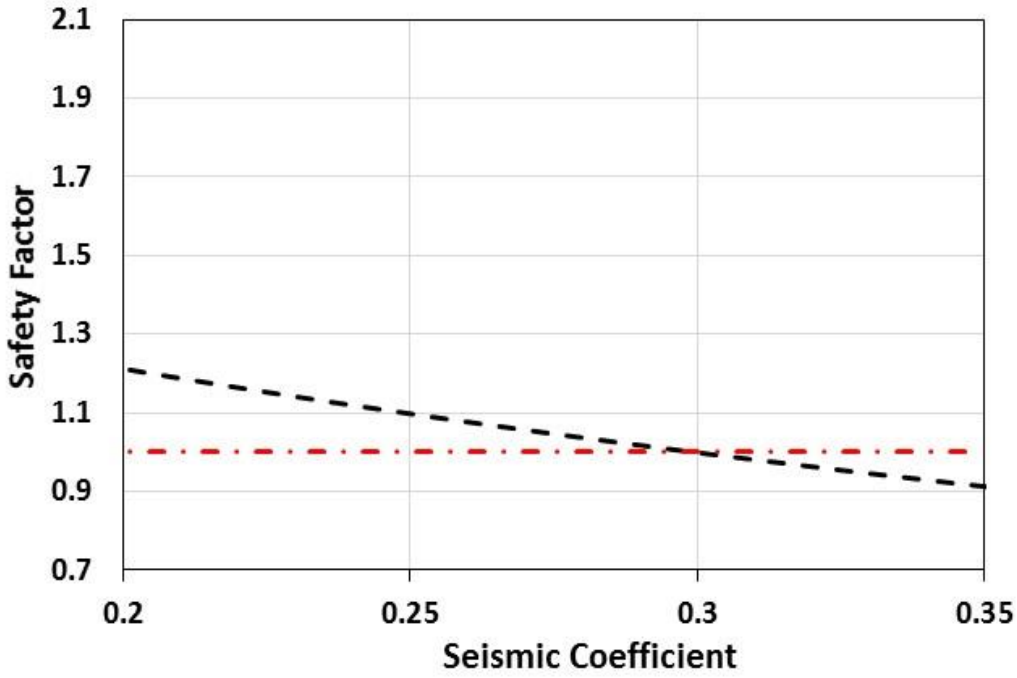

Figure A.6. Estimation of the yield coefficient for the Surikamigawa dam (k_y=0.30).

Figure A.7. Top: Failure of the upstream slope of Coihueco dam bottom: Longitudinal crack along crest (Verdugo et al. 2012).

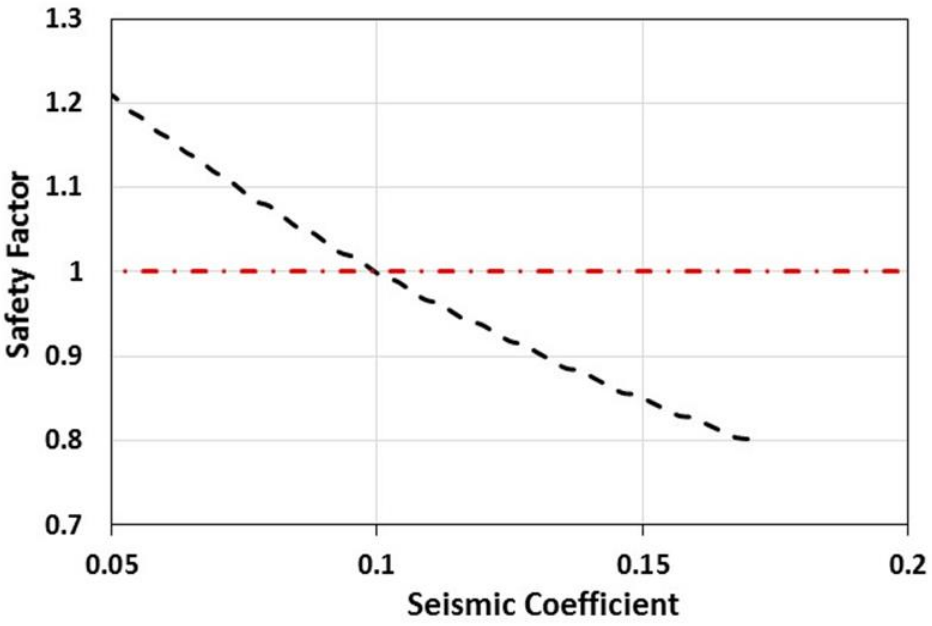

Figure A.8. Estimation of the yield coefficient for Coihueco dam (k_y=0.10).

APPENDIX B.1: MATHEMATICAL FORMULATION FOR THE INTEGRATION BY PARTS PROCEDURE

This appendix presents the derivations for the Integration of parts procedure, which is used to perform the convolution of the intensity measure (*IM*) hazard curve and the seismic displacement (*D*) model. The derivations are presented for the case of shallow crustal settings without magnitude dependence, shallow crustal settings with magnitude dependence and subduction settings with magnitude dependence.

SHALLOW CRUSTAL SETTINGS WITHOUT MAGNITUDE DEPENDENCE

The seismic displacement model from Bray and Travasarou (2007) is used. The probability of "zero" displacement and the median value of the amount of "non-zero" seismic displacement for the shallow crustal earthquake case without magnitude dependence are given by Equations B.1 and B.2, respectively.

$$P(D = \text{"0"}) = 1 - \Phi(-1.76 - 3.22Ln(k_y) - 0.484T_sLn(k_y) + 3.52Ln(S_a)) \quad \text{(B.1)}$$

$$Ln(\hat{d}) = -1.10 - 2.83Ln(k_y) - 0.333\left(Ln(k_y)\right)^2 + 0.566Ln(k_y)Ln(S_a) + 3.04Ln(S_a) - 0.244\left(Ln(S_a)\right)^2 + 1.5T_s \quad \text{(B.2)}$$

Where Φ is the standard normal cumulative distribution function, k_y is the yield coefficient, T_s is the initial fundamental period, S_a is the spectral acceleration at the system's degraded period (taken as 1.5 times the initial fundamental period), and $(\hat{d})$ is the median seismic displacement. The first term in Equation B.2 should be replaced by -0.22 when $T_S < 0.05s$.

The first term inside the integral in Equation 3.1 from chapter 3 can be evaluated as:

$$P(D > d|\, S_a, k_y, T_s) = \left[1 - P(D = \text{"0"}|\, S_a, k_y, T_s)\right]\left[P(D > d|\, S_a, k_y, T_s, D > \text{"0"})\right] \quad \text{(B.3)}$$

Considering a lognormal distribution for seismic displacements (*D*), the probability of *D* greater than a threshold *d*, for given values of S_a, k_y and T_s, is estimated from Equation B.4:

$$P\left(D > d\,\middle|\, k_y, T_s, S_a, D > \text{"0"}\right) = 1 - \Phi\left(\frac{Ln(d) - Ln(\hat{d})}{\sigma_{LnD}}\right) \quad \text{(B.4)}$$

Where σ_{LnD}= 0.67, which corresponds to the standard deviation of the error in Equation B.2. To simplify the expressions in Equation B.1 and B.4, the variables $\Phi 1$ and $\Phi 2$ are defined as:

$$\Phi 1 = \Phi(-1.76 - 3.22Ln(k_y) - 0.484T_sLn(k_y) + 3.52Ln(S_a)) \quad \text{(B.5)}$$

$$\Phi 2 = \Phi\left(\frac{Ln(d) - Ln(\hat{d})}{\sigma_{LnD}}\right) \quad \text{(B.6)}$$

Considering only the integral over the spectral acceleration (I_{S_a}) and remembering $\Delta\lambda(S_a)$s the derivative of the hazard curve (*Ha*), Equation 3.1 in chapter 3 can be represented as:

$$I_{S_a} = \int_0^\infty \Phi 1(1 - \Phi 2)\left|\frac{dHa}{dS_a}\right| dS_a \quad \text{(B.7)}$$

Using Equations B.5, B.6 and.B.3. Employing integration by parts and noticing that the derivative of the hazard curve is negative, one arrives with:

$$I_{S_a} = \Phi(1 - \Phi 2)Ha|_0^\infty + \int_0^\infty Ha\frac{d}{dS_a}[\Phi(1 - \Phi 2)]dS_a \quad \text{(B.8)}$$

Where Φ1 and Φ2 are function of k_y, $T_s$and S_a. *Ha* is function of S_a.

The first term in Equation B.8 vanishes, because the hazard function *Ha* evaluated at an "infinite" $S_a$value is zero, and the functions Φ1 or $(1-\Phi 2)$ are zero when evaluated at S_a equal to zero. Performing a change of variables to evaluate the integral in a logarithmic space, I_{S_a} reduces to:

$$I_{S_a} = \int_{-\infty}^{\infty} Ha(Ln(Sa)) \frac{d}{dLn(S_a)} \left[\left(\Phi 1 \left(k_y, T_s, \text{Ln}, (S_a) \right) \right) \right] dLn(S_a) \quad \text{(B.9)}$$

The derivative inside the integral is:

$$\frac{d}{dLn(S_a)} [\Phi(1-\Phi 2)] = (1-\Phi 2). \frac{d}{dLn(S_a)} (\Phi 1) + \Phi 1. \frac{d}{dLn(S_a)} (1-\Phi 2) \quad \text{(B.10)}$$

Using Equation B.5 and the chain rule:

$$\frac{d}{dLn(S_a)} (\Phi 1) = 3.52 PDF1(k_y, T_s, \text{Ln}, (S_a)) \quad \text{(B.11)}$$

where $PDF1(k_y, T_s, \text{Ln}, (S_a))$is the normal standard distribution that corresponds to the cumulative distribution function in Equation B.5. Using Equations B.6, B.2, and the chain rule:

$$\frac{d}{dLn(S_a)} (1-\Phi 2) = \frac{PDF2(k_y, T_s, \text{Ln}, (S_a))}{\sigma_{LnD}} \left[0.566 Ln(k_y) - 0.488 Ln(S_a) + 3.04 \right] \quad \text{(B.12)}$$

where $PDF2(k_y, T_s, \text{Ln}(S_a))$ is the normal standard distribution that corresponds to the cumulative distribution function in Equation B.6. Finally, using Equations B.10, B.11, and B.12 in Equation B.9 results in:

$$I_{S_a} = \int_{-\infty}^{\infty} \left\{ 3.52 PDF1(Ha)(1-\Phi 2) + (Ha)(\Phi 1) \left(\frac{PDF2}{\sigma_{LnD}} \right) \begin{bmatrix} 0.566 Ln(k_y) - \\ 0.488 Ln(S_a) + 3.04 \end{bmatrix} \right\} dLnS_a \quad \text{(B.13)}$$

Equation B.13 can be used directly in Equation 3.1 in chapter 3 to estimate the displacement hazard curve if the best estimated values (e.g. mean) for k_y and T_s are considered (i.e. their weighting factors are set to 1 in Equation 3.1 in chapter 3). To account for material inhomogeneity and variability in the strength of the soil, the epistemic variability for the yield coefficient (k_y) and the system's initial fundamental period (T_s) can be considered through a logic tree scheme as described in chapter 3.

SHALLOW CRUSTAL SETTINGS WITH MAGNITUDE DEPENDENCE

Bray and Travasarou (2007) prefer the use of their Equation to estimate the median "non-zero" seismic displacements which includes the magnitude term:

$$Ln(\hat{d}) = -1.10 - 2.83 Ln(k_y) - 0.333 \left(Ln(k_y) \right)^2 + 0.566 Ln(k_y) Ln(S_a) + 3.04 Ln(S_a) - 0.244 Ln(S_a)^2 + 1.5 T_s + 0.278 (M-7) \quad \text{(B.14)}$$

The probability of "zero" displacement relationship does not include magnitude, so it remains as defined previously as Equation B.1. The probability of a seismic displacement *D* greater than

a given value d and for given values of k_y, T_s, S_a, and M, is estimated from Equation B.4 with σ_{LnD} equal to 0.66 (which corresponds to the standard deviation of the error term in Equation B.14).

Using the "integration by parts" approach, $Ha_M(S_a, M)$ is defined for a specified magnitude as:

$$Ha_M(S_a, M) = Ha(S_a)P(M|S_a) \tag{B.15}$$

where, $Ha(S_a)$ represents the hazard function at the degraded period of the system and $P(M|S_a)$ can be estimated from the hazard deaggregation for the magnitude term. Thus, for a selected magnitude (representative of a magnitude bin), the first integral in Equation 3.2 in chapter 3 can be expressed as:

$$I2_{S_a} = \int_0^{\infty} P(D > d|S_a, M, k_y, T_s) \left|\frac{dHa_M(S_a,M)}{dS_a}\right| dS_a \tag{B.16}$$

With the terms defined as in Equations 3.2 in chapter 3 and B.15. Thus, the first two integrals in Equation 3.2 in chapter 3 can be approximated as:

$$I2_{S_a,M} = \sum_{i=1}^{Mtot^{\infty}} \int_0^{\infty} P(D > d|S_a, M, k_y, T_s) \left|\frac{dHa_M(S_a,M)}{dS_a}\right| dS_a \tag{B.17}$$

where *Mtot* is the total number of magnitude bins, and the magnitude is kept constant in each bin. A magnitude bin of 0.2 is used in this study. The parameter $I2_{S_a}$ in Equation B.16 can be evaluated following the same procedure as presented before for the no magnitude dependence case. However, the function Ha_M, as expressed by Equation A.15, needs to be used in lieu of the hazard function *Ha*, which was used previously. The function Φ1 or its derivative (Equation B.5 and B.11) do not need to be modified; however, Φ2 is defined by Equation A.6 with $Ln(\hat{d})$ now defined by Equation B.14. The derivative of $1 - \Phi 2$ is as in the previous case (Equation B.12). As indicated in Equation B.17, the procedure needs to be repeated for each magnitude bin. Uncertainty of k_y and T_s can be considered if necessary through a logic tree scheme as described in chapter 3.

SUBDUCTION INTERFACE SETTING WITH MAGNITUDE DEPENDENCE

Bray et al. (2017) provide a predictive Equation to estimate the probability of "zero" displacements and the median "non-zero" displacement for subduction interface earthquakes. These Equations include a dependence on the magnitude term for the median "non-zero" seismic displacement and can be used in the same way as described before for the predictive Equations for the shallow crustal settings with magnitude dependence. The required Bray et al. (2017) relations are:

$$P(D = \text{"0"}) = 1 - \Phi\left(-2.64 - 3.20Ln(k_y) - 0.17\left(Ln(k_y)\right)^2 - 0.49T_sLn(k_y) + 2.09T_s + 2.91Ln(S_a)\right) \quad \text{for cases where } T_s \leq 0.7s \tag{B.18}$$

$$P(D = \text{"0"}) = 1 - \Phi\left(-3.53 - 4.78Ln(k_y) - 0.34\left(Ln(k_y)\right)^2 - 0.30T_sLn(k_y) + 0.67T_s + 2.66Ln(S_a)\right) \quad \text{for cases where } T_s > 0.7s \tag{B.19}$$

The amount of the "nonzero" median seismic slope displacement ($\hat{d}$) in centimeters is estimated as:

$$Ln(\hat{d}) = a1 - 3.353Ln(k_y) - 0.390\left(Ln(k_y)\right)^2 + 0.538Ln(k_y)Ln(S_a) + 3.060Ln(S_a) - 0.225\left(Ln(S_a)\right)^2 + a2T_s + a3(T_s)^2 + 0.550M \pm \varepsilon \quad \text{(B.20)}$$

where k_y, T_s, and $S_a(1.5T_s)$ are as defined previously, M is moment magnitude, and is a normally distributed random variable with zero mean and standard deviation $\sigma = 0.73$. In Equation B.2, for systems with $T_s \geq 0.10$ s, $a1 = -6.896$, $a2 = 3.081$, and $a3 = -0.803$, and for $T_s < 0.10$ s, $a1 = -5.864$, $a2 = -9.421$, and $a3 = 0.0$. There is only a slight change in the calculated seismic displacement across the value of $T_s = 0.10$ s. And $\Phi 1$ and $\Phi 2$ are defined as:

$$\Phi 1 = \Phi\left(-2.64 - 3.20Ln(k_y) - 0.17\left(Ln(k_y)\right)^2 - 0.49T_sLn(k_y) + 2.09T_s + 2.91Ln(S_a))\right) \quad \text{If } T_s \leq 0.7 \quad \text{(B.21)}$$

$$\Phi 1 = \Phi\left(-3.53 - 4.78Ln(k_y) - 0.34\left(Ln(k_y)\right)^2 - 0.30T_sLn(k_y) + 0.67T_s + 2.66Ln(S_a))\right) \quad \text{If } T_s > 0.7 \quad \text{(B.22)}$$

$$\Phi 2 = \Phi\left(\frac{Ln(d) - Ln(\hat{d})}{\sigma_{LnD}}\right), \quad \sigma_{LnD} = 0.73 \quad \text{(B.23)}$$

The derivatives of $\Phi 1$ and $\Phi 2$ with respect to $Ln(S_a)$, required to solve Equation B.10 are calculated using Equations B.21, B.22 and B.23. The seismic displacement hazard curve is derived using Equations B.16, B.17, and Equation 3.2 in chapter 3. Uncertainty of k_y and T_s can be considered if necessary through a logic tree scheme as described in chapter 3.

APPENDIX B.2: IMPLEMENTATION OF THE PROCEDURES TO ESTIMATE THE SEISMIC DISPLACEMENT HAZARD CURVE

As part of supplemental materials for publication, we provided the files in the link below, which are used to perform 1) the calculations to estimate the seismic displacement hazard curve and 2) the performance-based estimation of the seismic coefficient to be used in pseudostatic stability analyses. Instructions to use the files are also provided.

https://www.dropbox.com/sh/kdlro8onr04indr/AACz4tS9GtvfMZhrGFQKqpEma?dl=0

APPENDIX C: ADDITIONAL EXAMPLE FOR ESTIMATION OF LIQUEFACTION-INDUCED SETTLEMENTS

The simplified liquefaction-induced building settlement procedure presented in this study (Chapter 5) is applied to an example case to offer an additional illustration of its use. The building considered in this case is the CTUC building, which was also one of the field case histories described in Chapter 5. The liquefaction-induced building settlement is assessed for the Christchurch earthquake. Figure C.1 shows the plan view of the building and Section A-A' with the soil profile under the building. Liquefaction-induced settlements are estimated for the southeast corner of the building (from CPT Z4-5 shown in Figure C.1) and for the northeast corner of the building (from CPT Z4-7 shown in Figure C.1).

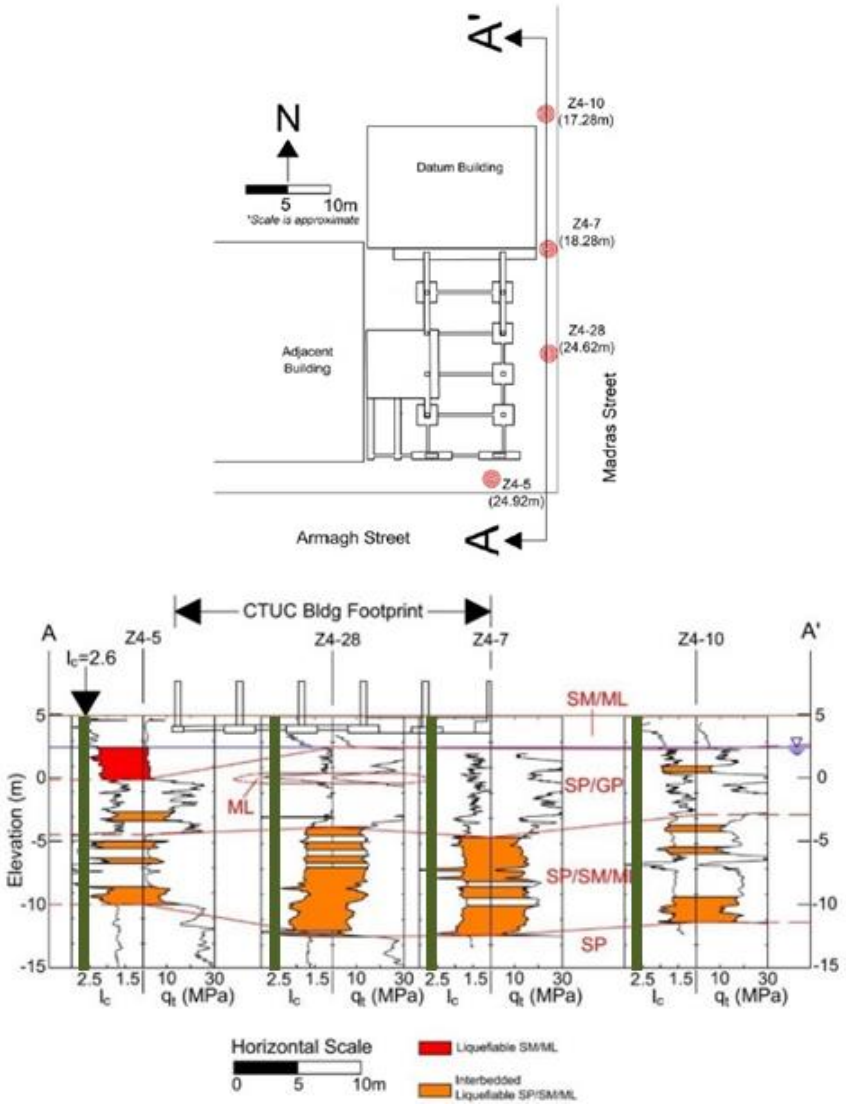

Figure C.1. Plan view (top) and section A-A' (bottom) of the CTUC building (Zupan 2014).

The groundwater depth was estimated to be 2.5 m for the Christchurch event. As described in Luque and Bray (2017), there is a fill at the surface which is underlain by a shallow silty sand/sandy silt (SM/ML) layer that extends down to a depth of 2.5 m across the site, except for at the building's

south side where this layer extends to 5 m depth. Its CPT tip resistance (q_t) is generally less than 5 *MPa*, and its Soil Behavior Type Index (I_c) is generally between 2.2 and 2.4. Thus, the loose SM/ML layer below the groundwater table is likely to liquefy when strongly shaken. A dense gravelly sand with q_t values of 20-30 *MPa* underlies the shallow SM/ML layer and extends to 7.5-9 m depth. The gravelly sand is underlain by a medium dense sand and silty sand with q_t values of 10-20 *MPa* and I_c values of 1.6-1.9, which extends down to a depth of 16-17 m. There are thin layers of silts and clayey soil layers, with I_c = 2.9-3.2 within this layer of medium dense sand and silty sand. A dense sand soil layer with q_t = 25-30 *MPa* and I_c = 1.6-1.8 is below a depth of 16-17 m and extends down to 21 m. An overconsolidated silty clay (I_c > 2.6) underlies this unit down to a depth of 21 m to 24 m. The dense Riccarton Gravel unit underlies the overconsolidated clay unit.

PGA and S_a1 are estimated from an appropriate GMPE. The NGA-West2 GMPEs are appropriate for shallow crustal earthquake events such as the Christchurch earthquake. Excel files with the implementation of these GMPE can be downloaded from: http://peer.berkeley.edu/ngawest/nga_models.html. CAV_{dp} is estimated from the Campbell and Bozorgnia (2011) GMPE, which has a similar set of input parameters as the NGA-West2 GMPE. With the earthquake parameters (e.g., rupture distance, magnitude, and fault type) and site conditions (e.g., V_{S30}) appropriate for this site and the Christchurch event, median values of *PGA*, S_a1, and CAV_{dp} are estimated. In this case, nearby ground motion recordings are available, so the values of *PGA* = 0.45 *g*, S_a1 = 0.90 *g* and CAV_{dp} = 1.00 *g-s* from these recordings are used. The total building pressure over its full width, and the contact pressure and width for individual footings were used in two calculations and the results averaged because the footings of this building are poorly connected. The combinations building width/contact pressure used for the calculations are 1) *B*=20 m, *Q*=70 kPa and 2) *B*= 1m, *Q*= 200 kPa, respectively.

Following the simplified procedure for estimating liquefaction-induced building settlement delineated in Chapter 5 of this study, these steps are carried out:

1. The safety factor against liquefaction triggering (*FSL*) is calculated for the site conditions shown in Figure C.1 using the CPT-based Boulanger and Idriss (2016) procedure. The colored soil layers have *FSL* values less than 1.0. The thickness of the liquefiable soil layers (*HL*) are estimated as the summation of the layers with safety factor against triggering lesser than 1.0. *HL* is estimated to be approximately 5m for the SE corner and 6 m for the NE corner of the building.
2. The post-liquefaction bearing capacity safety factor (*FS*) is calculated to be 0.9 using the Meyerhof and Hanna (1978) method with a post-liquefaction residual strength of the liquefied soil layer of 8 kPa (based on Idriss and Boulanger 2008) and using an average shear strength of the non-liquefied crust layer of 35 kPa. As the post-liquefaction bearing capacity *FS* is less than 1.0, the proposed simplified procedure may underestimate liquefaction-induced building settlement. However, the calculation is continued to develop a rough estimate of the potential liquefaction-induced building settlement for this case, because the post-liquefaction bearing capacity *FS* is close to one.
3. At the SE corner, there is the presence of liquefiable materials close to the surface; whereas that is not the case at the NE corner. The *LSN* value at the SE corner is 28 and the *LPI* is 22; whereas at the NE corner, *LSN* is 5 and *LPI* is 7. Considering the relatively high *LSN* and *LPI* values at the SE corner of the building and considering the Ishihara (1985) ground failure design chart, ejecta is assumed to occur at the southern part of the building. An average estimate of about 100 mm of sediment ejecta-induced settlement (*De*) is assumed to occur with an estimated range of 75 mm to 150 mm.

4. The 1D post-liquefaction volumetric-induced building settlement (*Dv*) of the soil profile is estimated using the Zhang et al. (2002) procedure. *Dv* is estimated to be 150-250 mm for the SE corner and 100-200 mm for the NE corner of the building.

5. LBS is estimated from Equation 7 using the Zhang et al. (2004) procedure with the FSL values for each layer estimated previously. The "clean sand" equivalent relative density is estimated from a combination of three correlations presented in Idriss and Boulanger (2008), Kulhawy and Mayne (1990), and Jamilkowski et al. (2001) with 0.4, 0.3 and 0.3 weights, respectively. *LBS* is estimated as 57 and 10 for the SE and NE corners of the building, respectively. The shear-induced building settlement (*Ds*) due to liquefaction is estimated using Equation 5.9 with these input parameters for the SE corner calculation: Sa= 0.90 g, CAV_{dp}= 1.0 g-s, *B*= 20,1 m, *Q*= 70,200 kPa, *HL*= 5 m, and *LBS*= 57, and for the NE corner calculation: S_a= 0.90 g, CAV_{dp}= 1.0 g-s, *B*= 20,1 m, *Q*= 70,200 kPa, *HL*= 6 m, and *LBS*= 10 (the settlements are averaged for the 2 B, *Q* scenarios as previously discussed. The estimated shear-induced building settlements (*Ds*) are 110-290 mm with a median estimate of 180 mm for the SE corner and 40-120 mm with a median estimate of 70 mm for the NE corner.

6. The median estimate of the total liquefaction-induced building settlement (*Dt*) of the SE building corner is:

Dt = *De* + *Dv* + *Ds* = 100 mm + 200 mm + 180 mm = 480 mm, with *Dt* ranging from 330 mm to 690 mm.

The median estimate of the total liquefaction-induced building settlement (*Dt*) of the NE building corner is:

Dt = *De* + *Dv* + *Ds* = 0 mm + 150 mm + 70 mm = 220 mm, with *Dt* ranging from 140 mm to 320 mm.

7. Considering the results of the analyses presented above, the estimated median differential settlement across the building footprint is 260 mm (i.e., 480 mm – 220 mm). The median estimated differential settlement is consistent with the observed differential settlement of 250 mm. As much of the differential building settlement will occur over the southernmost two bays (see Figure C.1), the seismic performance of the building is judged to be unsatisfactory in terms of likely exceeding the angular distortion threshold for structural damage (i.e., $\alpha > 1/150$). It is not likely that this level of settlement will cause collapse; however, a structural engineer would need to make this assessment.